UNIVERSITY OF CALIFORNIA

Los Angeles

Modeling and Optimization of Light Transfer in Outdoor Microalgae Cultivation Systems

A dissertation submitted in partial satisfaction

of the requirements for the degree

Doctor of Philosophy in Mechanical Engineering

by

Jack Hoeniges

2022

ABSTRACT OF THE DISSERTATION

Modeling and Optimization of Light Transfer in Outdoor Microalgae Cultivation Systems

by

Jack Hoeniges
Doctor of Philosophy in Mechanical Engineering
University of California, Los Angeles, 2022
Professor Laurent G. Pilon, Chair

Value-added products derived from photosynthetic microalgae could serve as a useful renewable resource in the face of mounting pressures on food, energy, and water systems from global climate change. In addition to acting as a carbon sink, microalgae are fast-growing organisms whose rich biodiversity is reflected in their variety of potential applications, ranging from cosmetics and pharmaceuticals to biofuels, food products, and animal feed. Light transfer plays a vital role in the productivity of outdoor microalgae cultivation systems. Indeed, in the case of optimal operating conditions such as temperature, pH, and nutrient availability, microalgae growth depends entirely on the rate of light absorption by the cells. However, large-scale microalgae cultivation typically takes place in outdoor raceway ponds where light transfer can be impacted by a variety of factors. For instance, outdoor raceway ponds may feature a transparent cover to achieve better control of the growth conditions. However, evaporation from the culture results in condensate droplets on the underside of the cover, potentially reducing the window transmittance and solar energy input to the culture. Furthermore, a variety of species of interest for value-added products readily form colonies either in the forms of aggregate-like clusters or of ordered spherical shells. Such a change in the arrangement of the cells may impact their ability to absorb the incoming photons. Finally, outdoor ponds are subject to low solar intensities and large angles of incidence in

winter, mornings, and evenings. These phenomena may result in limiting light transfer conditions and low biomass productivity and remain major barriers to unlocking the potential of microalgae as a sustainable and inexpensive source of value-added products. Therefore, a comprehensive understanding of light transfer in microalgae cultivation systems is necessary to optimize their performance.

This dissertation aims (1) to quantify the impact of small and large condensate droplets on the transmittance of transparent windows and on the performance of outdoor raceway ponds, (2) to assess the impact of colony formation on light absorption by microalgae cells, and (3) to investigate the use of external reflecting surfaces to increase light availability in dense cultures and increase raceway pond productivity. First, light transmittance through horizontal and tilted windows supporting large pendant droplets was predicted for various droplet volumes, contact angles, and window tilt angles. Compared to windows supporting small droplets, the transmittance of windows supporting large droplets was up to 37% smaller for horizontal windows and up to 14% larger for tilted windows. Then, light transfer through a window supporting small, cap-shaped droplets was coupled with a growth kinetics model to elucidate the impact of condensate droplets on the biomass productivity of an outdoor raceway pond. Biomass productivity was predicted to decrease by up to 18% when condensate droplets were present. Second, light transfer in aggregate-like colonies of *Botryococcus braunii* was also investigated both experimentally and numerically. Good agreement was found between the experimental and predicted absorption cross-sections. This approach was also applied to study light absorption in larger, ordered colonies like those observed in species of the *Volvocaceae* family. In both cases, mutual shading between the cells in the colonies decreases light absorption by up to 23% compared to single cells, which may decrease the algae growth rate. Third, the performance of a novel reflecting outdoor raceway pond design was predicted throughout the year for two locations and several different design configurations. A single south-facing mirror was predicted to increase biomass productivity by as much as 73% in the winter months. Overall, the biomass productivity was found to improve throughout the year thanks to the increased solar energy input provided by the additional sunlight reflected onto the culture surface. This approach could extend the growing season for outdoor cultivation

of microalgae.

The dissertation of Jack Hoeniges is approved.

Pei-Yu Chiou

Adrienne G. Lavine

Aaswath Pattabhi Raman

Jeremy Pruvost

Laurent G. Pilon, Committee Chair

University of California, Los Angeles

2022

To my partner, Tiffany Lam

TABLE OF CONTENTS

LIST OF FIGURES

LIST OF TABLES

ACKNOWLEDGMENTS

First, I would like to thank my advisor, Professor Laurent Pilon. His innate curiosity, breadth of knowledge, and dedication to his craft has given myself and my labmates a career to aspire to. I will be forever grateful for his time, candor, and genuine care for my personal and professional success. I would also like to thank Professor Jeremy Pruvost for his support and encouragement and for sharing his expertise on all things bioprocesses. I would equally like to express my gratitude to Professors Eric Chiou, Adrienne Lavine, and Aaswath Raman for serving on my doctoral committee.

This work would not be possible without the collaboration of researchers that came before me. To that effect, I acknowledge the work of Professor Keyong Zhu for his assistance with the ray tracing simulations used in Chapters 2 and 3, Professor Gaurav Bhutani for his assistance with the *Surface Evolver* program used in Chapter 2, Dr Razmig Kandilian for his experimental work included in Chapter 4, Dr Arka Bhowmik for sharing his work which served as the basis for the study performed in Chapter 5, and Dr Refet Yalçin for his assistance with the T-matrix simulations performed in Chapter 5.

I thank my labmates who made my time at UCLA so memorable, namely Dr Eylul Simsek Turan, Dr Tiphaine Galy, Dr Sara Vallejo-Castano, Matevž Frajnkovič, Ali Dashti, Sun Woong Baek, Dr Ampol Likitchatchawankun, William Welch, Yucheng Zhou, Ricardo Martinez, Abhinav Bhanawat, Dr Michal Marszewski, and Dr Obaidallah Munteshari. To my family I express my profound gratitude for their encouragement and comfort. Finally, I thank my love, Tiffany Lam. In many ways this dissertation is a testament to the unending support, and compassion that she has graciously given me throughout the past years.

I would like to thank the Mechanical and Aerospace Engineering at UCLA for their support via the departmental Graduate Fellowship. This research was supported in part by the National Science Foundation NRT-INFEWS: Integrated Urban Solutions for Food, Energy, and Water Management (Grant No. DGE-1735325) and the DISCUS project of the NExT Initiative (Nantes Excellence Trajectory) International Research Partnership. I would

also like to acknowledge the International Research Network (ex-GDRI) WONDER (World Oilalg Network for Design of Processes and Strains for Elaboration of Renewable Energy from Microalgae) of the French Centre National de la Recherche Scientifique (CNRS) for its support.

VITA

2013–2018 B. S., Mechanical Engineering and French, Summa Cum Laude
Valparaiso University

2018–2019 M.S., Mechanical Engineering
University of California, Los Angeles

2019–2022 Ph.D., Mechanical Engineering
University of California, Los Angeles

PUBLICATIONS

J. Hoeniges, R. Kandilian, C. Zhang, J. Pruvost, J. Legrand, D. Grizeau, and L. Pilon, "Effect of colony formation on light absorption by *Botryococcus braunii''*, *Algal Research*, vol. 50, no. 101985, 2020.

J. Hoeniges, K. Zhu, J. Pruvost, J. Legrand, and L. Pilon, "Impact of dropwise condensation on the biomass production rate in covered raceway ponds", *Energies*, vol. 14, no. 268, 2021.

J. Hoeniges, K. Zhu, W. Welch, E. Simsek, L. Pilon,"Transmittance of transparent horzontal and tilted windows supporting large non-absorbing pendant droplets", *Journal of Quantitative Spectroscopy and Radiative Transfer*, vol. 275, no. 107876, 2021

J. Hoeniges, W. Welch, J. Pruvost, L. Pilon,"A novel external reflecting raceway pond for improved biomass productivity", *Algal Research*, vol. 65, no. 102742, 2022

E. Simsek, M. J. Williams, **J. Hoeniges**, K. Zhu, L. Pilon, "Infrared radiation transfer through semitransparent windows supporting absorbing droplets", International Journal of Heat and Mass Transfer, vol. 194, no. 123043, 2022.

J. Hoeniges, A. Bhowmik, R. A. Yalcin, V. J. Partusch, L. Pilon, "Light absorption by *Volvocaceae* colonies consisting of equidistant optically soft photosynthetic cells in a transparent extracellular matrix", *Algal Research* (under review)

R. Martinez, **J. Hoeniges**, W. Welch, L. Pilon "Impact of condensate droplet formation on the freshwater productivity of tilted solar stills" *In preparation*

CHAPTER 1

Introduction

1.1 Motivation

The reality of an anthropogenic climate crisis is a well-established fact [1]. Burning fossil fuels for human economic activity has driven atmospheric levels of carbon dioxide, methane, and nitrous oxide to their highest levels in the past 800,000 years [1]. This has resulted in a net positive radiative forcing effect causing global temperatures to rise consistently over the last 30 years. Such global warming poses a variety of risks, including rising sea levels and more frequent and intense droughts, floods, and heat waves [1]. These events strain existing systems of food production and exacerbate water scarcity [1]. Furthermore, the impacts of the climate crisis are disproportionately felt by disadvantaged populations and developing countries [1].

Addressing the challenges posed by the climate crisis will require a multitude of innovations at the nexus of food, energy, and water systems. In particular, photosynthetic microalgae have garnered interest as a fast-growing crop for human and animal feed [2], as a source of biomass for carbon-neutral biofuels [3], and as a valuable ingredient in food supplements, nutraceuticals, and cosmetics [4]. Thanks to their rapid growth and high nutrient and protein content, microalgae cultivation uses significantly less resources than conventional agriculture [5]. Furthermore, a variety of microalgae species can grow in brackish or wastewater for simultaneous bioremediation and biomass production [6–8]. Moreover, microalgae can metabolize carbon in the form of CO_2 and can therefore be used to fixate CO_2 from flue gases emitted from industrial processes and coal or natural gas power plants [9].

Table 1.1: Various microalgae species and their corresponding products (adapted from Ref. [12]).

Algal species	**Products**
Arthrospira (Spirulina) platensis	Biomass feedstock, protein, Vitamin B12, Phycocyanin
Scenedesmus sp.	Biomass feedstock, protein
Aphanizomenon flos-aquae	Fatty acids, β-Carotene
Dunaliella salina	β-Carotene, carotenoids
Haematococcus pluvialis	Carotenoids, astaxanthin
Chlorella vulgaris	Biofuel production, carbohydrate

1.2 Microalgae species and value-added products

Microalgae are found in diverse forms including unicellular and multicellular organisms as well as colonies. Thanks to their impressive biodiversity, different microalgae species can produce a variety of useful products. Some examples are given in Table 1.1. The first commercially available microalgae-based products were health-foods mainly derived from robust and fast-growing species such as *Spirulina* and *Chlorella* [10], pictured in Figures 1.1a and 1.1b, respectively. These species remain among the most commonly cultivated microalgae species today [11]. The carotenoid β-carotene was the among the first high-value commercialized products produced from the microalgae *D. salina*, sold for approximately $300-1500 per kilogram [10]. Currently, a myriad of microalgae-based products have been made available for industrial and commercial use. The current worldwide market for microalgae is estimated at around $6.5 billion, 38% of which is accounted for by food supplements [12].

Colony-forming microalgae species have also been studied for use in a wide range of biotechnological applications. Figure 1.1c shows an example of a spherical colony of *Volvox aureus*. For instance, microbial proteins derived from *Volvox carteri* which respond to photostimulation by yellow light have been studied for potential application in optogenetics [13]. Furthermore, flocculation in non-colony forming microalgae such as *Chlamydomonas rein-*

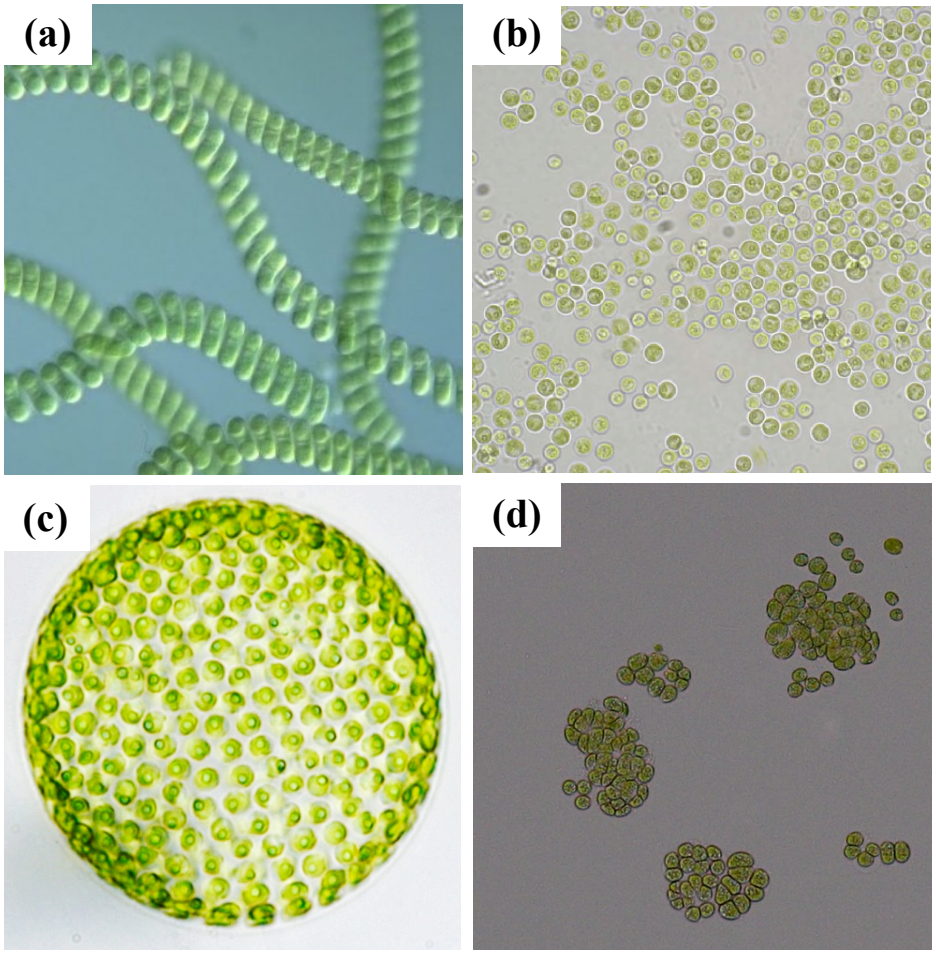

Figure 1.1: Micrographs of (a) the filamentous *Arthrospira platensis* (*Spirulina*), (b) the predominately single-cell algae *Chlorella vulgaris*, and the colony-forming species (b) *Volvox aureus* and (c) *Botryococcus braunii*

hardtii can be induced by heterologous expression of a cell adhesion molecule also found in *Volvox carteri* [14]. Additionally, *Eudorina elegans* has been studied for its potential use in phycoremediation. Indeed, the high levels of surface mucilage present on the surface of the colony extracellular matrix (ECM) of *Eudorina elegans* enable superior absorption of heavy metals such as copper compared to single cell species such as *Chlorella vulgaris* [15]. *Eudorina elegans* has also been used as part of a biosensor featuring a consortium of microalgae strains immobilized on a permeable membrane for real-time monitoring of water-soluble herbicides [16].

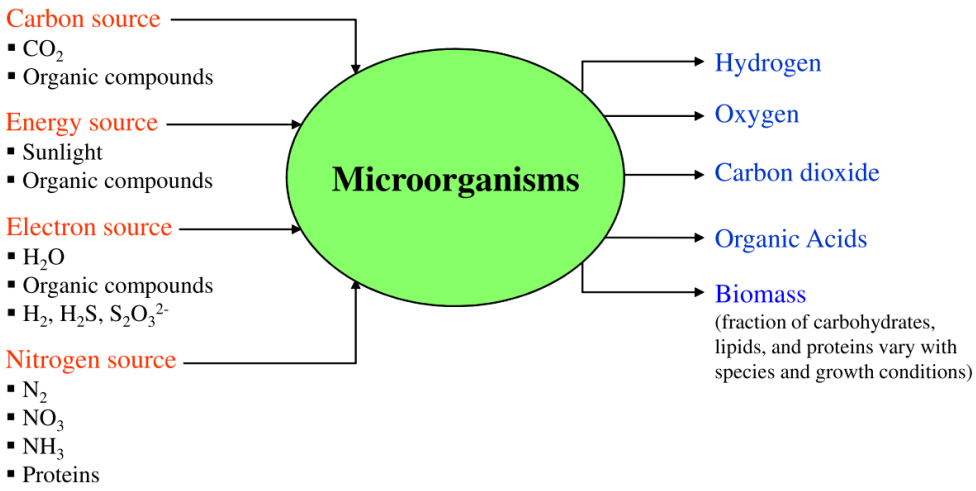

Figure 1.2: A schematic depiction of microalgae cultivation, including required inputs and various output products.

Botryococcus braunii is another colony forming microalgae that has been widely studied for (i) its potential integration into wastewater treatment [6, 7], (ii) its capacity to produce antibacterial and antioxidant extracts [17–19], and (iii) its superior ability to produce hydrocarbons [7, 20–27]. Indeed, *B. braunii* can achieve up to 75% of its dry weight in hydrocarbons, mainly located outside the cells in the colony ECM [20, 22]. In particular, the B race of *B. braunii* produces hydrocarbon botryococcenes of the general formula C_nH_{2n-10} where n ranges from 30-37 [24]. Its aggregate-like colony structure is illustrated in Figure 1.1d.

1.3 Microalgae cultivation

Figure 1.2 illustrates the basic elements required to grow microalgae for biomass and other useful byproducts. Microalgae are mainly composed of proteins, carbohydrates, and lipids, in various proportions, depending on the species and growth conditions [12]. As a photoautotroph, microalgae require an organic carbon, typically in the form of dissolved CO_2, and light as their energy source [28]. For photosynthesis to occur, the light delivered to the microalgae must be in the photosynthetically active radiation (PAR) region, defined by

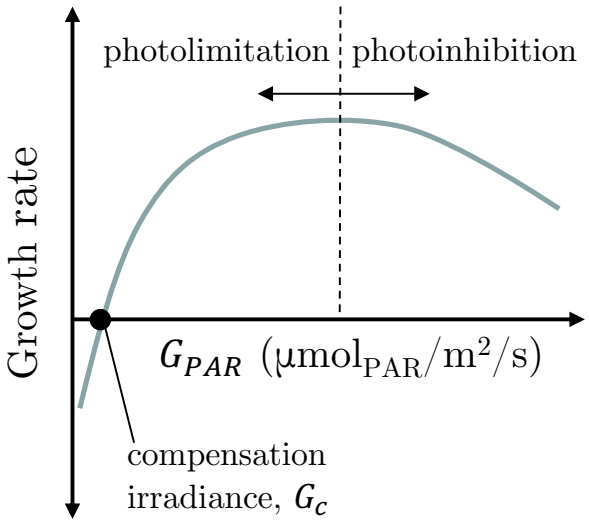

Figure 1.3: Photosynthetic growth response of microalgae subjected to a given photosynthetic irradiance G_{PAR}. Adapted from Ref. [30].

wavelength ranging from 400 to 750 nm [28]. This light can come from artificial or natural sources [29]. Microalgae are generally grown in liquid media containing nutrients such as N, P, and S and other micronutrients such as Mg, Ca, Mn, Cu, and Fe [29]. The majority of microalgae species grow best in neutral to slightly alkaline medium with pH from 7-9 [12].

Figure 1.3 illustrates the growth rate of a microalgae cell subjected to a given photosynthetic irradiance, denoted by G_{PAR}. The compensation irradiance, denoted by G_c, represents the threshold where oxygen produced by photosynthesis is completely consumed by cell respiration and no net growth occurs [30, 31]. At larger values of irradiance, the growth rate increases with increasing irradiance up to a maximum value [30, 31]. This is the so-called "photolimited" regime. Finally, at high values of irradiance, excess light results in damage to the light reaction centers and growth decreases with increasing light availability [31]. This is the so-called "photoinhibited" regime.

While natural microalgae growth occurs readily in a variety of conditions, optimizing their growth for industrial-scale cultivation poses a number of technical challenges [32]. Cultivation systems must be optimized to deliver light and nutrients to the microalgae, while also maintaining other growth conditions near their optimum, such as temperature, pH, and

dissolved O_2. In addition, the costs associated with construction, operation, land use, water use, and nutrient sourcing must be minimized [33]. In general, microalgae cultivation systems are classified as open or closed. Open systems, such as the raceway ponds depicted in Figure 1.4a, are the most widespread method for large-scale microalgae cultivation, due to their relatively low construction and operating costs [33]. These systems are generally shallow and feature paddle-driven flow to prevent sedimentation and facilitate CO_2 and nutrient mixing. However, open raceway ponds can be easily contaminated, lack effective temperature control, suffer from water loss by evaporation, and have relatively high harvesting costs, due to their low cell concentration compared to closed systems [32]. Their operation also results in CO_2 degassing [34].

By contrast, closed cultivation systems, such as the closed raceway pond shown in Figure 1.4b, typically have a lower risk of contamination and a higher biomass productivity than open systems [32, 36]. In a closed raceway pond, a transparent window covering the culture and containing an over-pressurized gas space can be used to limit culture contamination, reduce CO_2 degassing [34], and improve control of the growth conditions [32]. The use of a transparent window enables the cultivation of a wider variety of species and thus greater potential for the production of high value-added products, without significantly increasing construction and maintenance costs [32, 36]. However, evaporation from the culture causes large condensate droplets to form on the underside of the transparent cover (see Figure 1.4). Previous numerical and experimental studies have demonstrated that the presence of small droplets can decrease the transmittance of windows and scatter transmitted photons [37–41]. However, to the best of our knowledge, the transmittance of windows supporting large droplets and the effect of scattering by droplets on the biomass productivity of covered raceway ponds has not been investigated.

For both open and closed raceway ponds in outdoor conditions, large solar incidence angles occur in the mornings and evenings and during the winter months when the solar elevation angle may be small depending on the latitude where the raceway pond is operated. As a result, the incident solar radiative flux decreases compared to situations when sunlight is nearly normally incident on the culture [42]. Moreover, sunlight delivered at oblique angles

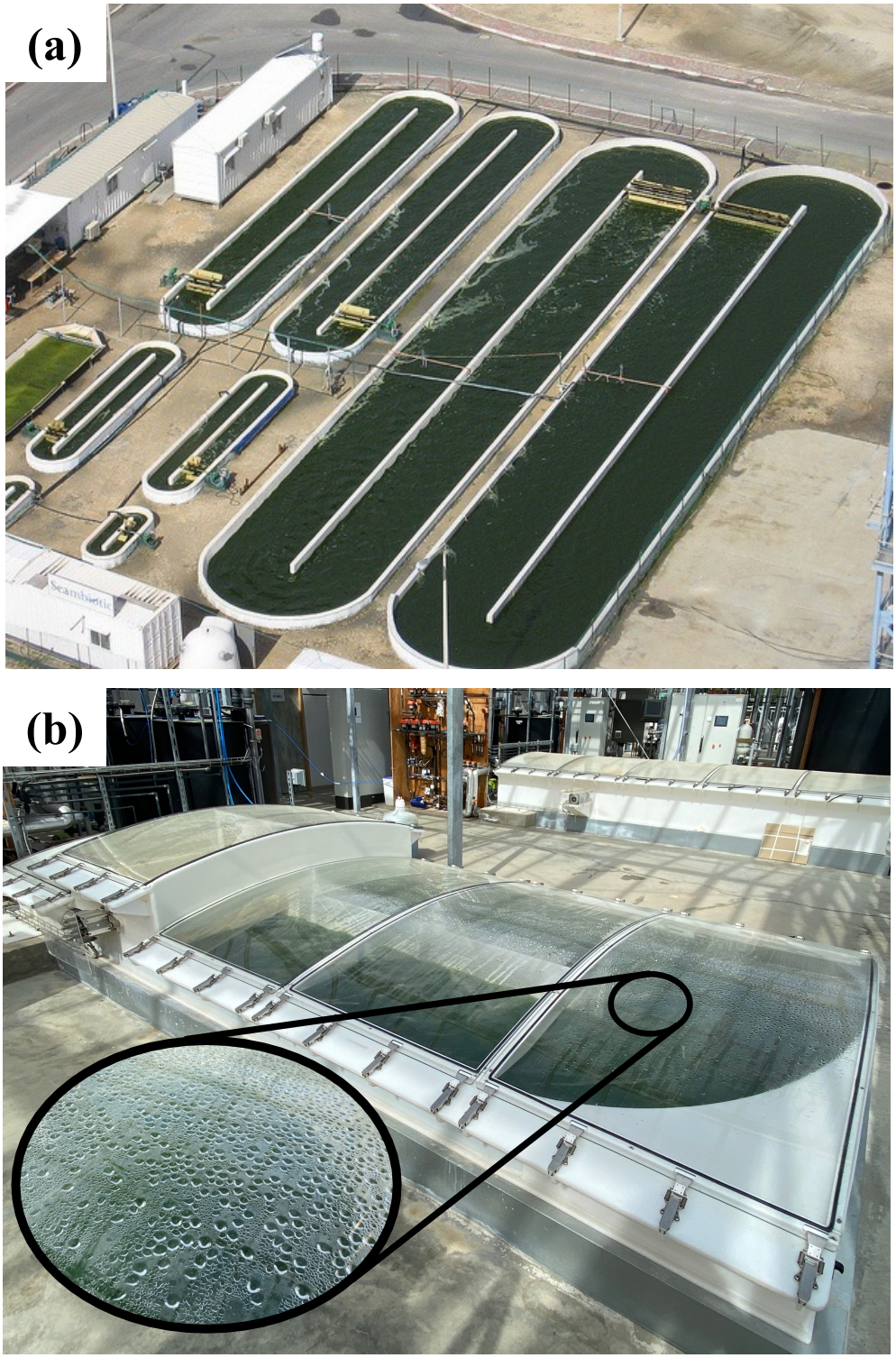

Figure 1.4: Examples of (a) an open raceway pond [35], (b) a closed raceway pond with large condensate droplets.

does not penetrate as deeply into the microalgae culture compared to normally incident light [30, 43]. Thus, non-normal incidence can increase dark zones in the culture where there is not enough light to drive photosynthesis. This phenomenon, combined with the decrease in solar irradiation in the mornings and evenings, negatively impacts microalgae growth and the productivity of the cultivation system.

1.4 Light transfer

Maximum productivity in microalgae cultivation systems occurs in the light-limited regime wherein operational parameters such as temperature, pH, and nutrient availability are optimized and culture growth depends only on the amount and distribution of photons absorbed by the cells [30]. The latter is represented by the local rate of photon absorption (LRPA) in $\mu\text{mol}_{\text{h}\nu}$/kg s at a given culture depth [30]. Predicting and controlling the LRPA in raceway ponds and photobioreactors is essential in order to maximize the growth rate and/or the production rate of the desired value-added product(s) [30].

Increasing the LRPA is one way to improve biomass productivity, since photosynthetic growth is directly related to the quantity of absorbed photons [28,31]. Scattering by droplets such as those observed in Figure 1.4 may negatively impact the LRPA due to changes in the direction and intensity of the incident light. However, the impact of pendant droplets on the culture LRPA and the productivity of covered raceway ponds is unknown. Moreover, while scattering by cap-shaped droplets has been thoroughly studied [37, 38, 44–46], scattering by large non-cap shaped droplets has not been rigorously quantified. Changes to the radiative properties of the microalgae species being cultivated also significantly impact the LRPA [47]. While previous studies have demonstrated that the LRPA can be accurately estimated using only the absorption cross-section [47, 48], the impact of colony formation on the absorption cross-section of microalgae remains unknown.

1.5 Objectives

The global objective of the present study is to build upon our current understanding of how various phenomena impact light transfer in microalgae cultivation systems and to increase biomass productivity by improving the radiative field within the culture. To this end, the present study first aims to numerically investigate light scattering by large pendant droplets and the corresponding impact on the biomass productivity of covered raceway ponds. This was done in two parts. First, the shape of large pendant water droplets was predicted accounting for gravitational and surface tension effects. The normal-hemispherical and directional-hemispherical transmittance of a transparent substrate supporting such droplets was predicted by simulating light transfer using a Monte Carlo ray-tracing (MCRT) algorithm. A variety of droplet volume, contact angle, surface area coverage, and window tilt angle were considered. Second, the temporal evolution of the directional-hemispherical and bidirectional transmittance of droplet-covered windows was predicted over the course of a day using the same MCRT algorithm. The microalgae growth rate was predicted by using the transmitted radiative field as an input into a coupled model of light transfer and growth kinetics within the microalgae culture. The impact of the time of year, droplet contact angle, and surface area coverage was considered. Overall, these results provide practical knowledge for design parameters of photobioreactors such as window tilt and material.

Next, the dissertation aims to quantify, for the first time, the effect of colony formation in microalgae on the absorption of photons by the cells in the culture. First, the mass-averaged absorption cross-section was experimentally measured for the microalgae species *Botryococcus braunii* in cultures with and without aggregate-like colonies. The MCRT method was used to predict the absorption cross-section and elucidate the impact of pigment content, cell arrangement, and colony extracellular matrix (ECM). Then, the same method was used to investigate the effect of colony formation on the absorption cross-section of spherical colonies which are often observed in species of the *Volvocaceae* family. These results can be used to predict the impact of colony formation on the local rate of photon absorption within a given culture, an important parameter for optimizing the performance of cultivation systems.

Finally, this dissertation aims to propose a method to improve the biomass productivity of outdoor raceway ponds by increasing the amount of sunlight available to the culture. To do so, the biomass productivity of several configurations of raceway ponds featuring vertical mirrors was predicting using a coupled light transfer and microalgae growth kinetics model. The impact of mirror orientation, pond dimensions, and location were considered. The results can serve as practical guidelines for the design and operation of outdoor raceway ponds featuring reflective surfaces for improved biomass productivity.

1.6 Organization of the document

Chapter 2 assess the impact of droplet volume on the transmittance of transparent substrates supporting pendant droplets. Chapter 3 quantifies the effect of scattering by the condensate droplets on the biomass productivity of covered raceway ponds. Chapters 4 and 5 quantify the impact of colony formation on the absorption cross-section of microalgae cultures. Chapter 6 investigates the use of vertical mirrors to increase the solar radiation flux incident upon outdoor raceway ponds and improve their biomass productivity. Finally, Chapter 7 summarizes the findings of this thesis and suggests directions for future research. Figure 1.5 summarizes the organization of this thesis in the context of a outdoor raceway pond.

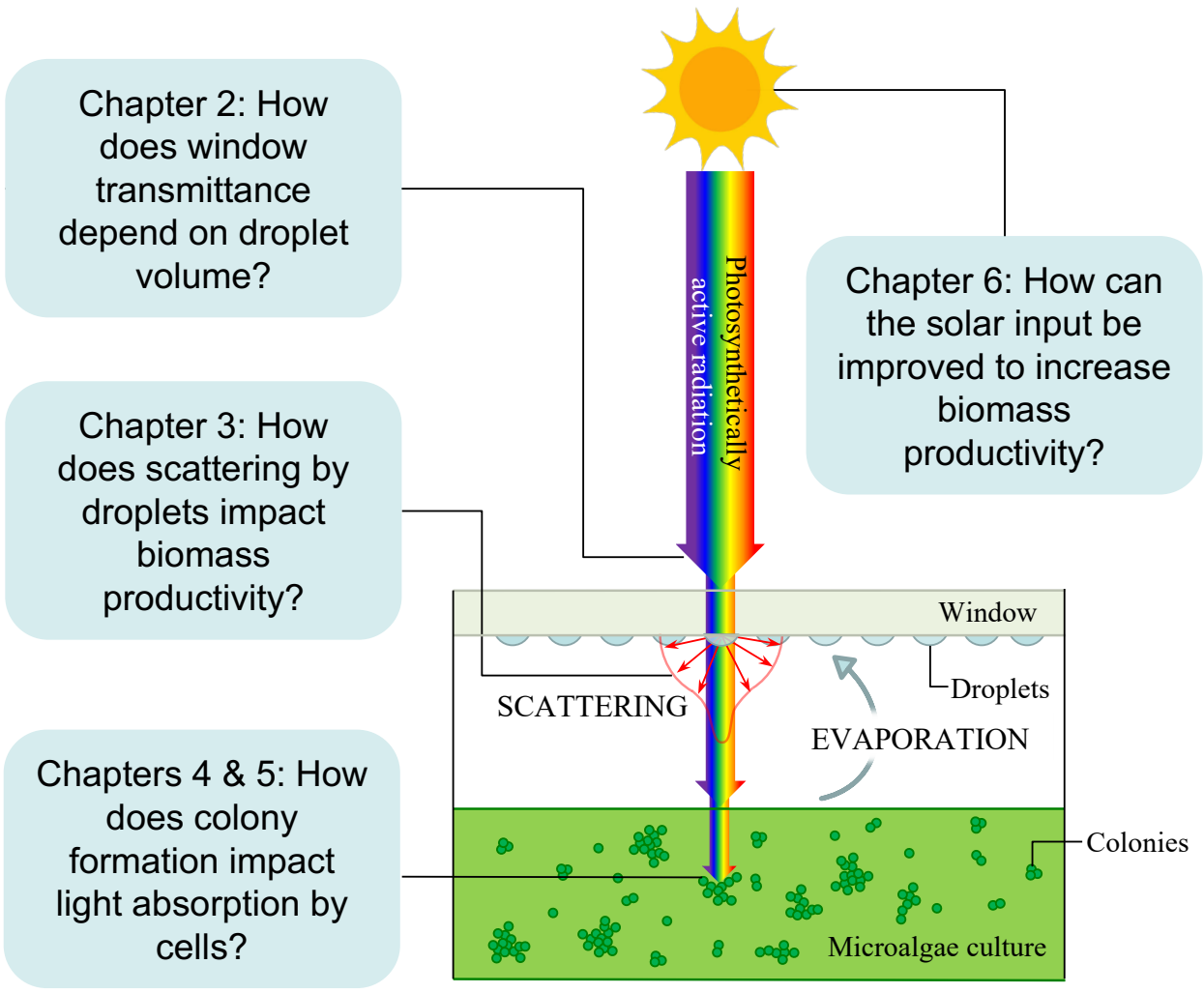

Figure 1.5: Organization of the dissertation.

CHAPTER 2

Transmittance of transparent horizontal and tilted windows supporting large non-absorbing pendant droplets

This chapter establishes that the deviation of large pendant droplets from an ideal cap-shape due to gravity can have significant and complex impacts on the normal-hemispherical and directional-hemispherical transmittances of light through horizontal and tilted transparent windows. First, the shape of pendant droplets larger than the capillary length was predicted numerically by balancing gravitational and surface tension forces for various droplet volumes, contact angles, and window tilt angles. Then, light transfer through windows supporting such numerically generated droplets was simulated using the Monte Carlo ray-tracing method. The window transmittance for large droplets was found to be nearly independent of droplet spatial arrangement and size distribution for relatively narrow size distributions. Assuming droplets to be cap-shaped caused the normal-hemispherical transmittance to be overestimated by as much as 37% for horizontal windows supporting droplets with volume $V > 10$ µL and contact angles $\theta_c > \theta_{cr}$ where θ_{cr} is the critical angle for total internal reflection at the water/air interface. This was due to gravity-induced deformation of the droplet shape resulting in increased reflection at the droplet/air interface. For tilted windows, the droplet deformation caused the normal-hemispherical transmittance to increase with increasing droplet volume and window tilt angle. For both horizontal and tilted windows, transmittance decreased linearly with increasing droplet surface area coverage. These results and numerical tools can be used to design energy efficient solar stills, greenhouses, and covered photobioreactors, for example.

2.1 Introduction

In many solar energy conversion applications such as solar stills, greenhouses, and microalgae cultivation systems, direct exposure to sunlight increases the temperature of the system and drives water evaporation, thus increasing the relative humidity within the system [49]. Then, condensate droplets form on the interior surface of the windows or cladding if their temperature falls below the dew point of the interior air due to emission of infrared radiation to the sky and exposure to colder outside air and wind. For example, Figure 2.1a depicts a solar still under operation wherein salt water is heated by the incident solar radiation resulting in evaporation and water droplets condensing on the inner surface of the tilted window cover to produce fresh water. Similarly, Figure 2.1b shows a greenhouse used to cultivate plants year-round with condensation present on its inner windows. Finally, Figure 2.1c pictures a covered raceway pond used for green microalgae cultivation with droplets condensing on the inner surface of the transparent cover [50].

The presence of droplets on transparent windows has been shown to decrease their transmittance in the visible part of the electromagnetic spectrum [38,40,46,51–53]. The reduction in the amount of energy entering the system limits the productivity of greenhouses and microalgae cultivation systems as they both rely on visible light to drive photosynthesis [50,53]. Furthermore, droplet shape has been shown to play an important role in the productivity of solar stills [54]. The use of hydrophobic windows with larger droplet contact angles was found to reduce solar still productivity by approximately 45% due to the decrease in the window transmittance compared to windows with smaller droplet contact angles [54]. Previous theoretical studies [37,38,40,44,46,55,56] considered small cap-shaped droplets whose shape was dominated by surface tension forces and featured a constant radius of curvature. This assumption is valid provided that the droplet size is much smaller than the capillary length l_c defined as [57]

$$l_c = \sqrt{\frac{\sigma}{\rho g}} \tag{2.1}$$

where σ is the surface tension of the droplet/air interface, ρ is the droplet density, and g is

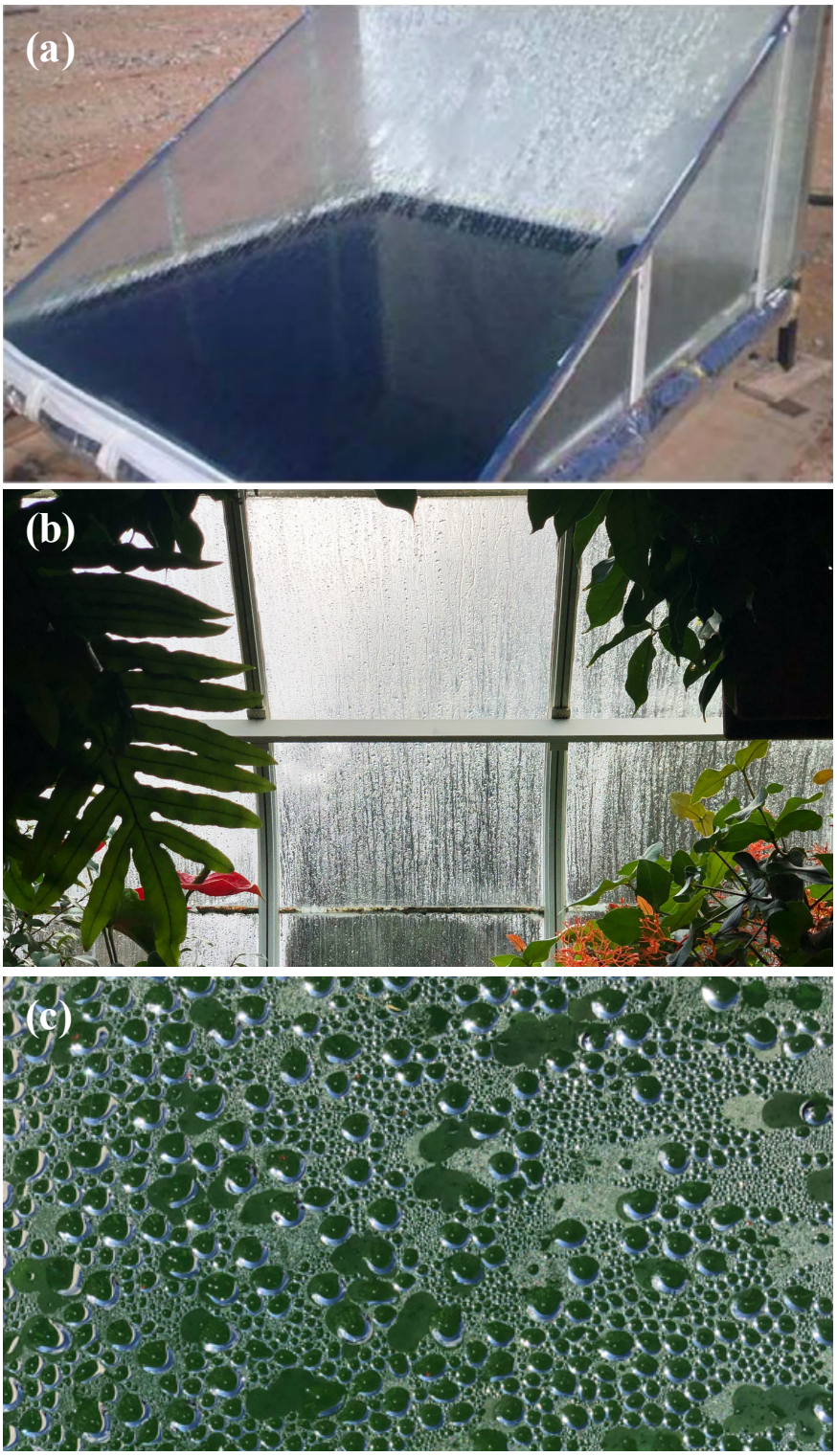

Figure 2.1: Examples of condensation in enclosed systems including **(a)** a solar still (photo used with permission of V-EnerTek, Chennai, India. All rights reserved. ©2021 V-EnerTek), **(b)** the interior of a greenhouse (image credit: www.finest greenhouse.com), and **(c)** a covered raceway pond for microalgae cultivation at the R&D facility AlgoSolis (Saint-Nazaire, France).

the gravitational acceleration. For water droplets in air, the capillary length is $l_c = 2.7$ mm. In the case of the solar stills, greenhouses, and covered microalgae raceway ponds illustrated in Figure 2.1, condensation occurs over the course of hours, enabling droplets to attain sizes on the same order or larger than the capillary length l_c. Then, droplets cannot be assumed to be cap-shaped as gravity can significantly affect their shape [57]. To the best of our knowledge, the effect of such large non-cap shaped pendant droplets on the transmittance of both horizontal and tilted windows has not been investigated to date.

This study aims to quantify the impact of the shape of large and non-absorbing pendant droplets on the transmittance of horizontal and tilted transparent windows. To do so, the droplet shape was predicted numerically by balancing gravitational and surface tension energies. Then, the normal-hemispherical and directional-hemispherical transmittances of the windows were predicted numerically for a wide variety of droplet configurations. The results were compared with those obtained for cap-shaped droplets with the same volume and contact angle.

2.2 Background

Briscoe and Gavin [40] theoretically investigated the normal-hemispherical transmittance, at wavelength of 650 nm, of a 1.1 mm thick transparent window ($n_w = 1.5$) supporting a single small cap-shaped droplet ($n_d = 1.33$). To do so, a ray-tracing analysis was performed for 200 rays evenly distributed along the radial direction of the droplet and incident on the dry side of the window. The window and droplets were assumed to have the same absorption coefficient $\kappa_w = \kappa_d = 0.04$ mm^{-1}. For a projected droplet diameter of 50 µm, the transmittance through the droplet was found to be essentially unchanged for contact angles $\theta_c \leq 40°$ and to decrease from approximately 90% to as low as 50% as the contact angle θ_c increased from 40° to 90°. The decrease was attributed to an increase in total internal reflection at the droplet/air interface for droplet contact angle $\theta_c > \theta_{cr}$ where the critical angle θ_{cr} is given by $\theta_{cr} = \sin^{-1}(n_a/n_d) = 48.6°$. For cap-shaped droplets, the droplet shape was self-similar over the range of projected diameters investigated for a given contact angle.

Thus, the transmittance was found to be independent of droplet projected diameter for the optical properties considered and was instead controlled by the droplet shape via the contact angle.

Pieters et al. [58] developed an experimental method to record the temporal evolution of the shape of an evaporating water droplet on a vertical polyethylene film. The contact angle of water droplets on polyethylene is approximately 100° [40]. The resulting 3D contours were used to theoretically predict the directional-hemispherical transmittance of a single drying droplet on a polyethylene film. The dry area around the droplet was not accounted for in the simulations, i.e., droplet surface area coverage was 100%. The results indicated an increase in the directional-hemispherical transmittance as the droplet evaporated. The authors attributed this observation to the decrease in curvature in the droplet profile as evaporation proceeded. Furthermore, the authors demonstrated that the directional-hemispherical transmittance of the experimentally measured non-cap shaped droplets on a vertical film deviated significantly from that of cap-shaped droplets with a contact angle of 90°, considered to be similar to that of water on polyethylene.

In a later study, Pieters et al. [55] experimentally and theoretically investigated the directional-hemispherical transmittance of light at 632.8 nm through vertical glass (n_w =1.526 $\kappa_w = 4$ µm^{-1}) or polyethylene (n_w =1.515 $\kappa_w = 165$ µm^{-1}) windows with condensate water droplets ($n_d = 1.333$, $\kappa_d = 0.4$ µm^{-1}) on their back side. The authors also simulated the directional-hemispherical transmittance of a single cap-shaped droplet with projected diameter as large as 12.75 mm. Here also, the normal-hemispherical transmittance was found to be independent of the droplet size and to decrease with increasing contact angle θ_c larger than 40°.

Pollet and Pieters [41, 51, 52] conducted an experimental investigation of light at wavelength 632.8 nm through greenhouse cladding materials including glass and standard, anti-drop-condensation, and anti-dust polyethylene films. The transmittance measurements of a vertically oriented glass window and standard polyethylene film were taken under laboratory conditions for a complete condensation cycle progressing from a dry window, to condensation without droplet run-off, to condensation with droplet run-off, to the evaporation phase. In

the presence of condensation, materials with smaller droplet contact angle (e.g., glass) were found to have transmittance up to 30% larger than those with larger contact angles (e.g., standard and anti-dust-polyethylene films).

Tow [37] theoretically investigated the antireflective potential of droplets on the back side of a glass window using the Monte Carlo ray-tracing (MCRT) method. The directional-hemispherical transmittance was predicted at wavelength 500 nm for a 3 mm thick non-absorbing glass window ($n_w = 1.5$) supporting monodisperse, ordered, and weakly absorbing droplets ($n_d = 1.33$, $\kappa_d = 2.5 \times 10^{-7}$µm). The author considered a window with a single droplet and periodic boundary conditions to simulate an infinitely large droplet-covered window. The droplet was assumed to be cap-shaped with a projected diameter equal to 2.7 mm and contact angle θ_c varying from 6° to 90°. The droplet surface area coverage ranged from 14% to 90%. The presence of droplets was found to slightly increase the normal-hemispherical transmittance compared to a dry window for contact angles θ_c less than the critical angle θ_{cr}. However, the transmittance was found to decrease with increasing contact angle for $\theta_c \geq \theta_{cr}$.

Recently, Zhu et al. [38,44,46] and Huang et al. [56] have systematically investigated the impact of non-absorbing and absorbing cap-shaped droplets on the normal-hemispherical [38,44,46], the directional-hemispherical [38,44,46], and the bidirectional transmittance [56] of horizontal windows supporting droplets on either their front or back side using the Monte Carlo ray-tracing method in the geometric optics limit. Unlike previous theoretical studies, a wide range of droplet diameter, contact angle, absorption index, and surface area coverage was considered. In addition, simulations were performed for a large number of monodisperse or polydisperse droplets arranged on the window in either a random or ordered hexagonal pattern [38]. The spectral absorptance and transmittance of an absorbing window and droplets for wavelengths from 0.4 to 5 µm were also predicted [46]. In all cases, the droplets were assumed to be small and cap-shaped. The dependence of transmittance on contact angle was found to have four distinct regimes for non-absorbing droplets with contact angle ranging from 10° to 180° [38]. The presence of droplets on the back side of a window was found to decrease its transmittance for droplet contact angles $\theta_{cr} < \theta_c < 180° - \theta_{cr}$ [38].

Furthermore, the different transmittances were found to be independent of droplet size, size distribution, or droplet arrangement provided that droplets were non-absorbing [38, 44, 56].

Simsek et al. [59], experimentally validated these results in the visible part of the spectrum for $\theta_c < 90°$ both quantitatively and qualitatively. Indeed, the normal-hemispherical transmittance and reflectance of glass windows supporting acrylic droplets was measured in the visible to near-infrared parts of the electromagnetic spectrum (0.4-1.1 µm). Various surface treatments were applied to achieve contact angles between 26° and 76°. The diameter and location of all the acrylic droplets on selected samples were characterized and used as input parameters into the MCRT algorithm to predict their normal-hemispherical transmittance and reflectance. Very good agreement was found between the theoretical predictions and experimental results.

This chapter aims to expand on previous studies to investigate the effect of large and non-absorbing droplets on the transmittance of horizontal and tilted droplet-covered windows. First, the droplet shape was found numerically by using energy minimization principles to balance gravitational and surface tension energies. Then, the normal-hemispherical and directional-hemispherical transmittances of the windows were predicted by the Monte Carlo ray-tracing method accounting for reflection and refraction at all interfaces. The impact of droplet (i) spatial arrangement, (ii) size distribution, (iii) volume, (iv) contact angle, (v) window tilt angle, and (vi) surface area coverage were systematically investigated.

2.3 Analysis

2.3.1 Problem statement

Let us consider a transparent window supporting large pendant droplets exposed to collimated radiation. The window was non-absorbing with thickness $H = 3$ mm, refractive index $n_w = 1.5$, and was positioned horizontally (Figure 2.2a) or tilted at an angle α with respect to the horizon (Figure 2.2b). The direction of the incident solar radiation was denoted by the polar θ_i and azimuthal γ_i angles of incidence defined with respect to the positive z-axis and

the positive x-axis, respectively. The shape of the droplet/air interface was defined by the radial coordinate $r_d(\psi, \phi)$ where the polar ψ and azimuthal ϕ angles are defined with respect to the negative z-axis and positive x-axis, respectively. The water droplet density ρ was taken as 1000 kg/m^3 and the surface tension σ of the air/droplet interface was 72.1 mN/m. Droplets on horizontal windows had a circular contact line with radius $R_c = r_d(\psi = \pi/2, \phi)$ and projected radius R_p while droplets on the tilted window had a non-circular contact line, as illustrated in Figures 2.2c and 2.2d, respectively. The droplets were non-absorbing and had refractive index n_d =1.33 and arbitrary volume V. The contact angle and the projected surface area coverage of the droplets on the window were denoted by θ_c and f_A, respectively. Droplets were either monodisperse or polydisperse with an arbitrary volume distribution. They were either randomly distributed on the window surface or arranged in an ordered hexagonal pattern. The incident photons underwent reflection or refraction at each interface and were either back-scattered or transmitted through the droplet-covered window.

2.3.2 Assumptions

The droplet shape was predicted based on the assumptions that the droplets were stationary and had constant volume, density, surface tension, and contact angle. Droplets were only subjected to gravitational and surface tension forces.

The simulations of light transfer through the droplet-covered window were performed using the Monte Carlo ray-tracing method based on the following assumptions: (1) the droplet and window dimensions were much larger than the wavelength of the impinging radiation such that geometric optics was valid. (2) All interfaces were considered optically smooth so that specular reflection and refraction were governed by Snell's law and Fresnel's equations. (3) Both the window and the droplets were non-absorbing.

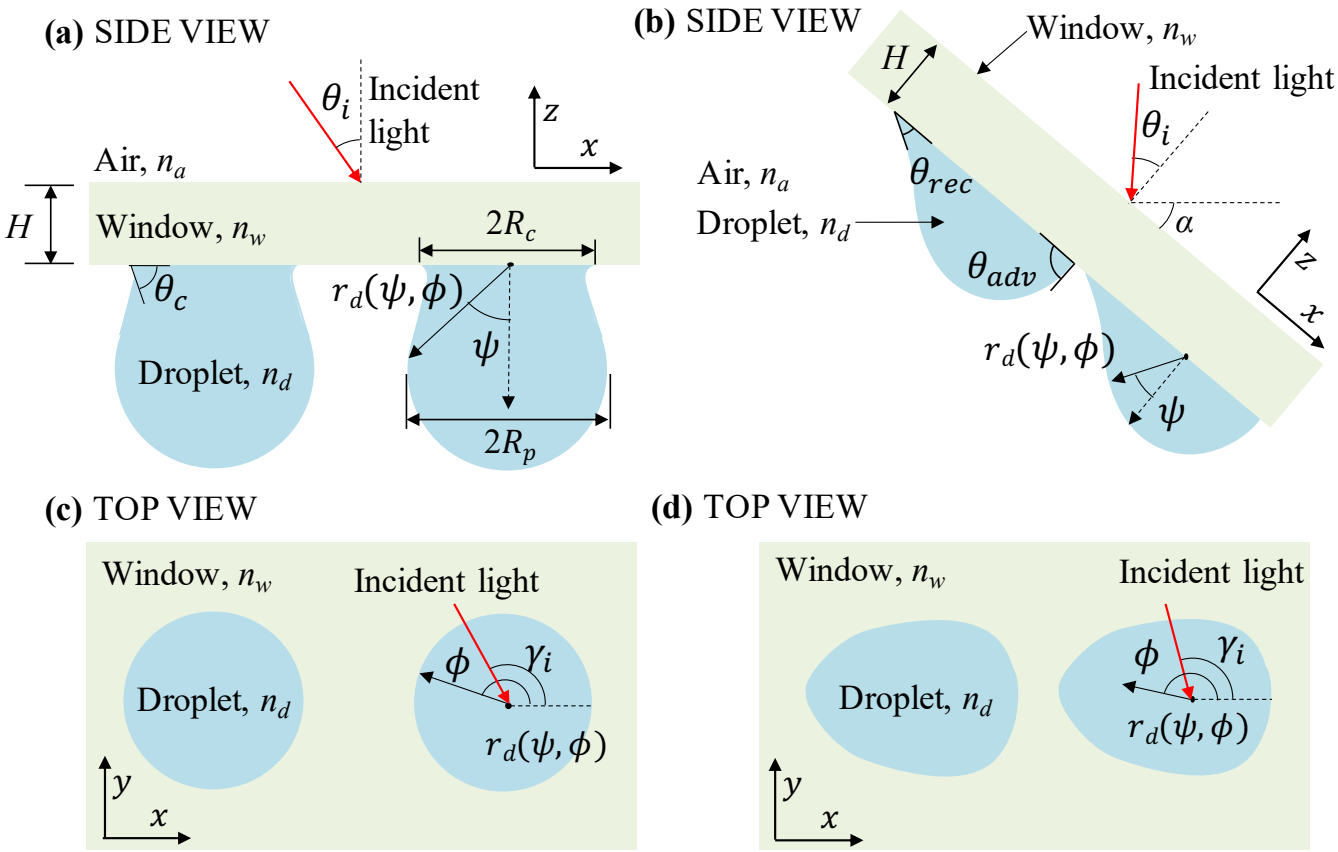

Figure 2.2: Side view and top view (not to scale) of **(a,c)** a horizontal window and **(b,d)** a tilted window supporting large non-cap shaped pendant droplets featuring the droplet/window contact area.

2.3.3 Method of solutions

Droplet shape

The droplet shape was determined using the open source *Surface Evolver* program [60]. This program approximates the droplet surface as an ensemble of vertices, edges, and triangular facets. It employs a gradient descent optimization algorithm to iteratively refine and adjust the droplet shape defined by the radial coordinate $r_d(\psi, \phi)$ so as to minimize the sum of its potential and surface energies for a given density ρ and air/droplet surface tension σ while maintaining an arbitrary constant volume V and contact angle θ_c [60]. On tilted windows, the droplet shape also depended on the window tilt angle α and the associated advancing

θ_{adv} and receding θ_{rec} droplet contact angles (Figure 2.2b). Then, the droplet contact angle varied along the contact line as a function of the azimuthal angle ϕ according to [61, 62]

$$\theta_c(\phi) = 2\left(\frac{\theta_{adv} - \theta_{rec}}{\pi^3}\right)\phi^3 - 3\left(\frac{\theta_{adv} - \theta_{rec}}{\pi^2}\right)\phi^2 + \theta_{adv}. \tag{2.2}$$

The resulting droplet contour was output in the form of a triangulation matrix for both horizontal and tilted windows. The triangulation matrix was then used as an input to the light transfer simulations to determine the location of the droplet/air interface and calculate the incidence angle of the photons.

Light transfer

Light transfer through droplet-covered windows was simulated using the Monte Carlo ray-tracing method. The method and algorithm were explained in detail in Refs. [38, 44, 46, 56] and validated against experimental results in Refs. [38,59] and need not be repeated. In brief, a large number of collimated photon bundles or "rays" were launched normally onto a window supporting pendant droplets generated by the *Surface Evolver* program [60]. At each interface a ray encountered (e.g., air/window, window/droplet, droplet/air interface), the angle of refraction and the reflectivity were determined from Snell's law and Fresnel's equations, respectively. Then, a random number from the uniform distribution was generated and compared to the calculated reflectivity to determine if the ray was reflected or refracted. The ray was then either specularly reflected or refracted. Next, the ray was traced to the location of the next interface in the 3D simulation domain. The boundary conditions on the side of the computational domain were periodic. In the case of a non-absorbing window and droplets, this process continued until a ray was either (i) back-scattered by or (ii) transmitted through the droplet-covered window. The normal-hemispherical-transmittance T_{nh} corresponded to the fraction of normally incident photons transmitted through the droplet-covered window in any direction, and was computed according to [38]

$$T_{nh}(n_d, V, \theta_c, n_w, \alpha, f_A) = \frac{N_t}{N_i} \tag{2.3}$$

where N_t is the number of transmitted photons and N_i is the total number of photons incident on the window. Similarly, the directional-hemispherical transmittance T_{dh} was expressed as

$$T_{dh}(n_d, V, \theta_c, n_w, \alpha, f_A, \theta_i, \gamma_i) = \frac{N_t}{N_i}. \tag{2.4}$$

In order to achieve numerical convergence, $N_i = 10^6$ rays were used for each simulation.

2.4 Results and Discussion

2.4.1 Droplet shape and maximum volume

Figure 2.3a shows a photograph of a pendant water droplet of volume $V = 50$ µL on a PVC slab with tilt angle $\alpha = 24°$ and contact angle $\theta_c = 86°$ when the slab substrate was horizontal (i.e., $\alpha = 0°$). Such a photograph was used to measure the advancing θ_{adv} and receding θ_{rec} contact angles plotted in Figure 2.3b as functions of droplet volume V for tilt angle α equal to 0°, $12 \pm 1°$, and $24 \pm 1°$. As droplet volume and tilt angle increased, gravity caused the shape of the droplet to be asymmetrical and the receding contact angle θ_{rec} decreased. The measured advancing θ_{adv} and receding θ_{rec} contact angles were used in the *Surface Evolver* model to predict the shape of pendant droplets on tilted surfaces. Figure 2.3c shows the resulting simulated droplet profile for droplet volume $V = 50$ µL and tilt angle $\alpha = 24°$. Comparing Figures 2.3a and 2.3c shows good agreement between the experimental and simulated droplet profiles. As such, the *Surface Evolver* model was considered to be also valid for tilted windows and was used to predict the shape of large pendant droplets on tilted surfaces.

Figure 2.3d plots the predicted maximum attainable droplet volume V_{max} corresponding to the maximum volume before the droplet detached from a horizontal surface as a function of droplet contact angle θ_c. On well-wetting surfaces with low droplet contact angle, adhesive forces between the water and the surface dominated and the surface was able to support droplets with large maximum volume V_{max} around 300 µL. As the contact angle increased, the adhesive forces between the droplet and the surface decreased and the maximum droplet volume V_{max} approached 0 µL for $\theta_c \geq 140°$.

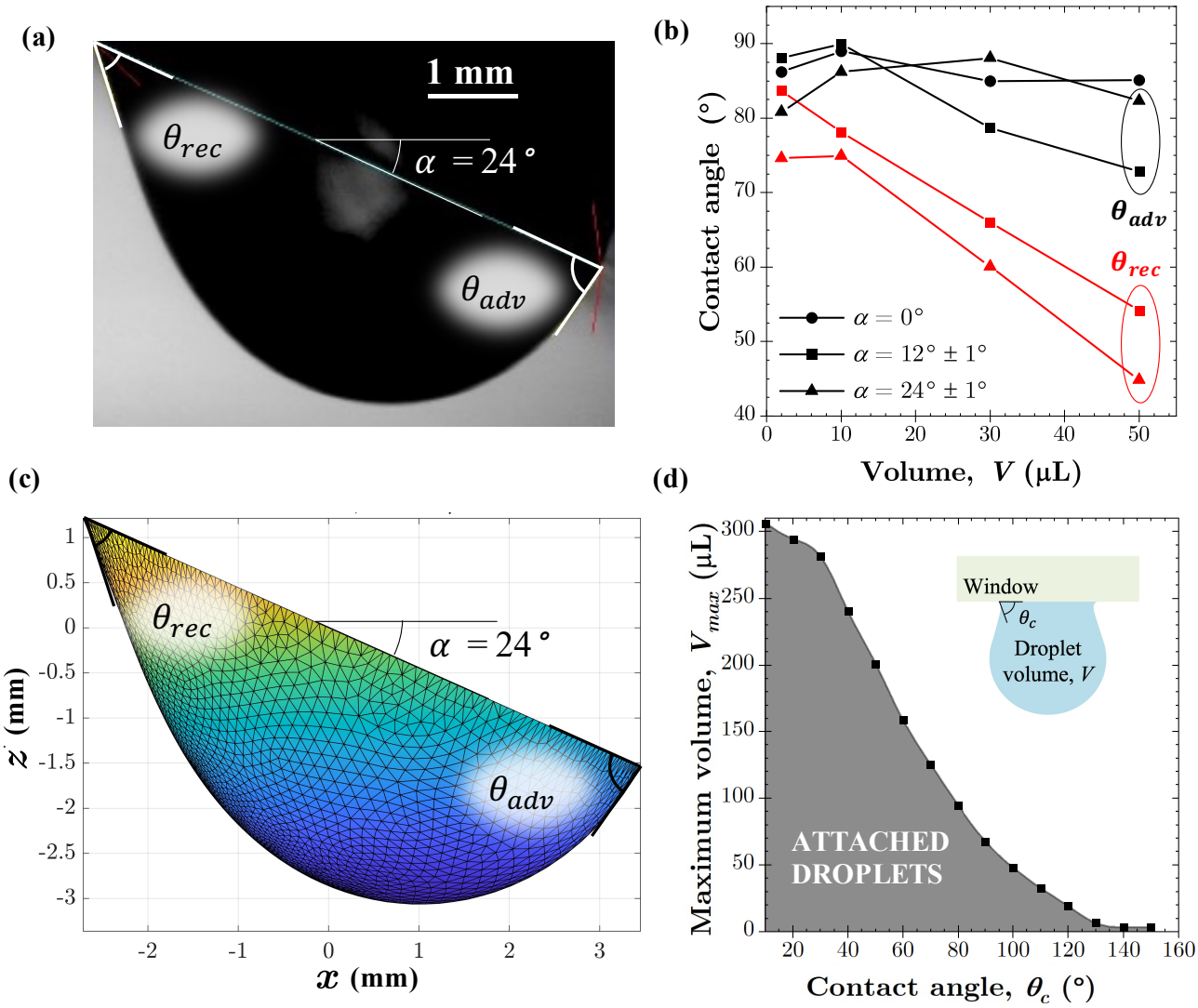

Figure 2.3: **(a)** Photograph of a droplet of volume $V = 50$ µL on a PVC slab with tilt angle $\alpha = 24°$. **(b)** Measured receding θ_{rec} and advancing θ_{adv} contact angles as a function of droplet volume V for tilt angle α equal to $0°$, $12 \pm 1°$, and $24 \pm 1°$. **(c)** Simulation of the tilted pendant droplet shape with volume $V = 50$ µL and tilt angle $\alpha = 24°$. **(d)** Maximum volume V_{max} before the pendant water droplet detaches from a horizontal window predicted as a function of contact angle θ_c.

2.4.2 Effect of droplet arrangement and size distribution

To investigate the impact of droplet spatial arrangement on the normal-hemispherical transmittance T_{nh} of horizontal windows, monodisperse pendant droplets were arranged either randomly or in an ordered hexagonal pattern. Similarly, to investigate the impact of the droplet size distribution, monodisperse or polydisperse droplets with a normal size distribution were simulated with a random spatial arrangement. For polydisperse droplets with mean volume $\bar{V}$, two normal droplet size distributions were simulated with standard deviation σ equal to $0.15\bar{V}$ or $0.3\bar{V}$. The droplet volume ranged from $0.1\bar{V}$ to $2\bar{V}$ and was discretized in increments of $0.1\bar{V}$. Table 2.1 summarizes the predicted normal-hemispherical transmittance T_{nh} of horizontal windows with droplet surface area coverage $f_A = 50\%$, droplet mean volume $\bar{V} = 25$ µL or 75 µL, and contact angle $\theta_c = 60°$ or 90°. It establishes that, for a given contact angle θ_c and mean droplet volume $\bar{V}$, the spatial arrangement of non-cap shaped droplets had a negligible effect on the window's normal-hemispherical transmittance. The same conclusions were previously obtained for non-absorbing cap-shaped droplets pendant from horizontal windows [38]. However, Table 2.1 indicates that the mean volume $\bar{V}$ had an important impact on the transmittance of windows for large droplets, unlike in the case of cap-shaped droplets [38, 40, 41, 51, 52, 55]. Despite the dependence of transmittance on the mean volume $\bar{V}$, the impact of the droplet size distribution was found to be negligible for relatively narrow size distributions.

2.4.3 Effect of droplet volume

Figure 2.4a plots the predicted normal-hemispherical transmittance T_{nh} as a function of the droplet volume V for large droplets pendant from a horizontal window with contact angle θ_c equal to 30°, 60°, and 90° and surface area coverage $f_A = 50\%$. Droplets were monodisperse and arranged in a hexagonal pattern. Note that the same results are expected for non-absorbing polydisperse and/or randomly distributed droplets with the same mean volume $\bar{V}$ and contact angle θ_c, as previously demonstrated. Droplet volume V ranged from 1 µL to V_{max} (see Figure 2.3d). The transmittances of a dry glass window and of a window

Table 2.1: Normal-hemispherical transmittance of horizontal windows supporting large droplets with contact angle θ_c of 60° or 90°, ordered or random spatial arrangements, and monodisperse or polydisperse with a normal size distribution. Simulations were performed for a window surface area of 400 cm^2 with projected surface area coverage $f_A = 50\%$.

			T_{nh}		
Spatial arrangement	**Size distribution**	**Standard deviation σ (µL)**	$\bar{V} = 75$ µL $\theta_c = 60°$	$\bar{V} = 25$ µL $\theta_c = 60°$	$\bar{V} = 25$ µL $\theta_c = 90°$
Hexagonal	Monodisperse	-	0.825	0.789	0.700
Random	Monodisperse	-	0.836	0.795	0.700
Random	Polydisperse	$0.15\bar{V}$	0.834	0.797	0.702
Random	Polydisperse	$0.30\bar{V}$	0.832	0.801	0.702

supporting cap-shaped droplets with the same contact angle θ_c and surface area coverage f_A are also plotted as references. The predicted normal-hemispherical transmittance T_{nh} of windows supporting large droplets was nearly identical to that supporting cap-shaped droplets for (a) droplet volume $V < 200$ µL and contact angle $\theta_c = 30°$ and for (b) $V < 10$ µL and contact angle $\theta_c = 60°$ and 90°. Beyond these droplet volumes, the transmittance T_{nh} was found to be up to 13% smaller for large non-cap shaped droplets than for cap-shaped droplets. This was due to distortions in the droplet shape caused by gravity. These distortions caused the incidence angle θ_i' at the droplet/air interface to exceed the droplet contact angle in certain areas. Such an increase in the angle of incidence θ_i' increased the number of photons undergoing total internal reflection at the droplet/air interface and decreased the normal-hemispherical transmittance T_{nh}. Therefore, assuming large droplets to be cap-shaped generally caused the transmittance T_{nh} of horizontal windows to be overestimated. However, it can provide an upper bound to the actual transmittance.

Figure 2.4b shows the droplet contours for contact angle $\theta_c = 60°$ and droplet volume V equal to 25 µL, 100 µL, and 150 µL. To compare the shapes of droplets of different volumes,

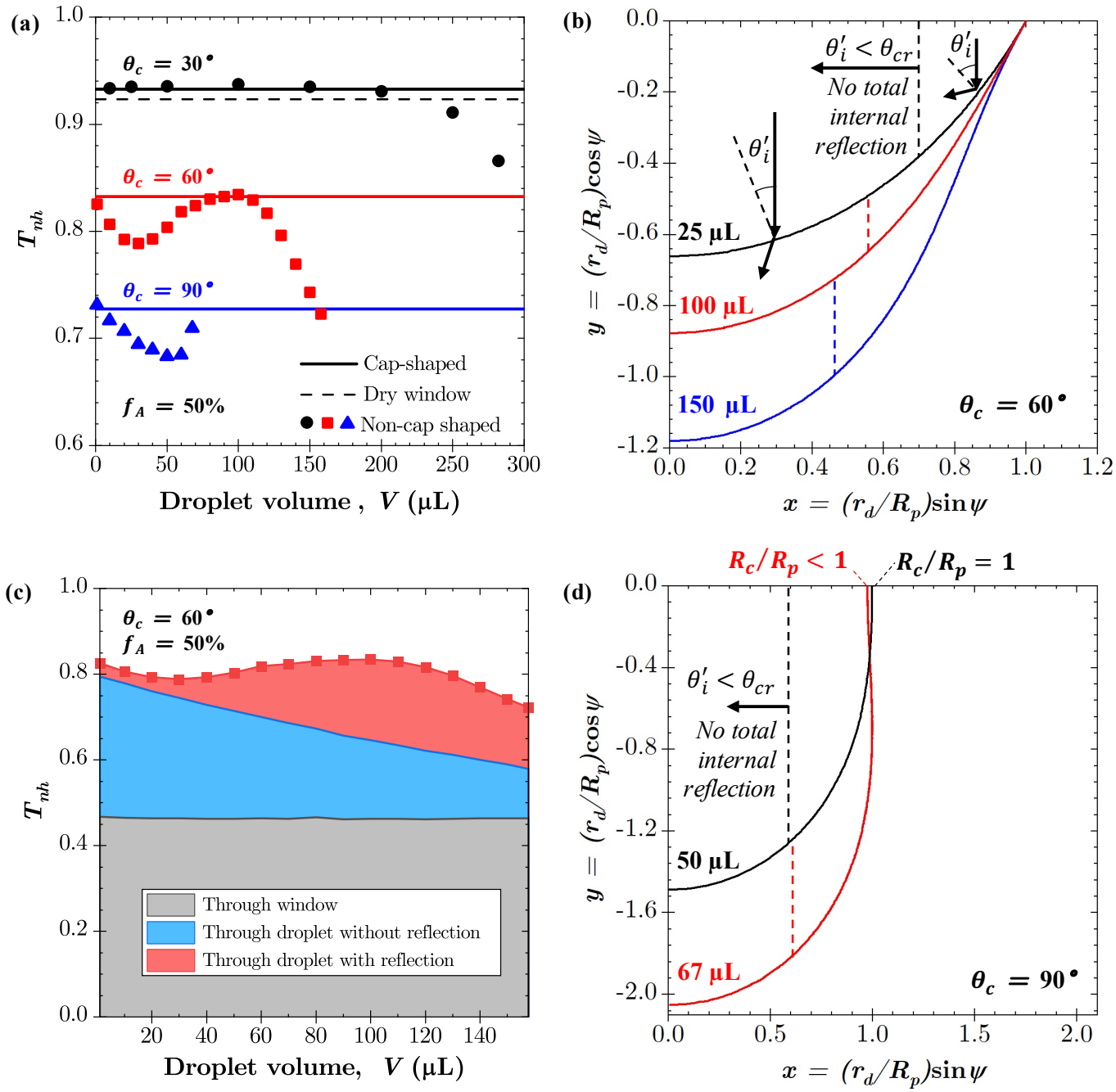

Figure 2.4: **(a)** Normal-hemispherical transmittance T_{nh} of a horizontal window with cap-shaped and large droplets as a function of droplet volume V for contact angle $\theta_c = 30°, 60°$, and $90°$. **(b)** Normalized droplet contours for droplet volume $V = 25$ μL, 100 μL, and 150 μL and contact angle $\theta_c = 60°$. **(c)** Transmittance as a function of droplet volume showing the fraction of photons transmitted through the window and transmitted through the droplets with and without reflection events. **(d)** Normalized droplet contours for $V = 50$ μL and 67 μL with contact angle $\theta_c = 90°$.

the droplet contours $r_d(\psi, \phi)$ were normalized with respect to their projected radius R_p. The incidence angle θ_i' at the droplet/air interface is shown schematically for normal incidence. Figure 2.4b illustrates that when the incidence angle θ_i' of a photon at the droplet/air interface was larger than the critical angle for total internal reflection, given by $\theta_{cr} = \sin^{-1}(n_a/n_w) = 48.6°$, i.e., $\theta_i' > \theta_{cr}$, it was reflected back inside the droplet. Figure 2.4c plots the fractions of rays that were (i) transmitted directly through the window, (ii) transmitted through the droplet without any reflection, and (iii) transmitted through the droplet with at least one reflection event as functions of droplet volume V for contact angle $\theta_c = 60°$ and $f_A = 50\%$. Figure 2.4b indicates that the fraction of the droplet/air interface such that $\theta_i' < \theta_{cr}$ decreased as the droplet volume V increased. This observation explained the decrease in the fraction of photons transmitted through the droplet without reflection with increasing droplet volume observed in Figure 2.4c. The same phenomenon was observed for contact angle θ_c of 30° and 90° and caused the transmittance T_{nh} to decrease with increasing droplet volume V, as observed in Figure 2.4a. For contact angle $\theta_c = 60°$, the fraction of photons transmitted through the droplet that experienced at least one reflection event increased as droplet volume V increased. Thus, despite a larger fraction of photons undergoing total internal reflection at the droplet/air interface, the droplet shape was such that these photons were eventually transmitted through the droplet. This phenomenon resulted in a maximum in the normal-hemispherical transmittance T_{nh} observed in Figure 2.4a for $\theta_c = 60°$ at $V = 100$ µL. For volume $V > 100$ µL, T_{nh} decreased with increasing volume due to a decrease in the fraction of photons transmitted with and without reflection.

Figure 2.4d shows the normalized droplet contours for contact angle $\theta_c = 90°$ and droplet volume $V = 50$ µL and $V_{max} = 67$ µL. Two main differences between the droplet contours at $V = 50$ µL and 67 µL were responsible for the corresponding increase in T_{nh} observed in Figure 2.4a. First, the droplet with $V_{max} = 67$ µL had a slightly larger fraction of its droplet/air interface such that $\theta_i' < \theta_{cr}$ compared to the droplet with $V = 50$ µL. As previously discussed, this tends to increase transmittance. Second, Figure 2.4d shows a slight bulge in the droplet contour at $V_{max} = 67$ µL that was not present at $V = 50$ µL. This caused the droplet projected radius R_p to exceed the droplet contact circle radius R_c, i.e.,

$R_c/R_p < 1$ unlike for droplet volume $V = 50$ µL where $R_c/R_p = 1$. Thus, for a given surface area coverage f_A (defined based on R_p), the fraction of the window in contact with droplets was equal to f_A for droplet volume $V = 50$ µL but it was less than f_A for droplet volume $V_{max} = 67$ µL. As a result, a smaller fraction of photons passed through the window/droplet contact surface and were then back-scattered at the droplet/air interface. This caused a corresponding increase in transmittance for droplet volume $V_{max} = 67$ µL and contact angle $\theta_c = 90°$ (Figure 2.4a).

2.4.4 Effect of droplet contact angle

Figure 2.5a plots the normal-hemispherical transmittance T_{nh} of a horizontal window supporting large droplets as a function of contact angle θ_c for monodisperse droplets of volume V equal to 10 µL, 25 µL, and 50 µL and surface area coverage $f_A = 50\%$. Figure 2.5a also shows the transmittances of a dry glass window and of a window supporting cap-shaped droplets with the same contact angle θ_c and surface area coverage f_A. Note that T_{nh} was independent of droplet volume V for cap-shaped droplets [38, 40, 55]. For contact angle $\theta_c \leq \theta_{cr}$, the normal-hemispherical transmittances T_{nh} of a window supporting cap-shaped or non-cap shaped droplets were nearly identical, independent of contact angle θ_c, and slightly larger than that of dry glass. However, for contact angles $\theta_c > \theta_{cr}$ the normal-hemispherical transmittance decreased sharply and even more so for large droplets. This was caused by an increase in total internal reflection of photons at the droplet/air interface when $\theta_c > \theta_{cr}$. It was also observed in previous studies on cap-shaped droplets [37, 38, 40]. The minimum normal-hemispherical transmittance T_{nh} occurred around $\theta_c = 90°$ for droplet volume $V \leq 25$ µL and cap-shaped droplets [37, 38, 40] and around $\theta_c = 80°$ for $V = 50$ µL. As contact angle θ_c increased further, T_{nh} increased as fewer photons were internally reflected at the droplet/air interface, as discussed in previous studies [37,38,40]. Overall, these results indicate that assuming large droplets to be cap-shaped causes the window transmittance T_{nh} to be overestimated for $\theta_{cr} \leq \theta_c \leq 90°$. They also suggest that hydrophilic windows with droplet contact angle $\theta_c < \theta_{cr}$ are preferable to maintain high window transmittance T_{nh} for both large droplets and small cap-shaped droplets.

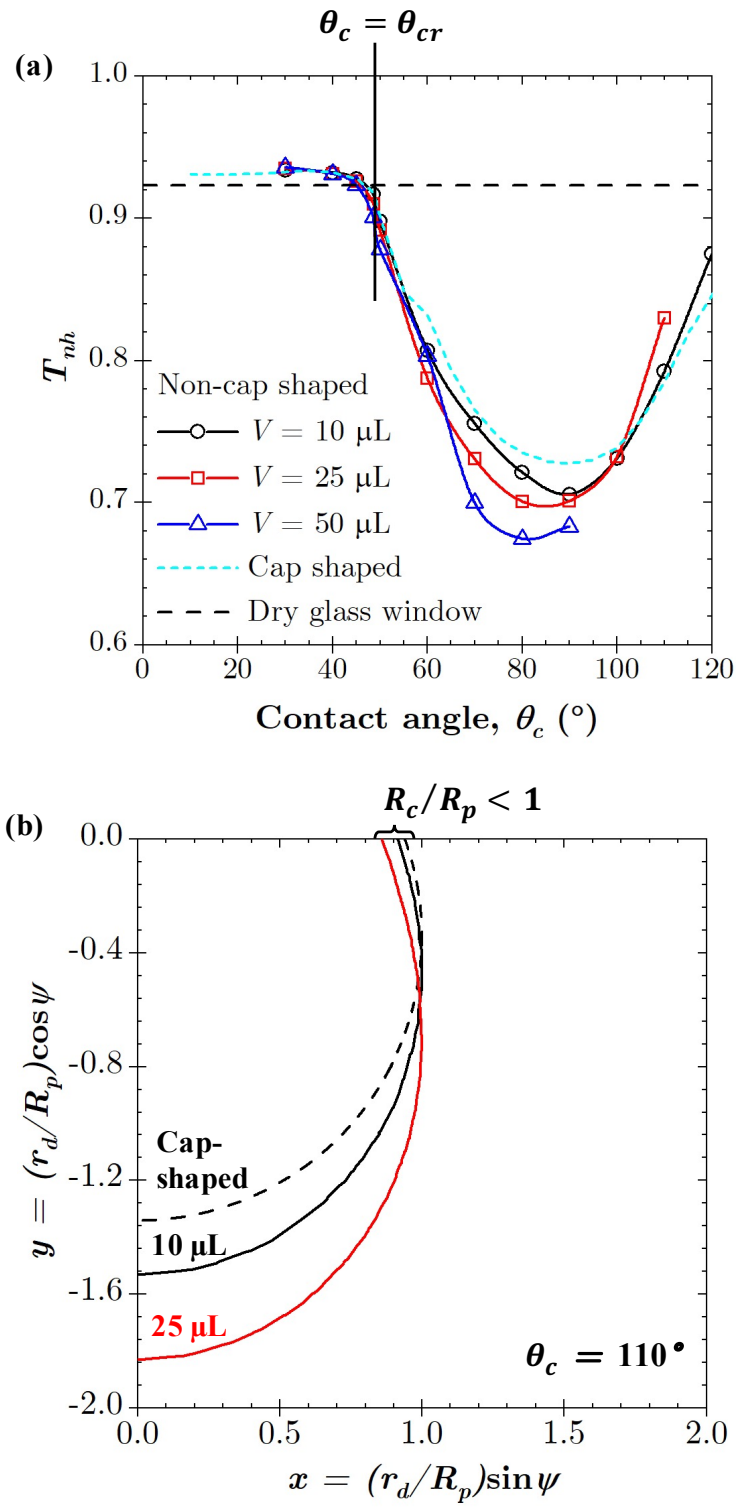

Figure 2.5: **(a)** Normal-hemispherical transmittance T_{nh} of a horizontal window with surface area coverage $f_A = 50\%$ supporting cap-shaped and non-cap shaped droplets as a function of contact angle θ_c for various droplet volumes V. **(b)** Normalized cap-shaped and non-cap shaped droplet contours for 10 µL and 25 µL with contact angle $\theta_c = 110°$.

Figure 2.5a indicates that transmittance decreased with increasing volume V for contact angle $\theta_c < 100°$. However, it slightly increased with increasing volume V for larger contact angles. Figure 2.5b plots the droplet contours for a cap-shaped droplet and large droplets with volume V of 10 µL and 25 µL and contact angle of $\theta_c = 110°$ normalized with respect to each droplet's projected radius $R_p = 1.41$ mm and 1.79 mm, respectively. Figure 2.5b indicates that R_c/R_p decreased with increasing droplet volume V as gravity pulled the droplet away from the surface. This further reduced reflection at the droplet/air interface, as discussed previously. It also caused T_{nh} for large droplets to exceed that of cap-shaped droplets with the same contact angle $\theta_c > 100°$, as observed in Figure 2.5a.

2.4.5 Effect of window tilt angle

Figure 2.6 plots the predicted normal-hemispherical transmittance T_{nh} as a function of droplet volume V for window tilt angle α equal to 0°, $12 \pm 1°$, and $24 \pm 1°$. It indicates that T_{nh} increased with increasing droplet volume V and/or window tilt angle $\alpha > 0°$. This was caused by gravitational forces which caused the droplet receding contact angle θ_{rec} to decrease with increasing volume V and tilt angle α (Figure 2.3b). This increasingly asymmetric shape reduced total internal reflection particularly in the upper part of the droplet/air interface (see Figure 2.3c). These results suggest that even a slight window tilt could be used to increase the normal-hemispherical transmittance of droplet-covered windows.

2.4.6 Effect of droplet surface area coverage

Figures 2.7a-2.7c plot the normal-hemispherical transmittance T_{nh} as a function of surface area coverage f_A for large pendant droplets on horizontal windows with various droplet volumes V and contact angles θ_c equal to (a) 30°, (b) 60°, and (c) 90°, respectively. Similarly, Figures 2.7d-2.7f plot the normal-hemispherical transmittance T_{nh} as a function of surface area coverage f_A for pendant droplets of various volume V on a window with tilt angle α equal to (d) 0°, and (e) $12° \pm 1°$, and (f) $24° \pm 1°$, respectively. In each case, the transmittance T_{nh} of a window supporting cap-shaped droplets as a function of surface area coverage f_A is

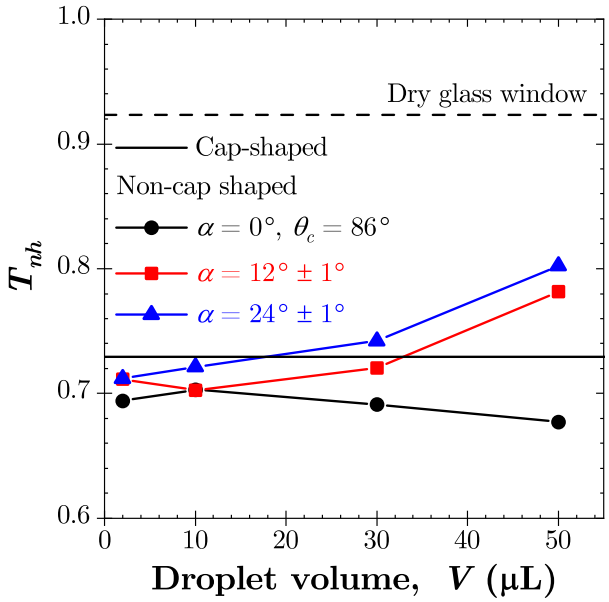

Figure 2.6: Normal-hemispherical transmittance T_{nh} of a tilted window supporting pendant droplets with surface area coverage $f_A = 50\%$ as a function of droplet volume V for tilt angles α equal to $0°, 12 \pm 1°$, and $24 \pm 1°$.

shown for the corresponding window tilt angle α and contact angle θ_c. For the horizontal window, θ_c was taken as 86° while for tilted surfaces the measured advancing θ_{adv} and receding θ_{rec} contact angles were reported in Figure 2.3b as functions of the droplet volume V. As observed with cap-shaped droplets [37, 38, 46], the presence of large droplets caused the transmittance T_{nh} to decrease linearly with increasing surface area coverage f_A for both horizontal and tilted windows. Indeed, for contact angle $\theta_c = 90°$, volume $V = 50$ µL, and surface coverage $f_A = 90\%$, the presence of large droplets reduced the window transmittance by 46% compared to a dry window.

Figures 2.7a-2.7c indicate that assuming droplets to be cap-shaped on a horizontal window caused T_{nh} to be overestimated. The discrepancy increased with increasing surface area coverage f_A and droplet volume V. Indeed, neglecting the gravity-induced deformation of large droplets caused the transmittance T_{nh} to be overestimated by a relative error as large as 37% for $\theta_c = 60°$, $f_A = 90\%$, and $V = V_{max}$. On the other hand, Figures 2.7e and 2.7f show that assuming large droplets to be cap-shaped on a tilted window caused T_{nh} to be

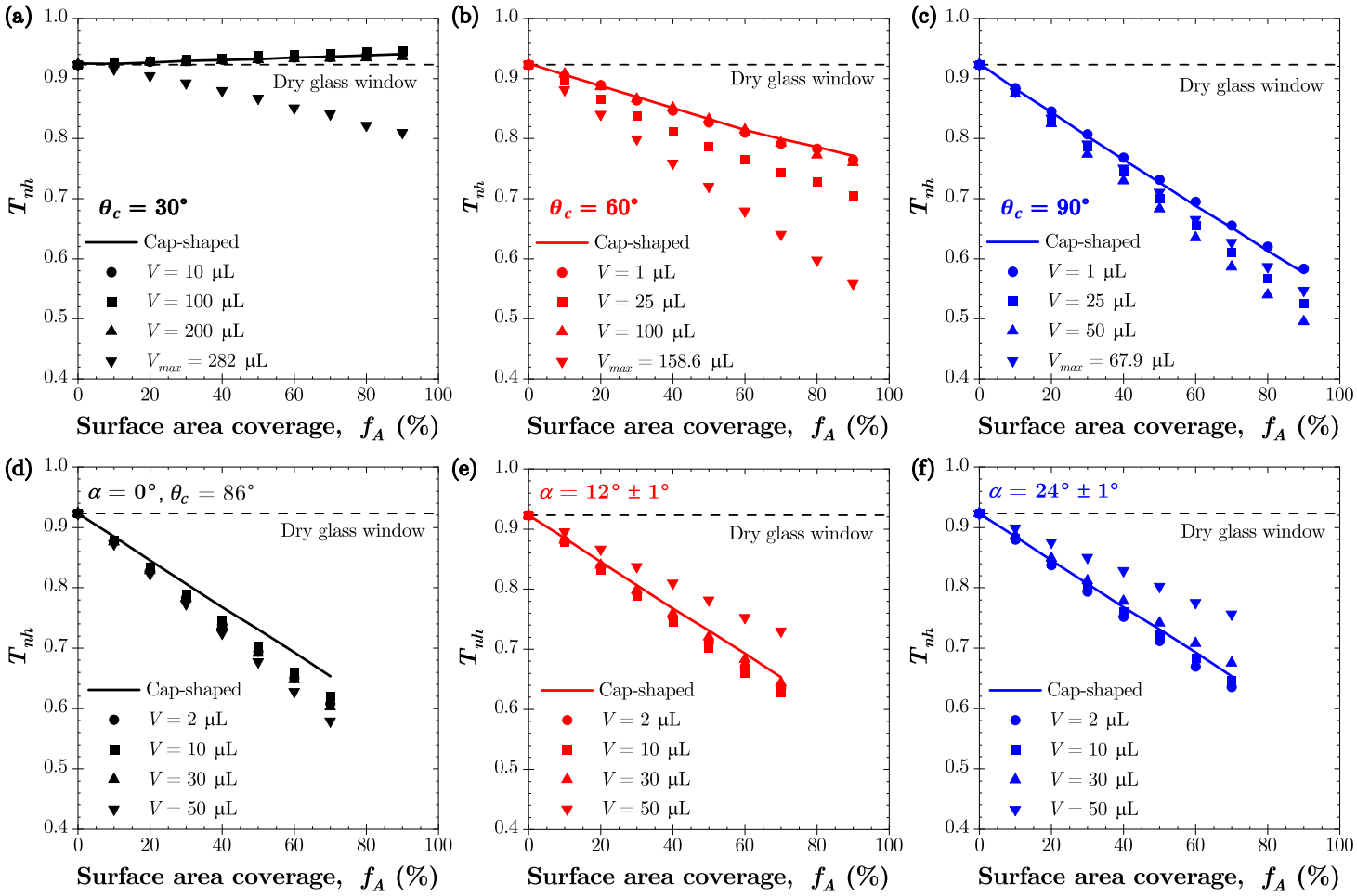

Figure 2.7: Normal-hemispherical transmittance T_{nh} of a horizontal window supporting large pendant droplets of various volumes V as a function of surface area coverage f_A for contact angles θ_c equal to **(a)** 30°, **(b)** 60°, and **(c)** 90°. Normal-hemispherical transmittance T_{nh} of a tilted window supporting large pendant droplets with various volumes V as a function of surface area coverage f_A for tilt angle α equal to **(d)** 0°, **(e)** 12° ± 1°, and **(f)** 24° ± 1°. For tilt angle $\alpha = 0°$ the droplet contact angle $\theta_c = 86°$. For nonzero tilt angle α, droplet advancing θ_{adv} and receding θ_{rec} contact angles were given by Figure 2.3b.

underestimated by as much as 14% for droplet volume $V \geq 50$ µL and surface area coverage $f_A = 70\%$. This was attributed to the asymmetrical shape of large droplets, as discussed previously. Note that, in practice, a tilted window tends to have a lower maximum droplet surface area coverage compared to a horizontal window since droplet run-off occurs more readily. As such, tilted windows may be preferable for minimizing the effects of droplets on the window transmittance.

2.4.7 Directional-hemispherical transmittance

Figure 2.8a plots the directional-hemispherical transmittance T_{dh} as a function of the polar angle of incidence θ_i for a horizontal window with surface area coverage $f_A = 70\%$ supporting large pendant droplets of contact angle θ_c equal to 30°, 60°, and 90° and volume V equal to 282 µL, 159 µL, and 50 µL, respectively. These droplet volumes V were selected since their normal-hemispherical transmittance T_{nh} differed the most from that of cap-shaped droplets (see Figure 2.4a). Note that the directional-hemispherical transmittance T_{dh} was independent of the azimuthal angle of incidence γ_i due to the axisymmetric shape of droplets pendant from a horizontal surface. The directional-hemispherical transmittances T_{dh} for a dry glass window and for windows supporting cap-shaped droplets with the same contact angle θ_c and surface area coverage f_A are also shown as references. The directional-hemispherical transmittance T_{dh} of a dry window decreased with increasing polar incidence angle θ_i due to reflection at the air/window interface. Figure 8a demonstrates that this was also the case for both cap-shaped and large droplets with contact angle $\theta_c = 30°$ where reflection at the air/glass interface dominated and the directional-hemispherical transmittance T_{dh} decreased monotonically with increasing polar incidence angle θ_i. However, for large droplets with contact angles $\theta_c = 60°$ and 90° as well as for cap-shaped droplets with contact angle $\theta_c = 90°$ the directional-hemispherical transmittance T_{dh} decreased with increasing polar incidence angle θ_i up to 50° due to decreasing reflection at the water/air interface [7,10]. Nonetheless, for $\theta_i > 50°$, reflection at the front air/glass interface began to dominate and T_{dh} decreased following the trends observed in the transmittance T_{dh} of a dry window.

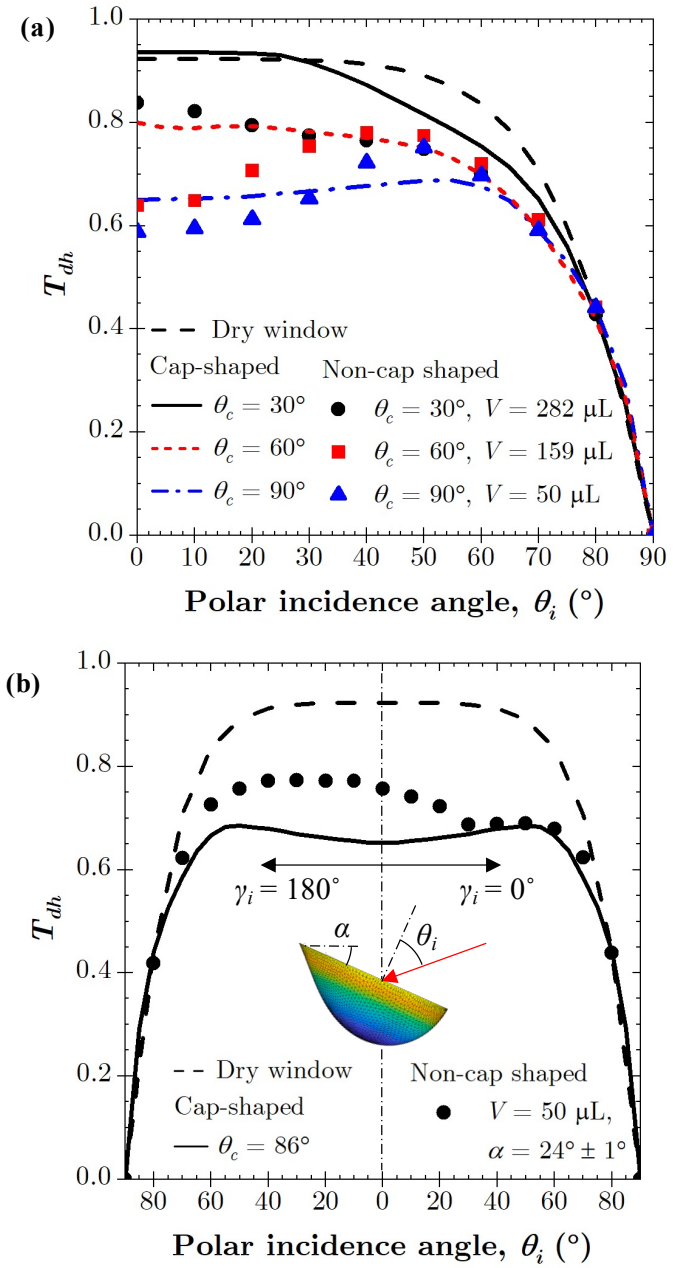

Figure 2.8: (a) Directional-hemispherical transmittance T_{dh} of a horizontal window supporting cap-shaped and large pendant droplets as a function of the polar incidence angle θ_i for contact angle θ_c equal to 30°, 60°, and 90° and droplet volumes V equal to 282 µL, 159 µL, and 50 µL, respectively, and (b) directional-hemispherical transmittance T_{dh} of a window with tilt angle $\alpha = 24° \pm 1°$ supporting cap-shaped and large pendant droplets with volume $V = 50$ µL as a function of the polar angle of incidence θ_i for azimuthal angle of incidence γ_i equal to 0° and 180°. For both horizontal and tilted windows the droplet surface area coverage f_A was equal to 70%.

Figure 2.8b plots the directional-hemispherical transmittance T_{dh} as a function of the polar angle of incidence θ_i for azimuthal angle of incidence γ_i equal to 0° and 180° for a window with tilt angle $\alpha = 24° \pm 1°$ and surface area coverage $f_A = 70\%$ supporting large droplets of volume V = 50 µL. The directional-hemispherical transmittances T_{dh} of a dry tilted window and a tilted window supporting cap-shaped droplets with contact angle θ_c = 86° and surface area coverage $f_A = 70\%$ are also shown. Figure 2.8b indicates that the directional-hemispherical transmittance T_{dh} of tilted windows supporting large droplets varied with the azimuthal angle of incidence γ_i, unlike for horizontal windows. This was due to the asymmetric shape of droplets on tilted windows and has also been observed in previous studies [58]. Furthermore, the directional-hemispherical transmittance T_{dh} of a tilted window covered with large non-cap-shaped droplets was larger than that with cap-shaped droplets for both values of azimuthal angle of incidence γ_i and all values of polar angle of incidence θ_i. This suggests that tilted windows are preferable to horizontal windows for maintaining high window transmittance when droplets are present regardless of the direction of the incident radiation.

2.5 Conclusion

This study established that the normal-hemispherical transmittance T_{nh} and the directional-hemispherical transmittances T_{dh} of horizontal and tilted transparent windows supporting large pendant and non-absorbing droplets may depend strongly and in a non-trivial way on the droplet volume, contact angle, surface area coverage, and window tilt angle. First, the shape of large pendant water droplets was simulated accounting for gravitational and surface tension forces using the *Surface Evolver* program. Then, the normal-hemispherical transmittance of a window supporting the simulated non-absorbing droplets was predicted using the Monte Carlo ray-tracing method. The droplet spatial arrangement on the window had no effect on the transmittance. The predicted transmittance was the same for monodisperse droplets and polydisperse droplets with the same mean volume and a relatively narrow size distribution. For small droplet volumes $V < 10$ µL and/or contact angles $\theta_c < \theta_{cr}$ the

droplets could be treated as cap-shaped for predicting the transmittance. However, for larger volumes $V \geq 10$ µL and/or contact angles $\theta_c \geq \theta_{cr}$, the transmittance T_{nh} of a horizontal window was smaller when supporting large droplets than when supporting cap-shaped droplets of equal contact angle by up to 27%. This was due to gravity-induced deformations in the droplet shape which increased the photon's incidence angle at the droplet/air interface and thus increased total internal reflection. In most cases, the transmittance T_{nh} of horizontal windows decreased with increasing droplet volume and contact angle. Conversely, droplets supported by tilted windows featured an asymmetrical shape that reduced total internal reflection and increased transmittance with increasing droplet volume and window tilt angle. The normal-hemispherical transmittance T_{nh} decreased linearly with increasing droplet surface area coverage for both horizontal and tilted windows. Based on the present results, windows made of hydrophilic materials and/or with a tilt are preferable for maintaining high window transmittance in situations where droplets tend to be large.

CHAPTER 3

Impact of dropwise condensation on biomass production rate in covered raceway ponds

The previous chapter demonstrated that the presence of pendant droplets decreases the transmittance of horizontal windows. Here, we investigate the corresponding impact of small condensed water droplets on the areal biomass productivity of outdoor culture systems with a free surface, protected by a transparent window or cover to prevent contamination and to control the growth conditions. Under solar radiation, evaporation from the culture causes droplets to condense on the interior surface of the cover. To quantify the effect of droplets on the system's performance, the bidirectional transmittance of a window supporting small cap-shaped droplets was predicted using the Monte Carlo ray-tracing method. It was combined with a growth kinetics model of *Chlorella vulgaris* to predict the temporal evolution of the biomass concentration on June 21$^{\text{st}}$ and September 23$^{\text{rd}}$ in Los Angeles, CA. Droplet contact angle of 30° or 90° and surface area coverage of 50% or 90% were considered. Light scattering by the condensed droplets changed the direction of the incident sunlight while reducing the amount of light reaching the culture by up to 37%. The combined effect decreased the daily areal biomass productivity with increasing droplet contact angle and surface area coverage by as much as 18%. Furthermore, the areal biomass productivity of the system was found to scale with the ratio X_0/a of the initial biomass concentration X_0 and the specific illuminated area a, as previously established for different photobioreactor geometries, but even in the presence of droplets. Finally, for a given day of the year, the optical thickness of the culture that yielded the maximum productivity was independent of the window condition. Thus, design and operation of such a system should focus on maintaining small droplet contact angle and surface area coverage and an optimum optical thickness to maximize productivity.

3.1 Background

Microalgae is cultivated in systems broadly classified as open or closed. In general, open systems such as raceway ponds are inexpensive to build and operate and have been widely used for large scale microalgae cultivation [33]. However open systems are susceptible to contamination, sub-optimal temperatures, evaporative losses, and low cell concentrations [32]. On the other hand, closed photobioreactors (PBRs) are more resilient to contaminates and feature higher biomass productivity thanks to more precisely controlled growth conditions [32, 36]. Specifically, in flat horizontal or inclined culture systems, a transparent window covering the culture and containing an over-pressurized gas space can be used to (i) limit culture contamination, (ii) reduce CO_2 degassing [34], and (iii) improve control of the growth conditions [32]. Such an outdoor PBR consisting of a race pond with a paddle wheel sealed by a transparent plastic cover is illustrated in Figure 3.1a. The use of a transparent window enables the cultivation of a wider variety of species and thus greater potential for the production of high value-added products without significantly increasing construction and maintenance costs [32, 36].

Regardless of the specifics of the cultivation system, water evaporation occurs when an outdoor microalgae culture is exposed to sunlight. When the culture is covered by a transparent window, evaporation leads to the formation of water droplets on the interior surface of the PBR cover, as illustrated in Figure 3.1b. However, the presence of droplets on the back side of a window has been shown to reduce its transmittance and change the direction of the transmitted light [38, 56]. Both of these phenomena could impact the PBR biomass productivity [33, 43]. However, to the best of our knowledge, the impact of droplet-covered windows on PBR performance has not been investigated to date.

The objective of this study is to quantify the effect of pendant droplets on the cover of outdoor microalgae cultivation systems on biomass productivity. To do so, light transfer was simulated through the PBR cover supporting pendant condensate droplets. The predicted bidirectional transmittance served as an input into combined light transfer and growth kinetics models in the culture of *Chlorella vulgaris*. Particular attention was paid to the effect

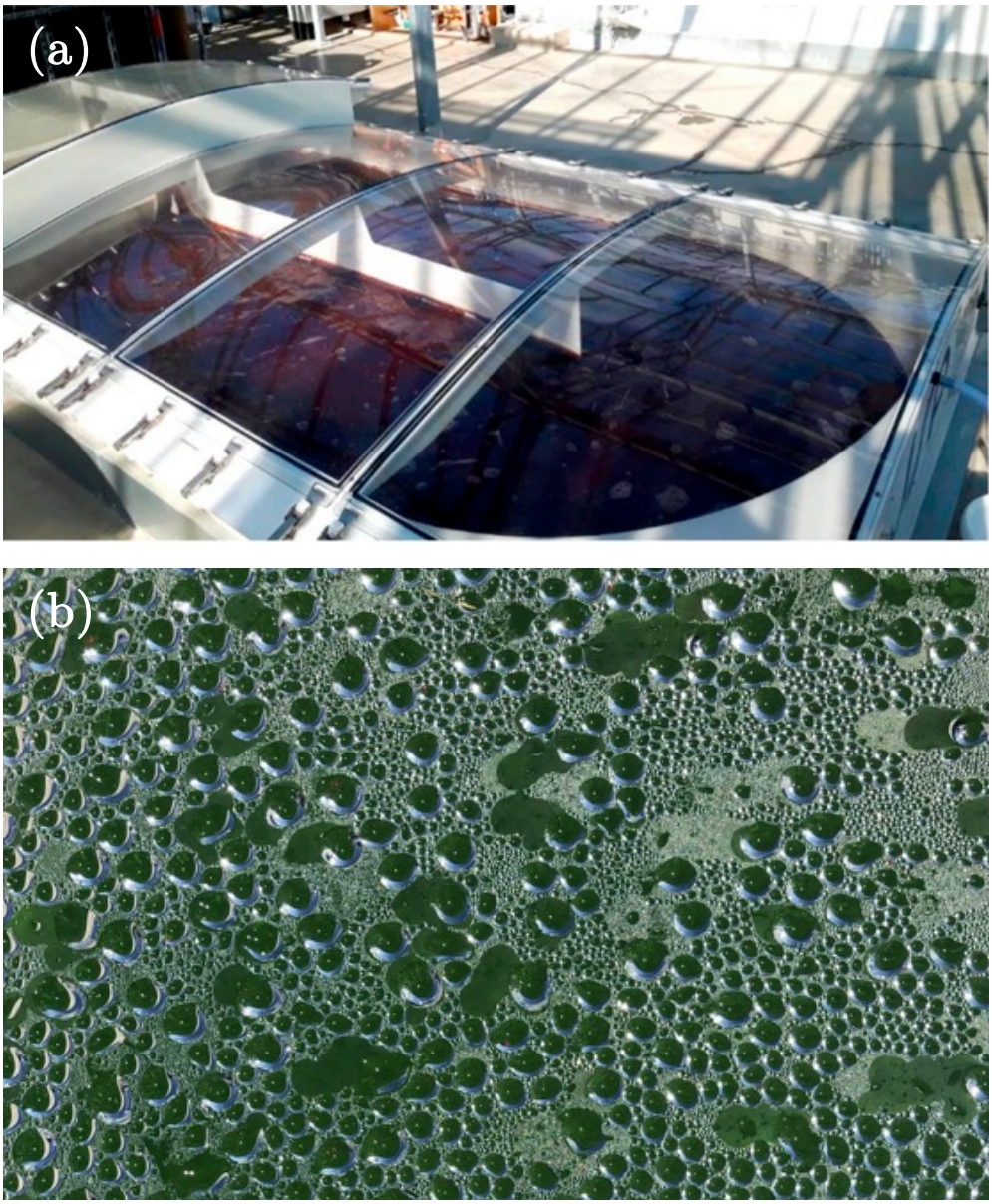

Figure 3.1: Photographs of (a) an outdoor photobioreactor at the R&D facility AlgoSolis (Saint Nazaire, France) with a clear window cover and (b) condensed droplets formed on the back side of a PBR window during a summer day.

of droplet contact angle, surface area coverage, culture depth, initial biomass concentration, and day of the year on the daily biomass production rate.

3.1.1 Light transfer through droplet-covered PBR windows

The interaction between light and droplet-covered windows has been studied both analytically [38,40,44,56,63] and experimentally [39–41,52,54,64]. Zhu et al. [38] simulated visible light transfer through a transparent window covered with non-absorbing cap-shaped water droplets on its back side. Light transfer was modeled using the Monte Carlo ray-tracing method for a wide range of droplet contact angle θ_c and surface area coverage f_A. Interestingly, both the normal-hemispherical transmittance T_{nh} and the directional-hemispherical transmittance T_{dh} of the droplet-covered window were found to be independent of droplet size distribution and droplet spatial arrangement. Similar results were observed for the bidirectional transmittance T_{bd} [56]. The normal-hemispherical transmittance T_{nh} was nearly independent of contact angle θ_c until it reached the critical angle θ_{cr} for total internal reflection at the droplet/air interface, i.e., for $\theta_c < \theta_{cr}$. However, for $\theta_c > \theta_{cr}$, the normal-hemispherical T_{nh} and directional-hemispherical transmittance T_{dh} decreased monotonically with increasing droplet surface area coverage f_A and/or increasing contact angle θ_c until reaching a minimum at $\theta_c = 90°$. Similar results were found experimentally by previous studies [39,40].

Zhu and Pilon [46] investigated the effect of absorption by the window and/or droplets on the transmittance of a window covered with cap-shaped droplets on its back side. In the case of a weakly absorbing window or droplets with absorption indices of $k_w = 10^{-6}$ and $k_d = 10^{-4}$, respectively, the normal-hemispherical transmittance T_{nh} was observed to decrease only slightly. Furthermore, the dependence on droplet contact angle θ_c was the same as that for a non-absorbing window and droplets. Thus, in the case of water on plexiglass, whose absorption indices are less than 1.6×10^{-7} and 1.8×10^{-6}, respectively over much of the photosynthetically active radiation (PAR) region from 400 to 700 nm, absorption by the window and droplets can be neglected [65,66].

3.1.2 Light transfer in microalgae culture

Light transfer through a well-mixed suspension of microalgae is governed by the radiative transfer equation (RTE) for a homogeneous absorbing, scattering, and non-emitting medium. The two-flux approximation can be used as an analytical solution to the one-dimensional RTE for flat plate PBRs or raceway ponds [48, 67]. This approximation has been used extensively [30, 48, 67–69] and has been successfully validated against results from a 3D RTE solver for ponds and flat plate PBRs [48].

Souliès et al. [43] theoretically and experimentally investigated the effect of incidence angle on the growth of *Chlorella vulgaris* in thin flat-panel PBRs artificially illuminated by collimated visible light with an incidence angle θ_i of 0° or 60°. The intensity of the light source was adjusted such that the PBRs received the same radiative flux for both incidence angles. Nonetheless, the experimentally measured volumetric biomass productivity was observed to decrease from 0.029 kg $m^{-3}h^{-1}$ for the PBR under normal incidence to 0.026 kg $m^{-3}h^{-1}$ for the PBR under oblique incidence at $\theta_i = 60°$. Compared to normal incidence, light propagating through the culture at an oblique angle had a longer pathlength to reach a given depth. This caused light to be fully absorbed at shallower depths and prevented it from penetrating deeper into the PBR. Thus, a smaller fraction of the culture volume was illuminated and the volumetric PBR biomass productivity decreased.

Pruvost et al. [30] theoretically investigated the maximum achievable productivity for outdoor PBRs cultivating *Arthrospira platensis*. Two scenarios were considered. The first was an idealized tracking PBR wherein the solar flux was normally incident throughout the day. The second was a fixed horizontal PBR that experienced oblique incidence during the day. Here, the oblique incidence was observed to decrease (i) the photon flux density incident on the PBR and (ii) the penetration depth of sunlight into the PBR culture, as demonstrated by Souliès et. al [43]. Together these two effects resulted in a 31% decrease in the areal biomass productivity from 55 tons $ha^{-1}year^{-1}$ to 38 tons $ha^{-1}year^{-1}$ for the "ideal" tracking PBR and the PBR under oblique incidence, respectively.

3.1.3 Microalgae growth kinetics

The time rate of change of the biomass concentration $X(t)$ in a PBR operated in batch mode can be modeled as [70]

$$\frac{dX}{dt} = \bar{\mu}(t)X(t) \tag{3.1}$$

where $\bar{\mu}(t)$ is the average specific growth rate (in h^{-1}) at time t. Various models have been proposed to predict the average specific growth rate $\bar{\mu}$ of microalgae as a function of the local spectral fluence rate $G_\lambda(z)$. Takache et al. [71] developed a growth kinetics model based on an energetic analysis of the excitation energy transfer in the photosynthetic apparatus. This model accounted for light limitation, photoinhibition, and cell respiration activity as a function of the local fluence rate [71]. Souliès et al. [43] further developed this model to account for the cell respiration activity based on the local rate of photon absorption (LRPA).

Lee et al. [48] studied the effect of PBR geometry on its daily biomass productivity. Microalgae growth in outdoor open ponds, vertical flat-plate PBRs, and tubular PBRs cultivating *Chlamydomonas reinhardtii* was modeled accounting for light saturation and photoinhibition using the Haldane model [72]. Biomass loss rate from cell respiration was assumed to be constant [48, 73]. Remarkably, for all PBR configurations, the biomass productivity was found to scale with the ratio of the initial biomass concentration X_0 and the specific illuminated area a (in m^{-1}) given by $a = S/V$ where S is the illuminated surface area and V is the culture volume [48,74]. In addition, the maximum PBR biomass productivity occurred at the same value of X_0/a for all PBR geometries. Similar results were obtained from both experimental and theoretical data reported in previous studies [75, 76] despite the use of different microalgae species and growth models.

The present study aims to quantify the negative effect of condensed droplets on the window of outdoor covered raceway ponds on the time-dependent LRPA, biomass concentration, growth rate, and daily biomass productivity. This was achieved by coupling simulations of light transfer through droplet covered windows with a simplified model for light transfer

through the microalgae culture and a growth kinetics model for various solar conditions, droplet contact angle, and surface area coverage.

3.2 Methods

3.2.1 Problem statement

Let us consider an outdoor raceway pond located in Los Angeles, CA, USA (34.07° N, 118.44°W) exposed to collimated solar radiation $G_{S,\lambda}$ on the summer solstice (June 21st) and on the autumn equinox (September 23rd). The PBR was covered by a transparent horizontal window of thickness H and refractive index n_w, as illustrated in Figure 3.2. The solar zenith angle θ_z was defined with respect to the outward pointing normal vector of the window surface and the solar azimuth angle γ_s was defined with respect to the due south direction where $\gamma_s = 90°$ corresponds to due west and $\gamma_s = -90°$ corresponds to due east. Figure 3.2a shows the situation when the PBR window was dry and droplet-free. Figure 3.2b schematically illustrates the PBR window partially covered by condensed droplets on its back side with surface area coverage f_A. The droplets were non-absorbing and cap-shaped with refractive index n_d, diameter d, projected diameter d_p, and contact angle θ_c. The incident radiation was either back-scattered or transmitted through the dry or through the droplet-covered window into the PBR culture undergoing reflection or refraction at each interface. The PBR contained a well-mixed culture of depth L and effective refractive index n_m growing *Chlorella vulgaris* with time-dependent biomass concentration $X(t)$ (in gL^{-1}) and spectral average mass absorption $\bar{A}_{abs,\lambda}$ and scattering $\bar{S}_{sca,\lambda}$ cross-sections (in m^{2}kg^{-1}), and spectral scattering phase function $\Phi_\lambda(\Theta)$. The culture depth L varied from 0.1 m to 0.3 m and the initial biomass concentration X_0 varied from 0.01 gL^{-1} to 1 gL^{-1}.

3.2.2 Assumptions

Light transfer through the droplet-covered windows was simulated using the Monte Carlo ray-tracing method [38,44,56]. To do so, the following assumptions were made [38]: (1) all in-

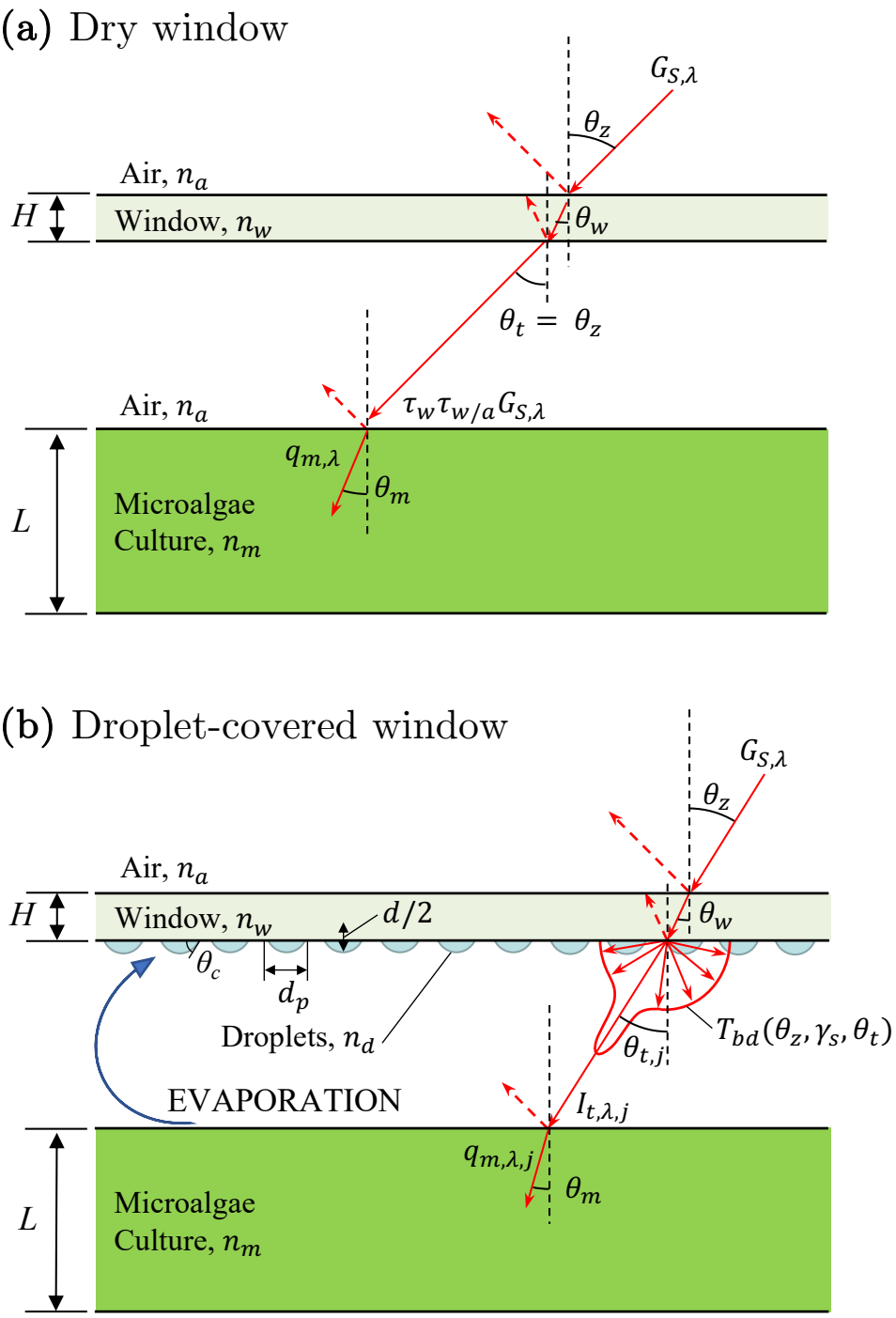

Figure 3.2: Side view (not to scale) of the covered outdoor PBRs studied with (**a**) a dry window and (**b**) a droplet-covered window. In both cases, a portion of the solar radiation was reflected at each interface before the radiative flux $q_{m,\lambda,j}$ was transmitted into the microalgae culture at angle θ_m. Scattering by cap-shaped droplets on the window's back side was described by the bidirectional transmittance T_{bd}.

terfaces were considered optically smooth. In other words, surface roughness was considered to be much less than the wavelength of light in the photosynthetically active region ($\lambda = 400$ - 700 nm) such that reflection and transmission were specular and Snell's law and Fresnel's equations were valid. (2) The dimensions of the droplets and windows were much larger than the wavelength of light such that geometric optics prevailed. (3) Both the window and the droplets were considered to be non-absorbing over the PAR region. (4) The droplets were considered to be cap-shaped with a constant curvature. (5) The droplets were monodisperse with an arbitrary diameter $d = 100$ μm since the bidirectional transmittance of transparent windows with non-absorbing droplets was found to be independent of the droplet size [38,56]. (6) The windows simulated had a surface area coverage f_A of 50% or 90%. Although local conditions may impact the amount of condensate present on the window, the range of f_A was selected to represent a moderate and a worst-case-scenario droplet coverage. (7) Droplet contact angle θ_c was 30° or 90°. These two angles were chosen to approximately represent water on glass and water on a hydrophobic cover, respectively. (8) The refractive index of the air, window, water droplets, and microalgae culture were taken as constant across the PAR region and equal to $n_a = 1.0$, $n_w = 1.5$, $n_d = 1.33$, and $n_m = 1.33$, respectively. Thus, light scattering by the droplets was independent of wavelength. (9) The diffuse part of the incident sunlight was neglected such that all solar radiation incident upon the PBR window was collimated and its direction (θ_s, γ_s) varied during the course of the day.

Predictions of light transfer and microalgae growth in the outdoor PBR were based on the assumptions that (10) the PBR was operated in the light-limited regime wherein growth was only a function of the amount of light available to the microalgae [30, 43, 48]. Thus, the PBR was not limited by any other operating parameters such as temperature, pH, and nutrient availability, and changes in PBR biomass productivity could be attributed to light scattering by the droplets. (11) The microalgae culture was well-mixed with uniform biomass concentration $X(t)$ throughout the PBR. (12) The cells were randomly oriented. (13) The liquid medium was non-scattering and non-absorbing over the PAR region. (14) The radiation characteristics of *Chlorella vulgaris* were constant throughout the day and taken from the literature [43]. (15) All walls of the PBR were considered non-reflective

and perfectly absorbing. (16) Edge effects and shading from the side walls were considered negligible so that light transfer in the PBR culture could be treated as one-dimensional and depended only on the culture depth z.

3.2.3 Light transfer through droplet-covered PBR windows

For PBRs covered by dry windows, Figure 3.2a illustrates that the incoming collimated spectral solar irradiance $G_{S,\lambda}$ (in $\mu\text{mol}_{h\nu}\text{m}^{-2}\text{s}^{-1}$) was reflected and refracted at the air/window interface, at the window/air interface, and at the air/microalgae culture interface before being transmitted into the PBR culture. The transmissivity at the air/window and the air/microalgae culture interface, denoted by $\tau_{a/w}$, and $\tau_{a/m}$, respectively, was determined from Fresnel's relation given by [42]

$$\tau_{1/2} = 1 - \frac{1}{2}\left[\frac{\tan^2(\theta_1 - \theta_2)}{\tan^2(\theta_1 + \theta_2)} + \frac{\sin^2(\theta_1 - \theta_2)}{\sin^2(\theta_1 + \theta_2)}\right] \tag{3.2}$$

where θ_1 and θ_2 are the incident and refracted angles across the Medium 1/Medium 2 interface given by Snell's law $n_1 \sin\theta_1 = n_2 \sin\theta_2$. Then, the spectral radiative flux at the upper boundary of the microalgae culture $q_{m,\lambda}$ (Figure 3.2a) was expressed as a function of the solar position (θ_z, γ_s) and the transmissivity at each interface as

$$q_{m,\lambda}(\theta_z, \gamma_s) = \tau_w \tau_{a/m} G_{S,\lambda}(\theta_z, \gamma_s) \cos\theta_z. \tag{3.3}$$

where τ_w is the transmissivity of the window given by $\tau_w = \tau_{a/w}/(2 - \tau_{a/w})$ [77].

For droplet-covered windows, the incident sunlight was scattered into the transmitted direction described by the polar θ_t and azimuthal φ_t transmission angles (Figure 3.2b). The resulting angular distribution of the transmitted light was described by the bidirectional transmittance T_{bd} in the transmitted direction (θ_t, φ_t) defined as [42, 77]

$$T_{bd}(\theta_z, \gamma_s, \theta_t, \varphi_t) = \frac{I_{t,\lambda}(\theta_z, \gamma_s, \theta_t, \varphi_t)}{G_{S,\lambda}(\theta_z, \gamma_s)\cos\theta_z} \tag{3.4}$$

where $I_{t,\lambda}$ is the spectral radiative intensity transmitted into the direction (θ_t, φ_t). Note that

T_{bd} is wavelength independent since the optical properties of the window and droplets were assumed to be constant over the PAR region.

In order to be coupled with the one-dimensional light transfer analysis in the microalgae culture, the bidirectional transmittance $T_{bd}(\theta_z, \gamma_s, \theta_t, \varphi_t)$ was averaged over the transmitted azimuthal angle φ_t to yield the one-dimensional bidirectional transmittance $\bar{T}_{bd}(\theta_z, \gamma_s, \theta_t)$ according to [56]

$$\bar{T}_{bd}(\theta_z, \gamma_s, \theta_t) = \frac{1}{2\pi} \int_0^{2\pi} T_{bd}(\theta_z, \gamma_s, \theta_t, \varphi_t) \mathrm{d}\varphi_t. \tag{3.5}$$

Then, $\bar{T}_{bd}(\theta_z, \gamma_s, \theta_t)$ (in sr^{-1}) gave the average intensity transmitted into direction θ_t due to solar radiation from the incident direction (θ_z, γ_s). The one-dimensional bidirectional transmittance $\bar{T}_{bd}(\theta_z, \gamma_s, \theta_t)$ was then used to express the transmitted intensity $I_{t,\lambda}$ through the droplet-covered window into direction θ_t as

$$I_{t,\lambda}(\theta_z, \gamma_s, \theta_t) = G_{S,\lambda}(\theta_z, \gamma_s) \cos\theta_z \bar{T}_{bd}(\theta_z, \gamma_s, \theta_t). \tag{3.6}$$

3.2.4 Light transfer in microalgae culture

For wet windows, droplets scattered the incident sunlight into different directions in the transmission hemisphere. The latter can be discretized into M directions $(\theta_{t,j})_{1\leq j\leq M}$. The spectral radiative flux $q_{m,\lambda,j}$ reaching the upper boundary of the microalgae culture in the $\theta_{t,j}$ direction can be written as

$$q_{m,\lambda,j}(\theta_z, \gamma_s, \theta_{t,j}) = \tau_{a/m} I_{t,\lambda,j} \cos\theta_{t,j} \Delta\Omega_{t,j} \tag{3.7}$$

where the solid angle is given by $\Delta\Omega_{t,j} = 2\pi \sin\theta_{t,j} \Delta\theta_{t,j}$. Due to refraction, radiation transmitted through the window at angle $\theta_{t,j}$ was then transmitted through the air/microalgae culture interface at an angle $\theta_{m,j} = \sin^{-1}(n_a \sin\theta_{t,j}/n_m)$. Then, according to the two-flux approximation, the resulting local fluence rate $G_{\lambda,j}(z)$ at depth z within the culture due to the spectral radiative flux $q_{m,\lambda,j}$ incident at angle $\theta_{t,j}$ on the upper boundary of the culture

was expressed as [67]

$$\frac{G_{\lambda,j}(z,\theta_{t,j})}{q_{m,\lambda,j}(\theta_{t,j})} = \frac{2}{\cos\theta_{m,j}} \frac{(1+\alpha_\lambda)e^{\delta_{\lambda,j}(L-z)} - (1-\alpha_\lambda)e^{-\delta_{\lambda,j}(L-z)}}{(1+\alpha_\lambda)^2 e^{\delta_{\lambda,j}L} - (1-\alpha_\lambda)^2 e^{-\delta_{\lambda,j}L}} \tag{3.8}$$

where α_λ and $\delta_{\lambda,j}$ were given by [67]

$$\alpha_\lambda = \sqrt{\frac{\bar{A}_{abs,\lambda}}{\bar{A}_{abs,\lambda} + 2b_\lambda \bar{S}_{sca,\lambda}}} \qquad \text{and} \qquad \delta_{\lambda,j} = \frac{\alpha_\lambda X}{\cos\theta_{m,j}}(\bar{A}_{abs,\lambda} + 2b_\lambda \bar{S}_{sca,\lambda}). \tag{3.9}$$

Here, the average spectral mass absorption $\bar{A}_{abs,\lambda}$ and scattering $\bar{S}_{sca,\lambda}$ cross-sections in $\mathrm{m^2 kg^{-1}}$ (shown in Figure B.1) are properties of the microalgae species being cultivated and were taken from Ref. [43] for a cell mean radius of 2 μm and Chlorophyll *a*, Chlorophyll *b*, and photoprotective carotenoids (PPC) concentrations of 3.3 wt.%, 0.85 wt.%, and 0.85 wt.%, respectively. Assuming axisymmetric scattering by the culture, the backward scattering ratio b_λ is defined as [67]

$$b_\lambda = \frac{1}{2}\int_{\pi}^{\pi/2} \Phi_\lambda(\Theta)\sin\Theta \mathrm{d}\Theta. \tag{3.10}$$

Here, $\Phi_\lambda(\Theta)$ is the so-called scattering phase function representing the probability that photons in the solid angle $\mathrm{d}\Omega_i$ about direction $\hat{\boldsymbol{s}}_i$ are scattered into the solid angle $\mathrm{d}\Omega$ about direction $\hat{\boldsymbol{s}}$ with Θ defined as the angle between the scattered direction $\hat{\boldsymbol{s}}$ and the incident direction $\hat{\boldsymbol{s}}_i$. The scattering phase function was predicted on a spectral basis for *Chlorella vulgaris* using Lorenz-Mie theory for a coated sphere according to the method described in reference Ref. [78]. The resulting spectral backward scattering ratio b_λ is shown in Figure B.1 of Appendix B.

For PBRs with droplet-covered windows, the solar radiation was transmitted through the window into many directions as depicted in Figure 3.2b. Thus, for a given solar position (θ_z, γ_s) the spectral local fluence rate $G_\lambda(z)$ inside the culture covered by a droplet-covered window was found by summing the contribution from all transmission directions $\theta_{t,j}$ according to

$$G_\lambda(z) = \sum_{j=1}^{M+1} G_{\lambda,j}(z, \theta_{t,j}). \tag{3.11}$$

For the dry window PBR, the light reaching the upper boundary of the microalgae culture was collimated and $G_\lambda(z)$ was given by Equation (6.8) for that specific direction.

The ability of the microalgae to absorb the local spectral fluence rate $G_\lambda(z)$ was then described by the local rate of photon absorption (LRPA) $\mathcal{A}(z)$ (in $\mu\text{mol}_{h\nu}\text{kg}^{-1}\text{s}^{-1}$) defined as [43].

$$\mathcal{A}(z) = \int_{PAR} \bar{A}_{abs,\lambda} G_\lambda(z) d\lambda. \tag{3.12}$$

3.2.5 Microalgae growth kinetics

The microalgae growth kinetic model proposed by Takache et al. [71] and further developed by Souliès et al. [43] for *Chlorella vulgaris* was employed to predict the average growth rate $\bar{\mu}$ of the microalgae culture. As discussed previously, this model accounted for light limitation, photoinhibition, and cell respiration activity as a function of the LRPA $\mathcal{A}(z)$ [71]. First, the local specific rate of oxygen production or consumption $J_{O_2}(z)$ (in $\text{mol}_{\text{O}_2}\text{kg}_{\text{X}}^{-1}\text{s}^{-1}$) was calculated according to [43]

$$J_{O_2}(z) = \left[\rho_M \frac{K}{K + \mathcal{A}(z)} \bar{\phi}'_{O_2} \mathcal{A}(z) - \frac{J_{NADH_2}}{\nu_{NADH_2-O_2}} \frac{K_r}{K_r + \mathcal{A}(z)} \right]. \tag{3.13}$$

Here, ρ_M is the maximum energy yield for photon conversion, $\bar{\phi}'_{O_2}$ (in $\text{mol}_{\text{O}_2}\mu\text{mol}_{h\nu}^{-1}$) is the mole quantum yield of O_2 for the Z-scheme of photosynthesis, K (in $\mu\text{mol}_{h\nu}\text{kg}^{-1}\text{s}^{-1}$) is the half-saturation constant for photosynthesis, J_{NADH_2} (in $\text{mol}_{\text{NADH}_2}\text{kg}_{\text{X}}^{-1}\text{s}^{-1}$) is the specific rate of cofactor regeneration on the respiratory chain, related to the oxygen consumption by the stoichiometric coefficient of cofactor regeneration on the respiratory chain $\nu_{NADH_2-O_2}$, and K_r (in $\mu\text{mol}_{h\nu}\text{kg}^{-1}\text{s}^{-1}$) is the half saturation constant describing the inhibition of respiration in light. These parameters were taken from Ref. [43] and are summarized in Table 6.1. These parameters and the absorption $\bar{A}_{abs,\lambda}$ and scattering $\bar{S}_{sca,\lambda}$ cross-sections corresponded to the

same culture [43]. The average specific rate of oxygen production $\bar{J}_{O_2}$ over the depth L of the PBR was defined as [43]

$$\bar{J}_{O_2} = \frac{1}{L}\int_0^L J_{O_2}(z)\mathrm{d}z. \tag{3.14}$$

Then, $\bar{J}_{O_2}$ was used to predict the average specific growth rate $\bar{\mu}$ (in s^{-1}) via the stoichiometric relationship between the production of oxygen and the production of biomass [43]

$$\bar{\mu} = \frac{\bar{J}_{O_2} M_x}{\nu_{O_2-X}} \tag{3.15}$$

where M_x (in $\mathrm{kg_x mol_C^{-1}}$) is the C-molar mass in the biomass given by $C_m H_p O_n$ and ν_{O_2-X} is the stoichiometric coefficient of the oxygen production.

Finally, the temporal evolution of the biomass concentration $X(t)$ was found by integrating Equation (6.11). Then, to assess the impact of droplets on PBR performance, the areal biomass productivity for a given day P (in kg $\mathrm{m^{-2} day^{-1}}$) was expressed as

$$P = (X_f - X_0)L \tag{3.16}$$

where X_0 and X_f are the initial and final biomass concentrations, respectively, given by $X_0 = X(t_0 = 7\text{ am})$ and $X_f = X(t_f = 7\text{ pm})$ on June 21$^{\text{st}}$ and $X_0 = X(t_0 = 9\text{ am})$ and $X_f = X(t_f = 5\text{ pm})$ on September 23$^{\text{rd}}$.

Another important PBR performance metric that can be used to assess the effect of droplets is the so-called illuminated fraction γ given by [30]

$$\gamma = \frac{z_c}{L} \tag{3.17}$$

where z_c is the maximum culture depth at which the local LRPA $\mathcal{A}(z)$ still yields positive photosynthetic growth, i.e., $\mathcal{A}(z_c) = \mathcal{A}_c$ where $\mathcal{A}_c$ is the minimum LRPA required to prevent biomass loss due to respiration [43]. When $\gamma = 1$, positive photosynthetic growth occurs throughout the entire culture and all incident light available for photosynthesis is absorbed

by the culture. Under these conditions, the maximum average growth rate $\bar{\mu}_{max}$ is reached for given light conditions [30]. When $\gamma < 1$, dark zones are present in the culture volume and biomass loss occurs due to respiration. By contrast, $\gamma > 1$ indicates that excess light is available for photosynthesis.

3.2.6 Initial and boundary conditions

The solar spectrum incident upon the PBR was determined by the PBR location and the time of year. Table 3.1 shows the value of the solar zenith θ_z and azimuth γ_s angles associated with each simulated time on June 21$^{\text{st}}$ and September 23$^{\text{st}}$. Figures 3.3a and 3.3b show the spectral solar direct normal irradiance $G_{S,\lambda}$ (in $\mu\text{mol}_{h\nu}\text{m}^{-2}\text{s}^{-1}$) in Los Angeles predicted by the Simple Model of the Atmospheric Radiative Transfer of Sunshine (SMARTS) [79] for wavelengths in the PAR region from 400 to 700 nm between 7 am to 7 pm on June 21$^{\text{st}}$ and 9 am to 5 pm on September 23$^{\text{rd}}$, respectively. As mentioned previously, edge effects were neglected and the bottom of the PBR was considered to be black. The initial biomass concentration $X_0 = X(t_0)$ was varied between 0.01 and 1.0 gL^{-1}.

3.2.7 Method of solution

Figure 3.4 shows a the block diagram of the procedure used to predict the final biomass concentration X_f and the PBR daily areal biomass productivity P. The droplet parameters (θ_c, f_A), the spectral solar irradiance $G_{S,\lambda}$, and the solar incidence angles (θ_z, γ_s) at initial time $t = t_0$ were input parameters for modeling light transfer through the PBR window. The appropriate light transfer model was then applied according to the window condition. Then, the resulting spectral radiative flux at the upper boundary of the microalgae culture $q_{m,\lambda}(t)$ and the PBR operating parameters (X_0, L) were used to model light transfer and growth kinetics in the culture to predict the biomass concentration $X(t)$. This process was then repeated for subsequent time steps until the final biomass concentration $X_f = X(t_f)$ and the daily areal biomass productivity P were computed.

Light transfer through the dry window and into the microalgae culture was modeled using

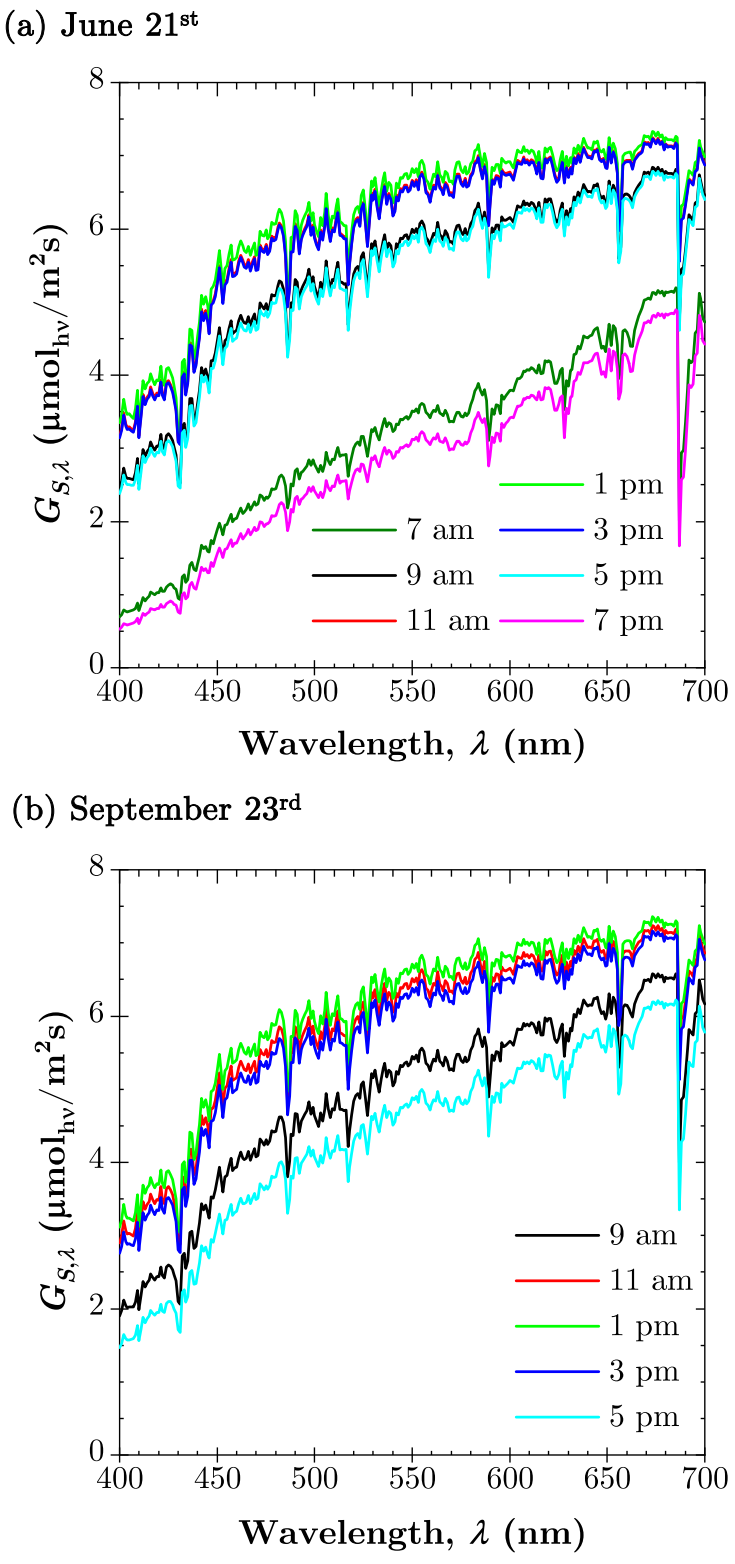

Figure 3.3: Incident collimated solar irradiance $G_{S,\lambda}$ over the PAR region at different times of day simulated on (**a**) June 21st and (**b**) September 23rd in Los Angeles, CA.

Table 3.1: Solar zenith θ_z and azimuth γ_s angles (in degrees) for the different times simulated on June 21st and September 23rd in Los Angeles, CA.

Time	**June 21st**		**September 23rd**	
	$\boldsymbol{\theta_z}$	$\boldsymbol{\gamma_s}$	$\boldsymbol{\theta_z}$	$\boldsymbol{\gamma_s}$
7 am	76.2	-109.2	-	-
9 am	52.0	-94.7	62.9	-69.6
11 am	27.3	-74.8	42.3	-41.6
1 pm	10.7	5.5	34.4	6.2
3 pm	29.1	76.9	46.5	49.5
5 pm	53.8	95.8	68.4	74.2
7 pm	77.9	110.3	-	-

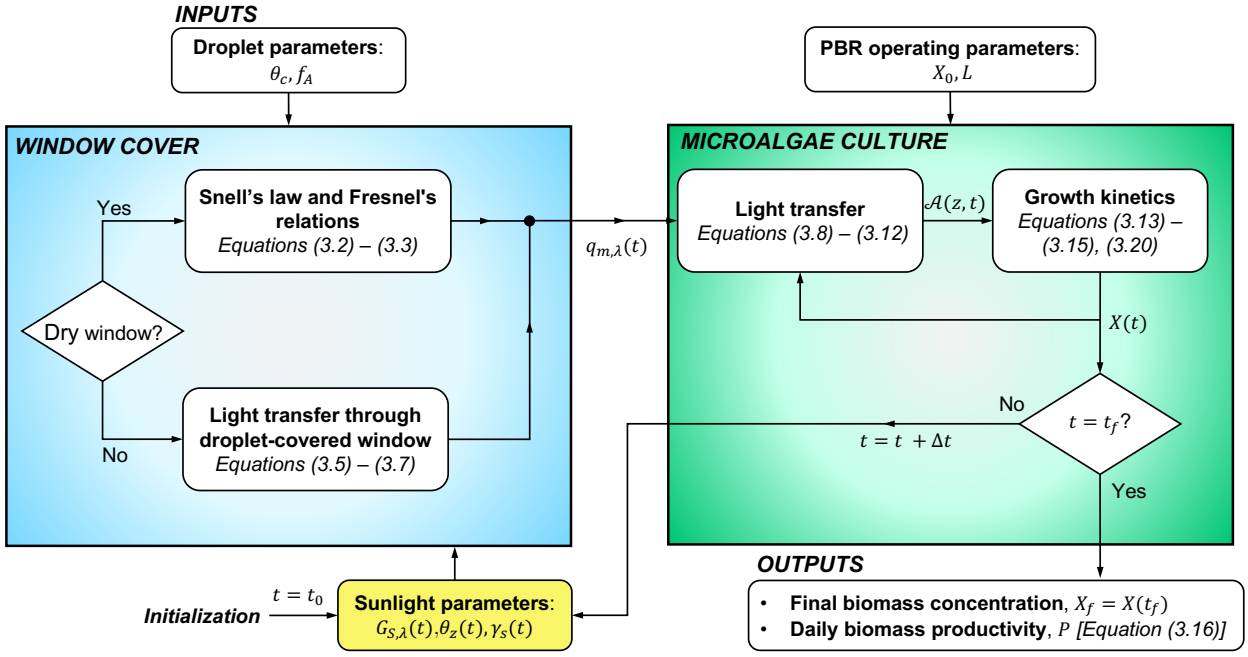

Figure 3.4: Block diagram of the procedure used to predict the final daily biomass X_f and daily areal biomass productivity P for PBRs with dry and droplet-covered windows.

Equations (3.2)-(3.3). For a droplet-covered window, the Monte Carlo ray-tracing method was used to predict the bidirectional transmittance $T_{bd}(\theta_z, \gamma_s, \theta_t, \gamma_t)$. Here, a large number of discrete collimated photon bundles or "rays" were launched in direction (θ_z, γ_s) towards the window covered by computationally-generated droplets. The method and algorithm are described in detail in Refs. [38, 44, 56] and need not be repeated. In brief, the polar transmission angle θ_t ranged from 0° to 90° and was discretized into $M+1$ angular intervals where $M = 90$, with $\Delta\theta_{t,j=1} = \Delta\theta_{t,j=M+1} = \pi/4M$ (in rad) for the first and last intervals at angles $\theta_{t,1} = \pi/8M$ (in rad) and $\theta_{t,M+1} = \pi/2 - \pi/8M$ (in rad) while the interval $(\Delta\theta_{t,j})_{2\leq j\leq M} = \pi/2M$ (in rad) was used for all other transmission angles. The azimuthal transmission angle φ_t ranged from 0° to 360° in uniform intervals of $\Delta\varphi_t = \pi/180$ (in rad). At each interface a ray encountered, the interface reflectivity was calculated using Fresnel's equations. Then, a random number selected from the uniform distribution was compared to the interface reflectivity to determine if the ray was reflected or refracted. The new ray direction was governed by specular reflection or Snell's law for refracted rays. The next interface the ray encountered was then determined using the geometry of the 3D simulation domain. For a non-absorbing window and droplets, this process continued until the ray was either (i) transmitted through the window and droplets or (ii) reflected away from the window. Then, the fraction of solar energy transmitted through the droplet-covered window for a given solar position (θ_z, γ_s) was represented by the directional-hemispherical transmittance T_{dh} expressed as [38]

$$T_{dh}(\theta_z, \gamma_s) = \frac{N_t}{N_i} \tag{3.18}$$

where N_i is the total number of rays incident on the window and N_t is the total number of transmitted rays. Furthermore, Equation (3.4) was recast to express the bidirectional transmittance for a given solar position (θ_z, γ_s) and transmitted direction $(\theta_{t,j}, \varphi_{t,k})$ from the output of the Monte Carlo ray-tracing simulation according to [56]

$$T_{bd,jk}(\theta_z, \gamma_s, \theta_{t,j}, \varphi_{t,k}) = \frac{N_{t,jk}}{N_i \cos\theta_t \Delta\Omega_{t,jk}} \tag{3.19}$$

where $N_{t,jk}$ is the number of rays transmitted into the solid angle $\Delta\Omega_{t,jk} = \sin\theta_{t,j}\Delta\theta_{t,j}\Delta\varphi_{t,k}$. In order to achieve numerical convergence for $T_{bd,jk}$, $N_i = 10^7$ rays were simulated [56]. Then, the resulting spectral radiative flux at the upper boundary of microalgae culture $q_{m,\lambda,j}$ was calculated using the bidirectional transmittance $T_{bd,jk}$ and Equations (3.5)-(3.7).

Next, the LRPA $\mathcal{A}(z,t)$ accounting for all transmitted directions was predicted via the two-flux approximation according to Equations (6.8)-(6.10). Then, the growth kinetics model was used to predict the average specific growth rate $\bar{\mu}(t)$ based on Equations (6.12)-(3.15). The biomass concentration at time $t + \Delta t$ was predicted from the biomass concentration $X(t)$ at time t by integrating Equation (6.11) according to [48]

$$X(t + \Delta t) = X(t)[1 + \bar{\mu}(t)\Delta t]. \tag{3.20}$$

Light transfer through the droplet-covered window was simulated in time increments of Δt = 2 h from 7 am to 7 pm on June 21$^{\text{st}}$ and 9 am to 5 pm on September 23$^{\text{rd}}$. To check for numerical convergence, $X(t)$ and $\bar{\mu}(t)$ were predicted by simulating light transfer through a dry window PBR using a time increment of Δt = 0.5 h and Δt = 2 h (see Figure B.2). The maximum relative errors throughout the day for the biomass $X(t)$ were less than 0.1% and 0.3% on June 21$^{\text{st}}$ and September 23$^{\text{rd}}$, respectively. Thus, a time increment of 2 h was considered to be an appropriate compromise between reasonable computation time and sufficient accuracy.

3.3 Results and Discussion

3.3.1 Light transfer through droplet covered PBR windows

Figures 3.5a and 3.5b show the one-dimensional bidirectional transmittance $\bar{T}_{bd}(\theta_z, \gamma_s, \theta_t)$ as a function of the transmission angle θ_t at 1 pm and 5 pm for various window conditions on June 21$^{\text{st}}$ and September 23$^{\text{rd}}$, respectively. On June 21$^{\text{st}}$ at 1 pm, all window conditions show a strong peak in $\bar{T}_{bd}$ at the transmission angle equal to the solar zenith angle (i.e., $\theta_t = \theta_z$) with a large surrounding lobe. At 5 pm, as the solar zenith angle θ_z increased,

the corresponding peak in $\bar{T}_{bd}$ decreased, and the surrounding lobes became wider for a given droplet configuration. This was indicative of increased scattering at larger solar zenith angles. Indeed, for a window with droplets of contact angle of $\theta_c = 90°$ and surface area coverage $f_A = 90\%$ on September 23$^{\text{rd}}$ at 5 pm, so much scattering occurred that $\bar{T}_{bd}$ peaked around $\theta_t = 45°$ despite a solar zenith angle θ_z of 68° at this time.

Figures 3.5c and 3.5d show the temporal evolution of the average transmission angle $\bar{\theta}_t$ defined as the transmission angle θ_t weighted by the one-dimensional bidirectional transmittance $\bar{T}_{bd}(\theta_z, \gamma_s, \theta_t)$ for a given solar position (θ_z, γ_s), i.e.,

$$\bar{\theta}_t = 2\pi \int_0^{\pi/2} \bar{T}_{bd}(\theta_z, \gamma_s, \theta_t)\theta_t \sin\theta_t \mathrm{d}\theta_t. \tag{3.21}$$

In the case of a dry window, no scattering occurred and the transmission angle was equal to the incident angle, i.e., $\theta_t = \theta_z$. However, for condensate-covered windows, at all times except between 11 am and 3 pm on June 21$^{\text{st}}$, light scattering by the droplets reduced the average transmission angle by as much as 27° and 20° on June 21$^{\text{st}}$ and September 23$^{\text{rd}}$, respectively. In other words, for large solar zenith angles θ_z the droplets reduced the transmittance but scattered sunlight in directions closer to normal incidence causing the transmitted light to penetrate deeper into the culture compared to a culture covered by a dry window.

Finally, Figures 3.5e and 3.5f show the temporal evolution of the directional-hemispherical transmittance T_{dh} for various window conditions on June 21$^{\text{st}}$ and September 23$^{\text{rd}}$, respectively. On both days, Figures 3.5e and 3.5f indicate that the directional-hemispherical transmittance T_{dh} for the dry window increased to reach a maximum around midday, before decreasing in the afternoon. This was due to the larger reflectance of glass at larger incidence angles [42]. Furthermore, Figures 3.5e and 3.5f show that the presence of droplets reduced T_{dh} for nearly all solar positions investigated on both days. Indeed, droplets with contact angle $\theta_c = 90°$ and surface area coverage $f_A = 90\%$ reduced T_{dh} by up to 37% on June 21$^{\text{st}}$. However, on the same day, T_{dh} increased slightly compared with a dry window for droplet contact angle $\theta_c = 30°$ and surface area coverage $f_A = 90\%$ at 11 am and 1 pm and for $\theta_c = 90°$ and $f_A = 90\%$ at 7 am and 7 pm. This was due to the smaller

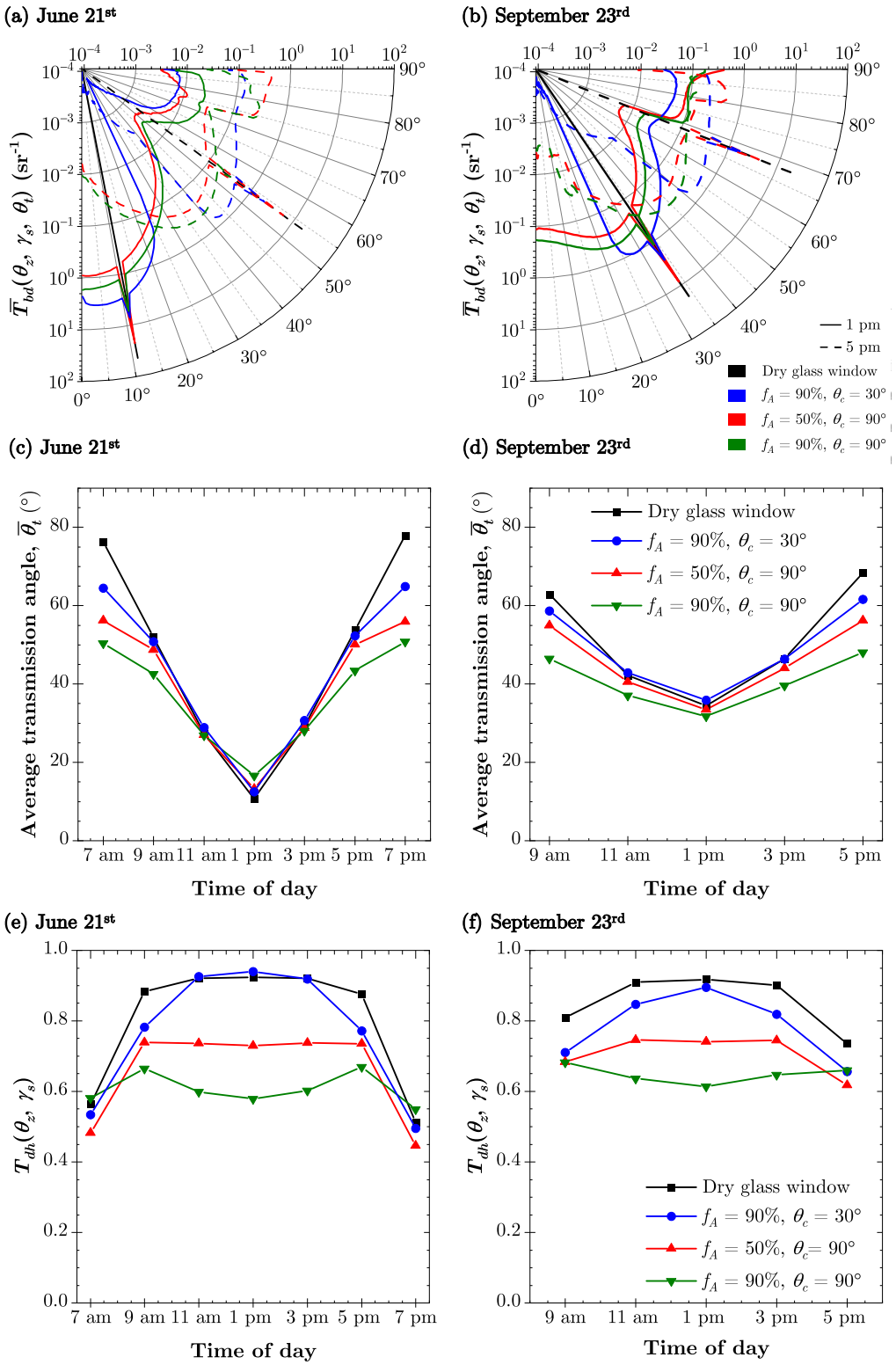

Figure 3.5: (**a, b**) One-dimensional bidirectional transmittance $\bar{T}_{bd}$ at 1 pm and 5 pm, (**c, d**) average transmission angle $\bar{\theta}_t$, and (**e, f**) directional-hemispherical transmittance $T_{dh}(\theta_z, \gamma_s)$ as functions of time for a variety of window conditions on (**a, c, e**) June 21st and (**b, d, f**) September 23rd.

refractive index mismatch between the window ($n_w = 1.5$) and the water droplets ($n_d = 1.33$) for droplet-covered windows than between the window ($n_w = 1.5$) and the air ($n_a = 1.0$) for dry windows. Then, the presence of droplets reduced reflection at the back side of the window resulting in slightly larger T_{dh} compared to the dry window case. In addition, Figure 3.5 indicates that for droplet contact angle $\theta_c = 90°$, increasing the droplet surface area coverage f_A resulted in smaller transmittance T_{dh} of the PBR window between 9 am and 5 pm on June 21st and at all times except 5 pm on September 23rd. Moreover, under normal incidence, previous studies have shown that for a given surface area coverage f_A, the normal-hemispherical transmittance T_{nh} decreased significantly with increasing droplet contact angle θ_c greater than the critical angle θ_{cr} for total internal reflection at the droplet/air interface such that $\theta_{cr} = \sin^{-1}(1/n_d) = 48.8°$ [38]. This phenomenon was also observed in Figures 3.5e and 3.5f at near-normal incidence angles (i.e., small solar zenith angles θ_z).

3.3.2 Light transfer in microalgae culture

Figures 3.6a and 3.6b show the normalized LRPA $\mathcal{A}/\mathcal{A}_c$ as a function of the normalized culture depth z/L for various window conditions at 1 pm and 5 pm in Los Angeles, CA on June 21st and September 23rd, respectively. Here, the initial biomass concentration of the PBR was $X_0 = 0.07$ gL^{-1} and the culture depth was $L = 0.3$ m. For both days, Figure 3.6 indicates that the normalized LRPA $\mathcal{A}/\mathcal{A}_c$ exceeded 1.0 at 1 pm throughout the culture while at 5 pm up to 58% of the culture volume features $\mathcal{A}/\mathcal{A}_c < 1.0$, i.e., an illuminated fraction γ as low as 0.42. This was caused by (i) the smaller solar irradiance later in the day, (ii) the increase in the pathlength of light through the culture for larger solar zenith angles θ_z, and (iii) the photosynthetic response that occurred between 1 pm and 5 pm. Thus, more of the incident radiation was absorbed at shallower culture depths at 5 pm than at 1 pm. These observations were also reported in previous studies [30,43]. On both days at 1 pm, the droplets were responsible for a decrease in the local rate of photon absorption throughout the PBR depth, with the exception of a window with $f_A = 90\%$ and $\theta_c = 30°$ on June 21st at 1 pm due to the increase in T_{dh} observed in Figure 3.5e. On the other hand, on both days at 5 pm, Figure 3.6 shows that the presence of droplets with contact angle $\theta_c = 90°$ resulted

in an increase of up to a 14% in the illuminated fraction γ of the PBR, compared to a dry window. This was due to light scattering by the droplets observed in Figures 3.5a - 3.5d which redistributed the incoming light into many directions and caused light to penetrate deeper into the culture.

3.3.3 Microalgae growth kinetics

Figures 6.13a and 6.13b plot the temporal evolution of the average growth rate $\bar{\mu}(t)$ (in h^{-1}) for PBRs with various window conditions on June 21$^{\mathrm{st}}$ and September 23$^{\mathrm{rd}}$, respectively. Here also, the initial biomass concentration X_0 was 0.07 gL^{-1} and the culture depth L was 0.3 m. For most of the day on June 21$^{\mathrm{st}}$, Figure 6.13a indicates that droplets reduced the average growth rate $\bar{\mu}(t)$. Furthermore, the average growth rate $\bar{\mu}(t)$ decreased with increasing droplet contact angle θ_c and surface area coverage f_A. A similar trend was observed on September 23$^{\mathrm{rd}}$. However, at 5 pm on September 23$^{\mathrm{rd}}$ and 7 am and 7 pm on June 21$^{\mathrm{st}}$, droplets with $\theta_c = 90°$ and $f_A = 90\%$ slightly increased $\bar{\mu}(t)$. This was attributed to the positive effect of light scattering by droplets towards the culture observed previously, which increased the illuminated fraction γ and light penetration in the culture late in the day (see Figure 3.6). Interestingly, on September 23$^{\mathrm{st}}$, this was the case despite a relative decrease in the directional-hemispherical transmittance T_{dh} of up to 24% compared to a dry window. Nonetheless, this phenomena occurred in the morning and evening, when the average growth rate $\bar{\mu}(t)$ was a fraction of its daily peak value and the impact on the final biomass concentration X_f was minimal.

Indeed, Figures 6.13c and 6.13d plot the temporal evolution of the biomass concentration $X(t)$ as a function of time for various window conditions on June 21$^{\mathrm{st}}$ and September 23$^{\mathrm{rd}}$, respectively. The figures indicate that the final biomass concentration X_f was smaller on September 23$^{\mathrm{rd}}$ compared to June 21$^{\mathrm{st}}$ for all configurations considered. This was due to the decrease in spectral solar irradiance $G_{S,\lambda}$ on September 23$^{\mathrm{rd}}$ (see Figures 3.3a and 3.3b) and the larger solar zenith angles θ_z (see Table 3.1) which led to a smaller window transmittance T_{dh} in the presence of droplets. The presence of droplets decreased the final biomass

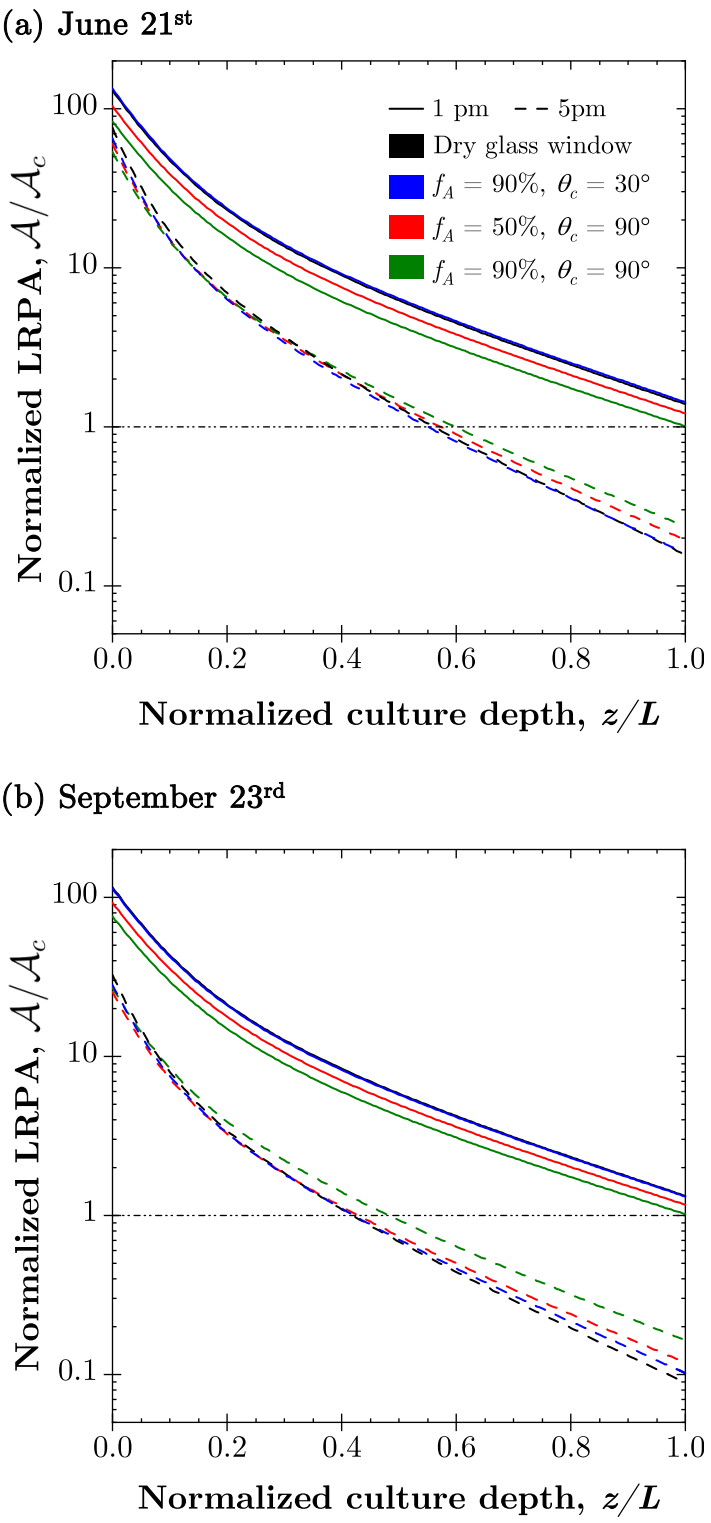

Figure 3.6: Normalized local rate of photon absorption (LRPA) $\mathcal{A}/\mathcal{A}_c$ as a function of the normalized culture depth z/L at 1 pm and 5 pm for a variety of window conditions on (**a**) June 21st and (**b**) September 23rd in Los Angeles, CA. Here, $L = 0.3$ and $\mathcal{A}_c = 2800$ $\mu\text{mol}_{h\nu}$ $\text{kg}^{-1}\text{s}^{-1}$

concentration X_f by up to 10.0% and 8.2% on June 21st and September 23rd, respectively.

3.3.4 PBR biomass productivity

Figures 3.8a and 3.8b show the daily areal biomass productivity P (in kg m^{-2}day^{-1}) as a function of the initial biomass concentration X_0 for various culture depths L and window conditions for PBR operation between 7 am and 7 pm on June 21st and 9 am and 5 pm on September 23rd, respectively. The trends in the daily biomass productivity P were similar for both days although P was smaller on September 23rd than on June 21st. On both days, for a given culture depth L, the culture did not fully absorb the incoming radiation for small initial biomass concentrations X_0. However, as X_0 increased, more of the incoming light was absorbed by the culture and P increased to reach a maximum P_{max}. As previously discussed, the optimal biomass productivity occurs for a light-limited PBR when the incoming radiation is fully absorbed in the culture, i.e., the microalgae suspension is fully illuminated with no dark zones. As X_0 increased further, dark zones appeared in the culture causing the areal biomass productivity P to decrease. Figures 3.8a and 3.8b indicate that as the culture depth L increased, the maximum biomass productivity occurred for smaller values of X_0.

Lee et al. [48] demonstrated that PBR productivity P scaled with X_0/a where a is the specific illuminated area. In the case of the simulated raceway pond, a is given by $a = S/V = 1/L$ where S is the illuminated surface area and V is the culture volume [74]. Furthermore, we note that the initial optical thickness of the PBR is defined as $\beta_{\lambda,0}L = (\bar{A}_{abs,\lambda} + \bar{S}_{sca,\lambda})X_0L$ where $\beta_{\lambda,0}$ is the initial culture extinction coefficient (in m^{-1}). Thus, the quantity $X_0L = X_0/a$ is representative of the culture initial optical thickness [48]. In order to test this scaling relationship for PBRs covered by windows supporting pendant droplets, Figures 3.8c and 3.8d plot the biomass productivity P with respect to the initial optical thickness represented by X_0/a for various window conditions. Both Figures indicate that, for a given day and window condition, all data collapse on the same line. Thus, the biomass productivity P depended solely on X_0/a, the PBR window conditions, and the day of the year. Furthermore, for a given day of the year, the optimum initial optical thickness $(X_0/a)_{opt}$

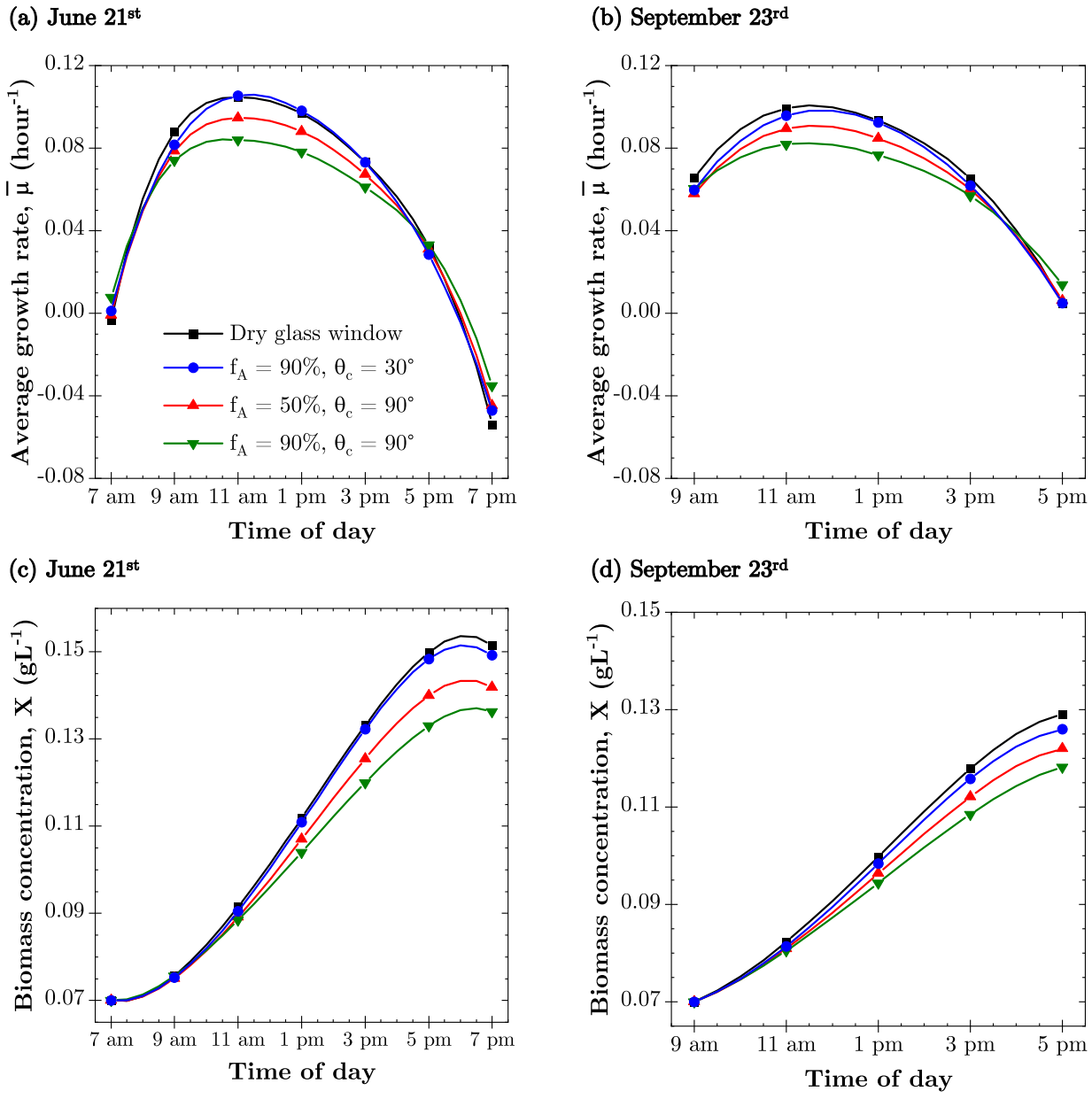

Figure 3.7: Average PBR growth rate $\bar{\mu}$ as a function of time for various window conditions on (**a**) June 21st and (**b**) September 23rd and corresponding biomass concentration $X(t)$ on (**c**) June 21st and (**d**) September 23rd.

corresponding to the maximum biomass productivity P_{max} was essentially independent of the window condition. Note that the same results were obtained by Lee et al. [48] albeit using a different growth kinetics model for open ponds as well as vertical and tubular PBRs without droplets cultivating *Chlamydomonas reinhardtii*. These results confirm the importance of the optical thickness represented by X_0/a for maximizing PBR biomass productivity through the PBR design (via $a = 1/L$) and its operation (via X_0) regardless of window condition and/or growth kinetics model. Figure 3.8d shows that on September 23$^{\text{rd}}$, all droplet configurations decreased the maximum biomass productivity P_{max}. By contrast, Figure 3.8c shows that, on June 21$^{\text{st}}$, the effect of droplets with $\theta_c = 30^\circ$ and $f_A = 90\%$ was essentially negligible, while droplets with $\theta_c = 90^\circ$ decreased P_{max}.

Table 3.2 summarizes the maximum biomass productivity P_{max} and the corresponding optimum initial optical thickness $(X_0/a)_{opt}$ for each droplet configuration for both June 21$^{\text{st}}$ and September 23$^{\text{rd}}$, as well as the change in P_{max} relative to the reference case of a PBR covered by a dry window. It is evident that the droplet contact angle strongly affected the maximum achievable PBR biomass productivity P_{max}. Indeed, the maximum biomass productivity P_{max} decreased by just 2.0% and 5.1% for droplet contact angle $\theta_c = 30^\circ$ and surface area coverage $f_A = 90\%$ on June 21$^{\text{st}}$ and September 23$^{\text{rd}}$, respectively. On the other hand, P_{max} decreased by 17.5% and 18.1% for $\theta_c = 90^\circ$ and $f_A = 90\%$ on June 21$^{\text{st}}$ and September 23$^{\text{rd}}$, respectively. Although hydrophobic surfaces may inhibit condensation [80], these results suggest that a hydrophilic cover featuring small droplet contact angle θ_c should be selected whenever possible to mitigate the effect of droplets on the light reaching the culture and on the PBR biomass productivity. Indeed, on a given day, the daily biomass productivity P was larger for droplet contact angle $\theta_c = 30^\circ$ and surface area coverage $f_A = 90\%$ than for $\theta_c = 90^\circ$ and $f_A = 50\%$ on both days and for all values of optical thickness X_0/a.

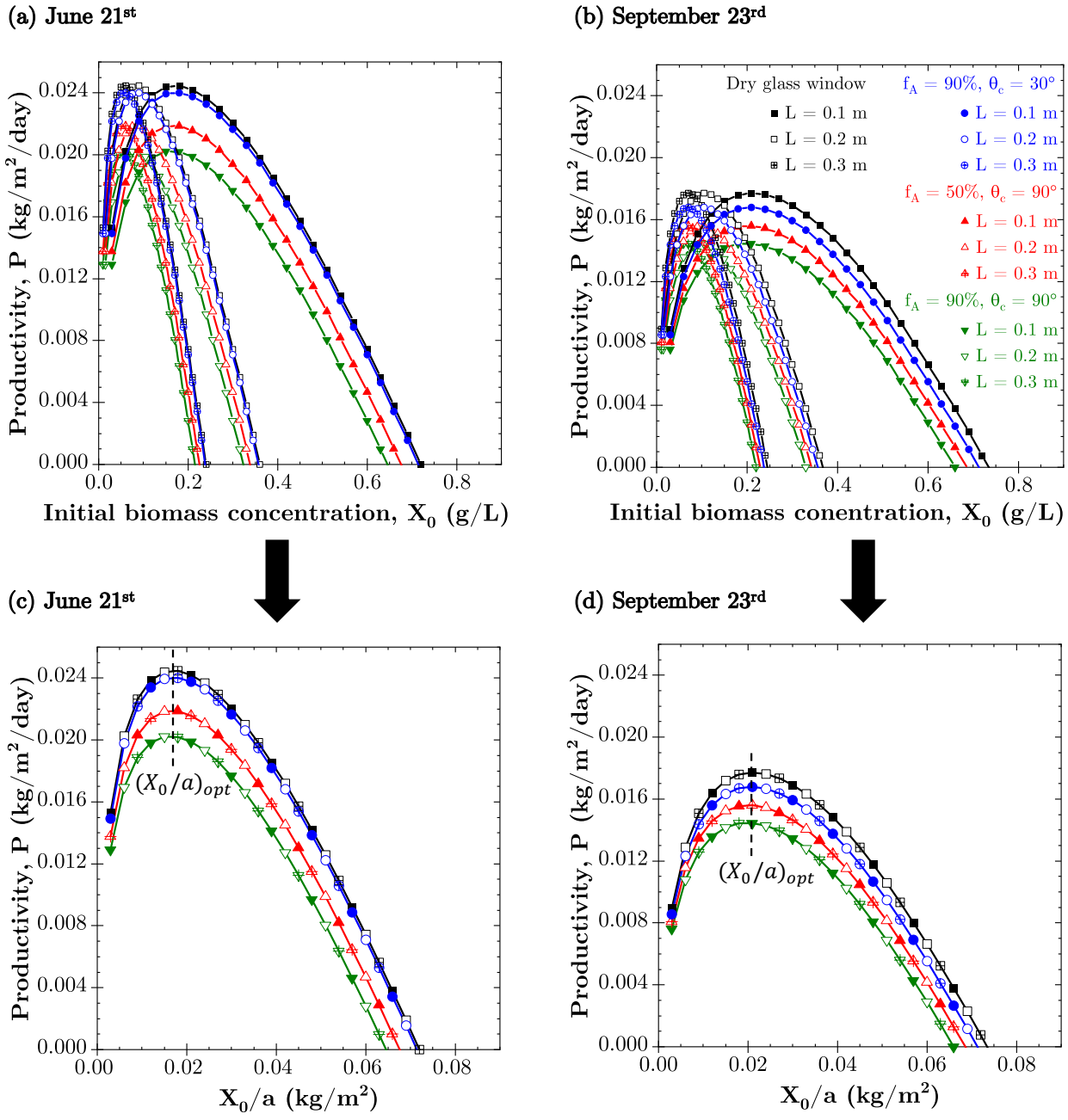

Figure 3.8: (**a, b**) Daily areal PBR biomass productivity P as a function of starting biomass concentration X_0 for various PBR depths L and window conditions and (**c, d**) the same daily areal PBR biomass productivity P as a function of the microalgae culture initial optical thickness represented by X_0/a, on (**a, c**) June 21st and (**b, d**) September 23rd

Table 3.2: Maximum biomass productivity P_{max} and the corresponding optimum optical thickness $(X_0/a)_{opt}$ for each window condition on June 21st and September 23rd. Percent change in P_{max} compared to that of a dry window ($f_A = 0\%$) is also shown.

June 21st				
$\boldsymbol{f_A}$	$\boldsymbol{\theta_c}$	$\boldsymbol{(X_0/a)_{opt}}$ **(kg m^{-2})**	$\boldsymbol{P_{max}}$ **(kg m^{-2} day^{-1})**	$\boldsymbol{P_{max}}$ **change**
0%	NA	0.018	0.0245	0%
90%	30°	0.018	0.0240	-2.0%
50%	90°	0.018	0.0219	-10.6%
90%	90°	0.018	0.0202	-17.5%
September 23rd				
$\boldsymbol{f_A}$	$\boldsymbol{\theta_c}$	$\boldsymbol{(X_0/a)_{opt}}$ **(kg m^{-2})**	$\boldsymbol{P_{max}}$ **(kg m^{-2} day^{-1})**	$\boldsymbol{P_{max}}$ **change**
0%	NA	0.021	0.0177	0%
90%	30°	0.021	0.0168	-5.1%
50%	90°	0.021	0.0156	-11.9%
90%	90°	0.021	0.0145	-18.1%

3.4 Conclusions

This study demonstrated the effect of condensate droplets on the biomass productivity of covered outdoor raceway ponds. Numerical simulations of light transfer were coupled to a microalgae growth kinetics to predict the performance of PBRs with and without condensate droplet-covered windows. The bidirectional transmittance of droplet-covered windows in Los Angeles, CA at different times throughout the day on June 21$^{\text{st}}$ and September 23$^{\text{rd}}$ was predicted by the Monte Carlo ray-tracing method. The local fluence rate within the horizontal culture of *Chlorella vulgaris* was predicted using the two-flux approximation for oblique incidence. A growth kinetics model accounting for photolimitation, photoinhibition, and respiration was applied. Droplets with contact angle $\theta_c = 90°$ decreased the maximum areal PBR biomass productivity P_{max} by up to 17.5% and 18.1% on June 21$^{\text{st}}$ and September 23$^{\text{rd}}$, respectively. On both days, the maximum daily areal PBR biomass productivity decreased with increasing droplet contact angle and surface area coverage compared with a dry window. Thus, hydrophilic PBR covers are preferable to minimize the adverse impacts of droplets on PBR biomass productivity. Additionally, the areal PBR biomass productivity scaled with the ratio X_0/a of the initial biomass concentration X_0 and the specific illuminated area $a = 1/L$ such that $X_0/a = X_0 L$ is proportional to the initial optical thickness of the PBR. Finally, for a given day of the year, the maximum biomass productivity occurred at the same initial optical thickness for all window conditions simulated. This optimal initial optical thickness can be used to maximize PBR biomass productivity through PBR design (via L) and operation (via X_0).

CHAPTER 4

Effect of colony formation on light absorption by *Botryococcus braunii*

This chapter elucidates the effect of colony formation on light absorption by *Botryococcus braunii* microalgae cells. The spectral average mass absorption cross-section of suspensions of *B. braunii* cultures with free-floating cells or colonies was measured experimentally across the photosynthetically active radiation region. The average mass absorption cross-section was found to decrease significantly across the spectrum in the presence of colonies. This observation could be attributed to (i) reduced pigment concentrations due to nutrient limitations, (ii) mutual shading of the aggregated cells, and/or (iii) the presence of the colonies' extracellular matrix. The Monte Carlo ray-tracing method was used to elucidate the contribution of each of these phenomena on the mass absorption cross-section of cells in colonies. Colonies were modeled either as fractal aggregates of monodisperse cells, as an ensemble of monodisperse cells regularly arranged at the periphery of a hollow sphere embedded in a spherical extracellular matrix, or as a volume and average projected area equivalent coated sphere. The change in pigment concentrations due to nutrient limitation was found to be the most important factor. In addition, the mass absorption cross-section of cells in colonies was found to decrease due to mutual shading among cells. This effect was stronger with increasing number of cells in the colony and increasing cell absorption index. The effect of extracellular matrix on the mass absorption cross-section was found to be negligible. Finally, good agreement was found between the equivalent coated sphere approximation and the colonies modeled as fractal aggregates comprised of monodisperse cells.

4.1 Background

The colony-forming microalgae species *Botryococcus braunii* has a variety of potential biotechnological applications from nutraceuticals [17–19] to biofuels [7,20–27]. A colony of *B. braunii* consists of an aggregate of cells embedded in an extracellular matrix (ECM). The ECM is a complex structure consisting of (i) rigid hydrocarbon polymers holding the cells in place, (ii) liquid hydrocarbons filling the intermediate space between the rigid hydrocarbons and the cells, and (iii) an extracellular polysaccharide (EPS) sheath surrounding the exterior of the colony [23, 81]. Figure 4.1 shows two micrographs of *B. braunii* race B cells from cultures grown for the present study featuring (a) single cells and (b) colonies.

In the above mentioned applications, *B. braunii* can be grown in various types of raceway ponds or photobioreactors (PBRs) exposed to sunlight, as the energy source, and fed with carbon dioxide, as the carbon source, while the medium contains nutrients (e.g., nitrates and phosphates) necessary to the growth of the microorganisms [33]. The raceway ponds and PBRs operated in the light-limited regime are not limited by any other operational parameters such as nutrients, pH, and temperature. Then, productivity depends only on the amount and distribution of photons absorbed in the culture [30, 43, 48]. This is represented by the local rate of photon absorption (LRPA) at a given location in the culture expressed in $\mu\text{mol}_{\text{h}\nu}/\text{kg s}$ [30, 68]. Predicting and controlling the LRPA in raceway ponds and PBRs is essential in order to maximize the growth rate and/or the production rate of the desired value-added product(s) [30]. Due to their large size compared with the wavelength of sunlight in the photosynthetically active radiation (PAR) region, microalgae cells and colonies are strongly forward scattering. Then, for a given culture configuration and biomass concentration, the LRPA depends entirely on the average mass absorption cross-section $\bar{A}_{abs,\lambda}$ and the incoming solar radiation flux [47, 67]. This has been demonstrated theoretically and numerically for various PBR geometries [48]. Thus, measuring or predicting the mass absorption cross-section $\bar{A}_{abs,\lambda}$ for the culture is sufficient to design and control raceway ponds and PBRs [30, 47].

Moreover, the formation of *B. braunii* colonies may significantly affect light transfer in

the culture via changes in the spectral mass absorption cross-section $\bar{A}_{abs,\lambda}$ [82–84]. Indeed, Kandilian et al. [84] used the T-matrix method in the PAR region to simulate the effects of multiple scattering and shading among constituent monomers on the absorption and scattering cross-sections and asymmetry factor of fractal aggregates consisting of up to 1000 monomers with size parameter x between 0.01 and 20 and defined as $x = 2\pi r/\lambda$ where r is the monomer radius and λ is the radiation wavelength. In particular, mutual shading was found to cause the normalized absorption cross-section, defined as the ratio of the aggregate's absorption cross-section to the product of the number of individual particles in the aggregate and their absorption cross-section, to decrease monotonically with increasing number of strongly absorbing monomers. Similarly, Mulholland et al [85] used the coupled electric and magnetic dipole method to study absorption and scattering by soot and silica particle agglomerates. For monomer size parameter $x > 0.25$ the authors observed a decrease in the normalized absorption cross-section as monomer size parameter increased. This was attributed to the "shielding effect" among the constituent monomers. Liu and Mishchenko [86] used the superposition T-matrix method to study the optical cross-sections of soot and soot-containing aggregates. Polydisperse aggregates were comprised of soot, dust, and sulfate particles of size parameters 10, 1.5, and 3 respectively. The optical cross-sections of such aggregates was smaller than their externally mixed values (i.e. widely separated with negligible particle interaction). The authors suggest this decrease may be attributed to "mutual shadowing". Liu et al [87, 88] employed the generalized multi-sphere Mie-solution method (GMM) to study the effect of fractal prefactor and fractal dimension on the optical properties of soot aggregates. Here also, the authors observed a non-linear decrease in the normalized absorption cross-section of aggregates as a function of the number of monomers. This was attributed to the "shielding effect" and was found to be more pronounced for more compact aggregates characterized by large fractal prefactor and/or fractal dimension. Unfortunately, the size parameter of *B. braunii* cells in colonies over the PAR region is larger than 20, which is greater than that of the particles used in previous studies. Then, applying the T-matrix or GMM method to such colonies is prohibitively time consuming. Thus, a different approach is necessary to predict the absorption cross-section of *B. braunii* colonies.

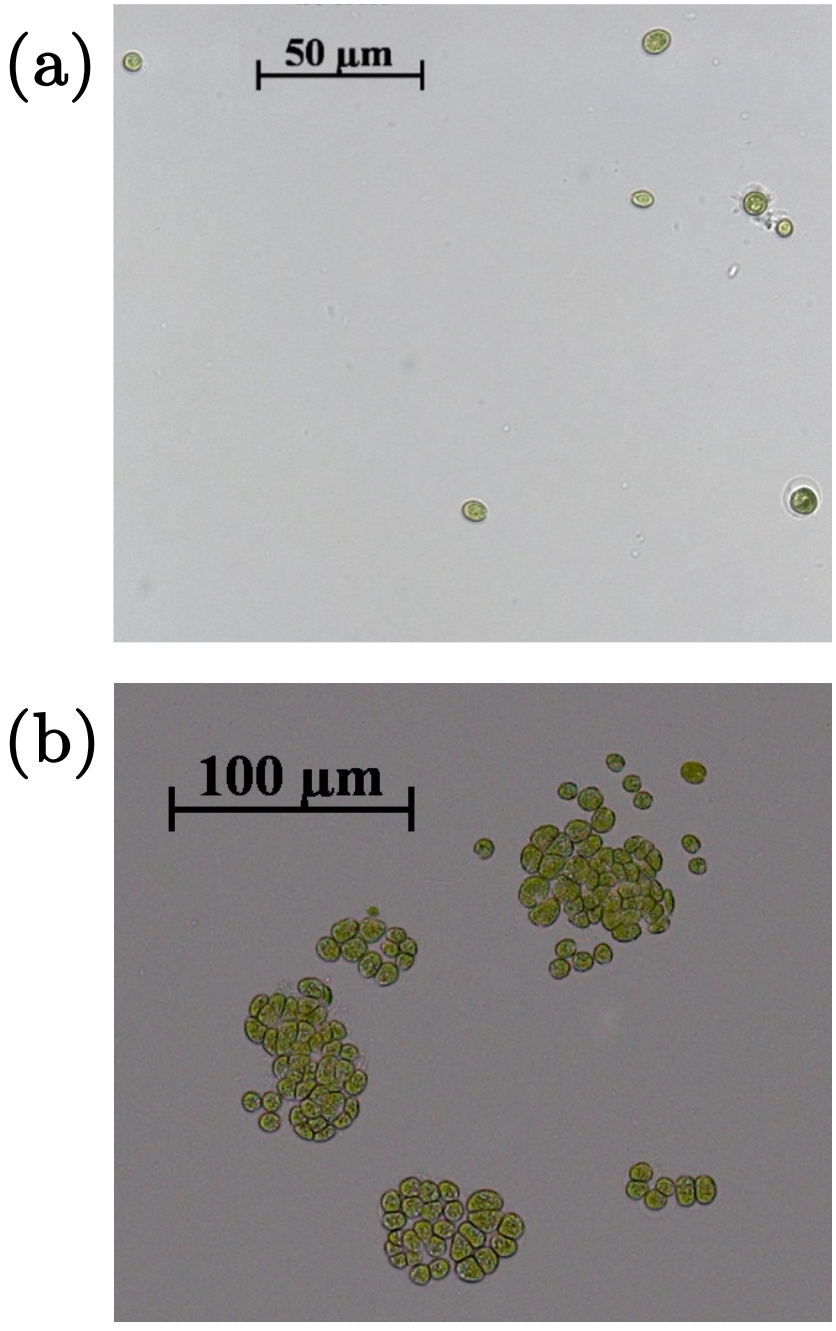

Figure 4.1: Micrographs of *B. braunii* grown for this study as (a) single cells (Culture A) and (b) colonies resembling fractal aggregates (Culture B).

The present study reports experimental measurements of the spectral average mass absorption cross-section of *B. braunii* in the PAR region, growing either as free-floating single cells or as colonies. To interpret the experimental results, a Monte Carlo ray-tracing algorithm was developed and used to assess the effects of pigment concentrations, colony spatial configuration, and colony extracellular matrix on the spectral average mass absorption cross-section of *B. braunii* cells.

4.2 Experiments

4.2.1 Species and cultivation

The *B. braunii* race B strain 761 was obtained from Algobank (Caen, France) [89]. The *B. braunii* microalgae were cultivated in a flat panel airlift photobioreactor with a working volume of 270 mL, thickness of 2 cm, and illuminated surface area of 135 cm^2. The PBR was designed to reduce the hydrodynamic stresses on the cells during cultivation [26]. A photon flux density of 300 $\mu mol_{h\nu}/m^2 s$ from warm white LEDs was delivered normally incident onto the PBR surface. Fresh medium was fed continuously into the PBR to maintain constant nutrient levels under chemostat operation [21]. Culture A was nutrient-replete and consisted mostly of free-floating cells (Figure 4.1a). By contrast, Culture B was nitrogen-limited and contained mostly colonies (Figure 4.1b). This can be explained by changes in EPS production, which is a main driver of colony formation and has been shown to increase in *B. braunii* under nitrogen starvation [20, 90, 91]. Culture A was cultivated in modified Chu 13 medium with the following composition (in g/L): KNO_3 (0.2), K_2HPO_4 (0.04), $MgSO_4 \cdot 7H_2O$ (0.1), $CaCl_2 \cdot 6H_2O$ (0.08), Fe citrate (0.01), citric acid (0.1); micro elements: B, Mn (both at 0.5 ppm), Zn (0.05 ppm), Cu, Co, Mo (0.02 ppm). The medium was sterilized by autoclaving at 121 °C for 25 minutes. Nutrient limitation in Culture B was achieved by cultivation in Chu13 medium without KNO_3 [92]. For both Cultures A and B the PBR dilution rate was set to 0.015 1/h. The culture medium pH was continuously monitored using a pH sensor (Mettler Toledo SG 3253) and was maintained at 7.5 by automatic injection of gaseous CO_2 via the pH-transmitter (Mettler Toledo M300).

4.2.2 Biomass concentration

The dry biomass concentration X (in kg/m^3) was measured by filtering 5 mL of culture through a pre-dried and pre-weighed 0.45 μm pore size cellulose filter. The filters were dried for a minimum of 24 h in an oven at 105 °C and weighed after being cooled in a desiccator for 30 min. Each sample was analyzed in triplicates and the mean value of the dry biomass concentration was reported.

4.2.3 Pigment concentrations

Photosynthetic pigments chlorophyll a and b and photoprotective carotenoids were extracted in pure methanol and quantified spectrophotometrically. First, a volume of 0.5 mL of the continuous airlift PBR culture at steady state was centrifuged at 13,400 rpm (12,100 g) for 10 min. The medium was then discarded and the cells were resuspended in 1.5 mL of pure methanol and sonicated for 20 s. The samples were placed in an oven at 45 °C for 1 h. The extract was then centrifuged again. Measurements of the spectral optical density OD_λ of the supernatant were taken at wavelengths 750, 665, 652, and 480 nm using a UV-vis spectrophotometer (Jasco V-730 Easton, MD). Here also, all extractions were performed in triplicates. Chlorophyll a and b concentrations, denoted by C_{Chla} and C_{Chlb}, were estimated according to [93]

$$\begin{aligned} C_{Chla}[\text{mg/L}] &= -8.0962(OD_{652} - OD_{750}) + 16.5169(OD_{665} - OD_{750}) \\ C_{Chlb}[\text{mg/L}] &= 27.4405(OD_{652} - OD_{750}) - 12.1688(OD_{665} - OD_{750}). \end{aligned} \tag{4.1}$$

Finally, *B. braunii* has no photosynthetic carotenoids [94, 95]. Thus, the concentration of photoprotective carotenoids C_{PPC} was estimated according to [96]

$$C_{PPC}[\text{mg/L}] = 4(OD_{480} - OD_{750}). \tag{4.2}$$

4.2.4 Size distribution

A cell count of Culture A was conducted using a 200 μm deep Malassez cell. The major a and minor b Ferret diameters of individual cells were measured using a Zeiss microscope and

ImageJ software for the single cell Culture A. Then, the cell aspect ratio ϵ was calculated as $\epsilon = a/b$. The radius of a surface-area equivalent sphere $r_{c,eq}$ was calculated as [97]

$$r_{c,eq} = \frac{1}{4}\left(2a^2 + 2ab\frac{\sin^{-1} e}{e}\right)^{1/2} \quad \text{where} \quad e = \frac{(\epsilon^2 - 1)^{1/2}}{\epsilon}. \tag{4.3}$$

The frequency distribution $f(r_{c,eq,i})$ of a given equivalent radius $r_{c,eq,i}$ was estimated according to [78]

$$f(r_{c,eq,i}) = \frac{N(r_{c,eq,i})}{N_T} = \frac{N(r_{c,eq,i})}{\sum_{i=1}^{M} N(r_{c,eq,i})} \tag{4.4}$$

Here, $N(r_{c,eq,i})$ is the number of cells per unit volume of culture with equivalent radius between $r_{c,eq,i}$ and $r_{c,eq,i} + \Delta r_{c,eq}$, and N_T is the total number density of cells per unit volume of culture (in cells/m^3). A minimum of 450 cells were counted for single cell Culture A, with a bin size $\Delta r_{c,eq}$ of 0.05 μm and $M = 78$ bins.

For Culture B, the number of cells per colony N_c was estimated manually. A total of 207 colonies containing more than 4000 cells were characterized. Due to the difficulty associated with counting cells in three-dimensional colonies from two-dimensional images the results are not considered a rigorous characterization of the colony size distribution. Instead, the count was performed to give a qualitative understanding of the range of colony sizes present in Culture B. Approximately 35% of the characterized cells were free-floating cells while 65% were in colonies of 2 or more cells. The vast majority of colonies had a number of cells $N_c < 100$. Yet, colonies with a number of cells N_c larger than 200 were observed.

4.2.5 Microalgae radiation characteristics

The procedure for measuring the radiation characteristics of microalgae has been described in previous references [98–100], and need not be repeated here. In brief, the normal-normal transmittance $T_{nn,\lambda}$ and normal-hemispherical transmittance $T_{nh,\lambda}$ of a 10 mm pathlength quartz cuvette containing a dilute suspension of microalgae in phosphate buffer saline (PBS) were measured at wavelengths λ between 400 and 750 nm in 1 nm increments using a UV-vis-NIR spectrophotometer (Agilent Cary 5000, Santa Clara, CA) and an integrating sphere attachment (Agilent Cary DRA-2500, Santa Clara, CA). The scattering phase func-

tion $\Phi_\lambda(\Theta)$ for single cell *B. braunii* reported in Ref. [100] was used to estimate the correction factor ϵ_n for Culture A using a detector with half acceptance angle of $\Theta_a = 3°$ such that $\epsilon_n^A = 0.37$. The correction factor for Culture B was taken as $\epsilon_n^B = 0.63$. It was estimated using a volume and average projected area equivalent coated sphere approximation demonstrated by Kandilian et al. [84] and the complex refractive index data for *B. braunii* reported in Ref. [101]. The values of ϵ_n^A and ϵ_n^B for each culture were assumed to be constant over the PAR region [102,103]. The spectral absorption κ_λ and scattering $\sigma_{s,\lambda}$ coefficients were calculated for different biomass concentrations to ensure that single scattering through the dilute suspension prevailed [100]. Then, the spectral average mass absorption $\bar{A}_{abs,\lambda}$ and scattering $\bar{S}_{sca,\lambda}$ cross-sections (in m^2/kg) were estimated according to [98]

$$\bar{A}_{abs,\lambda} = \kappa_\lambda / X \text{ and } \bar{S}_{sca,\lambda} = \sigma_{s,\lambda} / X \tag{4.5}$$

where X is the dry biomass concentration in each culture (in kg/m^3).

4.3 Modeling

4.3.1 Problem statement

Let us consider a spherical cell of *B. braunii* with radius $r_{c,eq}$ and spectral effective complex index of refraction $m_{c,\lambda}$. The cell can be approximated as optically homogeneous, as demonstrated by Bhowmik et al. [104]. The cell is surrounded by a non-absorbing PBS solution whose spectral refractive index is given by the Cauchy dispersion relation [105]

$$n_{m,\lambda} = A + \frac{B}{\lambda^2} + \frac{C}{\lambda^4}. \tag{4.6}$$

Here, the wavelength λ is expressed in μm and the coefficients for PBS are $A = 1.32711$, $B = 2.6 \times 10^{-3}$ μm^2, and $C = 5 \times 10^{-5}$ μm^4 [106].

In addition to simulating light absorption by a single *B. braunii* cell, colonies were simulated as either fractal aggregates of monodisperse cells embedded (or not) in a spherical ECM or as ordered monodisperse cells at the periphery of a hollow spherical colony embedded (or not) in a spherical ECM. The former configuration was chosen to approximately represent

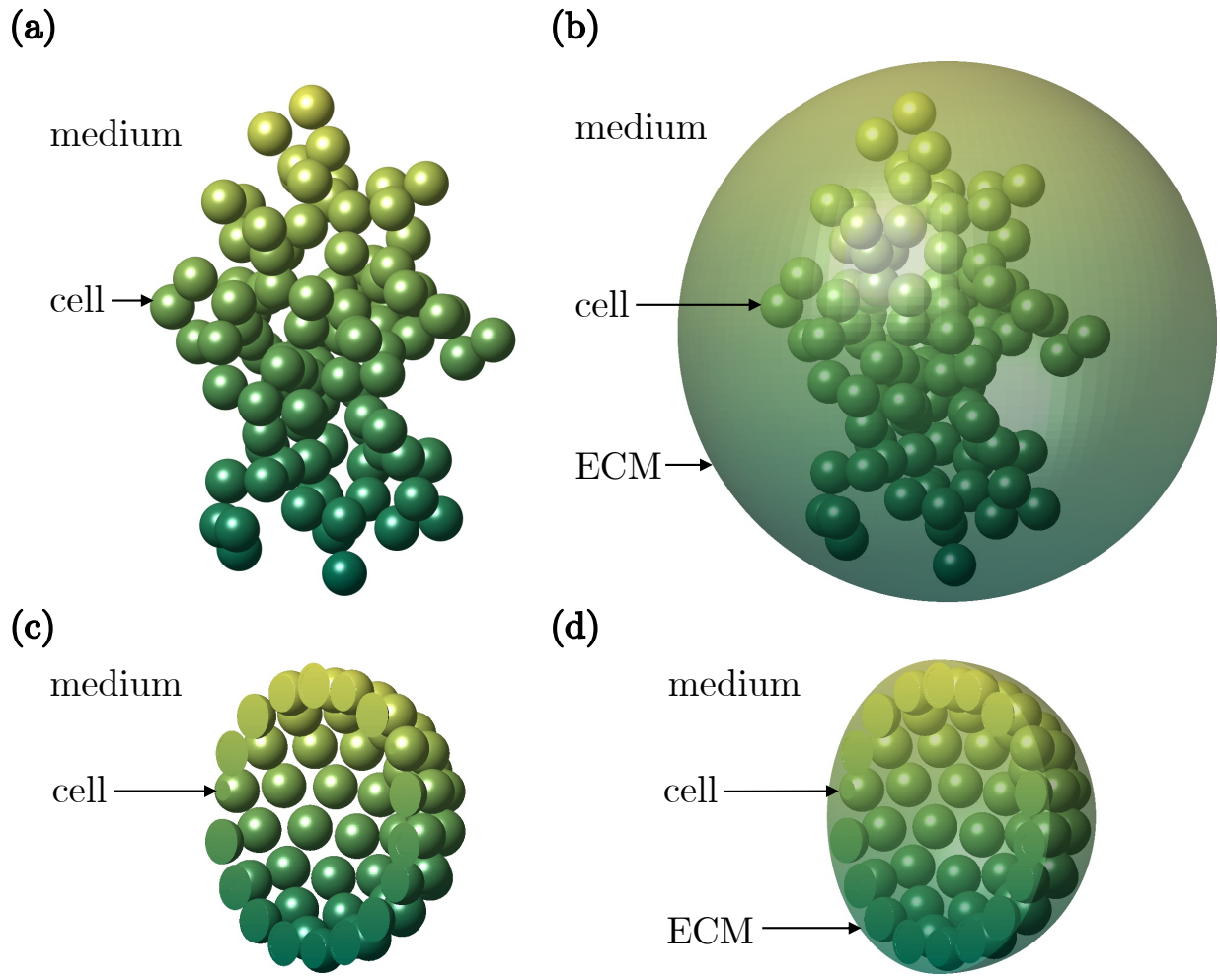

Figure 4.2: Simulated configurations of *B. braunii* colonies as (a) a fractal colony of $N_c = 100$ cells with radius $r_{c,eq}$, refractive index $m_{c,\lambda}$ in surroundings with refractive index $n_{m,\lambda}$, (b) a fractal colony of $N_c = 100$ cells in a non-absorbing, spherical extracellular matrix (ECM) of radius r_{ECM} and refractive index n_{ECM}, section view of (c) a spherical colony of $N_c = 100$ cells, and (d) a spherical colony of $N_c = 100$ cells in a spherical ECM illustrating the hollow spherical shape.

the colonies observed in Figure 4.1b. The latter configuration was chosen to approximately represent the quasi-spherical hollow colony configuration observed by Weiss et al. [81] for a different strain of *B. braunii*. Figure 4.2 illustrates the four different colony configurations simulated. Each colony was exposed to collimated visible photons of wavelength λ. The latter was considered to be much smaller than the cell radius $r_{c,eq}$ such that the cell size

parameter $x_c = 2\pi r_{c,eq}/\lambda \gg 1$ and geometric optics prevailed. Then, photons were (a) reflected or refracted at the cell/medium interface, at the medium/ECM interface, and at the ECM/cell interface, (b) transmitted through the cell(s) and/or ECM, or (c) absorbed within the cell volume.

4.3.2 Optical Properties

First, the spectral complex index of refraction $m^A_{c,\lambda} = n^A_{c,\lambda} + ik^A_{c,\lambda}$ of *B. braunii* cells in Culture A was determined experimentally. To do so, the cell size distribution as well as the spectral average absorption $\bar{C}_{abs,\lambda}$ and scattering $\bar{C}_{sca,\lambda}$ cross-sections of Culture A over the PAR region were obtained experimentally. This information was used to retrieve the cell spectral refractive $n^A_{c,\lambda}$ and absorption $k^A_{c,\lambda}$ indices via an inverse method developed in Ref. [101] based on Lorenz-Mie theory and assuming that the scatterers were spherical and polydisperse [107].

For Culture B, the refractive index $n^B_{c,\lambda}$ of the cells in the colonies was assumed to be identical to that of the single cells in Culture A, i.e., $n^A_{c,\lambda} = n^B_{c,\lambda}$. On the other hand, a general expression for the cell absorption index $k_{c,\lambda}$ can be written as [67]

$$k_{c,\lambda} = \frac{\lambda}{4\pi} \sum_j C_j Ea_{\lambda,j}. \tag{4.7}$$

Here, C_j (in kg/m^3) is the concentration of pigment "j" in the cell and $Ea_{\lambda,j}$ (in m^2/kg) is the spectral mass absorption cross-section of pigment "j". The pigment mass fraction can be defined as $x_j = C_j/C_{pig}$ where C_{pig} is the total pigment concentration in the cell (in kg/m^3) i.e., $C_{pig} = \sum_j C_j$. Then, Equation (4.7) can be written as

$$k_{c,\lambda} = \frac{\lambda}{4\pi} C_{pig} \sum_j x_j Ea_{\lambda,j} = \frac{\lambda}{4\pi} C_{pig} Ea_{\lambda,eff} \tag{4.8}$$

where $Ea_{\lambda,eff}$ (in m^2/kg) is the effective mass absorption cross-section for a kg of pigment with a given combination of pigment mass fractions x_j.

Assuming that the pigment mass fractions x_{Chla}, x_{Chlb}, and x_{PPC} in Cultures A and B are identical, then $Ea_{\lambda,eff}$ can be retrieved from $k^A_{c,\lambda}$. This assumption was verified in Cultures

A and B, as discussed later. Then, assuming equal dry biomass densities and cell water fractions between Cultures A and B the absorption index $k^B_{c,\lambda}$ of the cells in the colonies of Culture B can be estimated using $k^A_{c,\lambda}$ and the total pigment concentrations in Cultures A and B such that [78]

$$k^B_{c,\lambda} = \frac{C^B_{pig}}{C^A_{pig}} k^A_{c,\lambda} = \frac{x^B_{pig}}{x^A_{pig}} k^A_{c,\lambda} \tag{4.9}$$

where x^A_{pig} and x^B_{pig} are the pigment mass fractions of Cultures A and B, respectively. Note that in the case of dissimilar pigment mass fractions between the two cultures, Equation (4.7) can be used to estimate the cell absorption index $k_{c,\lambda}$ based on the pigment spectral mass absorption cross-section $Ea_{\lambda,j}$ reported in the literature [108].

4.3.3 Computational colony generation

As previously discussed, the *B. braunii* colonies were modeled as either fractal aggregates (Figures 4.2a and 4.2b) or ordered spherical colonies where the cells were arranged on the surface of a sphere (Figures 4.2c and 4.2d). These two configurations were chosen to approximately represent the colony structures observed in Figure 4.1b and in Ref. [81], respectively. All computationally generated colonies were comprised of monodisperse spheres of radius $\bar{r}_{c,eq} = 3.71$ μm corresponding to the equivalent average radius of the cells in polydisperse Culture A.

Fractal colonies of N_c monodisperse cells of radius $\bar{r}_{c,eq}$ satisfied the expression [83]

$$N_c = k_f \left(\frac{R_g}{\bar{r}_{c,eq}} \right)^{Df} \tag{4.10}$$

where R_g is the radius of gyration defined as the the mean-squared of the distances between the aggregate center of mass and the centers of the cells, D_f is the fractal dimension, and k_f is the fractal prefactor. Here, the fractal dimension was prescribed as $D_f = 2.3$ corresponding to phytoplankton [109]. The prescribed fractal prefactor was $k_f = 1.6$. Colonies were generated using a ballistic fractal aggregate technique [110]. To generate aggregates, cells were added to the simulation domain one at a time and set on a random walk. The domain initially contained two touching cells. The marching cell stopped when the distance between the closest cell in the aggregate and the new cell was less than the maximum allowed distance

imposed as 1% of the cell radius i.e., 4 nm. No cell overlap was permitted. If the radius of gyration R_g of the new aggregate satisfied Equation (4.10) to within ± 1% using the prescribed values of D_f and k_f, the cell was permitted to stay in the aggregate. Otherwise it was removed. This process was repeated until the desired number of cells N_c was attained. This technique yielded aggregates with average fractal dimension D_f and prefactor k_f within ± 1% of their prescribed values.

Ordered spherical colonies were generated using an algorithm that uniformly distributes a given number of points on the surface of a sphere [111]. These points were taken as the geometric center of monodisperse spherical cells of radius $\bar{r}_{c,eq}$ in the colonies. The minimum allowed distance between the center of two adjacent cells was $2\bar{r}_{c,eq}$ corresponding to point contact.

Finally, to assess the effects of ECM on light absorption by colonies, the previously generated fractal or ordered spherical colonies were placed at the center of a spherical non-absorbing ECM of refractive index $n_{ECM} = 1.48$ [112]. Absorption by the colony ECM was assumed to be negligible compared to that by the strongly absorbing pigmented cells over the PAR region and based on the transparent appearance of the ECM in Figure 4.1b. The center of the ECM was located at the center of mass of the cell ensemble. The ECM thickness was defined as the minimum distance between the cell/ECM interface and the ECM/medium interface and taken as one tenth of the cell radius, i.e., $t_{ECM} = r_{c,eq}/10 = 371$ nm. This morphological model can lead to areas where ECM in fractal colonies is unrealistically thick (see Figure 4.2b). However, this simplification was used to determine if the effect of ECM on the mass absorption cross-section $\bar{A}^{co}_{abs,\lambda}$ of cells in a colony was significant enough to warrant a more refined geometric representation of a colony in its ECM.

4.3.4 Monte Carlo ray-tracing method

In order to predict the spectral average mass absorption cross-section $\bar{A}_{abs,\lambda}$ of *B. braunii* cells in the form of a single cell or a colony, a Monte Carlo ray-tracing (MCRT) method similar to that used by Zhu et al. [45, 46] was employed. A large number of discrete collimated

photon bundles or "rays" emanating from randomized locations on a square plane of area A_d were launched at the different colony configurations under investigation. At each interface, the probability of reflection or refraction was determined by Fresnel's equations and the eventual outcome was decided by a random number between 0 and 1 selected from a uniform distribution. The new ray direction was governed by specular reflection for reflected rays and Snell's law for refracted rays [42]. The location of the next interface the ray encountered was calculated from the new ray direction and the geometry of the cell or colony. Throughout the lifespan of the ray, its total pathlength through the single cell or the cells in the colony was recorded. This process continued until the ray was either reflected away from or transmitted through the cell or colony. Then, the transmissivity associated with its pathlength, $\tau_\lambda(l_p)$ was calculated using Beer-Lambert's law given by [42]

$$\tau_\lambda(l_p) = e^{-\kappa_{c,\lambda} l_p}. \tag{4.11}$$

Here, the cell absorption coefficient $\kappa_{c,\lambda}$ (in m^{-1}) was expressed as $\kappa_{c,\lambda} = 4\pi k_{c,\lambda}/\lambda$ where $k_{c,\lambda}$ is the cell absorption index retrieved from experimental data using the inverse method previously discussed [101] or predicted by Equation (4.9) [42]. A random number between 0 and 1 was then chosen from the uniform distribution and compared with the value of τ_λ. If the random number was greater than τ_λ, the ray was counted towards the total number of rays absorbed $N_{abs,\lambda}$. Otherwise the ray was considered transmitted or reflected and was counted towards the total number of rays scattered by the cell or colony $N_{sca,\lambda}$. Once the fate of all rays was determined, the spectral absorption efficiency factor of the single cell (superscript "sc") or colony (superscript "co") was calculated as the ratio of the number of rays absorbed $N_{abs,\lambda}$ to the total number of rays attenuated $N_{ext,\lambda} = N_{sca,\lambda} + N_{abs,\lambda}$, i.e.,

$$Q_{abs,\lambda} = \frac{N_{abs,\lambda}}{N_{ext,\lambda}}. \tag{4.12}$$

For each type of colony comprised of N_c cells, $N_{co} = 100$ different colonies were generated. The number of cells present in the colony N_c ranged from 10 to 900 cells. Then, for each one of these colonies, the computation of $Q_{abs,\lambda}$ was repeated for N_o =10 different colony orientations with respect to the incident collimated photons. For a given colony and colony

orientation, 10^4 rays were simulated to predict the value of $Q_{abs,\lambda}$. Then, the $N_{co} \times N_o$ values of $Q_{abs,\lambda}$ were averaged to obtain the orientation-averaged absorption efficiency factor. Note that increasing by one order of magnitude the number of rays simulated resulted in a change of less than 0.1% in $Q_{abs,\lambda}$ for any value of N_c at 680 nm which approximately corresponds to one of the absorption peaks of chlorophyll *a*. Thus, simulating 10^4 rays was deemed sufficient to achieve numerical convergence (see Supplementary Material). Spectral simulations were performed in 10 nm increments between 400 and 750 nm.

Furthermore, the results from the Monte Carlo ray-tracing simulations were not extended to the scattering efficiency factor $Q_{sca,\lambda} = N_{sca,\lambda}/N_{ext,\lambda}$. Indeed, the MCRT method ignored diffraction and interference effects and could not capture the associated enhancement or suppression of the scattering field. Thus, the total number of rays attenuated $N_{ext,\lambda}$ was always equal to the total number of incident rays so that the value of the extinction efficiency factor $Q_{ext,\lambda}$ was always equal to unity, i.e., $Q_{ext,\lambda} = 1 = Q_{abs,\lambda} + Q_{sca,\lambda}$. The MCRT method is valid in the limiting case of the geometric optics approximation i.e., when $x_c \gg 1$ and $|m_\lambda - 1|x_c \gg 1$, where $x_c = 2\pi r_{c,eq}/\lambda$ is the cell size parameter and $m_\lambda = n_\lambda + ik_\lambda$ is the relative complex index of refraction $m_\lambda = m_{c,\lambda}/n_{m,\lambda}$. However, due to the optically soft nature of microalgae cells, the condition $|m_\lambda - 1|x_c \gg 1$ was not satisfied in the PAR region. Nonetheless, the MCRT method remains capable of predicting the absorption efficiency factor of microalgae cells and colonies, as demonstrated later for both single cells and aggregates of cells.

The spectral absorption cross-section of a single spherical cell $C^{sc}_{abs,\lambda}$ (in m^2) is a function of (i) the cell size parameter x_c, (ii) the cell relative complex index of refraction m_λ, and (iii) the cell equivalent radius $r_{c,eq}$ and can be expressed as [107]

$$C^{sc}_{abs,\lambda}(x_c, m_\lambda) = Q^{sc}_{abs,\lambda}(x_c, m_\lambda)\pi r^2_{c,eq}. \tag{4.13}$$

For a suspension of polydisperse single cells, the average absorption cross-section $\bar{C}^{sc}_{abs,\lambda}$ can be expressed as a weighted sum of the absorption cross-sections of all simulated cells according to

$$\bar{C}^{sc}_{abs,\lambda} = \int_0^\infty C^{sc}_{abs,\lambda}(x_c, m_\lambda) f(x_c) \mathrm{d}x_c \tag{4.14}$$

where $f(x_c)$ is the fraction of cells having size parameter between x_c and $x_c + \mathrm{d}x_c$. For Culture A, the average absorption cross-section can be estimated according to

$$\bar{C}^{sc}_{abs,\lambda} = \sum_{i=1}^{M} C^{sc}_{abs,\lambda}(x_{c,i}, m_\lambda) f(r_{c,eq,i}). \tag{4.15}$$

Similarly, the spectral orientation-averaged absorption cross-section $\bar{C}^{co}_{abs,\lambda}$ (in m^2) of colonies with a given number of cells N_c can be expressed as

$$\bar{C}^{co}_{abs,\lambda} = \frac{1}{N_{co} N_o} \sum_{k=1}^{N_{co}} \sum_{j=1}^{N_o} Q^{co}_{abs,\lambda,j,k} A^{co}_{p,j,k}. \tag{4.16}$$

Here, $Q^{co}_{abs,\lambda,j,k}$ and $A^{co}_{p,j,k}$ are the absorption efficiency factor and projected area of colony "k" with orientation "j" (in m^2). As described previously, $N_{co} = 100$ different colonies were generated and $N_o = 10$ random orientations were simulation for each colony. The orientation-averaged absorption cross-section $\bar{C}^{co}_{abs,\lambda}$ not only depends on the cell size parameter x_c and relative complex index of refraction m_λ but also the number of cells and their arrangement as well as the presence, size, and optical properties of the ECM. For colonies with spherical ECM, the projected area $A^{co}_{p,j,k}$ was readily calculated from the colony ECM radius $r_{ECM,k}$, i.e., $A^{co}_{p,j,k} = \pi r^2_{ECM,k}$. Otherwise, the colony projected area for colony "k" and orientation "j" was estimated from the surface area A_d of the plane from which the collimated incident photons emanated, the number of photons absorbed or scattered $N_{ext,j,k} = N_{abs,j,k} + N_{sca,j,k}$, and the total number of collimated photons N_{total}, i.e.,

$$A^{co}_{p,j,k} = \frac{N_{ext,j,k}}{N_{total}} A_d. \tag{4.17}$$

Finally, to enable comparison between experimental measurements and numerical simulations for both single cells and colonies, the average absorption cross-section on a unit mass basis $\bar{A}^{sc}_{abs,\lambda}$ (in m^2/kg) of single cells can be estimated from the predicted average absorption cross-section $\bar{C}^{sc}_{abs,\lambda}$ according to [101]

$$\bar{A}^{sc}_{abs,\lambda} = \bar{C}^{sc}_{abs,\lambda} \frac{N_T}{X} \tag{4.18}$$

where N_T is the cell density (in cells/m^3) of Culture A and X is the corresponding dry biomass concentration (in kg/m^3). Similarly, the predicted average mass absorption cross-

section $\bar{A}^{co}_{abs,\lambda}$ (in m^2/kg) of cells in computationally generated colonies of N_c monodisperse cells is given by

$$\bar{A}^{co}_{abs,\lambda} = \bar{C}^{co}_{abs,\lambda} \frac{N_T}{X} \frac{1}{N_c}. \tag{4.19}$$

4.3.5 Validation

In order to validate the Monte Carlo ray-tracing algorithm and confirm that the geometric optics approximation can be used to predict the absorption cross-section of optically soft microalgae, we considered *Chlamydomonas reinhardtii* strain CC125 whose spectral complex index of refraction in the PAR region (400-750 nm) was retrieved by Lee et al. [101] from measurements of their absorption and scattering cross-sections and size distribution $f(r_{c,eq})$. Note that for the reported values of cell equivalent radius $r_{c,eq}$ and complex index of refraction $m_{c,\lambda}$, the geometric optics requirement $|m_\lambda - 1|x_c \gg 1$ was not satisfied. To validate the MCRT algorithm, the absorption cross-section $\bar{C}_{abs,\lambda}$ of the polydisperse cells over the PAR region was calculated using both the Lorenz-Mie theory and the MCRT method. The cell size parameter x ranged from 19 to 99, while the relative refractive m_λ and absorption index k_λ ranged from 1.008 to 1.024 and 10^{-6} to 0.006, respectively. Figure 5.3a compares $\bar{C}_{abs,\lambda}$ obtained from both methods as a function of wavelength λ. It indicates that excellent agreement was found between Lorenz-Mie theory and the MCRT method confirming that the geometric optics approximation is appropriate for predicting the spectral absorption cross-section of a single optically soft microalgae cell. However, as a result of neglecting diffraction effects, the predicted values of the spectral scattering cross-section $\bar{C}_{sca,\lambda}$ from the MCRT method differed significantly from the values predicted using Lorenz-Mie theory (not shown).

Furthermore, Figure 5.3b compares the average absorption cross-section $\bar{C}^{co}_{abs}$ of aggregates of large monodisperse spheres as a function of the number of spheres N_c predicted by the MCRT method and by the superposition T-matrix method reported in Ref. [84]. The superposition T-matrix method numerically solves Maxwell's equations for aggregates by summing the contribution of each sphere to the electromagnetic field at any given loca-

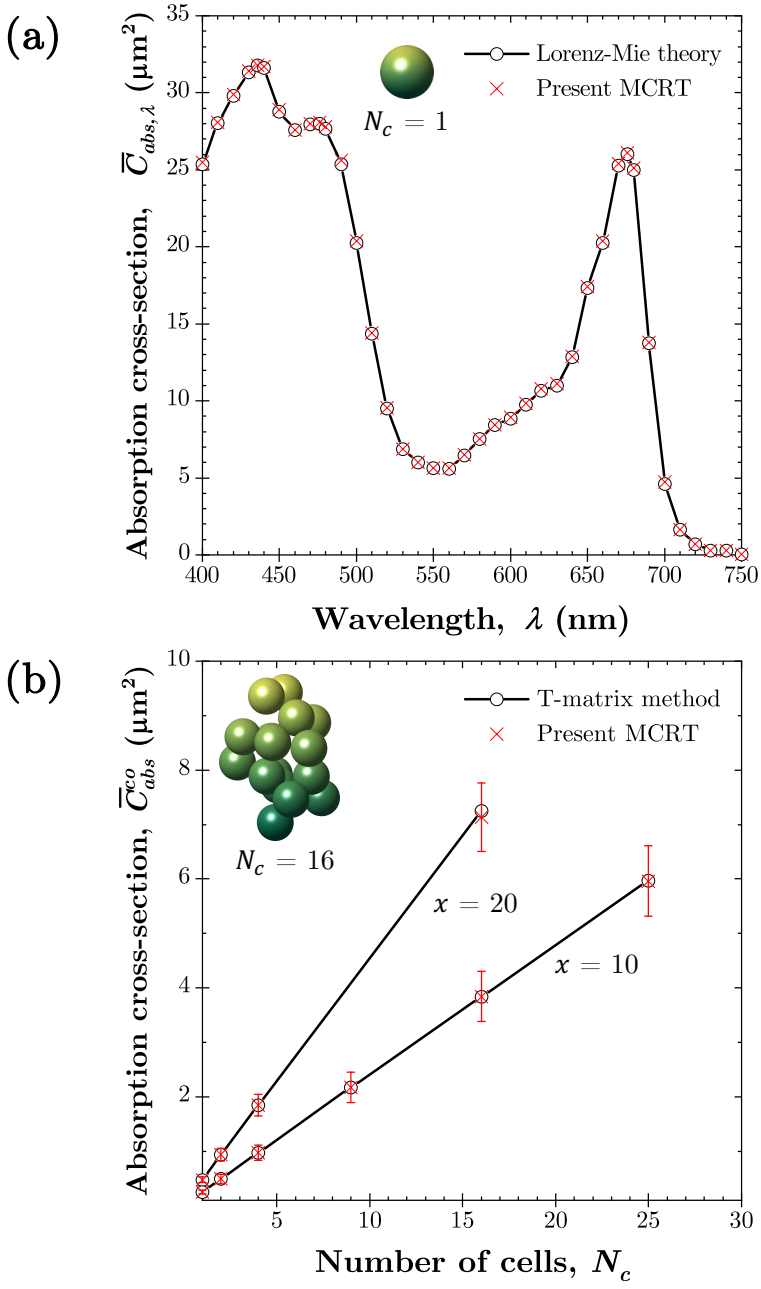

Figure 4.3: (a) Spectral average absorption cross-section $\bar{C}_{abs,\lambda}$ for *Chlamydomonas reinhardtii* strain CC125 over the photosynthetically active radiation (PAR) region using experimental size distribution and spectral optical properties reported in Ref. [101] and (b) average absorption cross-section $\bar{C}^{co}_{abs}$ of fractal aggregates ($k_f = 1.6$ and $D_f = 2.3$) as a function of the number of spheres N_c of size parameter x of 10 and 20 predicted by the T-matrix method and obtained from Ref. [84] and the present Monte Carlo ray-tracing (MCRT) algorithm. Error bars correspond to 95% confidence intervals.

tion [113]. Unlike the MCRT method which accounts only for reflection and refraction, the superposition T-matrix method accounts for all phenomena contributing to scattering including reflection, refraction, diffraction, and interferences [113]. Aggregates with up to 25 large spheres of size parameter x of 10 or 20 and complex index of refraction of $m = 1.0165 + i0.003$ were simulated. The fractal prefactor and dimension was $k_f = 1.6$ and $D_f = 2.3$, respectively. Here also, excellent agreement was observed between the values of $\bar{C}_{abs}^{co}$ predicted by the T-matrix method and the MCRT method. This indicates that the MCRT method is capable of accurately predicting the absorption cross-section of aggregates of large and optically soft cells such as microalgae colonies.

4.4 Results and discussion

4.4.1 Experiments

Table 4.1 summarizes the growth conditions and the corresponding biomass concentration, pigment concentrations, and pigment mass fractions of both cultures considered. Culture A was grown under nutrient-replete conditions and contained free-floating single cells. Culture B was grown under nutrient-limited conditions and contained colonies. Under steady-state continuous operation, Cultures A and B achieved a dry biomass concentration X of 1.78 kg/m^3 and 1.29 kg/m^3, respectively. Table 4.1 indicates that the pigment mass fractions x_{Chla}, x_{Chlb}, and x_{PPC} remained nearly unchanged between Cultures A and B. These results confirm the assumption of constant pigment mass fractions made in estimating the cell absorption index k_λ^B using Equation (4.8). Table 4.1 also indicates that total pigment concentration C_{pig} was lower in the nutrient-limited Culture B. Indeed, under nutrient-replete conditions, *B. braunii* tends to synthesize more photosynthetic pigments namely chlorophyll *a* and *b* [20, 90]. However, under the stress of nutrient-limited conditions less pigments are synthesized and more lipids and hydrocarbons are produced [20, 90]. Figure 4.4 shows the experimentally measured cell size distribution $f(r_{c,eq})$ in Culture A. The average equivalent radius of cells was $\bar{r}_{c,eq} = 3.71$ μm.

Culture	PFD (μmol/m^{2}s)	Nutrient Status	Dilution Rate (1/h)	X (kg/m^3)	$x_{\mathrm{Chl}a}$ (wt. %)	$x_{\mathrm{Chl}b}$ (wt. %)	x_{PPC} (wt. %)	x_{pig} (wt. %)	Colonies
A	300	replete	0.015	1.78	58.5	23.1	18.0	4.8	No
B	300	N limited	0.015	1.29	59.3	20.3	20.3	1.9	Yes

Table 4.1: Experimental conditions of *Botryococcus braunii* cultures A and B including photon flux density (PFD), nutrient status, dilution rate, biomass concentration (X), and pigment mass fractions of chlorophyll a, b, photoprotective carotenoids, and total pigment mass fraction designated by $x_{\mathrm{Chl}a}, x_{\mathrm{Chl}b}, x_{PPC}$ and x_{pig}, respectively.

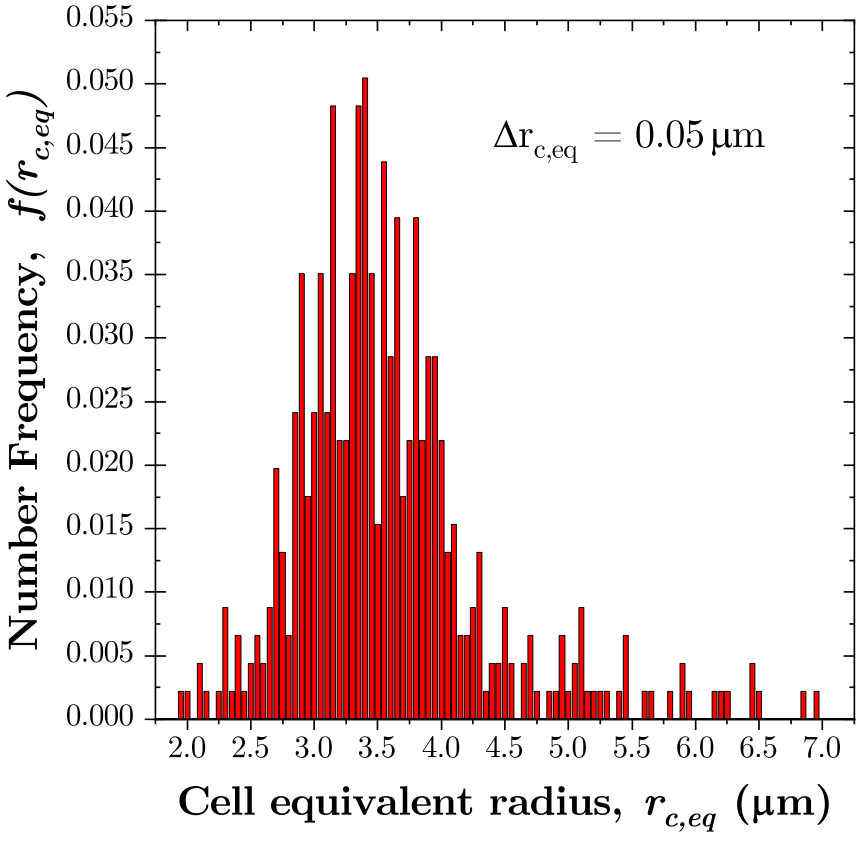

Figure 4.4: Experimentally measured size distribution $f(r_{c,eq})$ of single-cell Culture A.

Figures 4.5a and 4.5b show the spectral average mass absorption $\bar{A}_{abs,\lambda}$ and scattering $\bar{S}_{sca,\lambda}$ cross-sections measured over the PAR region, respectively for Culture A and B. For both cultures, the spectral average mass absorption cross-section $\bar{A}_{abs,\lambda}$ exhibited several peaks including (i) at 437 and 678 nm corresponding to the absorption peaks of *in vivo* chlorophyll *a* and (ii) at 475 nm and 653 nm corresponding to *in vivo* chlorophyll *b* [108]. Moreover, $\bar{A}_{abs,\lambda}$ decreased significantly across the PAR region for the colony containing Culture B compared to Culture A. This change could be attributed to (i) the lower pigment concentrations, (ii) the morphology of the colonies leading to shading effects and/or (iii) the presence of ECM. Unlike $\bar{A}_{abs,\lambda}$, the spectral average mass scattering cross-section $\bar{S}_{sca,\lambda}$ did not change significantly between Cultures A and B. Since $\bar{S}_{sca,\lambda}$ depends strongly on the cell refractive index, this observation supported the assumption that the cells in both cultures had the same refractive index, i.e., $n^A_{c,\lambda} = n^B_{c,\lambda}$. For both cultures, the spectral average mass scattering cross-section $\bar{S}_{sca,\lambda}$ exhibited several troughs at wavelengths corresponding to the absorption peaks observed in $\bar{A}_{abs,\lambda}$. This phenomenon has also been observed in other microalgae species [102, 103, 114].

Figure 4.6a shows the refractive index $n^A_{c,\lambda}$ over the PAR region for cells in Culture A retrieved via the inverse method previously discussed [101]. Figure 4.6a shows that cell refractive index varied only slightly over the PAR region. Additionally, Figure 4.6a indicates that the refractive index retrieved for the current study was similar to that reported in Ref. [101] even though the two *B. braunii* strains were sourced from different suppliers, cultivated in different conditions, and had different cell sizes. Similarly, Figure 4.6b plots the absorption index $k^A_{c,\lambda}$ over the PAR region for cells in Culture A retrieved via the same inverse method [101]. Here, the cell absorption index $k^A_{c,\lambda}$ exhibited peaks corresponding to the *in vivo* absorption peaks of chlorophyll *a* and *b*, as observed in Figure 4.5a. These values of $n^A_{c,\lambda}$ and $k^A_{c,\lambda}$ were used to estimate $n^B_{c,\lambda}$ and $k^B_{c,\lambda}$ necessary for the MCRT method to predict the spectral orientation-averaged mass absorption cross-section $\bar{A}_{abs,\lambda}$ of the four colony configurations investigated.

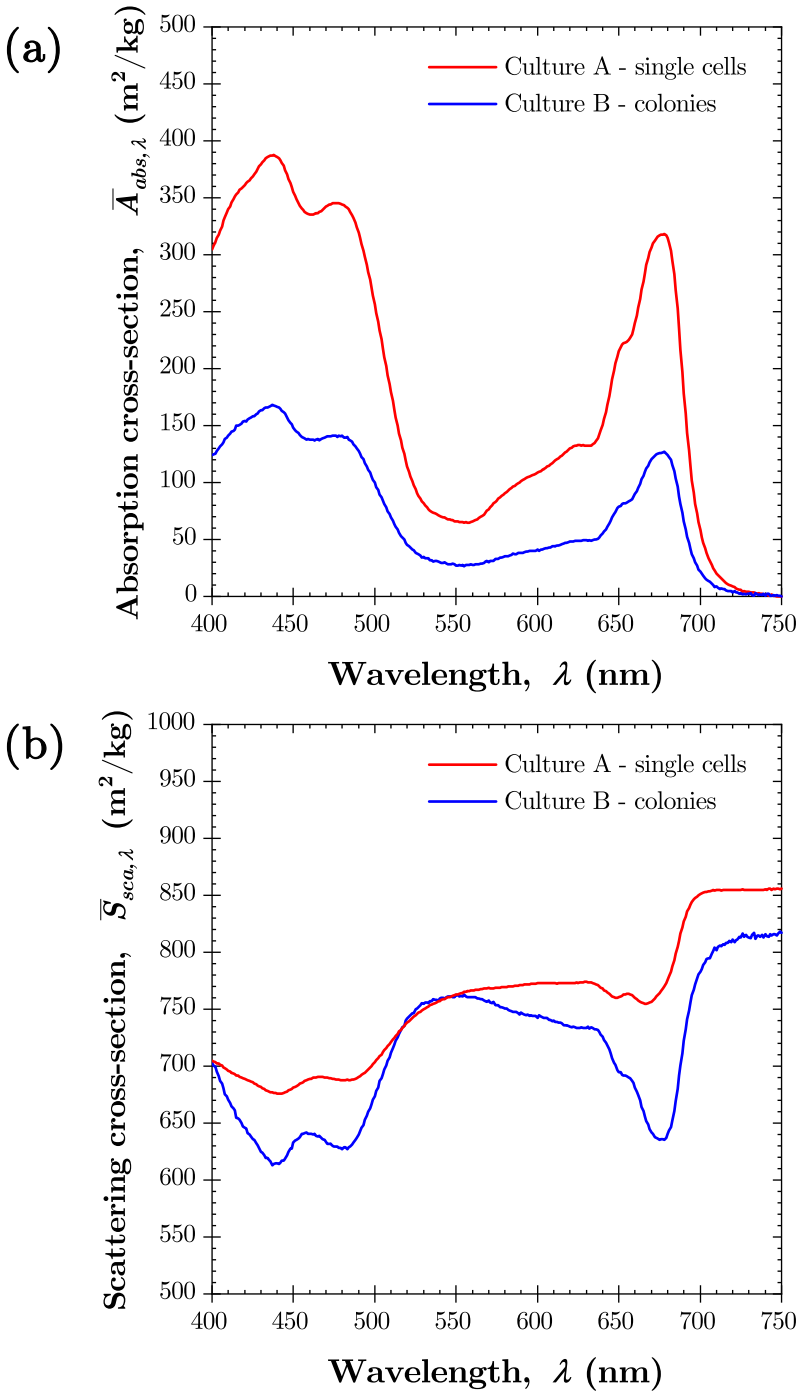

Figure 4.5: Experimentally measured spectral average mass (a) absorption $\bar{A}_{abs,\lambda}$ and (b) scattering $\bar{S}_{sca,\lambda}$ cross-sections over the photosynthetically active radiation (PAR) region for Culture A featuring single cells and Culture B consisting of colonies of *B. braunii* race B.

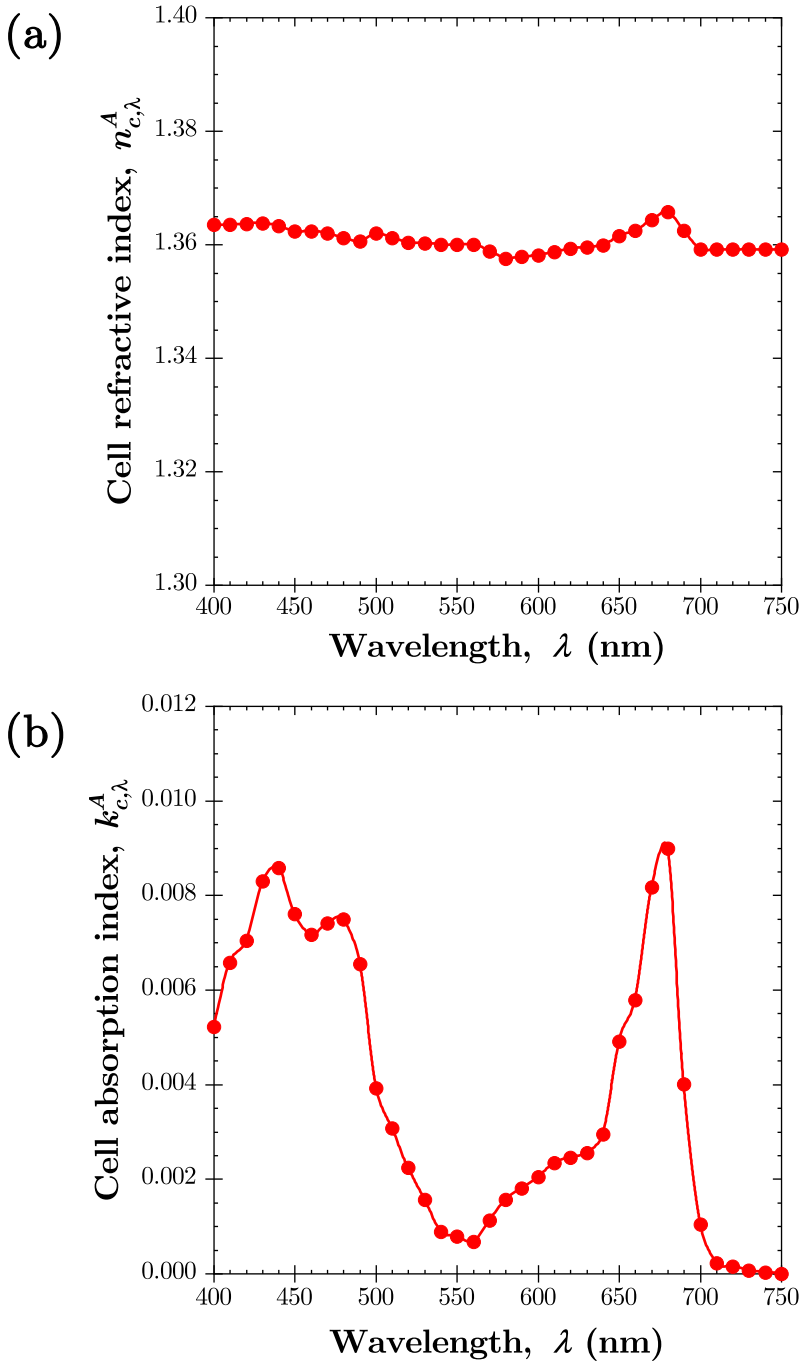

Figure 4.6: Spectral (a) refractive $n^A_{c,\lambda}$ and (b) absorption $k^A_{c,\lambda}$ index for single cell *B. braunii* Culture A obtained from the measured average absorption $\bar{C}_{abs,\lambda}$ and scattering $\bar{C}_{sca,\lambda}$ cross-sections and an inverse method from Ref. [101].

4.4.2 Simulations

Effect of colony morphology and ECM

In order to assess the effect of colony morphology and of the presence of ECM on the mass absorption cross-section of *B. braunii* cells, the different colony configurations of Figure 4.2 were simulated at wavelength $\lambda = 680$ nm with cell relative complex index of refraction $m_c^B = 1.026 + i0.0035$ for a number of cells N_c in the colony ranging from 10 to 900. The wavelength of 680 nm was selected because it approximately corresponds to one of the absorption peaks of chlorophyll *a* [108]. Figure 4.7 plots the orientation-averaged absorption cross-section of colonies $\bar{C}_{abs}^{co}$ predicted by the MCRT method, normalized by the product of the absorption cross-section of a single cell of radius $\bar{r}_{c,eq}$ and the number of cells N_c in the colony $\bar{C}_{abs}^{co}(N_c)/N_c C_{abs}^{sc}$ as a function of N_c for the four different colony configurations considered (see Figure 4.2). Figure 4.7 also plots the normalized absorption cross-section $\bar{C}_{abs}^{co}(N_c)/N_c C_{abs}^{sc}$ of colonies simulated using Lorenz-Mie Theory based on the volume and average projected area equivalent coated sphere approximation suggested in Ref. [84]. The core and shell of the equivalent coated sphere had a complex index of refraction equal to that of the surrounding medium and of the cells, respectively. In addition, the outer shell radius r_o and inner core radius r_i for a given number of N_c of cells in the colony were given by [84]

$$r_o = \left(\frac{\bar{A}_p^{co}(N_c)}{\pi} \right)^{1/2} \qquad \text{and} \qquad r_i = (r_o^3 - N_c \bar{r}_{c,eq}^3)^{1/3} \tag{4.20}$$

where $\bar{A}_p^{co}$ is the average projected area of the fractal aggregate with N_c cells. The error bars correspond to two standard deviations or 95% confidence intervals among the $N_o \times N_{co}$ colonies and orientations simulated. Figure 4.7 indicates that the value of the normalized absorption cross-section varied less for spherical colonies as evidenced by the smaller error bars compared to those of fractal colonies. This was due to the fact that the structure of fractal colonies varies widely from one colony and/or orientation to another, unlike for spherical colonies.

Moreover, a ratio of $\bar{C}_{abs}^{co}(N_c)/N_c C_{abs}^{sc}$ independent of N_c and equal to unity would indicate

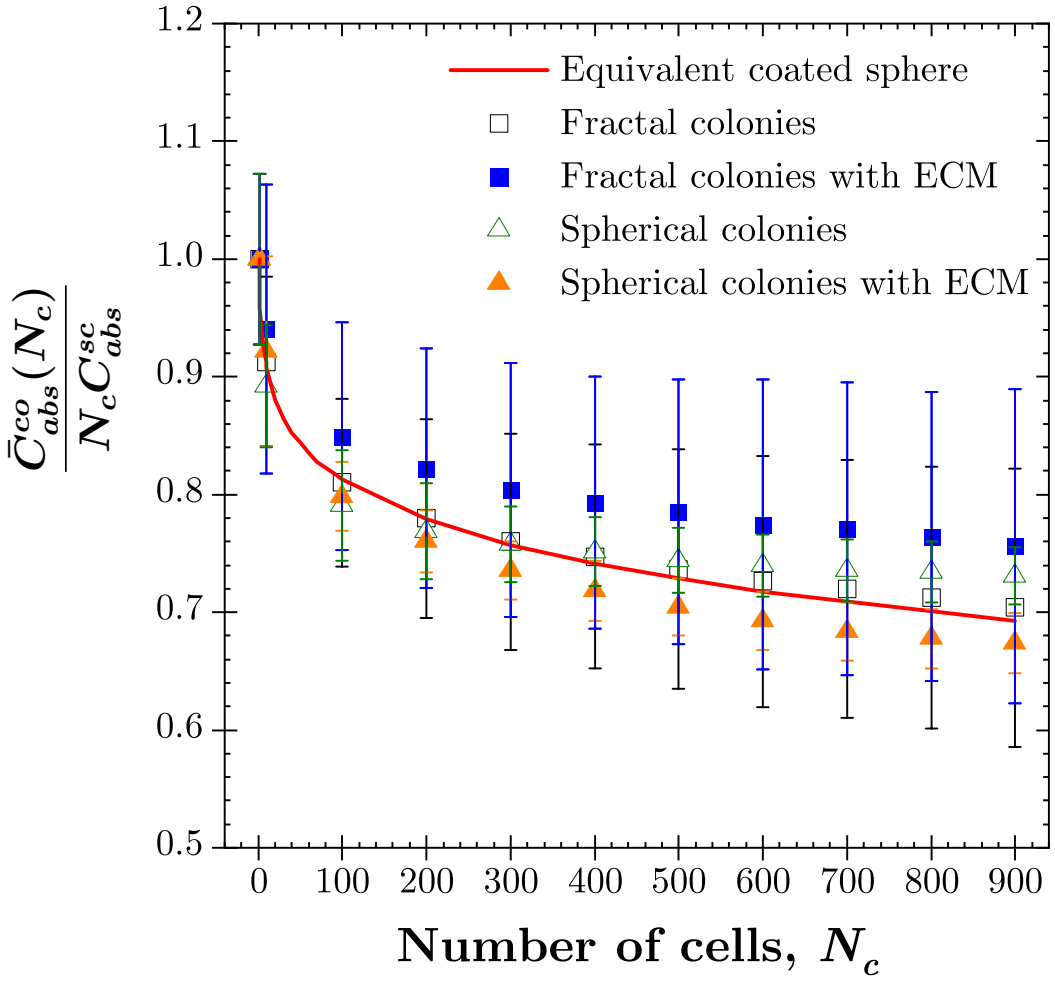

Figure 4.7: Normalized orientation-averaged absorption cross-section of colonies $\bar{C}_{abs}^{co}(N_c)/N_c C_{abs}^{sc}$ as a function of the number of cells in the colony N_c for an equivalent coated sphere approximation and colonies consisting of fractal aggregates or ordered cells at the periphery of a sphere, with and without an extracellular matrix (ECM) (see Figure 4.2). The equivalent coated sphere was simulated using Lorenz-Mie theory while the fractal and spherical colonies were simulated using the Monte Carlo ray-tracing (MCRT) method. The cell complex index of refraction was $m_c^B = 1.026 + i0.0035$. Error bars correspond to 95% confidence intervals.

that the absorption cross-section of a colony is equal to the sum of the contributions of each constitutive cell, i.e., the spatial arrangement of cells in colonies would not matter. However, Figure 4.7 indicates that for all colony configurations considered, the ratio of $\bar{C}^{co}_{abs}(N_c)/N_c C^{sc}_{abs}$ was less than 1.0 and decreased monotonically as the number of cells N_c in the colonies increased. This was due to the shading effects among the cells as their number N_c in the colony grew. Good agreement was found between the volume and average projected area equivalent coated sphere approximation and the normalized absorption cross-sections of fractal colonies predicted by the MCRT. However, assuming $\bar{C}^{co}_{abs}(N_c) = N_c C^{sc}_{abs}$ would overestimate $\bar{C}^{co}_{abs}(N_c)$ as it neglects shading effects which can be significant for large values of N_c and increasing values of $k_{c,\lambda}$. In practice however, the absorption cross-section of colonies with less than 10 cells can be approximated as $\bar{C}^{co}_{abs}(N_c) \simeq N_c C^{sc}_{abs}$ within ~10% error for the refractive index used here.

Furthermore, Figure 4.7 suggests that the effect of ECM on the colonies' absorption cross-section was twofold. In the presence of ECM, photons were (i) reflected at the ECM/cell interface and (ii) internally reflected at the ECM/surrounding medium interface due to the index mismatch between ECM ($n_{ECM} = 1.48$) and the cells ($n_c = 1.366$) as well as between ECM and the surrounding medium ($n_m = 1.333$). Internal reflection at the ECM/medium interface caused photons to be reflected back into the ECM thus increasing the probability that they are eventually absorbed by the cells. This was particularly true in fractal colonies where the spherical ECM geometry exaggerated the increase in projected area (see Figure 4.2b). This caused more photons to be internally reflected at the ECM/medium interface and slightly increased the absorption cross-section of cells. Unlike fractal colonies, the presence of ECM did not significantly increase the projected area of spherical colonies (see Figure 4.2d). Instead, Figure 4.7 indicates a decrease in the normalized absorption cross-section of cells in spherical colonies with ECM due to increased reflection at the ECM/cell boundary. Similar results were obtained at other wavelengths. Despite these nuances, the overall effect of ECM was minor compared to the decrease in absorption cross-section due to changes in pigment concentration and mutual shading. Thus, the effect of the ECM can be considered negligible for most practical situations.

Effect of pigment concentrations

Figure 4.8 plots the spectral average mass absorption cross-section $\bar{A}_{abs,\lambda}$ as a function of wavelength over the PAR region obtained experimentally and predicted by the MCRT method for (i) single cells using pigment concentrations of Culture A, (ii) single cells using pigment concentrations of Culture B, (iii) fractal colonies without ECM, and (iv) spherical colonies without ECM. Since ECM had a negligible effect on $\bar{A}_{abs,\lambda}$ as discussed previously, colonies with ECM are only shown in Supplementary Materials. All simulated colonies had total pigment concentration C_{pig} equal to that of Culture B and consisted of $N_c = 41$ monodisperse cells. This value of N_c was calculated by matching the average projected area of the colonies in Culture B with that of the simulated fractal aggregates. To do so, the average projected area of colonies in Culture B was estimated from microscope images of colonies. In addition, a power law fit of the projected area of the numerically generated fractal aggregates was performed as a function of N_c (see Supplementary Material). First, Figure 4.8 indicates that good agreement was obtained between the experimental measurements and model predictions of the spectral average mass absorption cross-section $\bar{A}_{abs,\lambda}$ for single cells in Culture A. This served as further validation that the MCRT method can predict the absorption cross-section of a polydisperse suspension of single microalgae cells.

Moreover, Figure 4.8 shows a notable decrease in the model predictions of $\bar{A}_{abs,\lambda}$ obtained for single cells using the total pigment concentration C_{pig} of Culture B compared with predictions using C_{pig} of Culture A. Nonetheless, the decrease observed in the experimental data of $\bar{A}_{abs,\lambda}$ between Culture A and Culture B was not entirely captured by the simulations considering the reduction in pigment concentration alone. However, for all colony configurations simulated with pigment concentrations of Culture B, predictions of $\bar{A}_{abs,\lambda}$ were smaller than for single cells. This establishes that, in addition to pigment concentrations, the physical arrangement of cells in the colonies contributed significantly to the reduction in their spectral orientation-averaged mass absorption cross-section $\bar{A}^{co}_{abs,\lambda}$. This was due to mutual shading between the cells. As discussed previously, the difference between the predicted values of $\bar{A}_{abs,\lambda}$ for single cells and for cells in colonies was larger at wavelengths where the

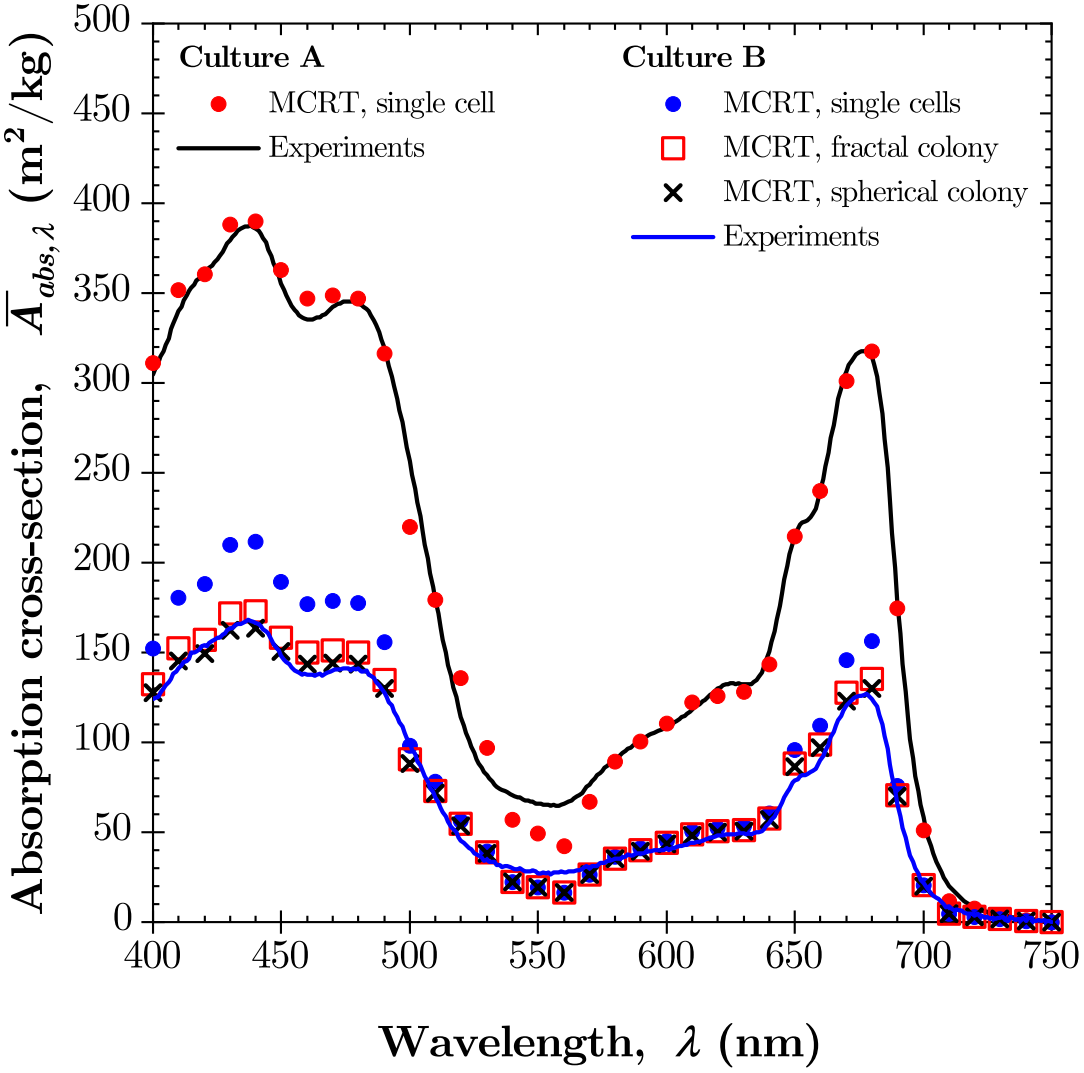

Figure 4.8: Experimental measurement and Monte Carlo ray-tracing (MCRT) predictions of the spectral average mass absorption cross-section $\bar{A}_{abs,\lambda}$ over the photosynthetically active radiation (PAR) region for cells in Cultures A and B. The simulation results were plotted for (i) single cells using pigment concentrations measured from Culture A and Culture B, (ii) fractal colonies without extracellular matrix (ECM), and (iii) spherical colonies without ECM. All colony configurations were simulated using $N_c = 41$ and pigment concentrations from Culture B.

cell absorption index $k_{c,\lambda}$ was larger. However, the difference in $\bar{A}^{co}_{abs,\lambda}$ between the cells in the fractal colonies and those in the spherical shell colonies was minor at all wavelengths. Then, a detailed geometric description of the cell spatial distribution in the colonies is not essential.

4.5 Conclusion

This study provided a qualitative understanding and a quantitative assessment of the effect of pigment concentrations, colony spatial arrangement, and colony extracellular matrix (ECM) on the spectral orientation-averaged mass absorption cross-section $\bar{A}^{co}_{abs,\lambda}$ of *B. braunii* cells in colonies. First, experimental measurements established that colony formation can significantly decrease $\bar{A}^{co}_{abs,\lambda}$ across the PAR region. Then, simulations showed that a large part of the observed decrease was readily explained by a decrease in pigment concentrations. Additionally, the arrangement of cells in colonies was found to significantly contribute to the reduction of the spectral average mass absorption cross-section of *B. braunii* cells due to mutual shading among cells. Good agreement was found between predictions of $\bar{A}^{co}_{abs,\lambda}$ by the Monte Carlo ray-tracing method for computationally generated fractal colonies and the volume and average projected area equivalent coated sphere approximation. Finally, the presence of ECM and the cell spatial distribution in the colony had negligible effects on the mass absorption cross-section $\bar{A}^{co}_{abs,\lambda}$ of cells in colonies.

CHAPTER 5

Light absorption by *Volvocaceae* colonies consisting of equidistant optically soft photosynthetic cells in a transparent spherical extracellular matrix

This chapter aims to expand upon the previous chapter by considering colonies with very large cell and extracellular matrix size parameters, such as those observed in colonies of the *Volvocaceae* family including *Eudorina*, *Pleodorina*, and *Volvox*. Here, we validate the previous methodology for predicting the absorption cross-section of microalgae colonies for the case of a colony consisting of an ordered assembly of large and optically soft absorbing cells embedded within a non-absorbing spherical ECM. The absorption cross-section of spherical colonies, such as *Eudorina*, containing 16, 32, and 64 equidistant photosynthetic cells distributed on the surface of a concentric sphere within an ECM was predicted by the superposition T-matrix method for ECM size parameters as large as 500 and by the Monte Carlo ray-tracing (MCRT) method for ECM size parameters as large as 900. The predicted absorption cross-sections given by the two methods were in excellent agreement despite the fact that the conditions for geometric optics were not rigorously satisfied. The absorption cross-section of the microalgae colonies considered was found to increase with increasing cell radius, absorption index, and/or number of cells. Shading among cells was increasingly important for colonies with strongly absorbing cells, large cell radius, and/or large number of cells. These results demonstrate that accounting for shading effects is necessary to accurately predict the absorption cross-section of microalgae colonies. Furthermore, the study demonstrates that the MCRT method is an accurate and efficient method for modeling light absorption by an ensemble of many large, ordered, and optically soft particles.

5.1 Background

Photosynthetic microorganisms or microalgae are found in diverse forms including unicellular and multicellular organisms as well as colonies. For example, colonial green microalgae *Eudorina*, *Pleodorina*, and *Volvox* in the *Volvocaceae* family, consist of an ensemble of independent and nearly equidistant unicellular photosynthetic cells embedded in an extracellular matrix (ECM) made of glycoprotein [115]. The cells are considered close relatives of the unicellular green microalgae *Chlamydomonas* [116]. In these colonial microalgae, cell division no longer results in unicellular individuals but instead leads to so-called autocolonies [115, 117, 118]. Figure 5.1 shows micrographs of (a) free floating *Chlamydomonas reinhardtii*, (b) *Eudorina elegans*, (c) *Pleodorina californica*, and (d) *Volvox aureus*.

Microalgae colonies such as *Eudorina*, *Pleodorina*, and *Volvox* have been studied due to their negative impact on aquatic ecosystems [119–123] and on water treatment plants [124, 125]. Indeed, their ability to reproduce rapidly in nutrient-rich water often leads to the formation of scum on the water surface [119]. This excessive growth may (a) change the taste and odor of public water supplies [124, 125], (b) interfere with the filtration process of water treatment plants [124], and (c) threaten the survival of other aquatic species by depleting their nutrient and oxygen supplies [120, 122]. These issues have drawn significant interest among limnologists, environmental agencies, water authorities, and human/animal health organizations to effectively monitor phytoplankton blooms in rivers, lakes, ponds, and coastal and open oceans using satellite remote sensing [126, 127]. In fact, remote sensing techniques are widely used to detect, identify, and monitor harmful algal blooms by monitoring spatiotemporal changes in Chlorophyll *a* (Chl. *a*) concentration maps obtained using multispectral imaging [126, 127]. To do so, Chl. *a* concentration maps are produced by fitting the measured spectral reflectance with a theoretical model based on some solution of the radiative transfer equation using the radiation characteristics of microalgae and colonies and in particular their absorption cross-section [128–130].

Furthermore, these microalgae species have been studied for their biotechnological applications [13–16] discussed previously in Chapter 1. For all such applications, efficient

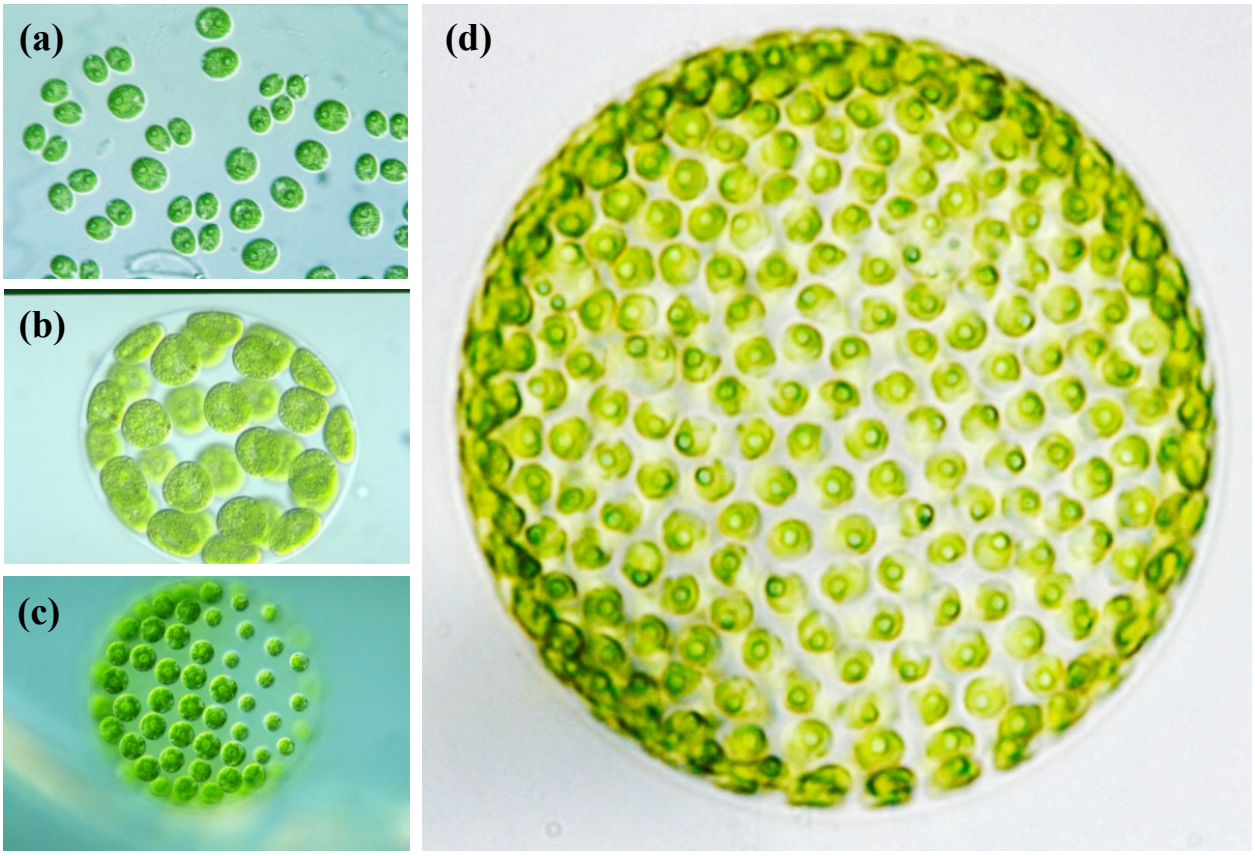

Figure 5.1: Micrographs of members of the *Volvocaceae* family and its close relatives: (a) free floating *Chlamydomonas reinhardtii*†, (b) *Eudorina elegans*†, (c) *Pleodorina californica*†, and (d) *Volvox aureus*. †Reproduced with permission from Prof. Yuuji Tsukii (Hosei University, http://protist.i.hosei.ac.jp/). The micrograph of *Volvox aureus* was imaged in our laboratory.

cultivation of colony-forming microalgae is essential. Then, knowledge of the absorption cross-section of microalgae cells and colonies is needed for predicting, optimizing, and controlling the biomass growth in PBRs as discussed in Chapter 4.

The absorption cross-section of microalgae in suspension has been determined either experimentally [101,114,130–133] or numerically [84,104,130,134–138]. Experimental methods can account for the actual shape and size distribution of microalgae in suspension. However, such methods are only valid for specific growth conditions and can be time-consuming and expensive as they require sophisticated equipment [99]. Previous numerical studies predicting the radiation characteristics of particle aggregates have used the superposition T-matrix method [82], the Monte Carlo ray-tracing (MCRT) method [138–140], the generalized multi-particle Mie method [141], the volume integral method [142], or the hybrid finite element-boundary integral method [143]. Specifically, the superposition T-matrix method has been used to predict the radiation characteristics of multicellular cyanobacteria [136,137] and fractal microalgae colonies [84]. However, this method can be prohibitively resource-intensive when the number of particles and/or their size is large. Thus, these studies only considered cells with relatively small size parameters, i.e., $x \leq 20$ where x is defined as $x = 2\pi r/\lambda$ with r being the radius of the particle and λ being the free space wavelength of the incident radiation. However, a colony of *Eudorina elegans*, for example, consists of 16, 32, or 64, equidistant reproductive cells, 5-10 µm in radius, embedded in an ECM with radius ranging from 45 to 75 µm depending on the maturity of the colony [118,144]. Then, the size parameters corresponding to the cell and ECM radii can range from approximately 40 to 90 and 400 to 1200, respectively, over the photosynthetically active radiation (PAR) region from 400 to 750 nm.

Our previous study [138] compared the absorption cross-section of suspensions of free-floating or fractal colonies of *Botryococcus braunii* cells measured experimentally and predicted by the MCRT method. Colonies were modeled as fractal aggregates of spherical cells of radius $r_c = 3.71$ µm. Colonies embedded in a non-absorbing spherical ECM with radius r_{ECM} were also considered. The MCRT method was shown to accurately model absorption by fractal colonies by comparing its predictions with those from the T-matrix method for

cell size parameter x equal to 10 and 20 for up to 25 and 16 constituent cells, respectively. Note also that the scattering cross-section of fractal colonies of optically soft cells could not be predicted using the MCRT method [138]. Indeed, large optically soft particles, such as microalgae cells and colonies, fall under the anomalous diffraction scattering regime wherein the scattering efficiency factor Q_{sca} remains dependent on diffraction and interference effects [42, 107]. However, these phenomena cannot be captured by the MCRT method since it neglects wave effects. Overall, the experimental measurements showed that the mass absorption cross-section (in m^2/kg) of *B. braunii* was much smaller for a culture containing colonies than for one containing only single cells. Part of this decrease was attributed to the lower pigment concentration in the culture with colonies present. However, for a given pigment concentration, the MCRT also predicted a decrease in the average mass absorption cross-section of colonies with increasing number of cells N_c due to mutual shading among cells. To assess the impact of cell arrangement colonies modeled as an ensemble of spheres embedded at the periphery of a spherical ECM were also considered. Interestingly, the impact of mutual shading on the average mass absorption cross-section was similar for both cell arrangements despite differences in the volume fraction $f_v = N_c r_c^3 / r_{ECM}^3$ occupied by the cells ranging from 0.83 to 0.98 for fractal colonies and from 0.14 to 0.41 for ordered spherical colonies. This suggests that mutual shading may impact the average cell absorption cross-section even at low volume fractions f_v like those observed for *Volvocaceae* including *Eudorina* for which f_v ranges from 0.02 to 0.15 [118, 144].

This study aims to predict, for the first time, the spectral absorption cross-section of microalgae colonies of the genus *Eudorina* as a representative case of the *Volvocaceae* family. To do so, these colonies were represented as large, absorbing, optically soft (i.e., weakly refracting) equidistant monodisperse spherical cells embedded at the periphery of a refracting but non-absorbing spherical extracellular matrix. The MCRT method was first validated by comparing, whenever possible, its predictions of the absorption cross-section of an ensemble of optically soft particles with those by the superposition T-matrix method. It was then used to simulate absorption in the PAR region for realistic colony dimensions where the superposition T-matrix method could not be used due to the excessively large cell and ECM

size parameters. The effects of the absorption index, radius, and number of photosynthetic cells in the colonies were investigated to gain a better understanding of their interaction with light and of the importance of shading effects.

5.2 Analysis

5.2.1 Problem statement

The genus *Eudorina* is comprised of approximately equidistant photosynthetic cells arranged at the periphery of a spherical ECM. A detailed discussion of the morphologies and the number of cells in these colonies can be found elsewhere [118,144] and need not be repeated. Figure 5.2 depicts a representative case of the idealized morphology of a *Eudorina* colony for the purpose of simulating their interaction with light, consisting of a large spherical ECM of radius $r_{ECM} = 60$ µm encompassing $N_c = 64$ monodisperse equidistant spherical inclusions corresponding to the reproductive photosynthetic cells with radius $r_c = 8$ µm. Colonies containing 16, 32, or 64 cells with cell radius r_c ranging from 5 to 13 µm were considered. The ECM radius r_{ECM} scaled with the cell radius r_c such that the volume fraction occupied by a cell was constant and equal to that of the colony shown in Figure 5.2, i.e., $r_{ECM} = (60/8)r_c$. The centers of the cells were located on the surface of an inner concentric sphere of radius $r_i = r_{ECM} - r_c$. Their positions were generated using a program developed for uniform triangular tessellation of sampling points on the surface of a sphere [111].

The refractive index of the non-absorbing surrounding medium n_m was assumed to be that of water, i.e., $n_m = 1.333$ [66]. The refractive index of the non-absorbing ECM was taken as $n_{ECM} = 1.36$ corresponding to glycoprotein hydroxyproline [145], one of the main constituents found in the ECM of *Volvocaceae* [146]. The complex index of refraction of the photosynthetic cell was taken as $m_c = n_c + ik_c = 1.355 + i0.004$. These values were representative of various microalgae species around the Chlorophyll *a* absorption peak in the PAR region [84, 101, 130]. Note that in the PAR region, the absorption index k_c of photosynthetic microalgae cells, including *C. reinhardtii*, is typically less than 0.007 [84,101,

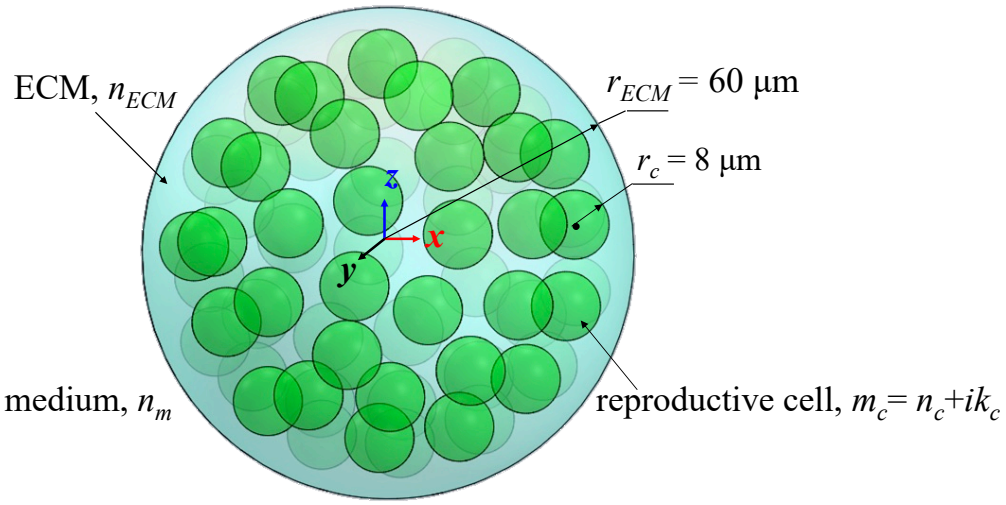

Figure 5.2: Schematic of the simulated idealized colony of *Eudorina* comprised of $N_c = 64$ photosynthetic cells with complex index of refraction $m_c = n_c + ik_c$ and radius $r_c = 8$ µm embedded within a non-absorbing extracellular matrix (n_{ECM}) of radius $r_{ECM} = 60$ µm surrounded by non-absorbing medium (n_m).

130]. The resulting relative refractive index of the ECM was $n_{ECM}/n_m = 1.0203$ and that of the cells was $m_c/n_m = 1.0165 + i0.003$, corresponding to optically soft scatterers. The size parameter $x_{ECM} = 2\pi r_{ECM}/\lambda$ of the simulated colonies ranged from 500 to 900.

5.2.2 Prediction of radiation characteristics of microalgae colonies

The absorption cross-section C_{abs} (in µm^2) of the ensemble of spheres was predicted using either the superposition T-matrix code developed by Mackowski and Mishchenko [113] or the Monte Carlo ray-tracing method developed in Ref. [138]. The superposition T-matrix method estimates the scattered electromagnetic (EM) field from an ensemble of spheres by superposing the scattered EM fields from each of the constituting spheres or monomers [147, 148]. Initially, the vector spherical harmonic expansion of the scattered and internal EM fields of each sphere is written about the sphere's origin. The EM field incident on each sphere consists of the external incident field reaching the sphere and the scattered fields from all other spheres in the ensemble. Then, the system of equations for unknown scattering

coefficients is inverted to obtain the T-matrix [147,148]. Finally, using an analytical rotation transformation rule to integrate the incident EM field over every propagation direction, the scattering Q_{sca} and extinction Q_{ext} efficiency factors are obtained from operations on the T-matrix [147,148]. Then, the absorption efficiency factor Q_{abs} is given by $Q_{abs} = Q_{ext} - Q_{sca}$.

The Monte Carlo ray-tracing method (MCRT) models light transfer through an ensemble of spheres and colonies by tracking a large number of discrete photon bundles or "rays". This method is valid when the size parameter x and phase shift parameter $|m-1|x$ of the scatterer are much larger than unity and geometric optics prevails, i.e., $x \gg 1$ and $|m-1|x \gg 1$, where m is the relative complex index of refraction of the absorber/scatterer. The method and algorithm have been described in detail in Ref. [138] and need not be repeated. In brief, the path of each incident ray was tracked through the colony. At each medium/ECM and ECM/cell interface the probability of reflection or refraction was determined by Fresnel's equations and the direction of the refracted rays was determined by Snell's law. The ray path length l_p through the absorbing cells was recorded and used to calculate the transmissivity τ for a given ray path according to $\tau = \exp\{(-\kappa_c l_p)\}$, where the cell absorption coefficient κ_c was given by $\kappa_c = 4\pi k_c/\lambda$. Then, a random number between 0 and 1 was generated and compared to the value of τ to determine if the ray was absorbed or transmitted. The absorption efficiency factor Q_{abs} was given by

$$Q_{abs} = \frac{N_{abs}}{N_{in}} \tag{5.1}$$

where N_{abs} is the number of rays absorbed by the colony and N_{in} is the total number of rays incident on the colony. Note that the scattering efficiency factor Q_{sca} was not predicted using the MCRT method. Indeed, large optically soft particles, such as microalgae cells and colonies, fall under the anomalous diffraction scattering regime wherein the scattering efficiency factor Q_{sca} fluctuates due to diffraction and interference effects [42,107]. However, these fluctuations cannot be captured by the MCRT method since wave effects are neglected. Thus, the MCRT was unable to accurately predict the scattering efficiency factor Q_{sca} of optically soft particles and ensembles of particles.

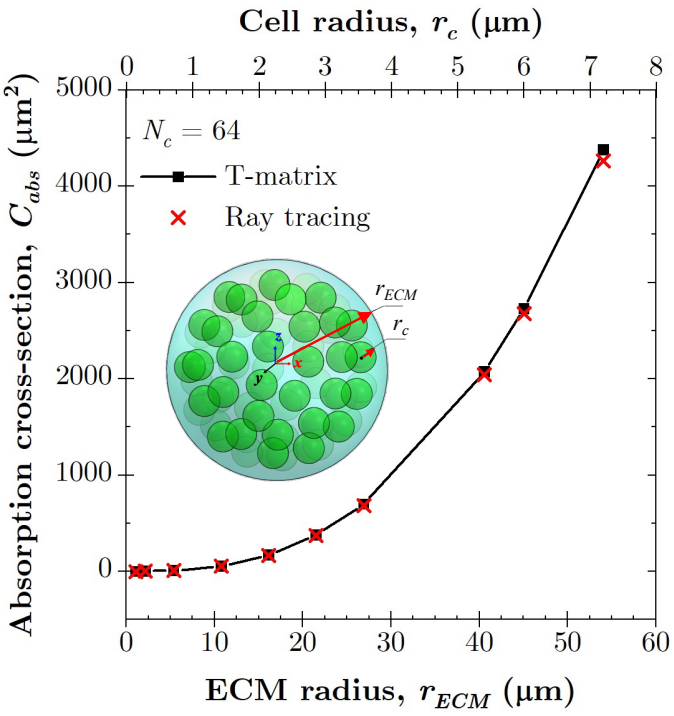

Figure 5.3: Validation of the absorption cross-section C_{abs} of an ensemble of 64 cells predicted by the Monte Carlo ray-tracing method against the superposition T-matrix as a function of ECM r_{ECM} and cell r_c radius.

For both methods, the absorption cross-section C_{abs} of the colony can be calculated from the computed absorption efficiency factor Q_{abs} according to [149]

$$C_{abs} = Q_{abs}\pi r_{ECM}^2. \tag{5.2}$$

As discussed previously, the superposition T-matrix method can be resource-intensive, particularly as the size of the colony and/or the number of photosynthetic cells therein increases. Therefore, the maximum ECM size parameter simulated by this method was limited computationally to $x_{ECM} \leq 500$ which required up to 2.6 TB of RAM. On the other hand, the MCRT method was used to simulate larger ECM size parameters.

5.3 Validation

Figure 5.3 compares the absorption cross-section C_{abs} (in µm^2) of an ensemble of 64 equidistant spherical cells distributed on a concentric sphere surface within a non-absorbing spherical ECM, analogous to the colonies described previously, predicted by the superposition T-matrix and by the Monte Carlo ray-tracing methods as a function of the cell r_c and ECM r_{ECM} radii. A range of radii were chosen such that the cell x_c and ECM x_{ECM} size parameters ranged from 0.13 to 67 and 1 to 500, respectively, in order to validate the MCRT method over the range of colony sizes that could be simulated by the T-matrix method. The wavelength λ of the incident radiation was equal to 676 nm. Here, the cell phase shift parameter $|m-1|x_c$ ranged from 4.8×10^{-4} to 0.25 and the ECM phase shift parameter $|m-1|x_{ECM}$ ranged from 0.02 to 10. Figure 5.3 demonstrates that the absorption cross-section C_{abs} predicted by the superposition T-matrix method and by the Monte Carlo ray-tracing method were in excellent agreement. This was the case despite the fact that the superposition T-matrix method accounted for diffraction effects while the MCRT method did not. This suggests that diffraction effects did not impact light absorption by an ensemble of optically soft spheres, despite playing an important role in their scattering and extinction cross-sections. This was attributed to the fact that diffraction is primarily in the forward direction for optically soft scatterers [42, 107]. Thus, the simplified ray-tracing approach used to simulate scattering was sufficient to model light transfer within the ensemble of spheres for the purpose of predicting absorption. These results validate the MCRT method for modeling light absorption by an ensemble of optically soft spheres even though the conditions for which geometric optics is valid (i.e., $x \gg 1$ and $|m-1|x \gg 1$) were not rigorously satisfied for the simulated colonies. This indicates that the MCRT method can serve as an alternative to the superposition T-matrix method for modeling light absorption by an ensemble of large optically soft spheres. Here, the MCRT method was used to predict the absorption cross-section of *Eudorina* colonies over the PAR region since their ECM size parameter was prohibitively large for the superposition T-matrix method.

5.4 Results and discussion

Figure 5.4a plots the absorption cross-section C_{abs} predicted by the MCRT method as a function of the radii of the ECM r_{ECM} and the cells r_c for *Eudorina* colonies with 16, 32, and 64 constituent cells. The wavelength λ of the incident radiation was equal to 678 nm corresponding to one of the absorption peaks of Chlorophyll *a*. Figure 5.4a indicates that the predicted absorption cross-section C_{abs} increased with increasing number of cells N_c and the radius r_c. This was due to the associated increase in the volume of absorbing substance (i.e., the cells) and the projected area πr_{ECM}^2 of the colony. Figure 5.4b plots the colony absorption cross-section C_{abs} normalized with respect to the product of the number of cells N_c and the absorption cross-section of a single coated cell C_{abs}^{cc} within an ECM equal in size to that of the colonies. The single cells were considered to be within an ECM for normalizing the colony absorption cross-section to account for scattering at the medium/ECM interface. Note that a ratio of $C_{abs}/N_c C_{abs}^{cc}$ equal to unity would indicate that the colony absorption cross-section can be approximated by the sum of the absorption cross-section of the constituent cells, i.e., $C_{abs} = N_c C_{abs}^{cc}$. Then, mutual shading between cells in the colony would be negligible. This was approximately the case for colonies with $N_c = 16$ where cells were the least densely packed. However, for colonies with a number of cells $N_c \geq 32$, the ratio $C_{abs}/N_c C_{abs}^{cc}$ was less than unity and decreased with increasing number of cells N_c for a given cell r_c or ECM r_{ECM} radius. Indeed, compared to a single coated cell, cells in a colony with $N_c = 64$ absorbed up to 23% less light due to mutual shading among cells. Finally, the ratio $C_{abs}/N_c C_{abs}^{cc}$ also decreased with increasing cell radius r_c. This observation indicates that the impact of mutual shading was stronger for larger cells (see Figure 5.4a).

Figure 5.5a plots the spectral absorption cross-section $C_{abs,\lambda}$ over the PAR region for *Eudorina* colonies with 16, 32, or 64 constituent cells with ECM radius $r_{ECM} = 60$ µm and cell radius $r_c = 8$ µm. The spectral absorption cross-section of a single coated cell C_{abs}^{cc} is also shown for reference as $N_c = 1$. Here, the spectral absorption index $k_{c,\lambda}$ of the cells was estimated according to the method presented in Refs. [78, 99] using pigment concentrations measured for *Chlamydomonas reinhardtii* [67], of which *Eudorina* is a close

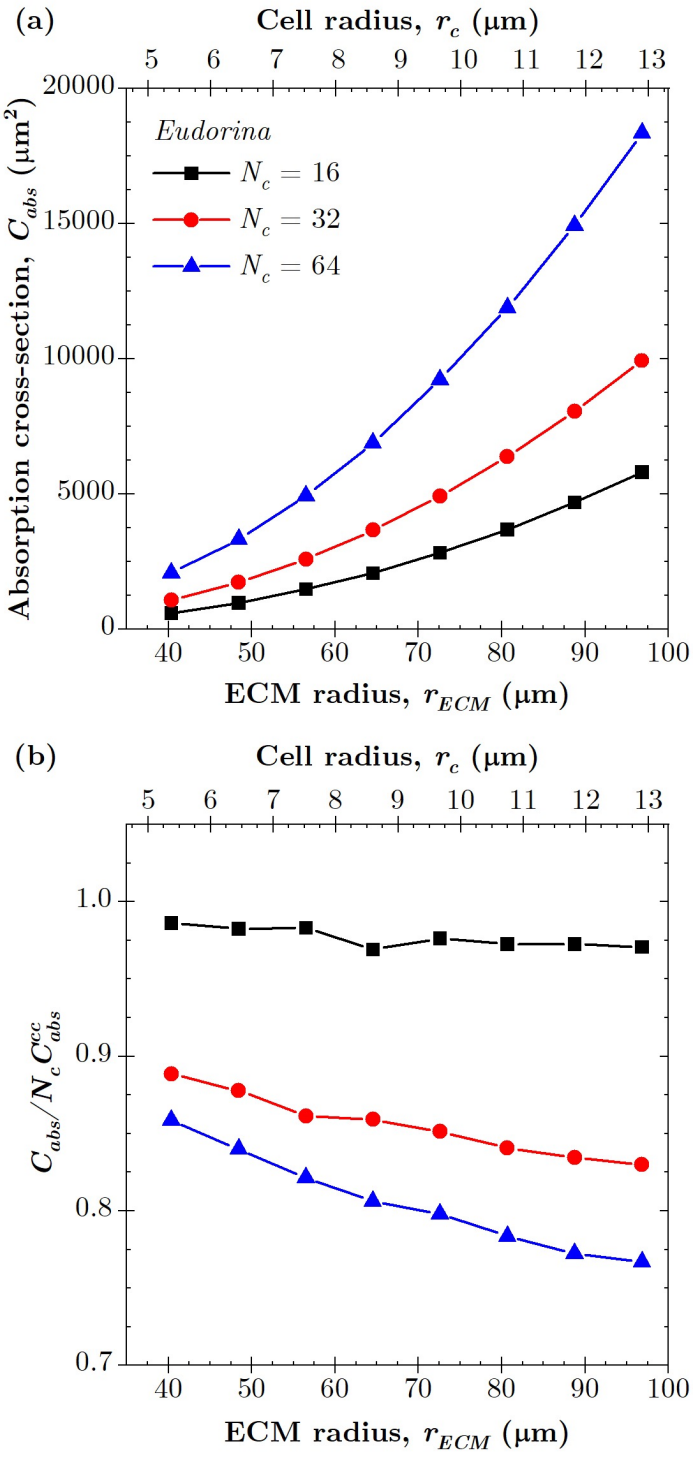

Figure 5.4: (a) Colony absorption cross-section C_{abs} and (b) normalized colony absorption cross-section $C_{abs}/N_c C_{abs}^{cc}$ predicted by the Monte Carlo ray-tracing method as functions of the ECM r_{ECM} and cell r_c radii for *Eudorina* colonies with number of cells N_c equal to 16, 32, and 64.

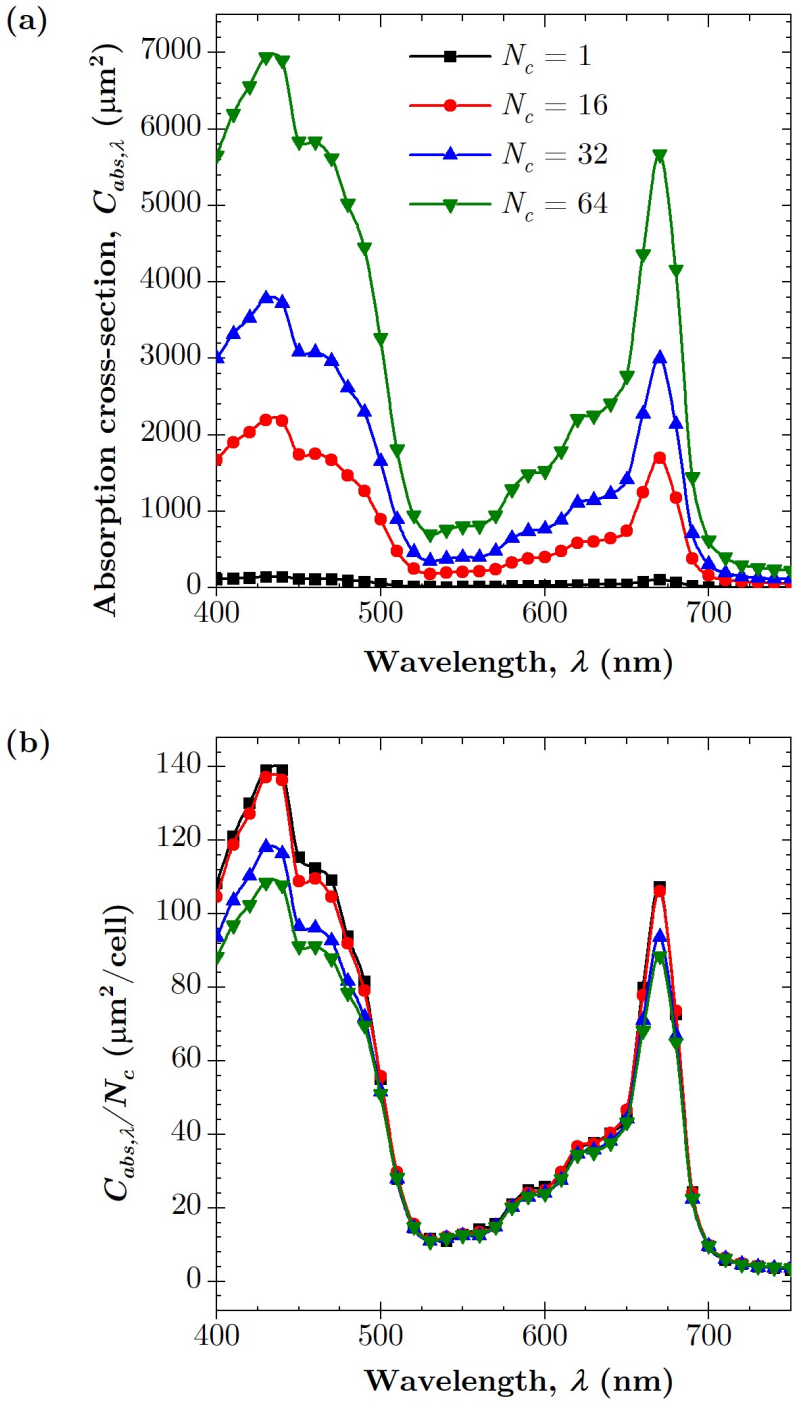

Figure 5.5: (a) Colony spectral absorption cross-section $C_{abs,\lambda}$ and (b) average cell spectral absorption cross-section $C_{abs,\lambda}/N_c$ over the PAR region for *Eudorina* colonies $r_{ECM} = 60$ µm and $r_c = 8$ µm and number of cells N_c equal to 1, 16, 32, and 64.

relative [116]. The cell and ECM refractive indices were assumed to be constant over the PAR region [138]. Figure 5.5a shows a clear increase in the spectral absorption cross-section $C_{abs,\lambda}$ of the colonies with increasing number of cells N_c and absorption peaks corresponding to those of Chlorophyll a at 437 nm and 678 nm and Chlorophyll b at 475 nm. Figure 5.5b plots the spectral average absorption cross-section $C_{abs,\lambda}/N_c$ of a cell in a given colony over the PAR region. It indicates that the spectral average absorption cross-section per cell decreased with increasing number of cells due to mutual shading. This effect was more pronounced at the absorption peaks of Chl. a and b where the absorption index k_c is the largest, resulting in increased shading. Indeed, neglecting shading effects would overestimate the colony absorption cross-section by as much as 29% for the colony containing 64 cells at wavelength $\lambda = 437$ nm. On the other hand, the value of $C_{abs,\lambda}/N_c$ was independent of the number of cells present for wavelengths λ between 500 and 650 nm and greater than 700 nm when $k_{c,\lambda}$ was small and shading effects were negligible. Then, the colony absorption cross-section could be approximated according to $C_{abs} = N_c C_{abs}^{cc}$.

5.5 Conclusion

The absorption cross-sections of colonial microalgae *Eudorina* consisting of 16, 32, and 64 equidistant absorbing photosynthetic cells distributed on a concentric sphere surface within a non-absorbing spherical extracellular matrix (ECM) were computed using the Monte Carlo ray-tracing method. The latter was validated against the superposition T-matrix method for modeling absorption by an ensemble of optically soft particles. At wavelengths where the cells were weakly absorbing, the absorption cross-section of colonies was equivalent to the cumulative absorption cross-sections of individual cells coated by an ECM with the same radius as the colonies. However, in the spectral range where cells absorb, the impact of shading effects on the colony absorption cross-section increased with increasing cell radius, number of cells, and cell absorption index. The MCRT method is a fast and accurate tool for predicting the spectral absorption cross-section of colonies by accurately capturing the impact of shading among cells.

CHAPTER 6

A novel external reflecting raceway pond design for improved biomass productivity

Outdoor raceway ponds for microalgae cultivation suffer from low biomass productivity due in part to the low photosynthetic photon flux received by the microalgae culture in the mornings and evenings and during the winter months at middle and high latitudes. This study explores the use of external mirrors to reflect additional sunlight onto the culture and increase the incident solar flux at critical times of the day and year. Four designs cultivating *Chlorella vulgaris* were considered: a raceway pond without mirrors (Configuration A), a pond oriented along the north/south axis with dual east/west mirrors (Configuration B), a pond oriented along the east/west axis with a single north mirror (Configuration C), and a solar tracking rotating pond with a single mirror (Configuration D). The biomass productivity was predicted by coupling the simulated radiative field within the culture to a microalgae growth kinetics model accounting for photolimitation and biomass loss due to respiration. Two different locations were considered, namely Los Angeles, CA, USA and Saint-Nazaire, France. The use of mirrors was predicted to increase the daily culture-area-based and volumetric biomass productivity at both locations and all months of the year. Overall, Configuration C was considered to be the simplest and most cost-effective method to increase raceway productivity. Indeed, this configuration improved the raceway pond volumetric and culture-area-based biomass productivity by as much as 73% in the winter months compared to Configuration A. Additionally, the impact of operational parameters (initial biomass concentration and culture depth) and design parameters (pond length-to-width ratio and mirror height) were assessed to provide practical recommendations for maximizing biomass productivity.

6.1 Background

Microalgae are often cultivated in large-scale outdoor raceway ponds consisting of a culture, at least 15 cm deep, and oriented along the north/south axis [32, 33]. For raceway ponds in outdoor conditions, large solar incidence angles occur in the mornings and evenings and during the winter months when the solar elevation angle may be small depending on the latitude where the raceway pond is operated. As a result, the incident spectral solar radiative flux $q''_{in,\lambda}(t)$ decreases compared to situations when sunlight is nearly normally incident on the culture according to [42]

$$q''_{in,\lambda}(t) = G_{S,\lambda}(t) \cos\theta_z(t) \tag{6.1}$$

where $G_{S,\lambda}$ is the time-dependent spectral collimated solar irradiation and θ_z is the solar zenith angle for a given time of day t, defined with respect to the outward pointing normal vector of the microalgae culture surface. Furthermore, sunlight delivered at oblique angles does not penetrate as deeply into the microalgae culture compared to normally incident light [30, 43]. Thus, non-normal incidence can increase dark zones in the culture where there is not enough light to drive photosynthesis. This phenomenon, combined with the decrease in solar irradiation in the mornings and evenings, negatively impacts microalgae growth by reducing the amount of light available to the suspended cells.

The aim of this study is to explore the use of mirrors to increase the biomass productivity of raceway ponds by increasing the solar radiative flux delivered to the microalgae culture at critical times of the day and year. The daily biomass productivity of a raceway pond with various configurations of vertical mirrors was predicted throughout the year using experimentally-validated models coupling light transfer and growth kinetics. The performance of each configuration was assessed in terms of areal and volumetric productivities and compared to the same raceway pond but without mirrors. The impact of operating parameters, such as initial biomass concentration and culture depth, and of design parameters including mirror height, pond length-to-width ratio, and cultivation location, were assessed.

6.2 Methods

6.2.1 Problem statement

Let us consider an outdoor rectangular raceway pond of width $W = 1$ m and length $L = 2$ m located in either Los Angeles, CA, USA (34.07° N, 118.44° W) or Saint-Nazaire, France (47.25° N, 2.26° W) growing a culture of *Chlorella vulgaris* of depth D equal to 0.1 m, 0.2 m, or 0.3 m. These locations were chosen due to their difference in latitude in the northern hemisphere. The pond was exposed to direct, collimated solar radiation $G_{S,\lambda}$ (in $\mu\text{mol}_{\text{h}\nu}\text{m}^{-2}\text{s}^{-1}$) from sunrise to sunset on September 21$^{\text{st}}$ as depicted in Figure 6.1A. September 21$^{\text{st}}$ was considered representative of an average day as there are approximately 12 hours of sunlight in Los Angeles, CA on this day. The daily biomass productivity was also simulated for the 21$^{\text{st}}$ day of each month of the year. The raceway ponds were considered to be operated in a semi-continuous mode where harvesting took place when the maximum daily biomass concentration X_{max} (in kg m^{-3}) was attained, i.e., at time $t(X = X_{max})$. The solar position for a given time and day was described by the solar zenith angle θ_z and the solar azimuth angle γ_s defined with respect to the due south direction, as illustrated in Figure 6.1A. Here, $\gamma_s = -90°$ corresponded to due east and $\gamma_s = 90°$ corresponded to due west.

Novel pond design and control

Four different designs were investigated to explore the use of vertical external mirror(s) as a simple way to reflect additional direct sunlight onto the culture and improve the microalgae growth rate, particularly when the sun was low on the horizon, i.e., when the solar zenith angle θ_z was large. Configuration A consisted of a standard raceway pond without mirrors oriented lengthwise along the north/south axis (Figure 6.1A). Configuration B consisted of the same raceway pond as in Configuration A but featuring two vertical mirrors on its east and west sides of time-dependent height $H_{B,E}(t)$ and $H_{B,W}(t)$, respectively (Figure 6.1B). Here, the eastern mirror was lowered and the western mirror was raised in the morning and vice versa in the afternoon. Similarly, Configuration C consisted of the same raceway pond

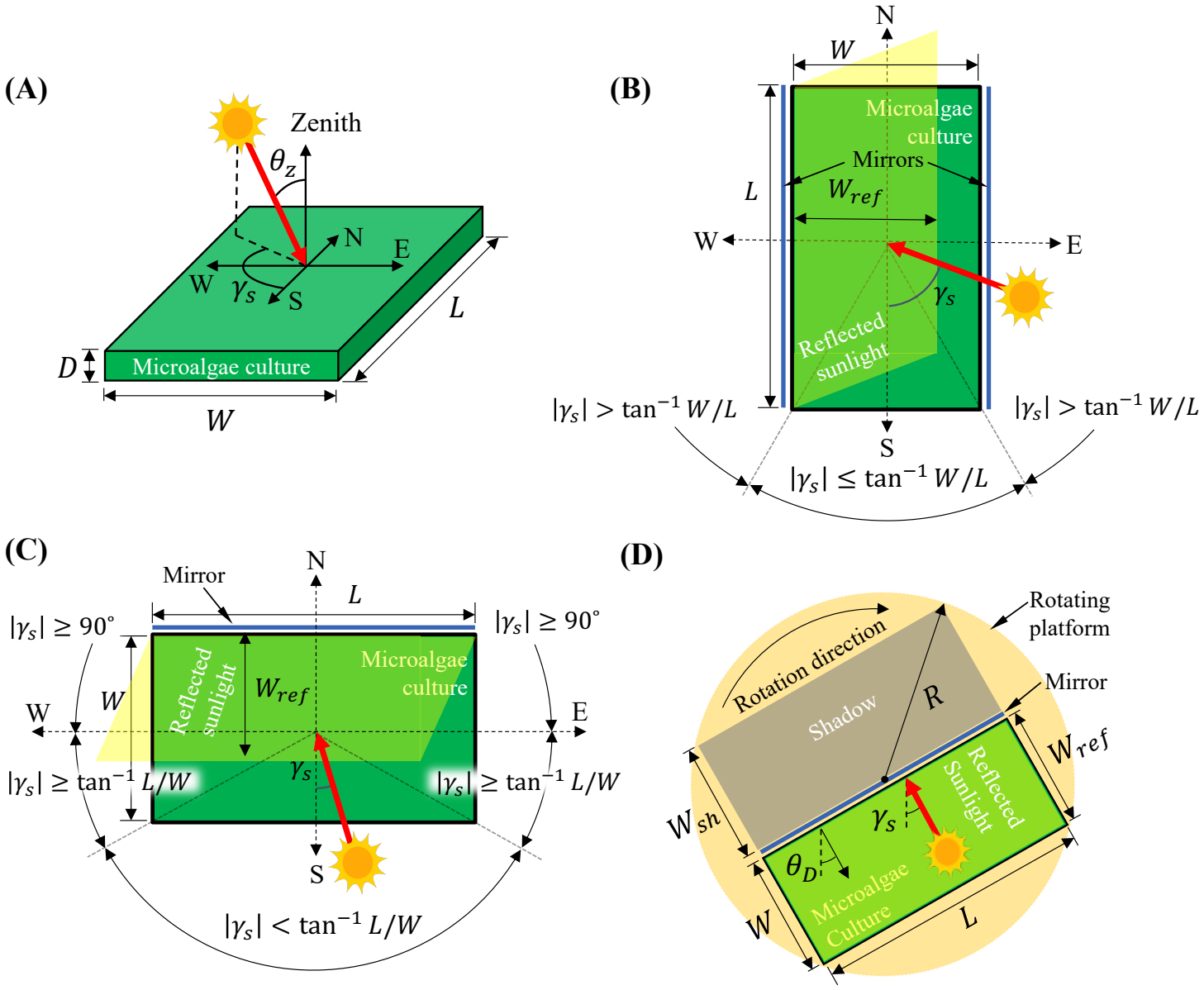

Figure 6.1: Top view (not to scale) of (A) Configuration A: a $L \times W$ raceway pond without mirrors, (B) Configuration B: a raceway pond featuring dual vertical mirrors on its east and west sides, (C) Configuration C: a raceway pond featuring a single vertical mirror on its north side, and (D) Configuration D: a raceway pond and mirror on a rotating platform tracking the sun throughout the day.

as in Configuration A but oriented lengthwise along the east/west axis and featuring a single vertical mirror on its north side with time-dependent height $H_C(t)$ (Figure 6.1C). Finally,

Configuration D consisted of the same raceway pond as in Configuration A but on a circular rotating platform of radius R tracking the movement of the sun throughout the day and featuring a single vertical mirror of time-dependent height $H_D(t)$ (Figure 6.1D). Here, the platform rotation angle θ_D was defined as the angle between the due south direction and the outward pointing normal vector of the mirror. As with the solar azimuth angle γ_s, a rotation angle of $\theta_D = -90°$ corresponded to a due east-facing mirror position and $\theta_D = 90°$ corresponded to a due west-facing mirror position. Configuration D was considered to assess the maximum productivity achievable with the use of mirrors in a manner similar to Pruvost et al. [150] who considered the ideal case of a solar tracking photobioreactor to assess the maximum theoretical productivity of a solar photobioreactor.

The time-dependent mirror height $H_{B/C/D}(t)$ for Configurations B-D was controlled to maximize the culture surface area S_{ref} subjected to reflected light while minimizing mirror height to avoid shading between adjacent raceway ponds. When the magnitude of the solar azimuth angle $|\gamma_s| > \tan^{-1} W/L$ for Configuration B and $|\gamma_s| < \tan^{-1} L/W$ for Configuration C (see Figure 6.1B and 6.1C) the reflected area was maximized by controlling the mirror height such that the reflected width W_{ref} was equal to the pond width, i.e., $W_{ref} = W$. However, when $|\gamma_s| \leq \tan^{-1} W/L$ for Configuration B and $|\gamma_s| \geq \tan^{-1} L/W$ for Configuration C, the reflected area was maximized for a reflected width $W_{ref} = L \tan|\gamma_s|$ and $W_{ref} = L/\tan|\gamma_s|$ for Configurations B and C, respectively. Then, the reflected width W_{ref} never exceeded the pond width W and shading between adjacent ponds was avoided for pond spacing width $W_{sp} = W$ for Configurations B and C and $W_{sp} = R = W\sqrt{2}$ for Configuration D. Figure 6.2a depicts a schematic of the side view of Configurations B-D illustrating the spacing width W_{sp}. For each configuration, the mirror height $H_{B/C/D}(t)$ which gave the desired reflected width W_{ref} was calculated based on the apparent solar zenith angle $\theta_{z,a}$, defined as the angle between the vertical axis and the incoming solar radiation as observed from a side view of a given configuration (see Figure 6.2a). The apparent solar zenith angle $\theta_{z,a}$ was given by $\theta_{z,a} = \tan^{-1}(\tan\theta_z \sin|\gamma_s|)$ for Configuration B and by $\theta_{z,a} = \tan^{-1}(\tan\theta_z \cos|\gamma_s|)$ for Configuration C. For Configuration D, the platform supporting the pond was rotated such that the mirror was always facing the sun and the rotation

angle θ_D was equal to the solar azimuth angle γ_s. Thus, the actual and apparent solar zenith angles were equal, i.e., $\theta_z = \theta_{z,a}$. Then, the mirror height $H_{B/C/D}$ for each configuration was given by

$$H_B(t) = \begin{cases} W/\tan\theta_{z,a}, & |\gamma_s| > \tan^{-1} W/L \\ L\tan|\gamma_s|/\tan\theta_{z,a}, & |\gamma_s| \leq \tan^{-1} W/L \end{cases} \tag{6.2}$$

$$H_C(t) = \begin{cases} 0, & |\gamma_s| > 90^\circ \\ L/\tan|\gamma_s|\tan\theta_{z,a}, & 90^\circ > |\gamma_s| \geq \tan^{-1} L/W \\ W/\tan\theta_{z,a}, & |\gamma_s| < \tan^{-1} L/W \end{cases} \tag{6.3}$$

$$H_D(t) = W/\tan\theta_{z,a}. \tag{6.4}$$

To avoid unreasonably large values of mirror height when $\theta_{z,a}$ was small, a maximum allowed height of $H^* = 1$ m was imposed. Then, the mirror height for a given time t was the minimum value between H^* and the mirror height for a given configuration from Equations (6.2)-(6.4). Note that, for Configuration B, the west mirror height $H_{B,W}(t)$ was given by Equation (6.2) while the east mirror was lowered in the morning when the solar azimuth angle was negative, i.e., $\gamma_z < 0$. Similarly, the east mirror height $H_{B,E}(t)$ was given by Equation (6.2) while the west mirror was lowered in the afternoon when the solar azimuth angle was positive, i.e., $\gamma_s > 0$. Note that the mirror height $H_C(t)$ was equal to zero for Configuration C when the sun was positioned behind the mirror, i.e., $|\gamma_s| > 90^\circ$. Figure 6.2b plots the resulting mirror heights $H_{B/C/D}(t)$ as a function of time for Configurations B-D on September 21$^{\text{st}}$ according to Equations (6.2)-(6.4) with an imposed maximum mirror height of $H^* = 1$ m.

6.2.2 Assumptions

Light transfer and microalgae growth were modeled based on the following assumptions: (1) all mirrors were considered to be specularly-reflecting with 100% reflectivity over the photosynthetically active radiation (PAR) region from 400 to 700 nm. (2) The raceway

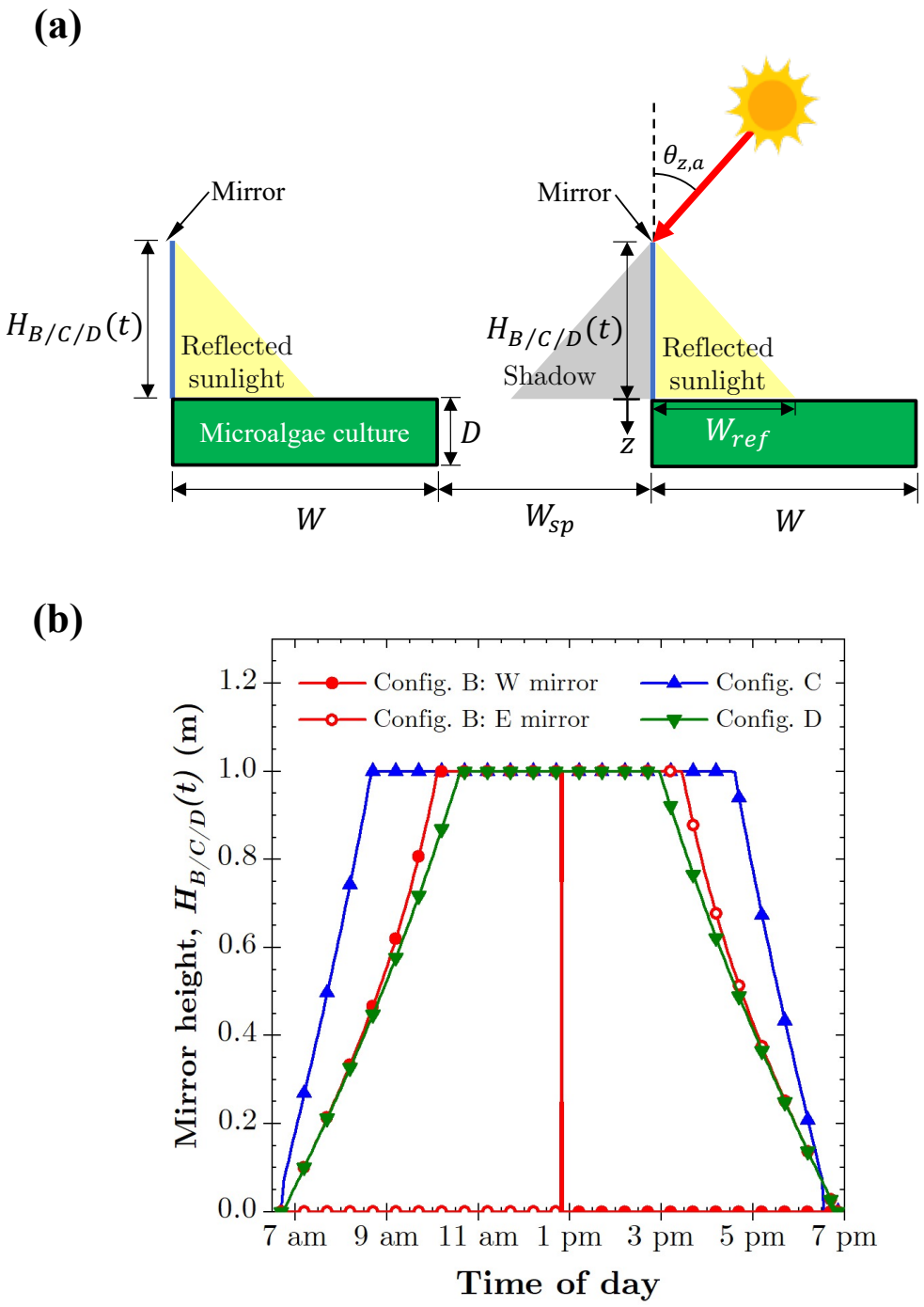

Figure 6.2: (a) A side view (not to scale) of Configurations B-D illustrating the reflection width W_{ref}, pond spacing width W_{sp}, and the apparent solar zenith angle $\theta_{z,a}$. (b) Mirror height $H_{B/C/D}(t)$ given by Equations (6.2)-(6.4) as a function of time of day on September 21st in Los Angeles, CA for maximum allowed mirror height $H^* = 1$ m.

pond was operated in the light-limited regime such that growth was only a function of the local rate of photon absorption (LRPA) within the culture. (3) Light transfer within the culture was considered to be one-dimensional along the z-axis and shading from the walls of the raceway pond was negligible, as demonstrated in Ref. [48]. (4) Diffuse solar radiation was neglected. (5) The culture was well-mixed with uniform biomass concentration. (6) The liquid medium was non-scattering and non-absorbing over the PAR region. (7) The radiative properties and kinetic growth parameters of *Chlorella vulgaris* were constant throughout the day. (8) The culture temperature was kept constant throughout the day. (9) The bottom of the raceway ponds were perfectly absorbing.

6.2.3 Reflected sunlight

The culture surface area subjected to reflected sunlight S_{ref} for a given configuration and solar position was calculated as the difference between the total surface area of light reflected by the mirror and the area of reflected light that fell outside of the culture surface (see Figures 6.1B and 6.1C) according to

$$S_{ref}(t) = \begin{cases} W_{ref}(t)L - \frac{1}{2}W_{ref}(t)^2/|\tan\gamma_s(t)| & \text{for Configuration B} \\ W_{ref}(t)L - \frac{1}{2}W_{ref}(t)^2\tan\gamma_s(t) & \text{for Configuration C} \\ W_{ref}(t)L & \text{for Configuration D.} \end{cases} \tag{6.5}$$

The amount of additional light reflected onto the culture for each pond configuration can be assessed by considering the ratio S_{ref}/S_C of the culture surface area subjected to reflected sunlight S_{ref} to the total culture surface area $S_C = WL$. The ratio of S_{ref}/S_C ranged from zero, when none of the culture surface was exposed to reflected light, to 1.0 when the entire culture surface area was exposed to reflected light. Then, the incident mean spectral radiative flux $\bar{q}''_{in,\lambda}$ (in $\mu\text{mol}_{\text{h}\nu}\text{m}^{-2}\text{s}^{-1}$) averaged over the culture surface area at a given time t was given by

$$\bar{q}''_{in,\lambda}(t) = \tau(\theta_z(t))G_{S,\lambda}(t)\cos\theta_z(t)\left(1 + \frac{S_{ref}(t)}{S_C}\right) \tag{6.6}$$

where $\tau(\theta_z(t))$ is the transmittance of the air/microalgae culture interface predicted by Fres-

nel's equations for an incidence angle equal to the solar zenith angle θ_z [42]. Note that since the mirror was perfectly vertical, the angle of incidence of reflected light was equal to that of light directly incident on the culture surface. The resulting incident mean photosynthetic photon flux $\bar{q}''_{in,PAR}(t)$ was obtained by integrating $\bar{q}''_{in,\lambda}(t)$ over the PAR region, i.e.,

$$\bar{q}''_{in,PAR}(t) = \int_{PAR} \bar{q}''_{in,\lambda}(t)\mathrm{d}\lambda. \tag{6.7}$$

6.2.4 Light transfer in microalgae culture

The two-flux approximation was used as an analytical solution to the one-dimensional radiative transfer equation governing light transfer in the microalgae culture. This method has been validated and used extensively in previous studies [30, 48, 67–69, 151]. The radiation transmitted through the air/microalgae culture interface was refracted at the interface at an angle $\theta_m = \sin^{-1}(n_a/n_m \sin\theta_z)$ where $n_a = 1.0$ and $n_m = 1.33$ are the refractive indices of the air and culture medium, respectively. Then, for a raceway pond with a perfectly absorbing bottom wall and exposed to the mean incident spectral radiative flux $\bar{q}''_{in,\lambda}(t)$, the local spectral fluence rate $G_\lambda(z,t)$ at a given culture depth z (see Figure 6.2a) was given by

$$\frac{G_\lambda(z,t)}{\bar{q}''_{in,\lambda}(t)} = \frac{2}{\cos\theta_m}\frac{(1+\alpha_\lambda)e^{\delta_\lambda(D-z)} - (1-\alpha_\lambda)e^{-\delta_\lambda(D-z)}}{(1+\alpha_\lambda)^2 e^{\delta_\lambda D} - (1-\alpha_\lambda)^2 e^{-\delta_\lambda D}} \tag{6.8}$$

where the parameters α_λ and δ_λ were expressed as [67]

$$\alpha_\lambda = \sqrt{\frac{\bar{A}_{abs,\lambda}}{\bar{A}_{abs,\lambda} + 2b_\lambda \bar{S}_{sca,\lambda}}} \qquad \text{and} \qquad \delta_\lambda = \frac{\alpha_\lambda X(t)}{\cos\theta_m}(\bar{A}_{abs,\lambda} + 2b_\lambda \bar{S}_{sca,\lambda}). \tag{6.9}$$

Here, $X(t)$ is the biomass concentration (in kg m^{-3}) at time t while the spectral average mass absorption $\bar{A}_{abs,\lambda}$ and scattering $\bar{S}_{sca,\lambda}$ cross-sections (in m^{2}kg^{-1}) and the backward scattering ratio b_λ of *Chlorella vulgaris* were obtained from experimental measurements, reported in Ref. [43] and shown Figure A.1 of the Supplementary Materials. Finally, the local rate of photon absorption (LRPA) by the microalgae cells, denoted by $\mathcal{A}(z,t)$ (in μmol$_{\mathrm{h}\nu}$kg^{-1}s^{-1}), was defined as [43]

$$\mathcal{A}(z,t) = \int_{PAR} \bar{A}_{abs,\lambda} G_\lambda(z,t)\mathrm{d}\lambda. \tag{6.10}$$

6.2.5 Microalgae growth kinetics

The time rate of change of the biomass concentration $X(t)$ in a microalgae batch culture can be expressed as [70]

$$\frac{dX}{dt} = \bar{r}_X(t) = \bar{\mu}(t)X(t) \tag{6.11}$$

where $\bar{r}_X(t)$ is the average volumetric growth rate (in kg $m^{-3}s^{-1}$) and $\bar{\mu}(t)$ is the volume-averaged specific growth rate (in s^{-1}). The growth kinetics model and corresponding parameters reported in Refs. [43, 71] for *Chlorella vulgaris* are given in Table 6.1 and were used to predict the specific growth rate $\bar{\mu}(t)$ of the microalgae culture as a function of time. This model accounted for light limitation and cell respiration activity [71].

First, the volume-averaged specific rate of oxygen production or consumption $\bar{J}_{O_2}(t)$ (in $\mathrm{mol_{O_2} kg_X^{-1} s^{-1}}$) as a function of the LRPA $\mathcal{A}(z,t)$ was calculated according to [43]

$$\bar{J}_{O_2}(t) = \frac{1}{D}\int_0^D \left[\rho_M \frac{K}{K+\mathcal{A}(z,t)}\bar{\phi}'_{O_2}\mathcal{A}(z,t) - \frac{J_{NADH_2}}{\nu_{NADH_2-O_2}}\frac{K_r}{K_r+\mathcal{A}(z,t)}\right]\mathrm{d}z. \tag{6.12}$$

Here, ρ_M is the maximum energy yield for photon conversion, $\bar{\phi}'_{O_2}$ (in $\mathrm{mol_{O_2}}{\mu\mathrm{mol_{h\nu}}}^{-1}$) is the molar quantum yield of O_2 for the Z-scheme of photosynthesis, K (in $\mu\mathrm{mol_{h\nu} kg^{-1} s^{-1}}$) is the half-saturation constant for photosynthesis, J_{NADH_2} (in $\mathrm{mol_{NADH_2} kg_X^{-1} s^{-1}}$) is the specific rate of cofactor regeneration on the respiratory chain related to the oxygen consumption by the stoichiometric coefficient of cofactor regeneration on the respiratory chain $\nu_{NADH_2-O_2}$, and K_r (in $\mu\mathrm{mol_{h\nu} kg^{-1} s^{-1}}$) is a saturation constant describing the inhibition of respiration in light.

Then, the stoichiometric relationship between the production of oxygen and the production of biomass was used to predict the volume-averaged growth rate $\bar{\mu}(t)$ (in s^{-1}) as a function of $\bar{J}_{O_2}(t)$ according to [43]

$$\bar{\mu}(t) = \frac{\bar{r}_X(t)}{X(t)} = \frac{\bar{J}_{O_2}(t)M_X}{\nu_{O_2-X}} \tag{6.13}$$

where M_X (in $\mathrm{kg_X mol_C^{-1}}$) is the C-molar mass in the biomass given by CH_pO_n and ν_{O_2-X} is the stoichiometric coefficient of the oxygen production.

Table 6.1: Growth kinetics parameters for *Chlorella vulgaris* [43].

Parameter	Value	Units
ρ_M	0.8	-
J_{NADH_2}	2.8×10^{-3}	$\mathrm{mol_{NADH_2}kg_X^{-1}s^{-1}}$
ν_{O_2-X}	1.13	-
$\bar{\phi}'_{O_2}$	1.1×10^{-7}	$\mathrm{mol_{O_2}}\mu\mathrm{mol}_{h\nu}^{-1}$
M_X	0.024	$\mathrm{kg_X mol_C^{-1}}$
$\nu_{NADH_2-O_2}$	2	-
K	40,000	$\mu\mathrm{mol}_{h\nu}\mathrm{kg}^{-1}\mathrm{s}^{-1}$
K_r	556.5	$\mu\mathrm{mol}_{h\nu}\mathrm{kg}^{-1}\mathrm{s}^{-1}$
$\mathcal{A}_c$	2,800	$\mu\mathrm{mol}_{h\nu}\mathrm{kg}^{-1}\mathrm{s}^{-1}$

6.2.6 Biomass productivity

The daily volumetric P_V, culture-area-based $P_{A,C}$, and land-area-based $P_{A,L}$ biomass productivities were considered as metrics to compare the performance of all four raceway pond configurations. The daily volumetric biomass productivity P_V (in kg $\mathrm{m}^{-3}\mathrm{day}^{-1}$) was defined as

$$P_V = \frac{(X_{max} - X_0)}{\Delta t} \tag{6.14}$$

where X_{max} is the maximum biomass concentration reached on a given day, X_0 is the initial biomass concentration, and the time increment Δt is equal to one day. Similarly, the daily culture-area-based biomass productivity $P_{A,C}$ (in kg $\mathrm{m}^{-2}\mathrm{day}^{-1}$) was defined as

$$P_{A,C} = \frac{(X_{max} - X_0)V}{S_C \Delta t} = P_V D \tag{6.15}$$

where S_C is the culture surface area. In addition, the daily land-area-based biomass productivity $P_{A,L}$ (in kg $\mathrm{m}^{-2}\mathrm{day}^{-1}$) was defined as

$$P_{A,L} = \frac{(X_{max} - X_0)V}{S_L \Delta t} \tag{6.16}$$

where S_L is the land area required to accommodate both the raceway ponds and the spacing between adjacent ponds. The land area S_L required for a single pond was $S_L = 2S_C = 4$ m^2 for Configurations B and C with pond width W and spacing width W_{sp} equal to 1 m. A circular land area $S_L = \pi R^2 = \pi(W^2 + L^2/4) = 6.28$ m^2 was required for Configuration D.

The volumetric P_V, culture-area-based $P_{A,C}$, and land-area-based $P_{A,L}$ productivities were considered as they are related to the different costs associated with producing a kilogram of biomass. The volumetric productivity P_V can be used to assess the biomass output relative to the operating costs that depend on the culture volume such as the energy required for water circulation and thermal regulation as well as downstream processing costs such as dewatering [29]. The daily culture-area-based $P_{A,C}$ and land-area-based $P_{A,L}$ productivities can be used to assess the biomass output relative to operating and capital costs that scale with the culture area (e.g., evaporation losses, pond liners) and land area (e.g., land cost), respectively [152]. The land-area-based productivity $P_{A,L}$ can also be used to estimate the size of the facility required for a desired yield of biomass.

6.2.7 Boundary and initial conditions

The incident spectral solar irradiance $G_{S,\lambda}(t)$ was determined using the Simple Model of the Atmospheric Radiative Transfer of Sunshine (SMARTS) for either Los Angeles, CA or Saint-Nazaire, France on the 21$^{\text{st}}$ day of each month [79]. The initial biomass concentration X_0 was varied between (i) 0.03 and 0.30 kg m^{-3} for culture depth $D = 0.3$ m, (ii) 0.03 and 0.45 kg m^{-3} for $D = 0.2$ m, and (iii) 0.03 and 0.70 kg m^{-3} for $D = 0.1$ m. These ranges of culture depth and biomass concentration were found to yield positive biomass productivity on September 21$^{\text{st}}$.

6.2.8 Method of solution

Figure 6.3 shows a block diagram describing the process for predicting the biomass concentration $X(t)$ as a function of time for Configurations A-D. First, the solar conditions at sunrise, i.e., $t = t_0$, were used to calculate the mean incident spectral radiative flux $\bar{q}''_{in,\lambda}$

[Equations (6.2) - (6.6)] for a given configuration, pond length L, width W, and maximum allowed mirror height H^*. Then, the two-flux model was applied to predict the LRPA $\mathcal{A}(z,t)$ within the culture [Equations (6.8) - (6.10)] for a given initial biomass concentration X_0 and culture depth D and using the radiative properties of *Chlorella vulgaris* [43]. Next, the growth kinetics model for *Chlorella vulgaris* was used to predict the volume-averaged specific growth rate $\bar{\mu}(t)$ [Equations (6.12) - (6.13)]. Then, the biomass concentration at subsequent times $X(t+\Delta t)$ was predicted by integrating Equation (6.11) and assuming that $\bar{\mu}(t)$ and $X(t)$ were constant over the time increment Δt according to

$$X(t+\Delta t) = X(t)[1+\bar{\mu}(t)\Delta t] \tag{6.17}$$

where the time increment Δt was equal to 3 minutes to obtain numerically converged results. This process was then repeated for the updated biomass concentration and sunlight parameters at $t = t+\Delta t$ until sunset, defined here as the time t where $\theta_z \geq 90°$.

6.3 Results and Discussion

6.3.1 Incident radiative flux

Figure 6.4a plots the fraction S_{ref}/S_C of the total culture area S_C receiving reflected light for Configurations A-D as a function of time on September 21st in Los Angeles, CA. Note that S_{ref}/S_C was zero throughout the day for Configuration A since no reflecting mirrors were present, i.e., $S_{ref} = 0$. Both Configurations B and D experienced a decrease in the reflected area S_{ref} at midday. This was due to the small apparent solar zenith angle $\theta_{z,a}$ at midday and the fact that the mirror height was limited to $H^* = 1$ m (see Figure 6.2b). The ratio of S_{ref}/S_C for Configuration B was nearly unity at the beginning and end of the day when the sun was positioned facing the west and east mirror, respectively. On the other hand, $S_{ref}/S_C = 1$ for several hours in the morning and evening for Configuration D thanks to the tracking system which ensured that the sun was always facing the mirror. Unlike Configurations B and D, the ratio S_{ref}/S_C for Configuration C was nearly zero in

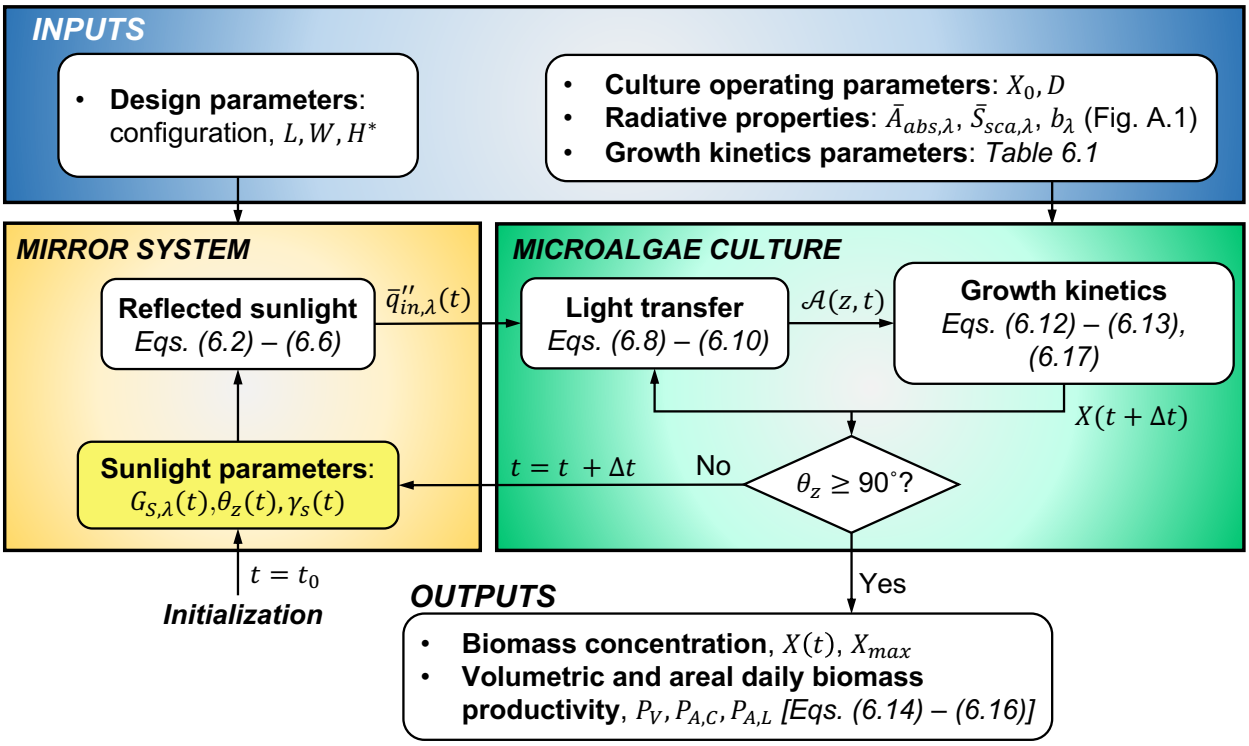

Figure 6.3: Block diagram illustrating the computational procedure used for predicting the temporal evolution of biomass concentration $X(t)$ and the daily biomass productivities for raceway Configurations A-D.

the morning and evening. At these times, the sun's rays were virtually parallel to the south-facing mirror and the reflected area S_{ref} was small. The ratio S_{ref}/S_C reached a maximum at midday for Configuration C but it never attained a value of unity, since the mirror height $H_C(t)$ was limited to H^* at midday when the sun was positioned facing the mirror (see Figure 6.2b).

Figure 6.4b plots the incident photosynthetic photon flux $\bar{q}''_{in,PAR}$ [Equation (6.7)] averaged over the culture surface area as a function of time on September 21st for Configurations A-D. It indicates that Configurations B-D increased the mean incident photosynthetic photon flux throughout the day compared to a raceway pond without mirrors. In the morning and evening, Configurations B and D exhibited the highest mean incident photosynthetic flux thanks to the east- and west-facing orientation of their mirrors. Nonetheless, the incident photosynthetic flux remained small in the early morning and late evening due to the

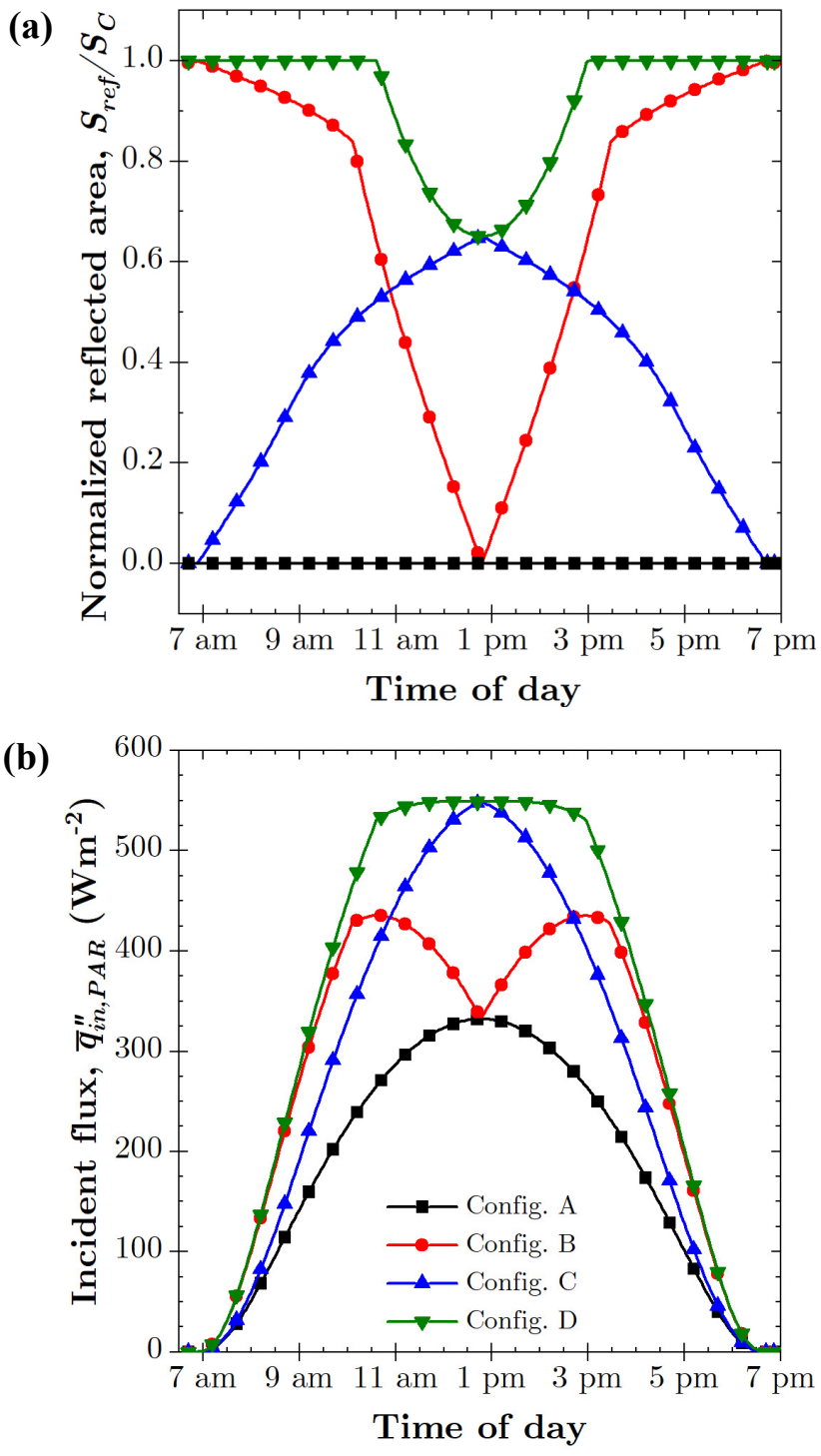

Figure 6.4: (a) Fraction S_{ref}/S_C of the total culture surface area $S_C = WL$ subjected to reflected sunlight and (b) incident photosynthetic photon flux $\bar{q}''_{in,PAR}$ averaged over the culture surface area as a function of time on September 21st for Configurations A-D in Los Angeles, CA.

weak solar irradiation $G_{S,\lambda}$ at these times. Furthermore, the mean incident photosynthetic flux of Configuration B decreased at midday to be equal to that of Configuration A as the sun aligned with the north-south axis and the reflected area S_{ref} went to zero (see Figure 6.4a). At midday, the mean incident photosynthetic flux was higher for Configuration C than Configuration B due to the south-facing orientation of the mirror.

6.3.2 Microalgae growth

Figures 6.5a and 6.5b show the temporal evolution of the volume-averaged specific growth rate $\bar{\mu}(t)$ and the biomass concentration $X(t)$ on September 21$^{\text{st}}$ in Los Angeles, CA for the four raceway pond configurations considered. For all configurations, the initial biomass concentration was $X_0 = 0.07$ kg m^{-3} and the culture depth was $D = 0.3$ m. Figure 6.5a indicates that the average specific growth rate $\bar{\mu}(t)$ was higher for the raceway ponds featuring mirrors compared to Configuration A at nearly all times of day. This was thanks to the increased solar collection surface provided by the mirrors which increased the incident photosynthetic photon flux $\bar{q}''_{in,PAR}$, as observed in Figure 6.4b. At midday, the effect of the mirrors in Configuration B was small and the average growth rate $\bar{\mu}(t)$ was briefly smaller than that of Configuration A. This was caused by the decrease in light penetration due to the higher biomass concentration $X(t)$ in Configuration B compared to Configuration A. In the morning and evening, Configuration B had a larger average growth rate $\bar{\mu}(t)$ than Configuration C, while the opposite was true at midday. This was attributed to the fact that the east/west facing mirrors increased the photosynthetic photon flux $\bar{q}''_{in,PAR}$ significantly in the mornings and evenings while the south-facing mirror increased $\bar{q}''_{in,PAR}$ the most at midday (see Figure 6.4b). On the other hand, Configuration D had the highest average growth rate $\bar{\mu}(t)$ until 11 am thanks to its solar tracking capability. Throughout the rest of the day, the average growth rate $\bar{\mu}(t)$ of Configuration D decreased slightly compared to Configurations B and C due to the higher biomass concentration which reduced light penetration.

Similarly, Figure 6.5b indicates that Configurations B-D yielded larger biomass concentration $X(t)$ than Configuration A at all times of the day on September 21$^{\text{st}}$. Configuration

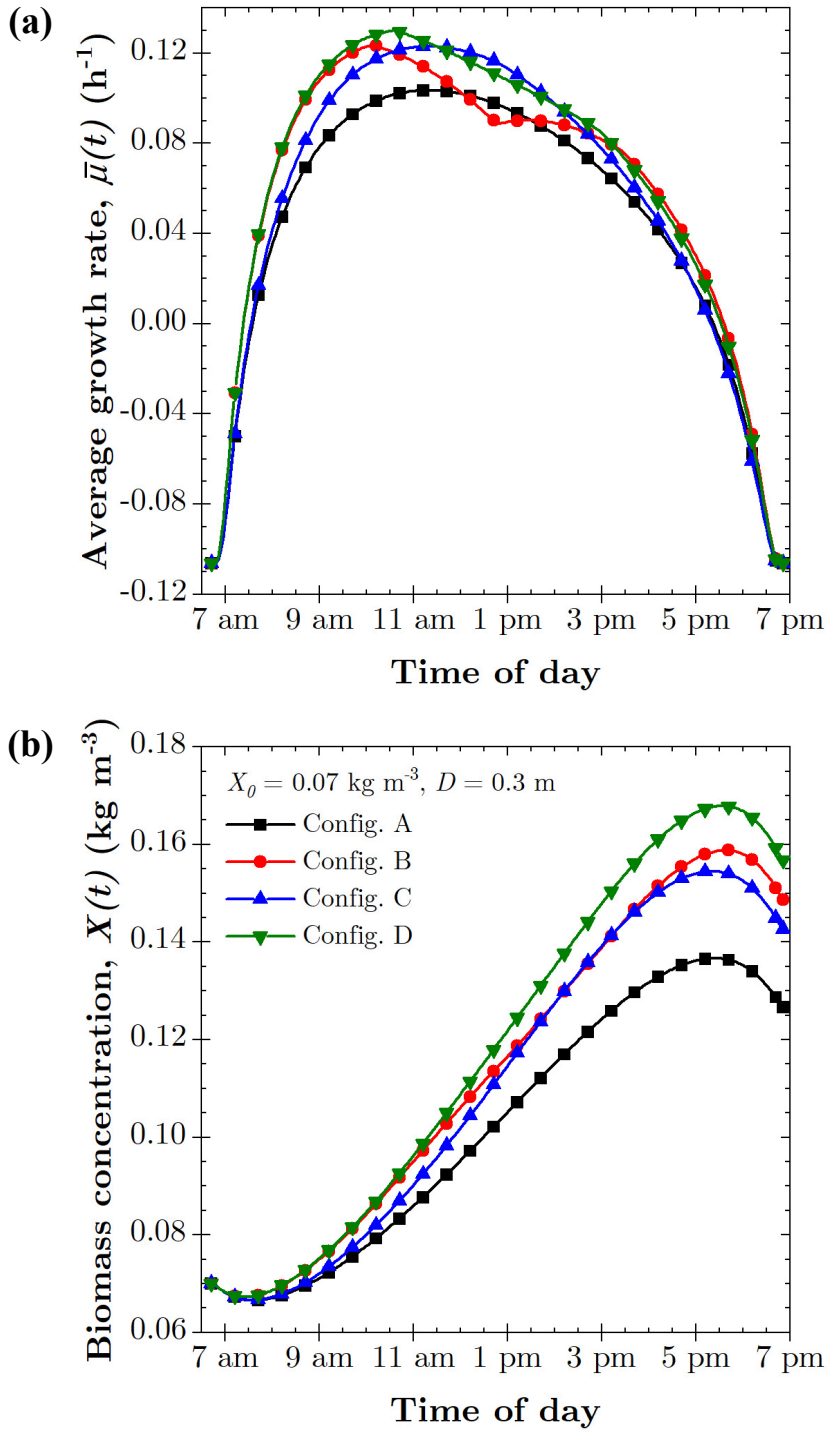

Figure 6.5: (a) Average specific growth rate $\bar{\mu}(t)$ and (b) biomass concentration $X(t)$ as functions of time on September 21st for Configurations A-D located in Los Angeles, CA with initial biomass concentration $X_0 = 0.07$ kg m^{-3} and culture depth $D = 0.3$ m.

D achieved the largest maximum biomass concentration of $X_{max} = 0.168$ gL^{-1} compared to $X_{max} = 0.137$ gL^{-1} for Configuration A. Configurations B and C reached a maximum biomass concentration X_{max} of 0.159 gL^{-1} and 0.155 gL^{-1}, respectively. For all configurations, X_{max} was attained around 5:30 pm. Interestingly, Configurations B and C exhibited similar growth curves despite marked differences in their designs (see Figures 6.1B and 6.1C) and corresponding average incident photosynthetic photon flux $\bar{q}''_{in,PAR}$ (see Figure 6.4b). Overall, the new reflecting pond designs increased the maximum biomass concentration X_{max} by 16%, 13%, and 23% for Configurations B, C, and D, respectively, compared to the traditional raceway pond of Configuration A. For all configurations, the biomass concentration $X(t)$ decreased after approximately 5:30 pm as the available photosynthetic photon flux was not sufficient to sustain growth resulting in biomass loss due to respiration.

6.3.3 Biomass productivity

Figure 6.6a shows the daily culture-area-based $P_{A,C}$ biomass productivity of Configurations A-D as a function of the initial biomass concentration X_0 for culture depths D equal to 0.1 m, 0.2 m, and 0.3 m on September 21st in Los Angeles, CA. Previous studies [48, 50] have demonstrated that the culture-area-based biomass productivity of photobioreactors and covered raceway ponds scales with X_0/a where a is the specific illuminated area given by $a = S_C/V$ such that $a = 1/D$ for the present raceway ponds. Note also that the initial culture optical thickness can be expressed as $\beta_{\lambda,0}D = (\bar{A}_{abs,\lambda} + \bar{S}_{sca,\lambda})X_0D$ where $\beta_{\lambda,0}$ is the initial extinction coefficient in m^{-1}. Thus, the product X_0D of the initial biomass concentration X_0 and the culture thickness D is representative of the culture's initial optical thickness [48]. Figure 6.6b plots the same data for biomass productivity $P_{A,C}$ shown in Figure 6.6a but as a function of X_0D. The results indicate that, even when using mirrors, the productivity $P_{A,C}$ collapsed onto a single line for all values of X_0 and D. Note that land-area-based biomass productivity $P_{A,L} = P_{A,C} \times S_C/S_L$ (not pictured) also collapsed onto a single line. This indicates that the scaling relation between areal biomass productivity (in kg m^{-2}day^{-1}) and the initial optical thickness represented by the product X_0D holds true for raceway ponds featuring external mirrors.

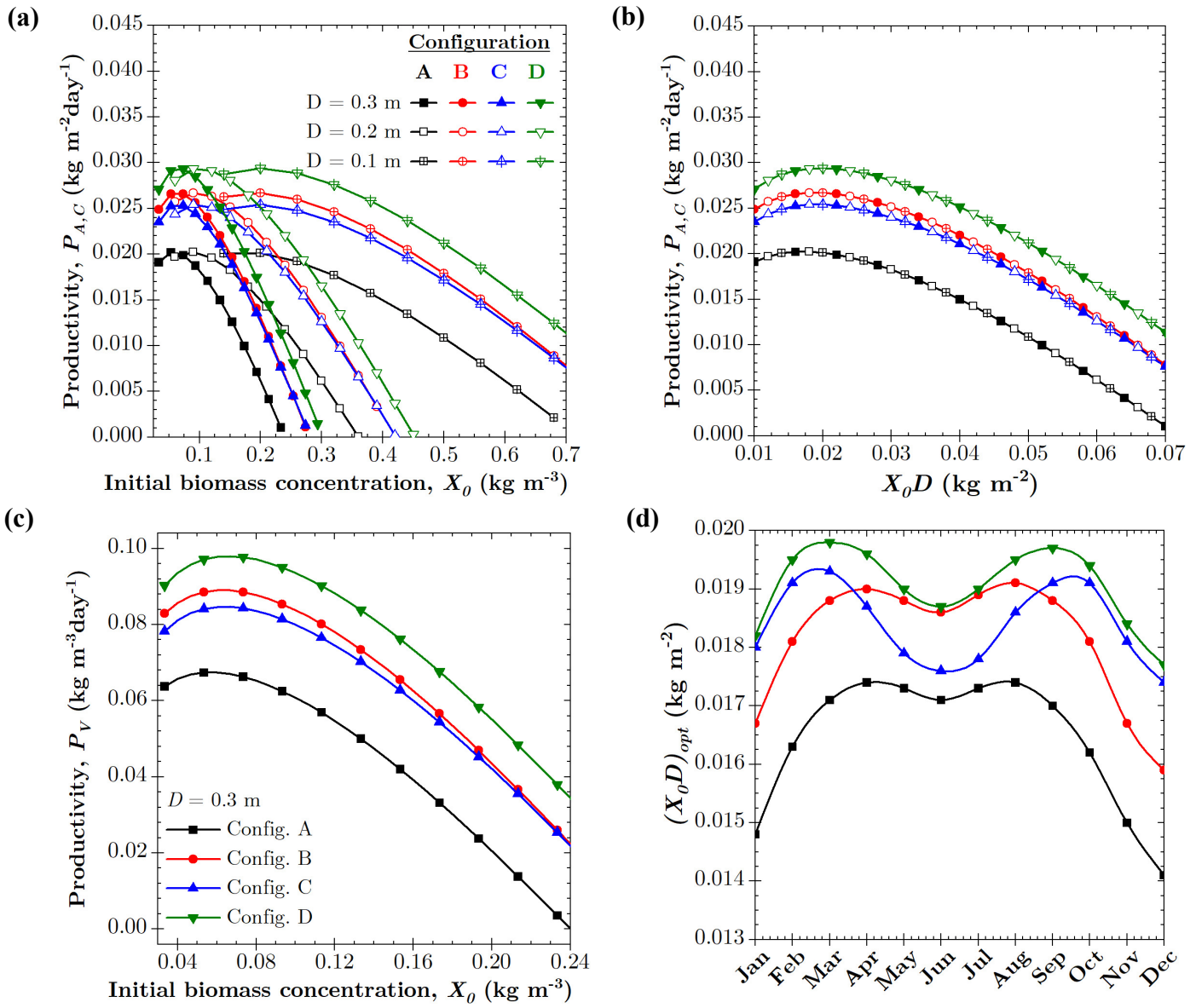

Figure 6.6: Daily culture-area-based $P_{A,C}$ productivity as a function of (a) initial biomass concentration X_0 and (b) the product X_0D for culture depth D equal to 0.1 m, 0.2 m, and 0.3 m on September 21st. (c) Volumetric P_V productivity as function of X_0 for a culture depth D = 0.3 m on September 21st. (d) Product of the initial biomass concentration and the culture depth $(X_0D)_{opt}$ which maximizes biomass productivity on the 21st day of each month of the year. All data shown is for Configurations A-D located in Los Angeles, CA.

Figure 6.6c shows the daily volumetric biomass productivity P_V for all four raceway pond configurations as a function of X_0 for a culture depth $D = 0.3$ m on September 21st in Los Angeles, CA. Note that volumetric productivity is given by $P_V = P_{A,C}/D$ and thus did not scale with the product X_0D. Configurations B-D significantly improved the daily culture-area-based $P_{A,C}$ and volumetric P_V biomass productivities for all values of X_0D and X_0, respectively. The maximum value of both $P_{A,C}$ and P_V increased by 32%, 26%, and 45% for Configurations B, C, and D, respectively, compared to Configuration A for which $P_{A,C,max} = 0.020$ kg m^{-2}day^{-1} and $P_{V,max} = 0.067$ kg m^{-3}day^{-1}. The predicted productivity of Configuration A was within the typical range of productivities for well-managed open raceway ponds reported as 0.020 to 0.025 kg m^{-2}day^{-1} from Ref. [32].

Figure 6.6d plots the optimum value of the product X_0D which yielded the maximum biomass productivity on the 21st day of each month of the year, denoted by $(X_0D)_{opt}$, for Configurations A-D in Los Angeles, CA. The smallest optimum initial optical thickness represented by $(X_0D)_{opt}$ occurred during the winter months for all four configurations. During this time of year, the optimum optical thickness was lower due to the decreased incident photon flux. Similarly, $(X_0D)_{opt}$ of Configuration A was smaller than that of Configurations B-D throughout the year due to its lower incident photon flux. However, all four configurations exhibited a local minimum in $(X_0D)_{opt}$ during June when the incident photon flux was the largest. This was attributed to the longer days during the summer months which led to higher biomass concentrations in the afternoon. Thus, $(X_0D)_{opt}$ was smaller to avoid low light penetration and small growth rates in the afternoon. The maximum in $(X_0D)_{opt}$ occurred in April and August for Configurations A and B and in March and September for Configurations C and D. These results suggest that both the solar intensity and duration of the day must be considered to identify $(X_0D)_{opt}$ for a given location and time of year.

Figures 6.7a and 6.7b show the maximum daily culture-area-based $P_{A,C,max}$, land-area-based $P_{A,L,max}$, and volumetric $P_{V,max}$ productivities of Configurations A-D obtained from simulations of biomass concentration $X(t)$ from sunrise to sunset on the 21st day of each month of the year using $(X_0D)_{opt}$ reported in Figure 6.6d. It is evident that adding mirrors to the raceway pond increased the maximum biomass productivities $P_{A,C,max}$ and $P_{V,max}$

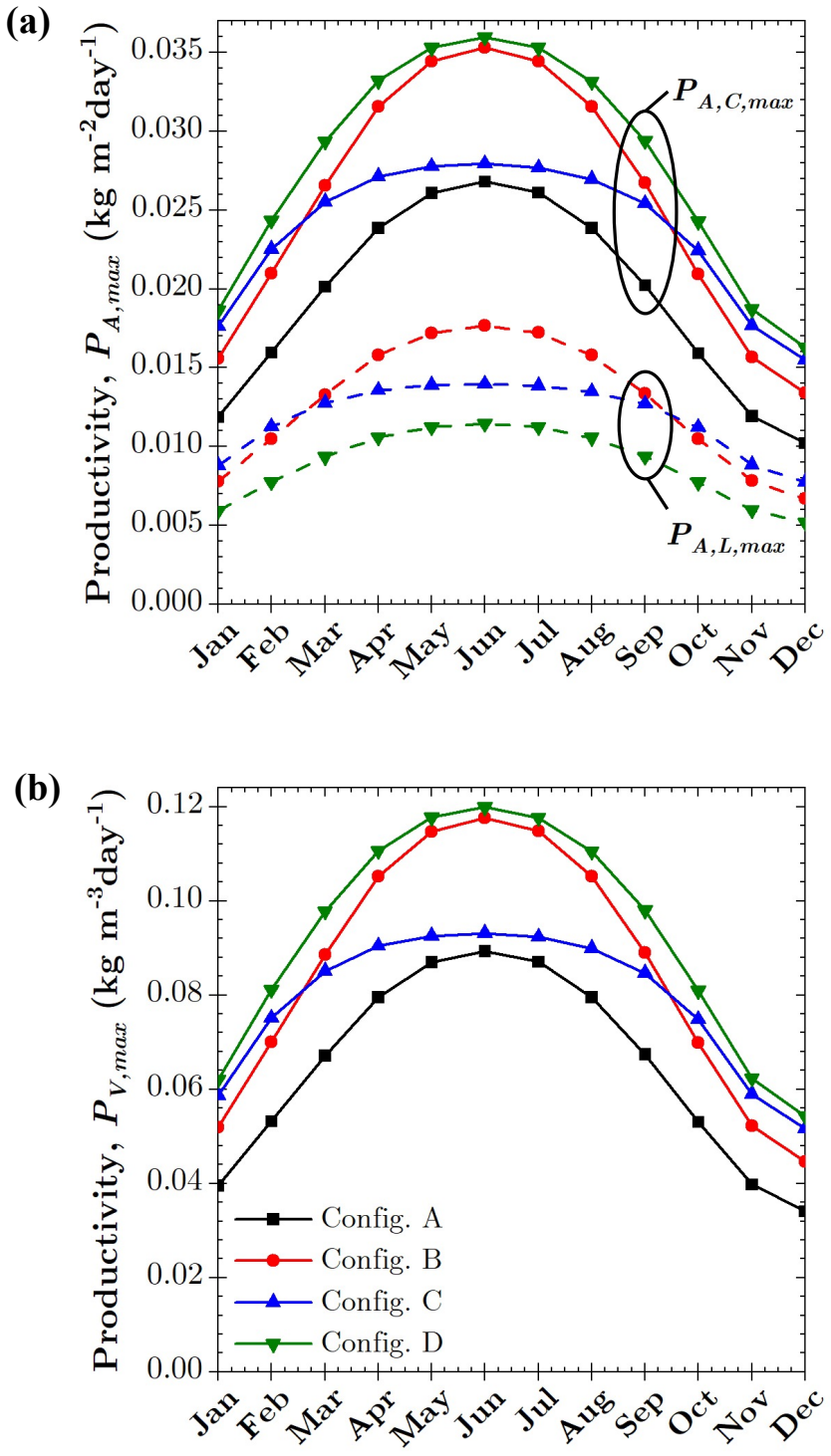

Figure 6.7: (a) Maximum daily culture-area-based $P_{A,C,max}$, land-area-based $P_{A,L,max}$, and (b) volumetric $P_{V,max}$ productivity over one year for raceway pond Configurations A-D in Los Angeles, CA.

throughout the year. Indeed, even the simple single-mirror design of Configuration C increased the culture-area-based $P_{A,C,max}$ and volumetric $P_{V,max}$ productivities by 52% in December. However, Configurations B-C also decreased the maximum land-area-based $P_{A,L,max}$ productivity throughout the year. Configuration D exhibited the largest culture-area-based $P_{A,C,max}$ and volumetric $P_{V,max}$ productivities as well as the smallest land-area-based $P_{A,L,max}$ productivity. This was due to the additional land area required to accommodate the rotating platform and prevent shading between adjacent ponds with external mirrors. Thus, a production facility featuring raceway ponds of Configuration D would require a larger land area to achieve the same annual yield as a raceway pond of Configuration A-C. Furthermore, Figure 6.7 indicates that Configuration B had larger productivities $P_{A,C,max}$, $P_{A,L,max}$, and $P_{V,max}$ from March to September than Configuration C while the opposite was true from October to February. This suggests that the dual mirror design of Configuration B is better suited to smaller solar zenith angles θ_z observed in the summer months. Conversely, the single mirror design of Configuration C is better suited to larger solar zenith angles θ_z observed in the winter months.

6.3.4 Impact of reflecting pond dimensions and location

The maximum daily culture-area-based biomass productivity $P_{A,C,max}$ was predicted for pond length-to-width ratio L/W ranging from 1 to 20 for Configurations A-D in Los Angeles, CA on September 21st. The results are shown in Figure D.1 of Supplementary Materials. The productivity $P_{A,C,max}$ of Configuration A was found to be independent of L/W as light transfer within the culture was modeled as one-dimensional and ignored edge effects. This was also the case for Configuration D thanks to its tracking feature which ensured that no reflected light fell outside of the culture surface (see Figure 6.1D). On the other hand, the biomass productivity $P_{A,C,max}$ of Configurations B and C increased as the length-to-width ratio L/W increased up to $L/W \sim 5$, beyond which a plateau was reached. This was due to a decrease in the fraction of total reflected light that fell outside of the culture surface (see Figures 6.1B and 6.1C) as L/W increased. Thus, raceway ponds featuring mirrors should have a length-to-width ratio $L/W \geq 5$ to mitigate this effect. The impact of L/W was found

to be the same throughout the year (see also Supplementary Materials).

Figures 6.8a and 6.8b plot the maximum daily culture-area-based biomass productivity $P_{A,C,max}$ as a function of the maximum allowed mirror height normalized with respect to the pond width H^*/W for Configurations A-D on September 21st in Los Angeles, CA and Saint-Nazaire, France. For the dual east/west mirror Configuration B, Figure 6.8 indicates that the productivity $P_{A,C,max}$ increased continuously with increasing H^*/W for both locations. This was due to the fact that the apparent solar zenith angle $\theta_{z,a}$ approached zero at midday which resulted in very large values of mirror height required to maximize the reflected area according to Equation (6.2). On the other hand, the productivity $P_{A,C,max}$ of Configurations C and D increased and then remained constant for $H^*/W \geq 1.6$ for Los Angeles, CA and $H^*/W \geq 1.0$ for Saint-Nazaire, France. Thus, these values represented the optimum value $(H^*/W)_{opt}$ of the maximum mirror height H^* normalized by the pond width W. Note that $(H^*/W)_{opt}$ for Configurations C and D on September 21st were given by the maximum value of mirror height $H_{C/D}(t)$ on that day from Equations (6.3) and (6.4), respectively.

Figure 6.9a plots the optimum mirror height normalized by the pond width $(H^*/W)_{opt}$ for the 21st day of each month in Los Angeles, CA and Saint-Nazaire, France for Configurations C and D. Note that $(H^*/W)_{opt}$ was not shown for Configuration B since it was infinite at midday as the apparent solar zenith angle $\theta_{z,a}$ approached zero [see Equation (6.2)]. Figure 6.9a indicates that $(H^*/W)_{opt}$ was smaller throughout the year at the higher latitude of Saint-Nazaire, France compared to that of Los Angeles, CA. This was due to the larger minimum solar zenith angle $\theta_{z,min}$ (see Figure 6.9b) which reduced the mirror height necessary to maximize the fraction S_{ref}/S_C of the culture area subjected to reflected light. Similarly, the larger solar zenith angles in the winter months resulted in smaller $(H^*/W)_{opt}$ compared to the summer months for both locations. Furthermore, Figure 6.9a demonstrates that the mirror heights required to optimize the performance of both configurations were small in the winter months, particularity for ponds located in Saint-Nazaire where $(H^*/W)_{opt}$ was less than unity from September to March.

Figures 6.9c and 6.9d plot the predicted maximum culture-area-based productivity $P_{A,C,max}$ throughout the year for the optimum maximum mirror height $(H^*/W)_{opt}$ from Figure 6.9a

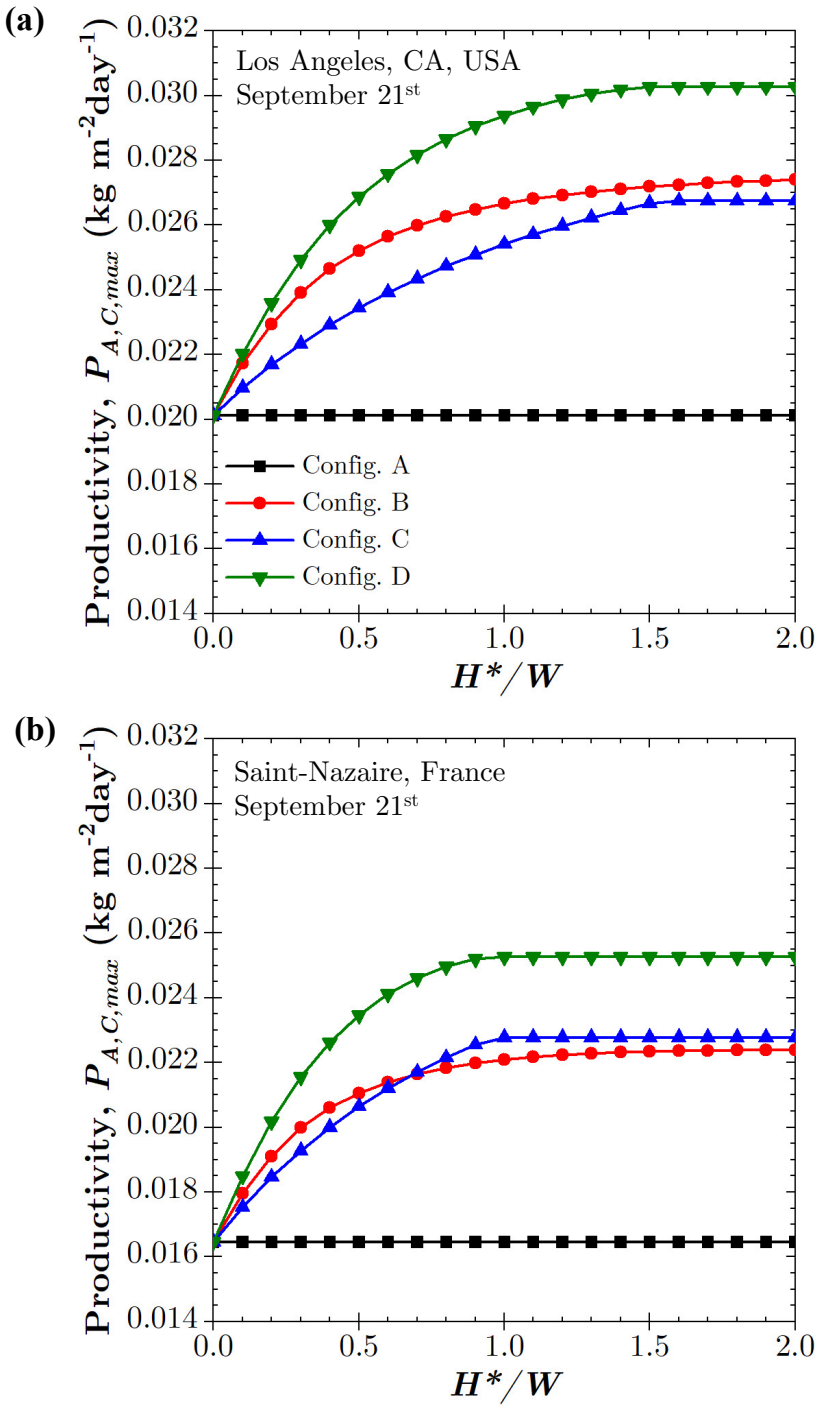

Figure 6.8: Maximum daily culture-area-based biomass productivity $P_{A,C,max}$ as a function of normalized maximum mirror height H^*/W on September 21st for Configurations A-D in (a) Los Angeles, CA and (b) Saint-Nazaire, France.

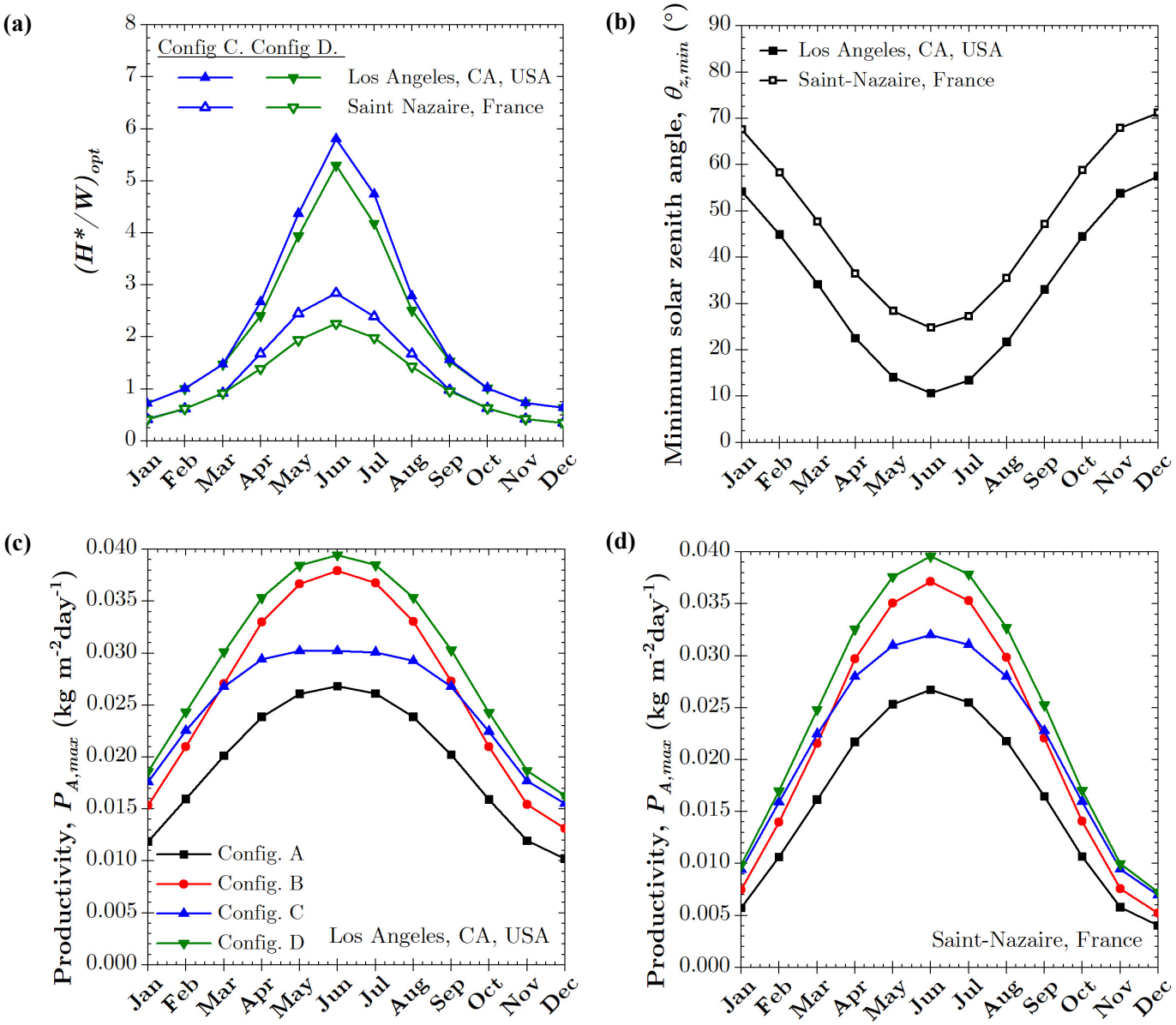

Figure 6.9: (a) Optimum mirror height normalized by the pond width $(H^*/W)_{opt}$ for Configurations C and D and (b) the minimum solar zenith angle $\theta_{z,min}$ on the 21st day of each month in Los Angeles, CA and Saint-Nazaire, France. Maximum daily culture-area-based biomass productivity $P_{A,C,max}$ throughout the year using $(H^*/W)_{opt}$ for Configurations A-D located in (c) Los Angeles, CA and (d) Saint-Nazaire, France.

for all four configurations in Los Angeles, CA and Saint-Nazaire, France, respectively. Here, the optimum maximum mirror height $(H^*/W)_{opt}$ for Configuration C was used for Configuration B. In general, Figures 6.9c and 6.9d indicate that the areal productivity $P_{A,C,max}$ for raceway ponds located in Los Angeles was greater than those located in Saint-Nazaire. This can be attributed in part to the smaller solar zenith angles (see Figure 6.9b) experienced by the ponds in Los Angeles thanks to its lower latitude. However, Configuration C yielded a slightly larger productivity in Saint-Nazaire than in Los Angeles during the month of June despite having a significantly smaller optimum mirror height H^* (see Figure 6.9a) and experiencing a larger solar zenith angle θ_z. This indicates that Configuration C was more effective at improving the biomass productivity of raceway ponds at higher latitudes. Furthermore, for Saint-Nazaire, the productivity of Configuration C was nearly equal to the ideal tracking case of Configuration D from October to February. Indeed, volumetric and culture-area-based productivity increased by up to 73% for Configuration C in Saint-Nazaire during these months despite the relatively small optimum maximum mirror height $(H^*/W)_{opt}$.

Overall, Configurations B-D enabled higher biomass yield per unit area and volume of culture by increasing the solar input to the microalgae culture. This would reduce the final cost per unit mass of biomass since the operating cost scales linearly with the culture surface area [152]. Moreover, by increasing productivity in the winter months, the growing season can be extended and yearly productivity can be improved in locations where year-long growth is currently inefficient. For example, Configuration C increased biomass production in Saint-Nazaire from September to March by 50%. Additionally, the increased incident solar flux achieved by using mirrors may decrease the energy required for thermal regulation of the culture in cooler months and/or climates where sunlight is a major source of heat for solar culture systems [153]. However, adding mirrors requires more land to prevent mutual shading between adjacent raceway ponds. Furthermore, the mirrors and control system required to implement the external reflecting pond design would increase the capital and maintenance costs compared to a standard raceway pond, particularly for Configuration B featuring two mirrors and for Configuration D featuring the rotating raceway pond. Thus,

Configuration C appears to be the most practical design as it requires a single mirror but still improved the raceway pond volumetric and culture-area-based biomass productivity significantly, particularity in the winter months. The concepts explored in this study are promising and should be explored experimentally.

6.4 Conclusion

The use of mirrors to increase the daily biomass productivity of outdoor raceway ponds by reflecting additional light onto the microalgae culture was investigated theoretically. Four designs were considered including a raceway pond without mirrors (Configuration A) used as a reference, a pond oriented along the north/south axis with mirrors on both its east and west sides (Configuration B), a pond oriented along the east/west axis with a single mirror on its north side (Configuration C), and a solar tracking rotating pond with a single mirror (Configuration D). The growth of *Chlorella vulgaris* was predicted using the two-flux approximation and a growth kinetics model accounting for light limitation and cell respiration activity. The use of external mirrors was found to improve the daily volumetric and culture-area-based biomass productivities throughout the year and by as much as 73% compared to a raceway pond without mirrors. Configuration B outperformed Configuration C in the summer months, while the opposite was true in the winter months. Furthermore, the culture-area-based biomass productivity of all four configurations was found to scale by the product of the initial biomass concentration and the culture depth X_0D. The product X_0D which yielded the maximum biomass productivity depended on the configuration and the time of year. The addition of mirrors was found to yield the largest improvement in biomass productivity for ponds with a pond length-to-width ratio greater than 5. Additionally, the optimum maximum mirror height was reported for Configurations C and D for both Los Angeles, CA, and Saint-Nazaire, France. Overall, Configuration C featuring a single mirror on the north side of a pond oriented along the east-west axis was considered to be the simplest and most cost-effective method for improving the biomass productivity in outdoor raceway ponds. These results provide practical guidelines for the design and operation of

raceway ponds featuring mirrors for improved biomass productivity.

CHAPTER 7

Conclusions and Future Work

7.1 Conclusions

The objective of this dissertation was to assess the impact of (1) condensate comprised of either small cap-shaped droplets or large non-cap shaped droplets, (2) microalgae colony formation, and (3) the presence of an external vertical reflecting surface on light transfer in outdoor microalgae cultivation systems and their performance.

The first objective was achieved by modeling light transfer through tilted and horizontal transparent windows supporting both small cap-shaped and large non-cap shaped non-absorbing droplets of various volume V and contact angle θ_c. The shape of large non-cap shaped droplets was predicted numerically accounting for both surface tension and gravitational forces. The transmittance of windows supporting cap-shaped droplets was nearly the same as those with small droplets ($V < 10$ µL) and contact angles $\theta_c < \theta_{cr}$ where θ_{cr} is the critical angle for total internal reflection at the water/air interface. As droplet volume increased, the transmittance of horizontal windows supporting non-cap shaped droplets decreased by up to 37% compared to that of a window supporting cap-shaped droplets of the same contact angle and volume. Conversely, for tilted windows supporting non-cap shaped droplets, increasing droplet volume increased window transmittance compared to that of a tilted window supporting cap-shaped droplets of equal volume. In all cases, window transmittance decreased linearly with increasing droplet surface area coverage. These results demonstrate that optical losses due to back-scattering of light by droplets in microalgae cultivation systems may be reduced by tilting the covers or by reducing the size, contact angle, and/or surface area coverage of condensate droplets.

A deeper understanding of the effects of condensate droplets on microalgae cultivation systems was achieved by coupling light transfer modeling of scattering by droplets and growth

kinetics in an outdoor covered raceway pond cultivating *Chlorella vulgaris*. Then, the resulting radiative field in the culture was coupled to a growth kinetics model for *Chlorella vulgaris*. Generally, the presence of droplets was found to decrease the solar energy input to the microalgae culture due to the reduced window transmittance. Indeed, compared to a raceway pond featuring a dry cover without droplets, a raceway pond with a cover featuring 90% droplet surface area coverage and 90° droplet contact angle experienced a decrease in biomass productivity by as much as 18%.

Moreover, a significant decrease in the average spectral mass absorption cross-section $\bar{A}_{abs,\lambda}$ of *Botryococcus braunii* was observed, both experimentally and numerically, between cultures containing (i) single cells or (ii) aggregate-like colonies. The decrease observed in $\bar{A}_{abs,\lambda}$ for cultures with colonies was explained, in part, by the decrease in pigment concentration. However, the arrangement of cells into colonies was also found to reduce the average spectral absorption cross-section $\bar{A}_{abs,\lambda}$ due to mutual shading between cells. This was the case for colonies containing as few as 10 cells.

The role of colony formation in light absorption was further investigated by considering colonies with an ordered spherical structure featuring very large cell and extracellular matrix size parameters. Such colony morphology is often observed in members of the *Volvocaceae* family such as *Eudorina*, *Pleodorina*, and *Volvox*. Here also, colony formation was found to decrease the mass absorption cross-section $\bar{A}_{abs,\lambda}$ due to shading effects. Furthermore, the impact of shading effects increased with increasing cell size, absorption index, and number of cells present in the colony. Indeed, a colony with 64 cells was found to absorb up to 23% less light compared to a equivalent number of free floating single cells. This may decrease the local rate of photon absorption at a given depth in microalgae cultures and result in reduced growth.

Finally, several designs of outdoor raceway ponds cultivating of *Chlorella vulgaris* in either Los Angeles, CA or Saint-Nazaire, France under solar incidence were considered to increase the biomass productivity by reflecting additional sunlight on to the culture surface via a vertical external mirror. The use of external mirrors was predicted to improve the volumetric and culture-area-based productivities throughout the year for both locations and

all mirror configurations considered. In particular, the simplest design featuring a single mirror on the north side of an east-west oriented pond was predicted to increase biomass productivity by as much as 73% in the winter months compared to a raceway pond with no mirror present. This was attributed to the larger solar energy input which increased the penetration depth of light and enabled the culture to reach higher biomass concentrations.

7.2 Future Work

7.2.1 Modeling the impact of condensate droplets on solar heating and biomass productivity of closed outdoor photobioreactors

The simulation results reported in Chapter 3 demonstrate that the presence of droplets can have negative consequences for the biomass productivity of covered solar raceway ponds. In our study, only the visible part of the solar spectrum was considered. However, the presence of droplets may also act as an infrared filter providing passive thermal regulation of the culture. Simsek et al. [154] recently demonstrated an experimental validation of the MCRT algorithm used in Chapter 3 for the infrared part of the spectrum. Therefore, future work should focus on modeling the impact of droplets on both light and heat transfer in outdoor cultivation systems. The tools developed in Chapter 3 can also be used to investigate the effect of dropwise condensation on solar stills for water production.

7.2.2 Experimental proof-of-concept of a novel external reflecting raceway pond design for improved biomass productivity

Chapter 6 theoretically demonstrates the advantages of including a vertical reflecting surface in the design of outdoor raceway ponds to increase the sunlight available to the culture for photosynthesis. Future work should validate this design using a pilot-scale outdoor raceway pond subjected to solar radiation during various seasons. This will consist of operating two raceway ponds, with and without a mirror, in parallel under solar incidence cultivating the same microalgae strain. The culture temperature, pH, and evaporation can be monitored and/or controlled continuously and the evolution of the biomass and pigment concentrations will be compared between the two systems. This will enable a more comprehensive assess-

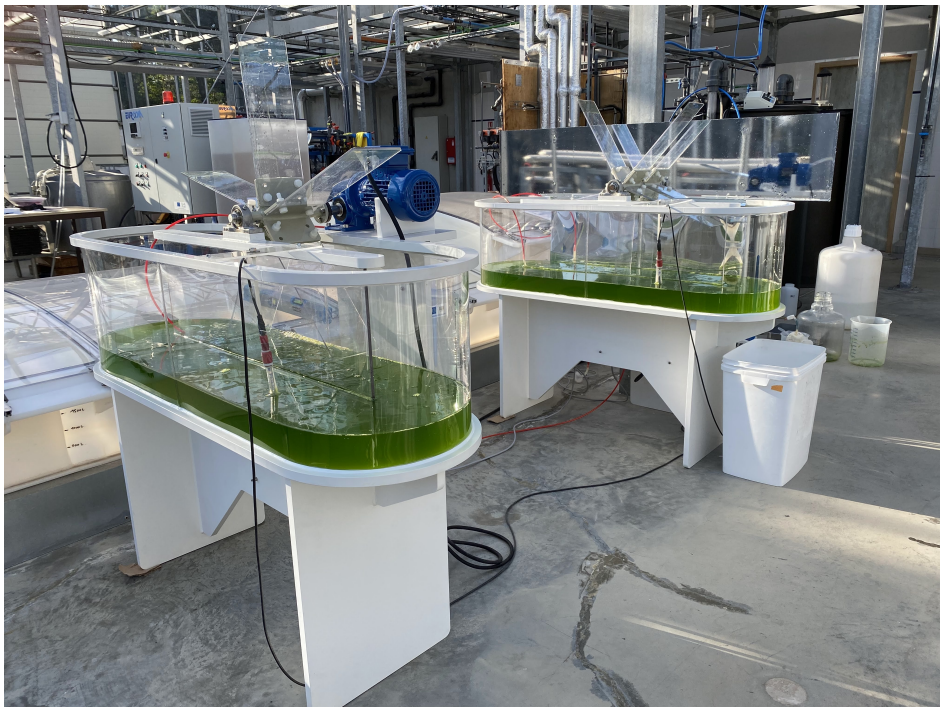

Figure 7.1: Experimental setup developed at AlgoSolis R&D facility in Saint-Nazaire, France for validating the reflecting raceway pond design. Microalgae is simultaneously cultivated in two raceways ponds, one with an external mirror (background) and the other and the one without (foreground) under identical solar conditions.

ment of operational challenges not considered by the current model such as temperature control, water evaporation, mirror design and material, and weather conditions.

7.2.3 Simulating light transfer in tubular photobioreactors

The current MCRT algorithms used in Chapters 3 - 5 can be adapted to model light transfer in a variety of systems such as tubular photobioreactors. Modeling of light transfer in tubular PBRs has often been simplified in the literature [48, 155, 156] by neglecting the effects of refraction, reflection, and mutual shading between tubes. However, these phenomenon may significantly affect the amount of light available to the cells. Thus, the performance of tubular PBRs may be impacted by design parameters including tube dimensions, tube arrangement, and the presence and material of adjacent surfaces. Future work should focus on modeling such systems to establish engineering guidelines for optimizing light transfer.

APPENDIX A

Supplementary Materials for Chapter 3

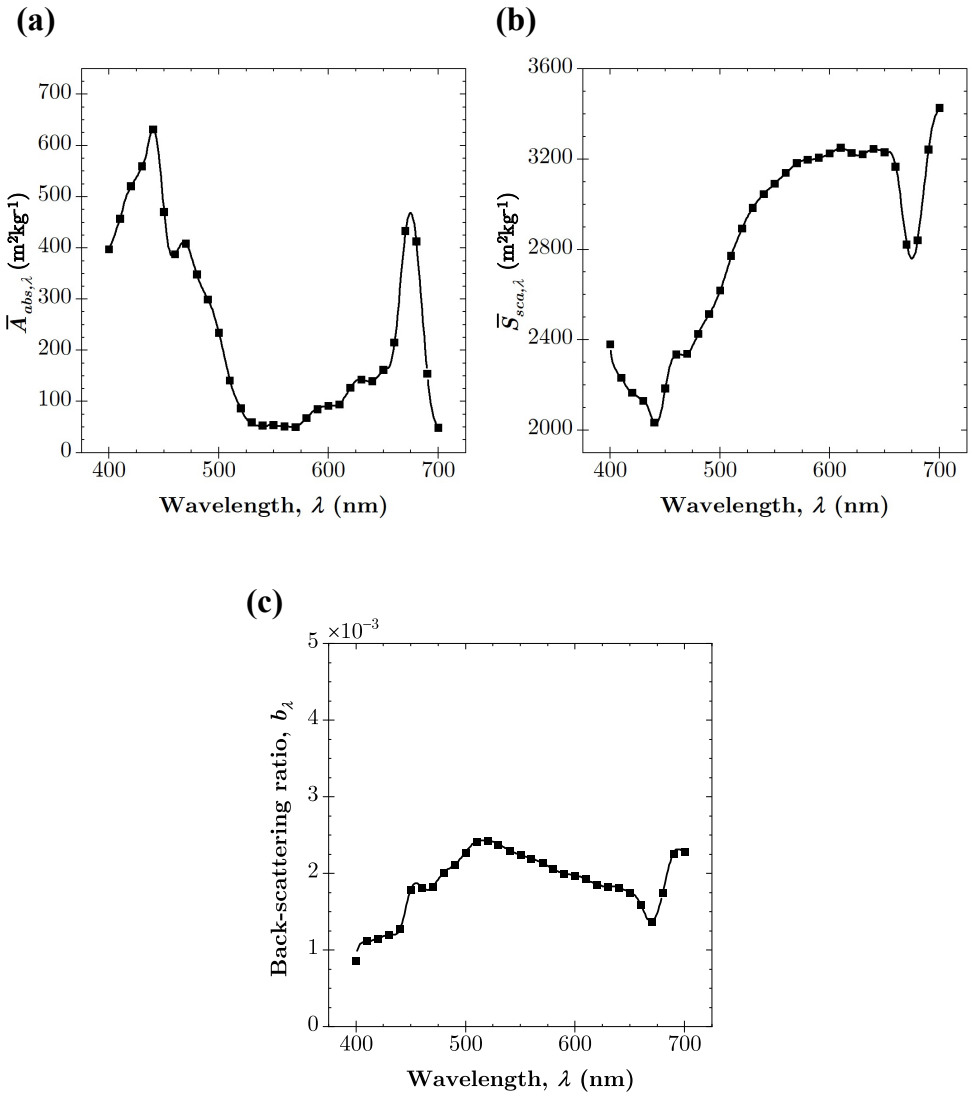

Figure A.1: Average spectral mass (a) absorption $\bar{A}_{abs,\lambda}$ and (b) scattering $\bar{S}_{sca,\lambda}$ cross-sections taken from [43] for Chlorella vulgaris with a mean cell radius of 2 µm and chlorophyll *a*, chlorophyll *b*, and photoprotective carotenoid (PPC) concentrations of 3.3 wt.%, 0.85 wt.%, and 0.85 wt.%, respectively. (c) Spectral backward scattering ratio b_λ as a function of wavelength λ calculated using the method presented in Ref. [78].

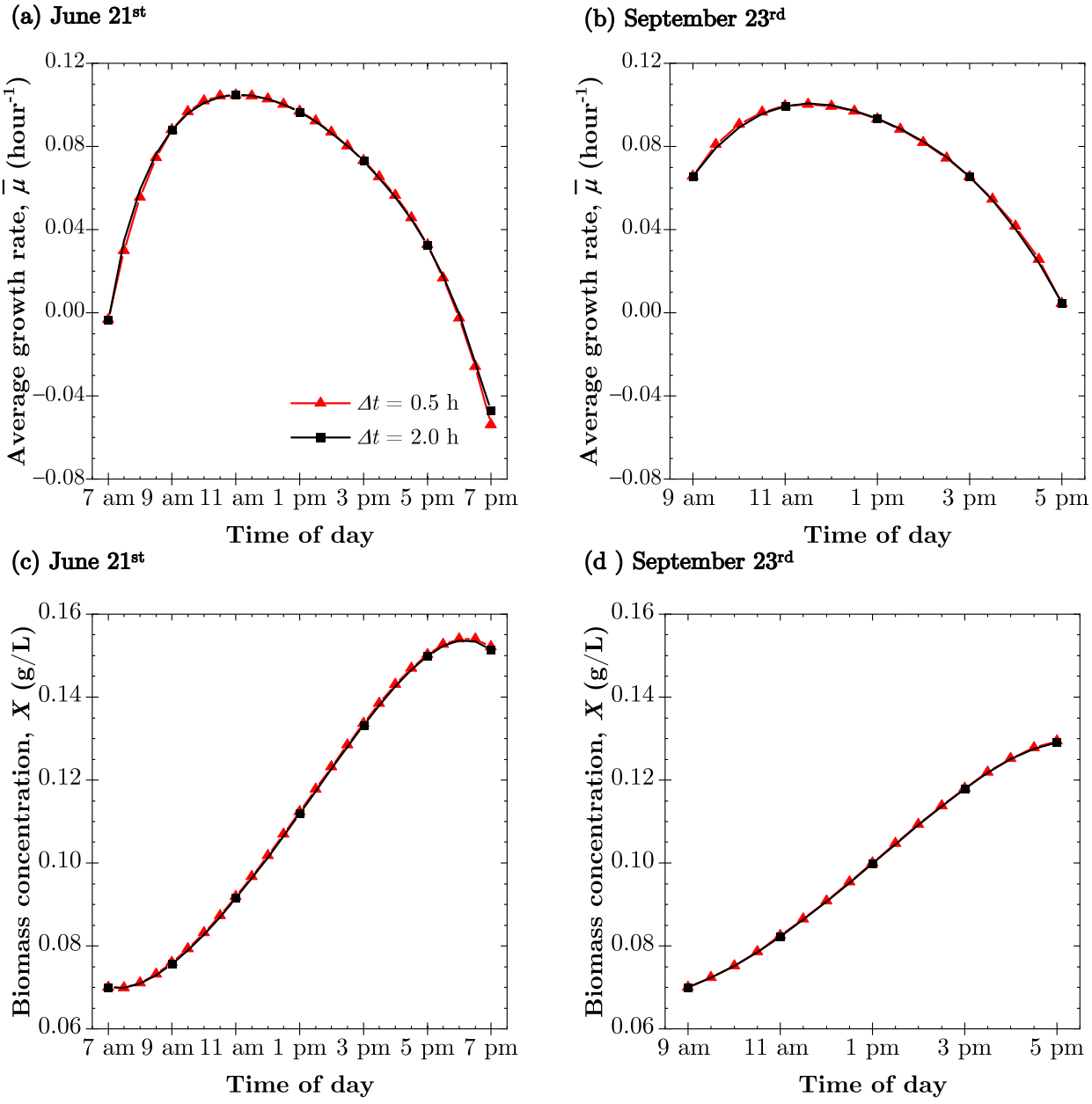

Figure A.2: Comparison of the average specific growth rate $\bar{\mu}(t)$ on (a) June 21$^{\text{st}}$ and (b) September 23$^{\text{rd}}$ and the biomass concentration $X(t)$ on (c) June 21$^{\text{st}}$and (d) September 23$^{\text{rd}}$ for droplet-free PBRs simulated using a time increment Δt of 0.5 h and 2 h. The PBRs had an initial biomass concentration X_0 of 0.07 gL^{-1} and a culture depth L of 0.3 m. The maximum relative error in the biomass concentration $X(t)$ was 0.1% and 0.3% on June 21$^{\text{st}}$ and September 23$^{\text{rd}}$, respectively

APPENDIX B

Supplementary Materials for Chapter 4

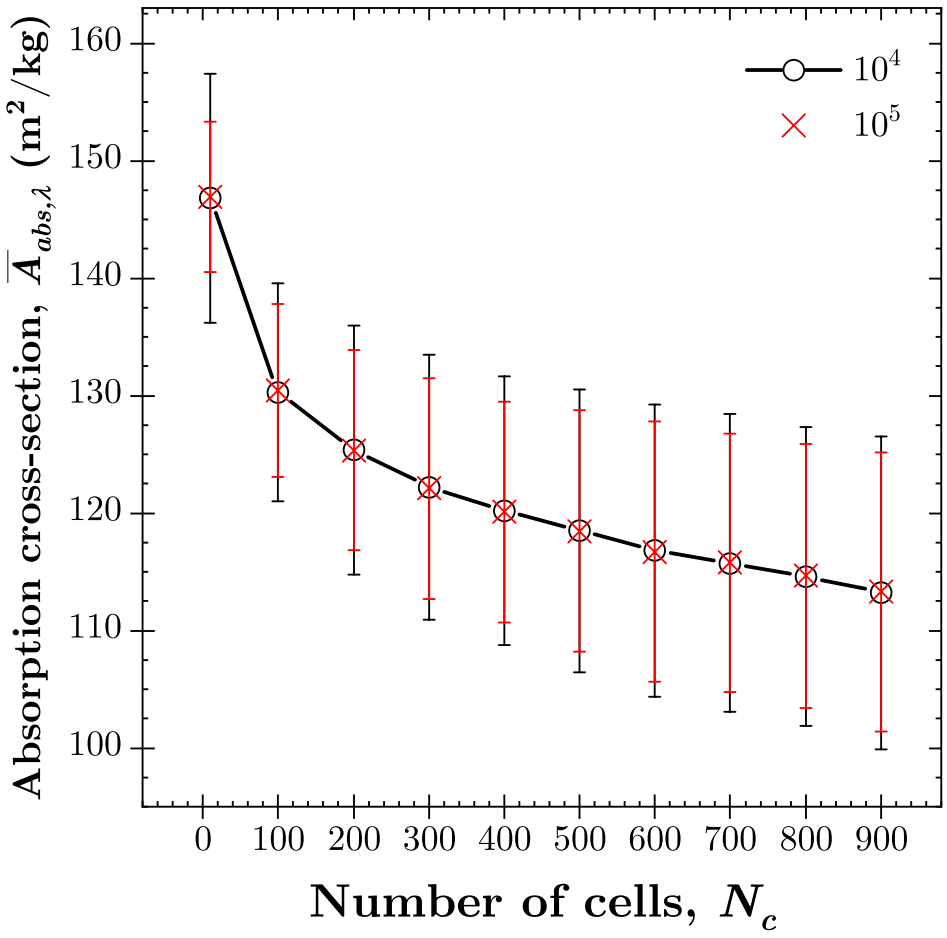

Figure B.1: Comparison of the Monte Carlo ray tracing (MCRT) results for the orientation-averaged absorption cross-section $\bar{A}^{co}_{abs}$ of colonies simulated using 10^4 or 10^5 rays for a given colony orientation of a given colony consisting of N_c cells. Fractal colonies were simulated with a cell complex index of refraction of $m^B_c = 1.026 + i0.0035$. Error bars correspond to 95% confidence intervals estimated from 100 colonies simulated at 10 orientations for each value of N_c.

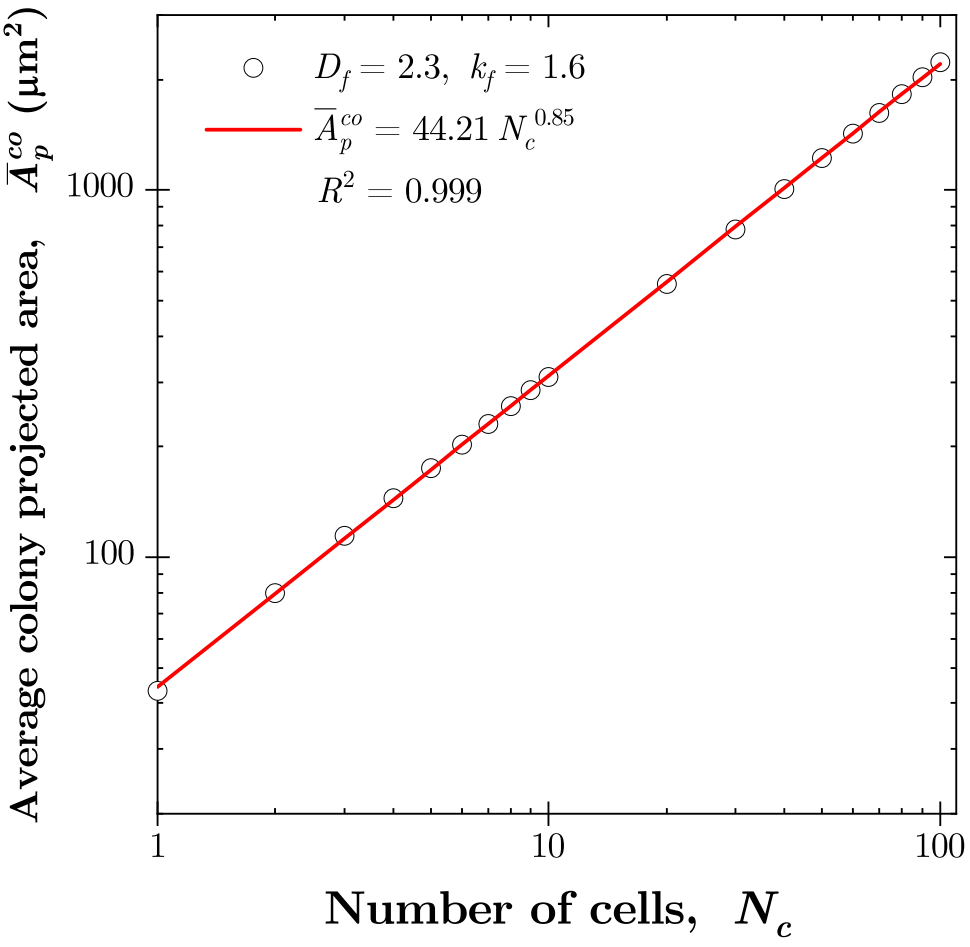

Figure B.2: Average projected area $\bar{A}_p^{co}$ of fractal colonies as a function of the number of cells N_c present in the colony. Aggregates were composed of cells of radius 3.71 μm and had fractal dimension and prefactor of $k_f = 1.6$ and $D_f = 2.3$, respectively.

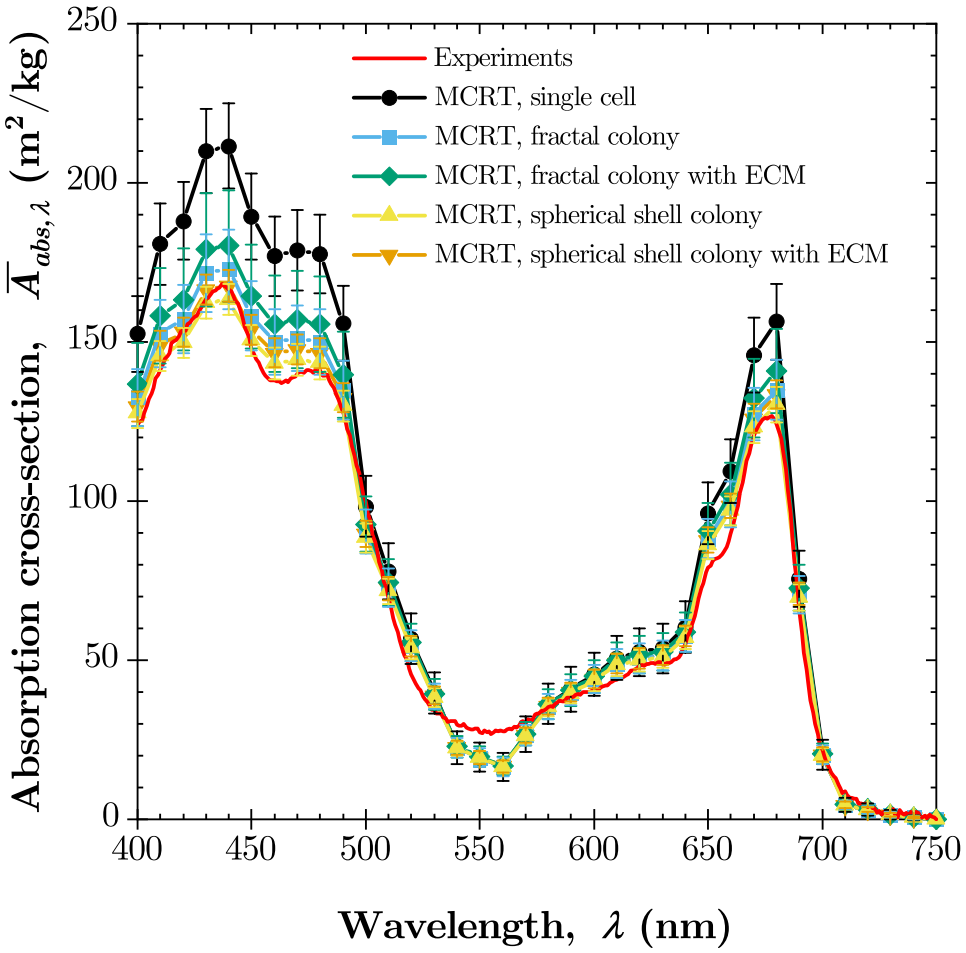

Figure B.3: Experimental measurements and Monte Carlo ray tracing (MCRT) predictions of the spectral average mass absorption cross-section $\bar{A}_{abs,\lambda}$ over the photosynthetically active radiation (PAR) region for cells in Culture B. The simulation results were plotted for (i) single cells, (ii) fractal colonies with and without extracellular matrix (ECM) and (iii) spherical colonies with and without ECM. All simulations used pigment concentrations from Culture B and all colony configurations were simulated using $N_c = 41$. Error bars correspond to 95% confidence intervals.

APPENDIX C

Supplementary Materials for Chapter 5

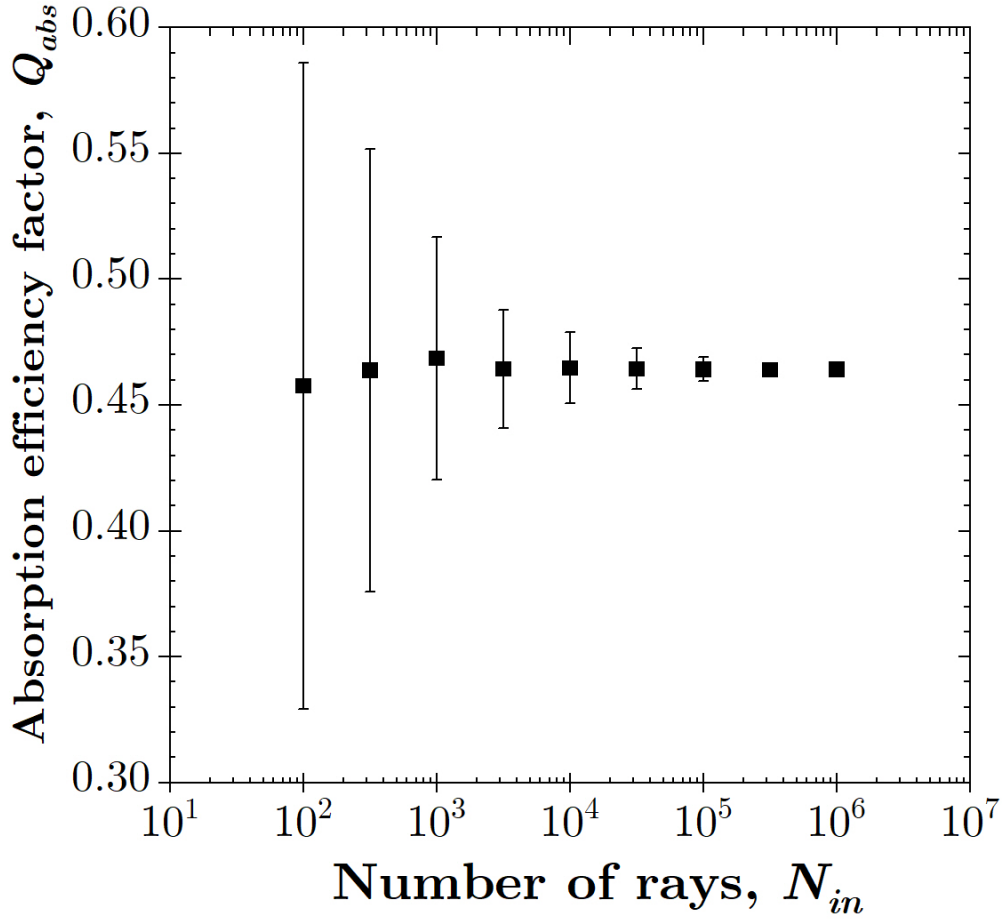

Figure C.1: Average absorption efficiency factor Q_{abs} of an ensemble of 64 cells as pictured in Figure 2 predicted by 100 trials of the MCRT method as a function of the number of incident rays N_{in} simulated. Error bars correspond to 95% confidence intervals.

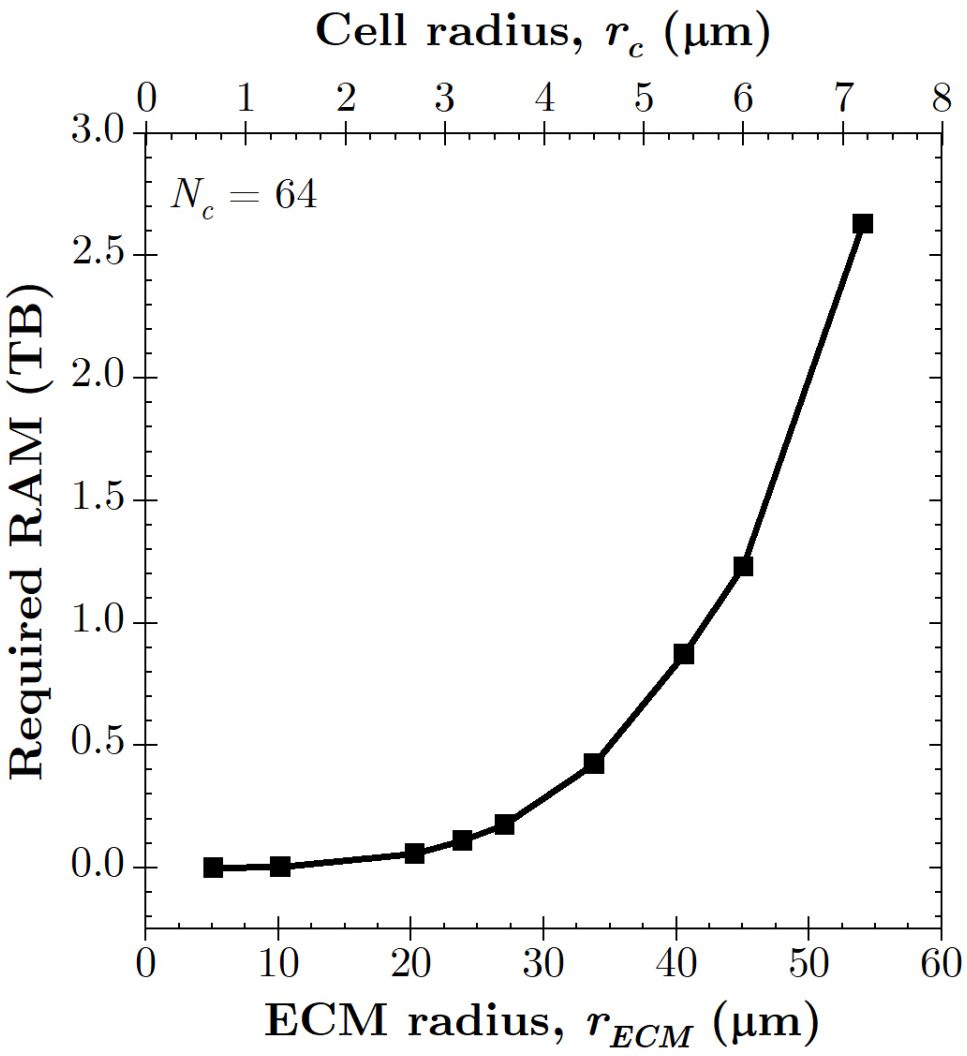

Figure C.2: RAM consumption for the superposition T-matrix simulations of a colony with $N_c = 64$ cells as a function of the radius of the ECM r_{ECM}.

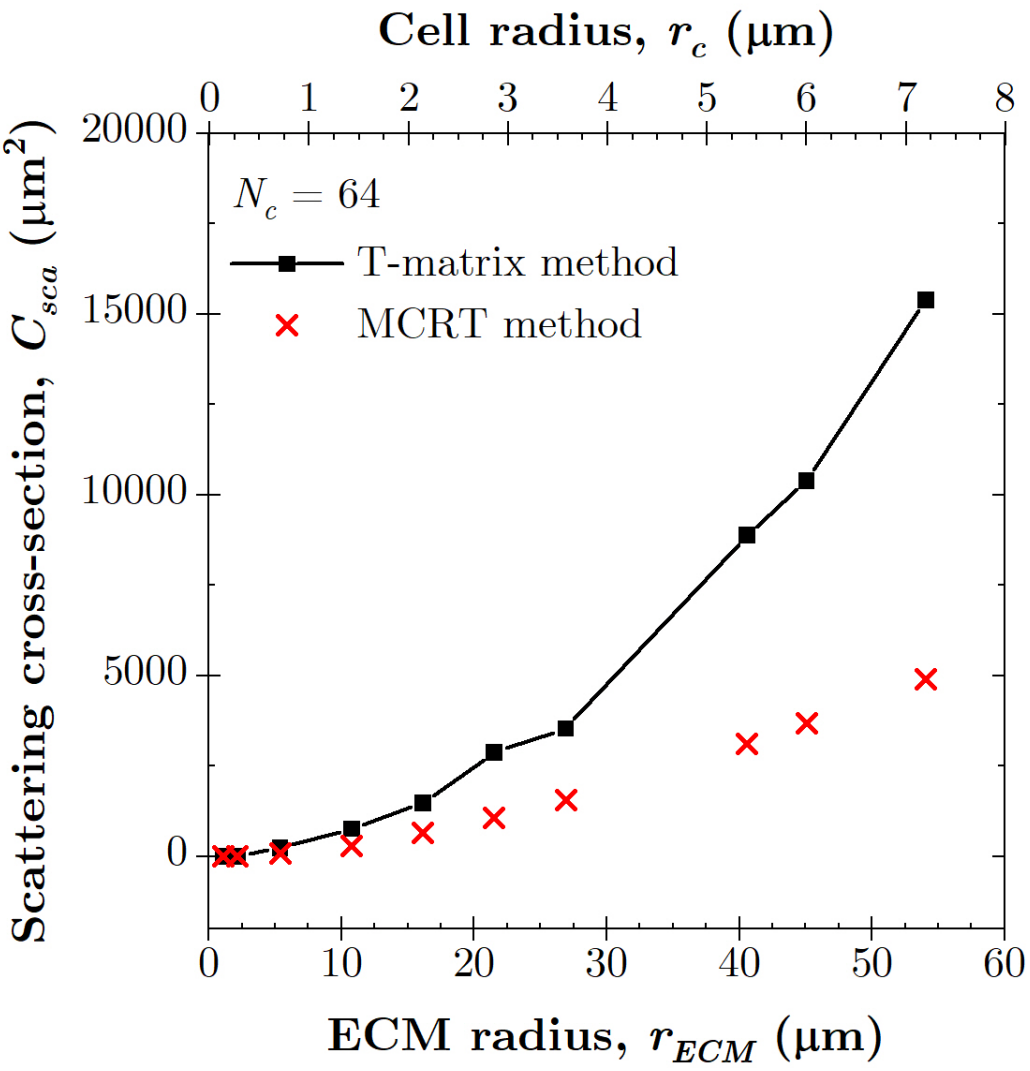

Figure C.3: Scattering cross-section C_{sca} of an ensemble of 64 cells predicted by the Monte Carlo ray tracing (MCRT) method and the superposition T-matrix as a function of ECM r_{ECM} and cell r_c radius.

APPENDIX D

Supplementary Materials for Chapter 6

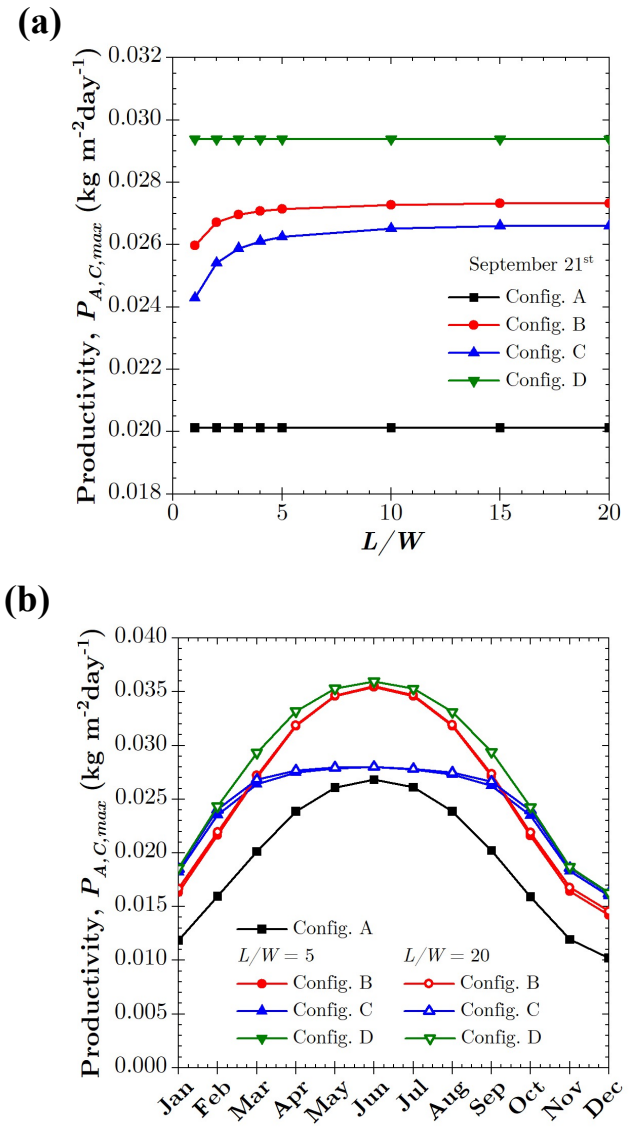

Figure D.1: (a) Maximum daily culture-area-based biomass productivity $P_{A,C,max}$ as a function of length-to-height ratio L/W on September 21st and (b) maximum daily culture-area-based biomass productivity $P_{A,C,max}$ over one year for Configurations A-D with L/W equal to 5 and 20 for raceway ponds located in Los Angeles, CA.

REFERENCES

[1] R. K. Pachauri and L. A. Meyer (eds.), "Climate Change 2014: Synthesis Report. Contribution of Working Groups I, II and III to the Fifth Assessment Report of the Intergovernmental Panel on Climate Change", Tech. Rep., IPCC, Geneva, Switzerland, 2014.

[2] J. Matos, C. Cardoso, N. M. Bandarra, and C. Afonso, "Microalgae as healthy ingredients for functional food: A review", *Food and Function*, vol. 8, no. 8, pp. 2672–2685, 2017.

[3] Y. Chisti, "Biodiesel from microalgae", *Biotechnology Advances*, vol. 25, no. 3, pp. 294–306, 2007.

[4] D. Jha, V. Jain, B. Sharma, A. Kant, and V. K. Garlapati, "Microalgae-based pharmaceuticals and nutraceuticals: An emerging field with immense market potential", *ChemBioEng Reviews*, vol. 4, no. 4, pp. 257–272, 2017.

[5] K. W. Chew, J. Y. Yap, P. L. Show, N. H Suan, J. C. Juan, T. C. Ling, D. J. Lee, and J. S. Chang, "Microalgae biorefinery: High value products perspectives", *Bioresource Technology*, vol. 229, pp. 53–62, 2017.

[6] Y. Shen, W. Yuan, Z. Pei, and E. Mao, "Culture of microalga *Botryococcus* in livestock wastewater", *Transactions of the ASABE*, vol. 51, no. 4, pp. 1395–1400, 2008.

[7] J. Y. An, S. J. Sim, J. S. Lee, and B. W. Kim, "Hydrocarbon production from secondarily treated piggery wastewater by the green alga *Botryococcus braunii*", *Journal of Applied Phycology*, vol. 15, no. 2-3, pp. 185–191, 2003.

[8] T. M. Mata, A. A. Martins, and N. S. Caetano, "Microalgae for biodiesel production and other applications: A review", *Renewable and Sustainable Energy Reviews*, vol. 14, no. 1, pp. 217–232, 2010.

[9] E. B. Sydney, W. Sturm, J. C. de Carvalho, V. Thomaz-Soccol, C. Larroche, A. Pandey, and C. R. Soccol, "Potential carbon dioxide fixation by industrially important microalgae", *Bioresource Technology*, vol. 101, no. 15, pp. 5892–5896, 2010.

[10] M. A. Borowitzka, "High-value products from microalgae-their development and commercialisation", *Journal of Applied Phycology*, vol. 25, no. 3, pp. 743–756, 2013.

[11] O. Pulz and W. Gross, "Valuable products from biotechnology of microalgae", *Applied Microbiology and Biotechnology*, vol. 65, no. 6, pp. 635–648, 2004.

[12] H. Chowdhury, B. Loganathan, I. Mustary, F. Alam, and S. M. A. Mobin, "Algae for Biofuels: The Third Generation of Feedstock", in *Second and Third Generation of Feedstocks: The Evolution of Biofuels*, A. Basile and F. Dalena, Eds., chapter 12, pp. 323–344. Elsevier Inc., Cambridge, MA, 2019.

[13] F. Zhang, M. Prigge, F. Beyrière, S. P. Tsunoda, J. Mattis, O. Yizhar, P. Hegemann, and K. Deisseroth, "Red-shifted optogenetic excitation: A tool for fast neural control derived from *Volvox carteri*", *Nature Neuroscience*, vol. 11, no. 6, pp. 631–633, 2008.

[14] L. G. Lowder and S. K. Herbert, "Heterologous expression of a *Volvox* cell adhesion molecule causes flocculation in *Chlamydomonas reinhardtii*", *Journal of Applied Phycology*, vol. 27, no. 2, pp. 721–731, 2015.

[15] C. J. Tien, D. C. Sigee, and K. N. White, "Copper adsorption kinetics of cultured algal cells and freshwater phytoplankton with emphasis on cell surface characteristics", *Journal of Applied Phycology*, vol. 17, no. 5, pp. 379–389, 2005.

[16] B. Podola and M. Melkonian, "Selective real-time herbicide monitoring by an array chip biosensor employing diverse microalgae", *Journal of Applied Phycology*, vol. 17, no. 3, pp. 261–271, 2005.

[17] A. R. Rao, R. Sarada, V. Baskaran, and G. A. Ravishankar, "Antioxidant activity of *Botryococcus braunii* extract elucidated in vitro models", *Journal of Agricultural and Food Chemistry*, vol. 54, no. 13, pp. 4593–4599, 2006.

[18] A. R. Rao, A. H. Reddy, and S. M. Aradhya, "Antibacterial properties of *Spirulina platensis*, *Haematococcus pluvialis*, *Botryococcus braunii* micro algal extracts", *Current Trends in Biotechnology and Pharmacy*, vol. 4, no. 3, pp. 809–819, 2010.

[19] L. Custódio, F. Soares, H. Pereira, M. J. Rodrigues, L. Barreira, A. P. Rauter, F. Alberício, and J. Varela, "*Botryococcus braunii* and *Nannochloropsis oculata* extracts inhibit cholinesterases and protect human dopaminergic SH-SY5Y cells from H_2O_2-induced cytotoxicity", *Journal of Applied Phycology*, vol. 27, no. 2, pp. 839–848, 2015.

[20] A. Banerjee, R. Sharma, Y. Chisti, and U. C. Banerjee, "*Botryococcus braunii*: A renewable source of hydrocarbons and other chemicals", *Critical Reviews in Biotechnology*, vol. 22, no. 3, pp. 245–279, 2002.

[21] J. Jin, C. Dupré, J. Legrand, and D. Grizeau, "Extracellular hydrocarbon and intracellular lipid accumulation are related to nutrient-sufficient conditions in pH-controlled chemostat cultures of the microalga *Botryococcus braunii* SAG 30.81", *Algal Research*, vol. 17, pp. 244–252, 2016.

[22] C. Largeau, E. Casadevall, C. Berkaloff, and P. Dhamelincourt, "Sites of accumulation and composition of hydrocarbons in *Botryococcus braunii*", *Phytochemistry*, vol. 19, no. 6, pp. 1043–1051, 1980.

[23] J. Jin, C. Dupré, K. Yoneda, M. M. Watanabe, J. Legrand, and D. Grizeau, "Characteristics of extracellular hydrocarbon-rich microalga *Botryococcus braunii* for biofuels production: Recent advances and opportunities", *Process Biochemistry*, vol. 51, no. 11, pp. 1866–1875, 2016.

[24] M. Kanda, A. Nakamura, H. Iwamoto, and S. Konosu, "Lipid composition of a green alga, *Botryococcus braunii*", *Agricultural and Biological Chemistry*, vol. 51, no. 2, pp. 493–498, 1987.

[25] B. Moutel, M. André, D. Kucma, J. Legrand, D. Grizeau, J. Pruvost, and O. Gonçalves, "Assessing the biofuel production potential of *Botryococcus braunii* strains by sensitive rapid qualitative chemotyping using chemometrically-assisted gas chromatography-mass spectrometry", *Algal Research*, vol. 11, pp. 33–42, 2015.

[26] B. Sadeghin, M. H. Sarrafzadeh, J. Jin, C. Dupré, M. M. Watanabe, J. Legrand, and D. Grizeau, "Variation of fatty acids composition in the hydrocarbon producer *Botryococcus braunii* BOT 22", *Biomass and Bioenergy*, vol. 119, pp. 456–461, 2018.

[27] H. Watanabe, D. Li, Y. Nakagawa, K. Tomishige, K. Kaya, and M. M. Watanabe, "Characterization of oil-extracted residue biomass of *Botryococcus braunii* as a biofuel feedstock and its pyrolytic behavior", *Applied Energy*, vol. 132, pp. 475–484, 2014.

[28] B. Ke, *Photosynthesis: Photobiochemistry and Photobiophysics*, Kluwer Academic Publishers, New York, NY, 2001.

[29] J. Pruvost, *Cultivation of Algae in Photobioreactors for Biodiesel Production*, Academic Press, San Diego, CA, 2 edition, 2019.

[30] J. Pruvost and J.-F. Cornet, "Knowledge models for the engineering and optimization of photobioreactors", in *Microalgal Biotechnology: Potential and Production*, C. Posten and W. Christian, Eds., chapter 10, pp. 181–224. De Gruyter, Berlin, DE, 2012.

[31] G. Torzillo and A. Vonshak, "Environmental Stress Physiology with Reference to Mass Cultures", in *Handbook of Microalgal Culture: Applied Phycology and Biotechnology*, A. Richmond and Q. Hu, Eds., chapter 6, pp. 90–113. Blackwell Publishing Ltd, Cornwall, UK, 2 edition, 2013.

[32] M. R. Tredici, "Mass Production of Microalgae: Photobioreactors", in *Handbook of Microalgal Culture: Biotechnology and Applied Phycology*, A. Richmond, Ed., chapter 9, pp. 178–214. Blackwell Publishing Ltd, Cornwall, UK, 2004.

[33] J. Pruvost, J.-F. Cornet, and L. Pilon, "Large-scale production of algal biomass: photobioreactors", in *Algae Biotechnology: Products and Processes*, F. Bux and Y. Chisti, Eds., pp. 41–66. Springer International Publishing, Switzerland, 2016.

[34] J. Pruvost, F. Le Borgne, A. Artu, and J. Legrand, "Development of a thin-film solar photobioreactor with high biomass volumetric productivity (AlgoFilm©) based on process intensification principles", *Algal Research*, vol. 21, pp. 120–137, 2017.

[35] Green Prophet, "Seambiotic Makes Algae for Food and Biofuel", https://www.greenprophet.com/2011/09/seabiotic-biofuel-algae/.

[36] J. U. Grobbelaar, "Factors governing algal growth in photobioreactors: The "open" versus "closed" debate", *Journal of Applied Phycology*, vol. 21, no. 5, pp. 489–492, 2009.

[37] E. W. Tow, "The antireflective potential of dropwise condensation", *Journal of the Optical Society of America A*, vol. 31, no. 3, pp. 493–499, 2014.

[38] K. Zhu and L. Pilon, "Transmittance of semitransparent windows with non-absorbing cap-shaped droplets condensed on their backside", *Journal of Quantitative Spectroscopy and Radiative Transfer*, vol. 194, pp. 98–107, 2017.

[39] E. Simsek, K. Zhu, G. N. Kashanchi, M. J. Williams, T. Galy, M. Marszewski, S. H. Tolbert, and L. Pilon, "Light transfer through semi-transparent glass panes supporting pendant droplets", *Journal of Quantitative Spectroscopy and Radiative Transfer*, 2020 (under review).

[40] B. J. Briscoe and K. P. Galvin, "The effect of surface fog on the transmittance of light", *Solar Energy*, vol. 46, no. 4, pp. 191–197, 1991.

[41] I. V. Pollet and J. G. Pieters, "Condensation and radiation transmittance of greenhouse cladding materials, Part 2: Results for a complete condensation cycle", *Journal of Agricultural and Engineering Research*, vol. 75, no. 1, pp. 65–72, 2000.

[42] M. F. Modest, *Radiative Heat Transfer*, Elsevier Inc., Oxford, UK, 3rd edition, 2013.

[43] A. Souliès, J. Legrand, H. Marec, J. Pruvost, C. Castelain, T. Burghelea, and J.-F. Cornet, "Investigation and modeling of the effects of light spectrum and incident angle on the growth of *Chlorella vulgaris* in photobioreactors", *Biotechnology Progress*, vol. 32, no. 2, pp. 247–261, 2016.

[44] K. Zhu, S. Li, and L. Pilon, "Light transfer through windows with external condensation", *Journal of Quantitative Spectroscopy and Radiative Transfer*, vol. 208, pp. 164–171, 2018.

[45] K. Zhu and L. Pilon, "Transmittance of semitransparent windows with absorbing cap-shaped droplets condensed on their backside", *Journal of Quantitative Spectroscopy and Radiative Transfer*, vol. 201, pp. 53–63, 2017.

[46] K. Zhu and L. Pilon, "Transmittance of semitransparent windows with non-absorbing cap-shaped droplets condensed on their backside", *Journal of Quantitative Spectroscopy and Radiative Transfer*, vol. 201, pp. 53–63, 2017.

[47] R. Kandilian, A. Soulies, J. Pruvost, B. Rousseau, J. Legrand, and L. Pilon, "Simple method for measuring the spectral absorption cross-section of microalgae", *Chemical Engineering Science*, vol. 146, pp. 357–368, 2016.

[48] E. Lee, J. Pruvost, X. He, R. Munipalli, and L. Pilon, "Design tool and guidelines for outdoor photobioreactors", *Chemical Engineering Science*, vol. 106, pp. 18–29, 2014.

[49] K. H. Mangi, Z. Larbi, J. Legrand, J. Pruvost, and E. K. Si-Ahmed, "Passive thermal regulation approach for Algofilm© photobioreactor through phase change", *Chemical Engineering Research and Design*, vol. 168, pp. 411–425, 2021.

[50] J. Hoeniges, K. Zhu, J. Pruvost, J. Legrand, and L. Pilon, "Impact of dropwise condensation on the biomass production rate in covered raceway ponds", *Energies*, vol. 14, no. 2, pp. 268, 2021.

[51] I. V. Pollet and J. G. Pieters, "Condensation and radiation transmittance of greenhouse cladding materials, Part 1: laboratory measuring unit and performance", *Journal of Agricultural and Engineering Research*, vol. 74, no. 4, pp. 369–377, 1999.

[52] I. V. Pollet and J. G. Pieters, "Condensation and radiation transmittance of greenhouse cladding materials, Part 3: Results for glass plates and plastic films", *Journal of Agricultural and Engineering Research*, vol. 77, no. 4, pp. 419–428, 2000.

[53] I. V. Pollet, J. G. Pieters, J. Deltour, and R. Verschoore, "Diffusion of radiation transmitted through dry and condensate covered transmitting materials", *Solar Energy Materials and Solar Cells*, vol. 86, no. 2, pp. 177–196, 2005.

[54] R. Bhardwaj, M. V. ten Kortenaar, and R. F. Mudde, "Influence of condensation surface on solar distillation", *Desalination*, vol. 326, pp. 37–45, 2013.

[55] J. G. Pieters, J. M. Deltour, and M. J. Debruyckere, "Light transmission through condensation on glass and polyethylene", *Agricultural and Forest Meteorology*, vol. 85, no. 1-2, pp. 51–62, 1997.

[56] Y. Huang, C. Feng, J. Hoeniges, K. Zhu, and L. Pilon, "Bidirectional transmittance of transparent windows with external or backside condensation of nonabsorbing cap-shaped droplets", *Journal of Quantitative Spectroscopy and Radiative Transfer*, vol. 251, pp. 107039, 2020.

[57] P. G. De Gennes and D. Brochard-Wyart, F. Quéré, *Capillarity and Wetting Phenomena: Drops, Bubbles, Pearls, Waves*, Springer Science & Business Media, New York, NY, 2013.

[58] J. G. Pieters, J. M. Deltour, and M. J. Debruyckere, "Experimental determination of the geometry of real drops on transparent materials", *Journal de Physique III*, vol. 6, no. 7, pp. 975–989, 1996.

[59] E. Simsek, K. Zhu, G. N. Kashanchi, M. J. Williams, T. Galy, M. Marszewski, S. H. Tolbert, and L. Pilon, "Light transfer through semi-transparent glass panes supporting pendant droplets", *Journal of Quantitative Spectroscopy and Radiative Transfer*, vol. 261, no. 107493, 2021.

[60] K. A. Brakke, "The Surface Evolver", *Experimental Mathematics*, vol. 1, no. 2, pp. 141–165, 1992.

[61] G. Bhutani, K. Muralidhar, and S. Khandekar, "Determination of apparent contact angle and shape of a static pendant drop on a physically textured inclined surface", *Interfacial Phenomena and Heat Transfer*, vol. 1, no. 1, pp. 29–49, 2013.

[62] A. I. El Sherbini and A. M. Jacobi, "Liquid drops on vertical and inclined surfaces: I. An experimental study of drop geometry", *Journal of Colloid and Interface Science*, vol. 273, no. 2, pp. 556–565, 2004.

[63] C. K. Hsieh and A. K. Rajvanshi, "The effect of dropwise condensation on glass solar properties", *Solar Energy*, vol. 19, no. 4, pp. 389–393, 1977.

[64] I. V. Pollet and J. G. Pieters, "PAR transmittances of dry and condensate covered glass and plastic greenhouse cladding", *Agricultural and Forest Meteorology*, vol. 110, no. 4, pp. 285–298, 2002.

[65] M. Rubin, "Optical properties of soda lime silica glasses", *Solar Energy Materials*, vol. 12, no. 4, pp. 275–288, 1985.

[66] G. M. Hale and M. R. Querry, "Optical constants of water in the 200-nm to 200-μm wavelength region", *Applied Optics*, vol. 12, no. 3, pp. 555–563, 1973.

[67] L. Pottier, J. Pruvost, J. Deremetz, J.-F. Cornet, J. Legrand, and C.-G. Dussap, "A fully predictive model for one-dimensional light attenuation by *Chlamydomonas reinhardtii* in a torus photobioreactor", *Biotechnology and Bioengineering*, vol. 91, no. 5, pp. 569–582, 2005.

[68] J. F. Cornet, C. G. Dussap, and G. Dubertret, "A structured model for simulation of cultures of the cyanobacterium *Spirulina platensis* in photobioreactors: I. Coupling between light transfer and growth kinetics", *Biotechnology and Bioengineering*, vol. 40, no. 7, pp. 817–825, 1992.

[69] J.-F. Cornet, C. G. Dussap, J. B. Gros, C. Binois, and C. Lasseur, "A simplified monodimensional approach for modeling coupling between radiant light transfer and growth kinetics in photobioreactors", *Chemical Engineering Science*, vol. 50, no. 9, pp. 1489–1500, 1995.

[70] I. Dunn, E. Heinzle, J. Ingham, and J. Prenosil, *Biological Reaction Engineering: Dynamic Modelling Fundamentals with Simulation Examples*, Wiley-VCH, Weinheim, Germany, 2nd edition, 2003.

[71] H. Takache, J. Pruvost, and J.-F. Cornet, "Kinetic modeling of the photosynthetic growth of *Chlamydomonas reinhardtii* in a photobioreactor", *Biotechnology Progress*, vol. 28, pp. 681–692, 2012.

[72] K.J. Versyck, J.E. Claes, and J.-F. van Impe, "Practical identification of unstructured growth kinetics by application of optimal experimental design", *Biotechnology Progress*, vol. 13, no. 5, pp. 524–531, 1997.

[73] S. Fouchard, J. Pruvost, B. Degrenne, M. Titica, and J. Legrand, "Kinetic modeling of light limitation and sulfur deprivation effects in the induction of hydrogen production with *Chlamydomonas reinhardtii*: Part I. Model development and parameter identification", *Biotechnology and Bioengineering*, vol. 102, no. 1, pp. 232–245, 2009.

[74] J.-F. Cornet and C.-G. Dussap, "A simple and reliable formula for assessment of maximum volumetric productivities in photobioreactors", *Biotechnology Progress*, vol. 25, no. 2, pp. 424–435, 2009.

[75] J. Pruvost, G. Van Vooren, B. Le Gouic, A. Couzinet-Mossion, and J. Legrand, "Systematic investigation of biomass and lipid productivity by microalgae in photobioreactors for biodiesel application", *Bioresource Technology*, vol. 102, no. 1, pp. 150–158, 2011.

[76] P. M. Slegers, R. H. Wijffels, G. van Straten, and A. J.B. van Boxtel, "Design scenarios for flat panel photobioreactors", *Applied Energy*, vol. 88, no. 10, pp. 3342–3353, 2011.

[77] J.R. Howell, M.P. Mengüç, and R. Siegel, *Thermal Radiation Heat Transfer*, CRC Press, Taylor and Francis, Boca Raton, FL, 6th edition, 2016.

[78] R. Kandilian, J. Pruvost, A. Artu, C. Lemasson, J. Legrand, and L. Pilon, "Comparison of experimentally and theoretically determined radiation characteristics of photosynthetic microorganisms", *Journal of Quantitative Spectroscopy and Radiative Transfer*, vol. 175, pp. 30–45, 2016.

[79] C. Gueymard, "Simple model of the atmospheric radiative transfer of sunshine (smarts)", http://rredc.nrel.gov/solar/models/SMARTS, Version 2.9.5, 2005.

[80] B. Figgis, A. Nouviaire, Y. Wubulikasimu, W. Javed, B. Guo, A. Ait-Mokhtar, R. Belarbi, S. Ahzi, Y. Rémond, and A. Ennaoui, "Investigation of factors affecting condensation on soiled PV modules", *Solar Energy*, vol. 159, pp. 488–500, 2018.

[81] T. L. Weiss, R. Roth, C. Goodson, S. Vitha, I. Black, P. Azadi, J. Rusch, A. Holzenburg, T. P. Devarenne, and U. Goodenough, "Colony organization in the green alga *Botryococcus braunii* (Race B) is specified by a complex extracellular matrix", *Eukaryotic Cell*, vol. 11, no. 12, pp. 1424–1440, 2012.

[82] L. Liu, M. I. Mishchenko, and P. W. Arnott, "A study of radiative properties of fractal soot aggregates using the superposition T-matrix method", *Journal of Quantitative Spectroscopy and Radiative Transfer*, vol. 109, no. 15, pp. 2656–2663, 2008.

[83] C. M. Sorensen, "Light scattering by fractal aggregates: A review", *Aerosol Science and Technology*, vol. 35, no. 2, pp. 648–687, 2001.

[84] R. Kandilian, R. L. Heng, and L. Pilon, "Absorption and scattering by fractal aggregates and by their equivalent coated spheres", *Journal of Quantitative Spectroscopy and Radiative Transfer*, vol. 151, pp. 310–326, 2015.

[85] G. W. Mulholland, C. F. Bohren, and K. A. Fuller, "Light Scattering by Agglomerates: Coupled Electric and Magnetic Dipole Method", *Langmuir*, vol. 10, no. 8, pp. 2533–2546, 1994.

[86] L. Liu and M. I. Mishchenko, "Scattering and radiative properties of complex soot and soot-containing aggregate particles", *Journal of Quantitative Spectroscopy and Radiative Transfer*, vol. 106, pp. 262–273, 2007.

[87] F. Liu, D. R. Snelling, and G. J. Smallwood, "Effects of the fractal prefactor on the optical properties of fractal soot aggregates", in *Proceedings of the ASME Micro/Nanoscale Heat and Mass Transfer International Conference 2009*, Shanghai, China, 2009, vol. 2, pp. 363–371, ASME.

[88] F. Liu, C. Wong, D. R. Snelling, and G. J. Smallwood, "Investigation of absorption and scattering properties of soot aggregates of different fractal dimension at 532 nm Using RDG and GMM", *Aerosol Science and Technology*, vol. 47, no. 12, pp. 1393–1405, 2013.

[89] B. Moutel, O. Gonçalves, F. Le Grand, M. Long, P. Soudant, J. Legrand, D. Grizeau, and J. Pruvost, "Development of a screening procedure for the characterization of *Botryococcus braunii* strains for biofuel application", *Process Biochemistry*, vol. 51, no. 11, pp. 1855–1865, 2016.

[90] K. C. Díaz Bayona and L. A. Garcés, "Effect of different media on exopolysaccharide and biomass production by the green microalga *Botryococcus braunii*", *Journal of Applied Phycology*, vol. 26, no. 5, pp. 2087–2095, 2014.

[91] K. Zhang and E Kojima, "Effect of light intensity on colony size of microalga *Botryococcus braunii* in bubble column photobioreactors", *Journal of Fermentation and Bioengineering*, vol. 86, no. 6, pp. 573–576, 1998.

[92] B. Moutel, Etude de la mircoalgue *Botryococcus braunii* en vue d'une application aux bioaérocarburants, PhD thesis Université de Nantes, Nantes, France, 2014 (in French).

[93] R. J. Ritchie, "Consistent sets of spectrophotometric chlorophyll equations for acetone, methanol and ethanol solvents", *Photosynthesis Research*, vol. 89, no. 1, pp. 27–41, 2006.

[94] O. Blifernez-Klassen, S. Chaudhari, V. Klassen, R. Wördenweber, T. Steffens, D. Cholewa, K. Niehaus, J. Kalinowski, and O. Kruse, "Metabolic survey of *Botryococcus braunii*: Impact of the physiological state on product formation", *PLoS ONE*, vol. 13, no. 6, pp. 1–23, 2018.

[95] R. G. Barlow, J. Aiken, G. F. Moore, P. M. Holligan, and S. Lavender, "Pigment adaptations in surface phytoplankton along the eastern boundary of the Atlantic Ocean", *Marine Ecology Progress Series*, vol. 281, pp. 13–26, 2004.

[96] J. D. H. Strickland and T. R. Parsons, *A Practical Handbook of Seawater Analysis*, Fisheries Research Board of Canada, Ottawa, 2nd edition, 1968.

[97] M. I. Mishchenko and L. D. Travis, "Light scattering by polydispersions of randomly oriented spheroids with sizes comparable to wavelengths of observation", *Applied Optics*, vol. 33, no. 30, pp. 7206, 1994.

[98] L. Pilon, H. Berberoğlu, and R. Kandilian, "Radiation transfer in photobiological carbon dioxide fixation and fuel production by microalgae", *Journal of Quantitative Spectroscopy and Radiative Transfer*, vol. 112, no. 17, pp. 2639–2660, 2011.

[99] L. Pilon and R. Kandilian, "Interaction between light and photosynthetic microorganisms", in *Advances in Chemical Engineering*, J. Legrand, Ed., vol. 48, chapter 2, pp. 107–149. Academic Press, Cambridge, MA, 2016.

[100] H. Berberoğlu, P. S. Gomez, and L. Pilon, "Radiation characteristics of *Botryococcus braunii*, *Chlorococcum littorale*, and *Chlorella sp.* used for CO_2 fixation and biofuel production", *Journal of Quantitative Spectroscopy and Radiative Transfer*, vol. 110, no. 17, pp. 1879–1893, 2009.

[101] E. Lee, R. L. Heng, and L. Pilon, "Spectral optical properties of selected photosynthetic microalgae producing biofuels", *Journal of Quantitative Spectroscopy and Radiative Transfer*, vol. 114, pp. 122–135, 2013.

[102] R. Kandilian, E. Lee, and L. Pilon, "Radiation and optical properties of *Nannochloropsis oculata* grown under different irradiances and spectra", *Bioresource Technology*, vol. 137, pp. 63–73, 2013.

[103] R. Kandilian, J. Pruvost, J. Legrand, and L. Pilon, "Influence of light absorption rate by *Nannochloropsis oculata* on triglyceride production during nitrogen starvation", *Bioresource Technology*, vol. 163, pp. 308–319, 2014.

[104] A. Bhowmik and L. Pilon, "Can spherical eukaryotic microalgae cells be treated as optically homogeneous?", *Journal of the Optical Society of America A*, vol. 33, no. 8, pp. 1495–1503, 2016.

[105] I. D. Nikolov and C. D. Ivanov, "Optical plastic refractive measurements in the visible and the near-infrared regions", *Applied Optics*, vol. 39, no. 13, pp. 2067, 2000.

[106] O. Zhernovaya, O. Sydoruk, V. Tuchin, and A. Douplik, "The refractive index of human hemoglobin in the visible range", *Physics in Medicine and Biology*, vol. 56, no. 13, pp. 4013–4021, 2011.

[107] H.C. Van De Hulst, *Light Scattering by Small Particles*, Dover Publications, Inc., Mineola, NY, 5th edition, 1981.

[108] R. R. Bidigare, M. E. Ondrusek, J. H. Morrow, and D. A. Kiefer, "In-vivo absorption properties of algal pigments", in *SPIE Proceedings Vol. 1302*, R. W. Spinrad, Ed., Orlando, FL, 1990, pp. 290 – 302, Ocean Optics X.

[109] G. A. Jackson, R. Maffione, D. K. Costello, A. L. Alldredge, B. E. Logan, and H. G. Dam, "Particle size spectra between 1 μm and 1 cm at Monterey Bay determined using multiple instruments", *Deep-Sea Research Part I: Oceanographic Research Papers*, vol. 44, no. 11, pp. 1739–1767, 1997.

[110] K. Skorupski, J. Mroczka, T. Wriedt, and N. Riefler, "A fast and accurate implementation of tunable algorithms used for generation of fractal-like aggregate models", *Physica A: Statistical Mechanics and its Applications*, vol. 404, pp. 106–117, 2014.

[111] A. Semechko, "Suite of functions to perform uniform sampling of a sphere", https://github.com/AntonSemechko/S2-Sampling-Toolbox, Version 1.6.0.0, 2012.

[112] M. Satou, H. Yamaguchi, T. Murai, S. Yokoyama, and Y. Sanada, "A method of estimating the refractive index of hydrocarbons in coal derived liquids by a group contribution method", *Journal of The Japan Petroleum Institute*, vol. 35, no. 6, pp. 466–473, 1992.

[113] D. W. Mackowski and M. I. Mishchenko, "A multiple sphere T-matrix Fortran code for use on parallel computer clusters", *Journal of Quantitative Spectroscopy and Radiative Transfer*, vol. 112, no. 13, pp. 2182–2192, 2011.

[114] H. Berberoğlu, L. Pilon, and A. Melis, "Radiation characteristics of *Chlamydomonas reinhardtii* CC125 and its truncated chlorophyll antenna transformants *tla1, tlaX* and *tla1-CW+*", *International Journal of Hydrogen Energy*, vol. 33, no. 22, pp. 6467–6483, 2008.

[115] L. Barsanti and P. Gualtieri, *Algae: Anatomy, Biochemistry, and Biotechnology*, CRC Press, Boca Raton, FL, 2014.

[116] I. Nishii and S. M. Miller, "Volvox: Simple steps to developmental complexity?", *Current Opinion in Plant Biology*, vol. 13, no. 6, pp. 646–653, 2010.

[117] J. Beardall, D. Allen, J. Bragg, Z. V. Finkel, K. J. Flynn, A. Quigg, T. A. V. Rees, A. Richardson, and J. A. Raven, "Allometry and stoichiometry of unicellular, colonial and multicellular phytoplankton", *New Phytologist*, vol. 181, no. 2, pp. 295–309, 2008.

[118] S. F. Gilbert, *Developmental Biology*, Sinauer Associates, Sunderland, MA, 2014.

[119] C. B. Lopez, Q. Dortch, E. B. Jewett, and D Garrison, "Scientific assessment of marine harmful algal blooms", Tech. Rep., Washington D. C., 2008.

[120] H. W. Paerl, "Nuisance phytoplankton blooms in coastal, estuarine, and inland waters", *Limnology and Oceanography*, vol. 33, pp. 823–843, 1988.

[121] J. Kiss, "Investigation of the water blooms of *Eudorina elegans* in the dead-arm of the river Tisza at the community Mártély", *Tiscia (Szeged)*, vol. 12, pp. 37–47, 1977.

[122] P. Znachor and J. Jezberová, "The occurrence of a bloom-forming green alga *Pleodorina indica* (*Volvocales*) in the downstream reach of the River Malše (Czech Republic)", *Hydrobiologia*, vol. 541, pp. 221–228, 2005.

[123] M. I. Gladyshev, N. N. Sushchik, G. S. Kalachova, and L. A. Shchur, "The effect of algal blooms on the disappearance of phenol in a small forest pond", *Water Research*, vol. 32, no. 9, pp. 2769–2775, 1998.

[124] C. N. Sawyer, "The need for nutrient control", *Journal of the Water Pollution Control Federation*, vol. 40, no. 3, pp. 363–370, 1968.

[125] E. A. Sigworth, "Control of odor and taste in water supplies", *American Water Works Association*, vol. 49, no. 12, pp. 1507–1521, 1957.

[126] D. Blondeau-Patissier, J. F. R. Gower, A. G. Dekker, S. R. Phinn, and V. E. Brando, "A review of ocean color remote sensing methods and statistical techniques for the detection, mapping and analysis of phytoplankton blooms in coastal and open oceans", *Progress in Oceanography*, vol. 123, pp. 123–144, 2014.

[127] S. C. J. Palmer, D. Odermatt, P. D. Hunter, C. Brockmann, M. Présing, H. Balzter, and V. R. Tóth, "Satellite remote sensing of phytoplankton phenology in Lake Balaton using 10 years of MERIS observations", *Remote Sensing of Environment*, vol. 158, pp. 441–452, 2015.

[128] T. Kutser, "Quantitative detection of chlorophyll in cyanobacterial blooms by satellite remote sensing", *Limnology and Oceanography*, vol. 49, no. 6, pp. 2179–2189, 2004.

[129] S. Sathyendranath, G. Cota, V. Stuart, H. Maass, and T. Platt, "Remote sensing of phytoplankton pigments: A comparison of empirical and theoretical approaches", *International Journal of Remote Sensing*, vol. 22, no. 2-3, pp. 249–273, 2001.

[130] G. R. Jonasz, M. Fournier, *Light Scattering by Particles in Water: Theoretical and Experimental Foundations*, Academic Press, San Diego, CA, 2007.

[131] A. Bricaud, A. L. Bédhomme, and A. Morel, "Optical properties of diverse phytoplanktonic species: Experimental results and theoretical interpretation", *Journal of Plankton Research*, vol. 10, no. 5, pp. 851–873, 1988.

[132] H. Berberoğlu and L. Pilon, "Experimental measurements of the radiation characteristics of *Anabaena variabilis* ATCC 29413-U and *Rhodobacter sphaeroides* ATCC 49419", *International Journal of Hydrogen Energy*, vol. 32, no. 18, pp. 4772–4785, 2007.

[133] C. Y. Ma, J. M. Zhao, L. H. Liu, L. Zhang, X. C. Li, and B. C. Jiang, "GPU-accelerated inverse identification of radiative properties of particle suspensions in liquid by the Monte Carlo method", *Journal of Quantitative Spectroscopy and Radiative Transfer*, vol. 172, pp. 146–159, 2016.

[134] A. Bricaud and A. Morel, "Light attenuation and scattering by phytoplanktonic cells: a theoretical modeling", *Applied Optics*, vol. 25, no. 4, pp. 571, 1986.

[135] D. Stramski, A. Bricaud, and A. Morel, "Modeling the inherent optical properties of the ocean based on the detailed composition of the planktonic community", *Applied Optics*, vol. 40, no. 18, pp. 2929, 2001.

[136] E. Lee and L. Pilon, "Absorption and scattering by long and randomly oriented linear chains of spheres", *Journal of the Optical Society of America A*, vol. 30, no. 9, pp. 1892–1900, 2013.

[137] R. L. Heng, K. C. Sy, and L. Pilon, "Absorption and scattering by bispheres, quadspheres, and circular rings of spheres and their equivalent coated spheres", *Journal of the Optical Society of America A*, vol. 32, no. 1, pp. 46, 2015.

[138] J. Hoeniges, R. Kandilian, C. Zhang, J. Pruvost, J. Legrand, D. Grizeau, and L. Pilon, "Effect of colony formation on light absorption by *Botryococcus braunii*", *Algal Research*, vol. 50, no. June, pp. 101985, 2020.

[139] L. Liu, M. I. Mishchenko, S. Menon, A. Macke, and A. A. Lacis, "The effect of black carbon on scattering and absorption of solar radiation by cloud droplets", *Journal of Quantitative Spectroscopy and Radiative Transfer*, vol. 74, no. 2, pp. 195–204, 2002.

[140] J. Charon, S. Blanco, J.-F. Cornet, J. Dauchet, M. El Hafi, R. Fournier, M. K. Abboud, and S. Weitz, "Monte Carlo implementation of Schiff's approximation for estimating radiative properties of homogeneous, simple-shaped and optically soft particles: Application to photosynthetic micro-organisms", *Journal of Quantitative Spectroscopy and Radiative Transfer*, vol. 172, pp. 3–23, 2016.

[141] H. Li, C. Liu, L. Bi, P. Yang, and G. W. Kattawar, "Numerical accuracy of "equivalent" spherical approximations for computing ensemble-averaged scattering properties of fractal soot aggregates", *Journal of Quantitative Spectroscopy and Radiative Transfer*, vol. 111, no. 14, pp. 2127–2132, 2010.

[142] M. F. Iskander, H. Y. Chen, and J. E. Penner, "Optical scattering and absorption by branched chains of aerosols", *Applied Optics*, vol. 28, no. 15, pp. 3083, 1989.

[143] Z. W. Cui, Y. P. Han, and C. Y. Li, "Characterization of the light scattering by ensembles of randomly distributed soot aggregates", *Journal of Quantitative Spectroscopy and Radiative Transfer*, vol. 112, no. 17, pp. 2722–2732, 2011.

[144] H. Hirose and T. Yamagishi, *Illustrations of the Japanese Freshwater Algae*, Uchida Rokakuho Pub (in Japanese), Tokyo, Japan, 1977.

[145] M. M. Brysk and M. J. Chrispeels, "Isolation of partial characterization of a hydroxyproline-rich cell wall glycoprotein and its cytoplasmic precursor", *Biochimica et Biophysica Acta*, vol. 257, no. 6, pp. 421–432, 1971.

[146] P. J. Shaw and G. J. Hills, "The three-dimensional structure of the cell wall glycoprotein of *Chlorogonium elongatum*", *Journal of Cell Science*, vol. 68, no. July 1984, pp. 271–284, 1984.

[147] D. W. Mackowski, "Calculation of total cross sections of multiple-sphere clusters", *Journal of the Optical Society of America A*, vol. 11, no. 11, pp. 2851, 1994.

[148] D. W. Mackowski and M. I. Mishchenko, "Calculation of the T matrix and the scattering matrix for ensembles of spheres", *Journal of the Optical Society of America A*, vol. 13, no. 11, pp. 2266, 1996.

[149] K. N. Liou, *An Introduction to Atmospherica Radiation*, Academic Press, San Diego, CA, 2002.

[150] J. Pruvost, J.-F. Cornet, F. Le Borgne, V. Goetz, and J. Legrand, "Theoretical investigation of microalgae culture in the light changing conditions of solar photobioreactor production and comparison with cyanobacteria", *Algal Research*, vol. 10, pp. 87–99, 2015.

[151] J. Pruvost and J.-F. Cornet, "Knowledge models for the engineering and optimization of photobioreactors", in *Microalgal Biotechnology: Potential and Production*, C. Posten and W. Christian, Eds., chapter 10, pp. 181–224. De Gruyter, Berlin, DE, 2012.

[152] I. Gifuni, A. Pollio, C. Safi, A. Marzocchella, and G. Olivieri, "Current bottlenecks and challenges of the microalgal biorefinery", *Trends in Biotechnology*, vol. 37, no. 3, pp. 242–252, 2019.

[153] J. Pruvost, V. Goetz, A. Artu, P. Das, and H. Al Jabri, "Thermal modeling and optimization of microalgal biomass production in the harsh desert conditions of State of Qatar", *Algal Research*, vol. 38, no. 101381, 2019.

[154] E. Simsek, M. J. Williams, J. Hoeniges, K. Zhu, and L. Pilon, "Infrared Radiation Transfer through Semitransparent Windows Supporting Absorbing Droplets", *Journal of Quantitative Spectroscopy and Radiative Transfer*, vol. 194, pp. 123043, 2022.

[155] P. M. Slegers, P. J. M. van Beveren, R. H. Wijffels, G. Van Straten, and A. J. B. Van Boxtel, "Scenario analysis of large scale algae production in tubular photobioreactors", *Applied Energy*, vol. 105, pp. 395–406, 2013.

[156] G. Marotta, J. Pruvost, F. Scargiali, G. Caputo, and A. Brucato, "Reflection-refraction effects on light distribution inside tubular photobioreactors", *Canadian Journal of Chemical Engineering*, vol. 95, no. 9, pp. 1646–1651, 2017.